LINEAR LIBRARY
C01 0068 3736
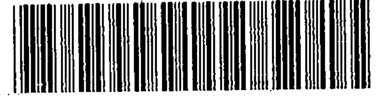

GROWTH AND CHARACTERISATION OF THIN FILM SUPERCONDUCTORS ON OXIDES, SILICON AND SILICIDES

by

R. Y. NAIDOO

Dissertation presented for the degree of

DOCTOR OF PHILOSOPHY

in the

Department of Physics
UNIVERSITY OF CAPE TOWN

Supervisor : Dr. R. Pretorius
Co-supervisor : Prof. C.M. Comrie

October 1993

University of Cape Town

The University of Cape Town has been given the right to reproduce this thesis in whole or in part. Copyright is held by the author.

The copyright of this thesis vests in the author. No quotation from it or information derived from it is to be published without full acknowledgement of the source. The thesis is to be used for private study or non-commercial research purposes only.

Published by the University of Cape Town (UCT) in terms of the non-exclusive license granted to UCT by the author.

University of Cape Town

DST 530 NAD.

94/9498

Acknowledgements

I wish to express my heartfelt gratitude, appreciation and thanks to some of the people without whose support, vision, assistance and help this work would not have been possible:

- Dr. R. Pretorius, Head of the Van de Graaff Group, National Accelerator, Faure, for his trust, guidance, encouragement and support that he gave during this investigation. His vision in initiating the superconductor programme and his confidence in my ability to successfully set up this project are commendable;
- Prof. C.M. Comrie, Physics Department, University of Cape Town, for the vast experience and thorough committment that he imparted to the project. His thought provoking discussions and meticulous attention to detail have left an indelible mark on this thesis and on me;
- Dr. D. Reitmann, Director of the National Accelerator Centre, for the use of facilities at the National Accelerator Centre;
- Dr. Terrence. K. Marais for his friendship, assistance and invaluable help with the computer programmes and word processors that made this thesis manageable;
- Dr. Terry Doyle and Dr. Richard Doyle, for the valuable lessons they have taught me and for making their low temperature facilities available for this project;
- Prof. W. Perold and Prof. D. McLachlan for the use of their laboratories;
- Prof. Frans Saris, for his valuable advice and expertise;
- Chris Theron, for the countless times he has helped with his computer expertise and for having to put up with sitting in the same room with the author for so many years;
- Stanley Hendricks, for his words of wisdom, display of common sense, his immense help with photographs, diagrams, figures and the final preparation of this document;

- Ginny Stone, who was forever cheerful and helpful in the face of unreasonable typing schedules and indecipherable handwriting;
- Karl Springhorn, John Pilcher and Cecil Churms for their assistance, advice and time, especially for helping with electronic equipment and their expertise with the mainframe computer;
- Piet Groenewald, for his assistance and immaculate preparation of some of the figures;
- William Gordon, Cupido Cloete, Willem Cloete, Stanley Hendricks and Henk Antonie, for their friendship, constant support and their words of wisdom,
- Bill Schmitt, Gert Ackermann, Piet Groenewald and Tobie Swart for their assistance with equipment, workshop facilities and the efficient running of the Van de Graaff accelerator;
- Randall Carolissen, Reggie Madjoe, Basil Julies and Hein Kesonk, for their support and friendship;
- To all my friends, the "Jones" clan, for their friendship and the regular volleyball games;
- To all my family, especially my mother and father, without whom none of this would have been possible;
- To Smokey, for all the times he kept me company late into the night, and for all the walks that he missed;
- Finally, and most importantly, to my wife Pam, who has had to sacrifice so much so that this was possible, who supported me with enthusiasm and love, who put her life on hold without question so that we may both achieve this, and for keeping my life in perspective through all of it. For her I reserve the greatest praise and say this one's for you.

Abstract

High T_c thin film superconductors are of great interest because of their potential applications, particularly in the microelectronics field. A successful superconductor microelectronic technology depends both on the ability to grow good quality superconducting thin films, and the need to incorporate these films into multilayer semiconductor devices. In this work the growth and characterisation of high T_c $Y_1Ba_2Cu_3O_7$ films by inverted cylindrical magnetron sputtering and pulsed ruby laser ablation on oxides, silicon and silicides is investigated. The inverted cylindrical magnetron sputter system has been effectively used to counter the problem of negative ion re-sputtering found in sputter deposition of oxide films. The optimal growth conditions for both these techniques have been determined. Rutherford backscattering spectrometry is used to obtain thickness and stoichiometry information, while X-ray diffraction gave phase and orientational data. Ion channeling was used for structural analysis and Auger electron spectroscopy was used to determine the homogeneity of the films. Electrical properties of the films were determined by resistivity and susceptibility measurements. Using the *in-situ* sputter deposition technique, high quality films were grown at 700°C on MgO and $SrTiO_3$ substrates. These films are c-axis oriented, display high transition temperatures (T_c) of up to 87 K, and have sharp transition widths, ΔT (1–2 K), and have low channeling yields (6–7%). Thin films of $Y_1Ba_2Cu_3O_7$ have also been grown on Si, Si<111>/silicide and Si<111>/silicide/metal oxide structures by sputter deposition at 700°C . The silicides considered were $CoSi_2$, $NiSi_2$, $CrSi_2$, PtSi and Pd_2Si. Direct deposition onto single crystal silicon and onto silicides resulted in severe interaction between the substrates and $Y_1Ba_2Cu_3O_7$. Buffer layers MgO, ZrO_2 and Y_2O_3 were therefore used in order to prevent such interaction and retain the superconducting properties of the film. The best superconducting films were obtained with buffer layers of MgO and ZrO_2 on single crystal silicon and on silicides of $CoSi_2$, $NiSi_2$ and PtSi. The formation of thin films of $Y_1Ba_2Cu_3O_7$ on Si<111>/$CoSi_2$/ZrO_2 structures, where the $CoSi_2$/ZrO_2 bi-layer structure was formed simultaneously by annealing an amorphous CoZr alloy layer in O_2, is also demonstrated. The $CoSi_2$ layer formed in this way is found to be aligned with the Si<111> substrate. $Y_1Ba_2Cu_3O_7$ films grown on this multilayered structure had fairly high T_c (81 K) and relatively sharp transition widths (3 K). $Y_1Ba_2Cu_3O_7$ films have also been grown on MgO (100) substrates by pulsed ruby laser ablation. The heatflow in the $Y_1Ba_2Cu_3O_7$ target irradiated with the pulsed ruby laser was simulated by a heatflow calculation. The laser energies required for the onset of melting and vaporisation were calculated, and were compared with experimentally determined values. It was found that the ruby laser can deposit superconducting material with near ideal stoichiometry. The spatial distribution of the deposited films display a $\cos^n(\theta)$ dependence ($8 < n < 12$) denoting a high degree of forward peaking. The amount of material deposited in an oxygen ambient of 10^{-1} mbar with an incident energy of 2 J/cm^2 was between 1.0 and 1.5 nm per pulse, for a target-substrate separation of 15 mm.

Contents

1 Introduction **3**

1.1 Growth of $Y_1Ba_2Cu_3O_7$ thin films 5
1.2 Solid state thermodynamics 9
1.3 Amorphous alloys 10
1.4 Scope of this investigation 12

2 Experimental details **15**

2.1 Substrate preparation 15
2.2 Laser ablation 16
2.3 Sputter deposition 18
2.3.1 Substrate heater 19
2.3.2 System preconditioning 23
2.3.3 Vacuum conditions 23
2.4 Electron-beam evaporation 24
2.5 Annealing 27
2.6 Sample characterization 28
2.6.1 Rutherford backscattering spectrometry 28
2.6.2 X-ray diffraction 30
2.6.3 Auger electron spectroscopy 31
2.6.4 Electrical measurements 31

3 Sputter deposition onto oxide substrates **35**

3.1 Films on MgO 36
3.1.1 Optimization of deposition conditions 36
3.1.2 Spatial distribution of deposited material 42
3.1.3 Effect of Substrate Temperature 44
3.1.4 Effect of substrate surface quality 52
3.1.5 Determination of oxygen content 56
3.1.6 Structural analysis by Ion Beam Channeling 58
3.2 Films on $SrTiO_3$ 65
3.3 Films on Al_2O_3 72
3.3.1 Direct deposition onto Al_2O_3 72
3.3.2 MgO buffer layer 77

3.4 Summary and discussion 82

4 **Thin film superconductors on silicon** **91**
4.1 Direct deposition onto silicon 92
4.2 Si/YBCO interactions 96
4.2.1 The Si-Cu system 96
4.2.2 The Si-Ba system 98
4.2.3 The Si-Cu-Ba system 99
4.2.4 The Si-Ba-Cu system 101
4.3 Oxide buffer layers 102
4.3.1 MgO buffer layers 104
4.3.2 Y_2O_3 buffer layers 107
4.3.3 ZrO_2 buffer layers 110
4.3.4 Electrical properties 113
4.4 Summary and discussion 117

5 **Thin film superconductors on silicides** **123**
5.1 Direct deposition of YBCO onto silicides 124
5.2 Silicon/silicide/metal oxide structures 128
5.2.1 Formation and characterisation 128
5.2.2 Thermal stability 130
5.3 Formation of YBCO on silicides with buffer layers 135
5.3.1 MgO buffer layers 136
5.3.2 Y_2O_3 buffer layers 140
5.3.3 ZrO_2 buffer layers 140
5.3.4 Electrical properties 145
5.4 Formation via amorphous CoZr alloys 150
5.4.1 Formation of $Si/CoSi_2/ZrO_2$ structures 151
5.4.2 YBCO on $Si/CoSi_2/ZrO_2$ formed via a CoZr alloy 158
5.5 Summary and discussion 161

6 **Pulsed ruby laser ablation of $Y_1Ba_2Cu_3O_7$** **173**
6.1 Modelling of heat flow 174
6.2 Experimental results 186
6.2.1 The effect of energy density 187
6.2.2 Thickness variation of deposited material 190
6.2.3 Thickness dependence on oxygen pressure 195
6.2.4 Superconducting characteristics 197
6.3 Laser annealing of YBCO films 201
6.4 Summary and discussion 204

7 **Summary and Conclusions** **211**

CHAPTER 1

Introduction

Thin films of the high T_c superconductor $Y_1Ba_2Cu_3O_7$ (YBCO) have generated a phenomenal amount of research activity since the discovery of these materials [**1–7**]. Prospects for practical electronic applications have driven the development of high T_c thin film technology at an unprecedented pace. Thin film technology has seen tremendous strides in fabrication, patterning and application of the high T_c material into useful devices and elements of devices. The application of superconducting thin films range from those requiring only single layers of superconductor-such as simple interconects, infra-red sensors and many passive microwave devices - to those based on complex multilayer devices. The development of high T_c superconductor electronic technology requires developing more than the superconducting films themselves. It also entails the development of a multilayer device technology that encompasses dielectric and normal-metal films.

The efforts to develop a superconducting thin film technology have faced unique challenges in terms of growing the highly anisotropic compounds, which has three metallic elements plus oxygen and whose properties are highly sensitive to crystal structure and oxygen content. In addition, the constituent elements from YBCO are highly reactive with a variety of other materials. This reactivity severely limits the choice of substrates and associated materials (dielectrics and normal metals) for making multilayer circuits. The high crystallisation temperature

of YBCO (600 - 900°C) also means that the reactivity between YBCO and other materials is enhanced during the formation of the superconducting phase.

Nevertheless, the development of films with chemical and structural purity, high transition temperature T_c and high current capacities J_c are just some of the aspects of thin film superconductor technology that have been almost perfected in the last few years [1–7]. The anisotropic nature of YBCO grains, where the current capacities in the a-b plane are 100 times higher than in the c-direction, have made the use of thin films particularly attractive. This is so because highly oriented or epitaxial films can be grown on a variety of substrates by various deposition methods [8–13]. The limiting of the density of grain boundaries and the high level of grain orientation means uniform high current capacities across the films and novel methods have been devised to use conventional thin film deposition methods to produce wires and films with high current carrying capacities.

The realization of a revolutionary generation of microelectronics based on high-T_c superconductors depends crucially on the ability to make high quality thin film microstructures. Such structures may be composed of multiple layers of superconducting films and dielectrics in combination with normal metals, low temperature superconductors and a variety of semiconductors. Such a structure will very likely be combined in a monolithic or integrated thin film structure. The basis of formation of such a structure is the deposition of good quality YBCO films and this remains a non-trivial issue.

Thin film superconductors can be grown by most of the known deposition methods [1–7]. The growth of high quality films generally requires epitaxial or heteroepitaxial layer formation. In this respect *in-situ* processing, as opposed to post-annealing processing, is the commonly used procedure [14–19]. In the high T_c thin film community, *in-situ* has come to signify a process whereby the film or multilayer is completely superconducting prior to removal from the deposition system. For the growth of *in-situ* superconducting films, pulsed laser deposition (laser ablation) and sputter deposition are currently the most widely used techniques.

1.1 Growth of $Y_1Ba_2Cu_3O_7$ thin films

Sputtering has long been the workhorse technique for the deposition of thin films. However, it is quite easy to imagine the difficulties that possibly arise from sputtering a target that has 3 metal components plus oxygen, is a ceramic and has low thermal conductivity. Surprisingly, though, the sputter deposition technique has been sucessfully applied to growing YBCO films [**3, 5, 20–26**]. Both single source and multi-source target sputtering can be used but single source sputtering of $Y_1Ba_2Cu_3O_7$ offers many advantages over multi source deposition, amongst which is the ease and simplicity of use. The multi-source sputter system relies on the concurrent deposition of the three metallic elements in an oxygen environment. For this technique the deposition rate of each element is virtually proportional to the power input. However, the drawback of multi source sputtering is the need to incorporate reactive oxygen into the deposited films. Even at low oxygen partial pressures (10^{-4} mbar) Ba and Y readily oxidize in the O^- discharge and the sputter rate of Y_2O_3 and BaO is orders of magnitude lower than that of elemental Y and Ba. The change of sputter rate varies for Y and Ba so it is almost impossible to compensate by adjusting power levels. Thus, the composition of the film will not be of the desired stoichiometry.

In general for alloys or compound targets, the flux of sputtered material contains the same ratio of elements as the bulk target (after sufficient presputter cleaning of the target) [**27**]. In principle, therefore the target can be made of bulk $Y_1Ba_2Cu_3O_7$. However, the use of a ceramic target must take into account the reduced sputtering yield and its low thermal conductivity. Heating of the target surface due to improper cooling can easily result in decomposition of the target into non-conducting oxides. A more severe problem in the sputter deposition of an oxide such as $Y_1Ba_2Cu_3O_7$ is the presence of negatively charged particles (O^-, O_2^-, BaO^-) emerging from the cathode and accelerated away from the cathode by the dark space voltage in the discharge [**22,28**]. These negatively charged species bombard the film surface and substrate with an energy comparable to that with which the argon ions bombard the target and can result in strong etching or resputtering of the deposited

film or radiation enhanced surface damage. These negative ions do not only arise from the target but also from the introduction of a reactive gas such as O_2, which is added to the sputter gas to compensate for oxygen deficiency in the film, generally due to a reduced sticking coefficient. The addition to the sputter gas has two effects [**18, 29–32**] : firstly, it increases the oxygen concentration on the target surface and the sputtered flux is enriched in oxygen, increasing the probability of incorporation into the film. Secondly, activated oxygen is provided directly onto the growing film; O_2 is dissociated in the discharge into atomic and ionic species that arrive at the film with a higher reactivity than the molecular species. While the introduction of oxygen increases the probability of film bombardment, increased gas pressure can lead to thermalization of the sputtered species and reduce the bombardment effects. Both reflected and sputtered atoms pass through the plasma region where they experience collisions with other atoms, electrons and ions. The number of collisions an atom makes is determined by the collision cross-section, while the probability of collision is determined by the mean free path, which is inversely proportional to the gas pressure. This means that the energy of the particles reaching the substrate will decrease with increasing gas pressure or (increased) distance between target and substrate. These low energy atoms are said to be thermalized in that they do not have directionality but appear to diffuse towards the substrate. The thermalization effect is especially important in preventing the bombardment of the deposited film. A correlation of target-substrate distance vs gas pressure [**27**] reveals the regions in which the sputtered atoms are considered energetic or thermalised (**Fig 1.1**). The diffusive nature of the thermal atoms implies that sputtered atoms can deposit onto the back of the substrate as well as on the front. The adverse aspect of thermalization is that the deposition rate will be greatly reduced as energetic atoms have more linear trajectories towards the substrate than thermal atoms and the amount of material deposited is statistically reduced. A balance has to be struck between deposition rate and particle bombardment rate, determined both by the sputter system geometry and the sputtering pressure. At this balance the atoms will have a distribution of energies and trajectories but will reach the substrate with some intermediate average

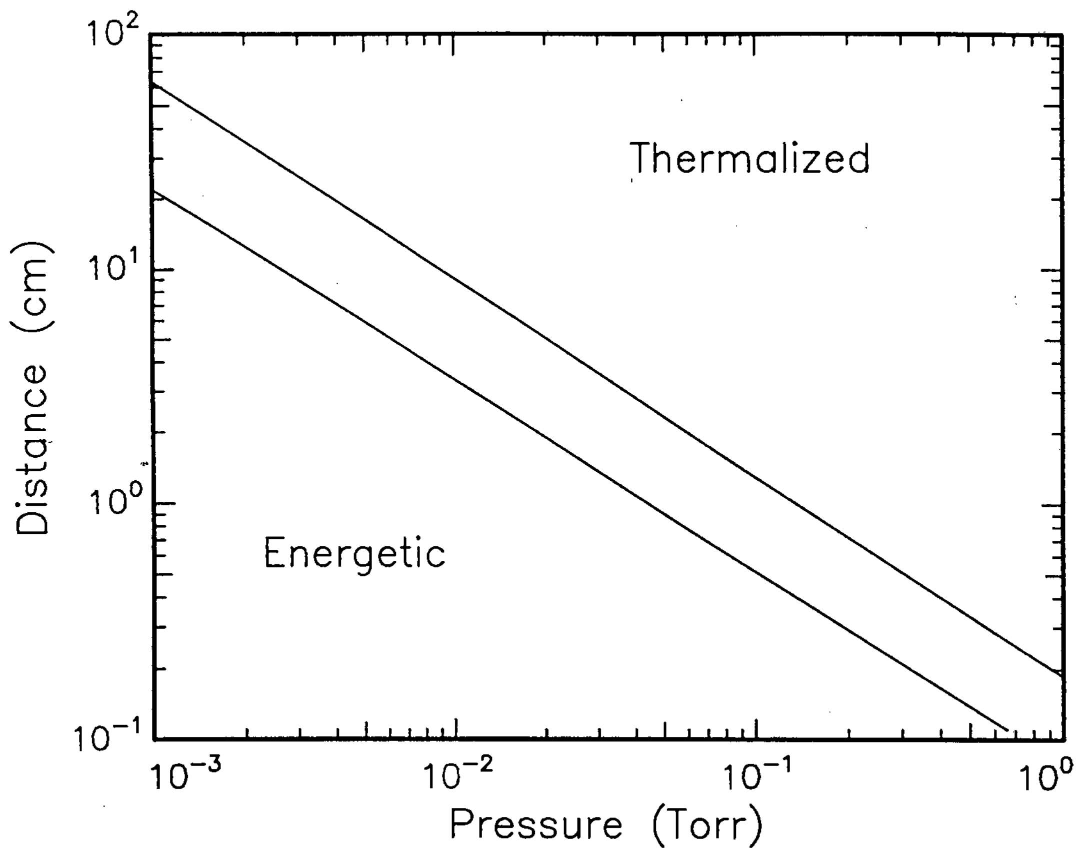

FIGURE 1.1: *Diagram of the target-substrate separation distance versus pressure describing the conditions in a sputter deposition experiment with the lower section denoting strong bombardment of the substrate by energetic particles. At high pressure and large separation distances the fast particles are thermalised before reaching the substrate (adapted from Ref.*[**27**]*).*

value.

The introduction of reactive gases implies that the target can be formed from an alloy of Y, Ba and Cu in $Y_1Ba_2Cu_3$, which will have better heat conduction and give a higher deposition rate than the ceramic. However, the 1-2-3 alloy does not form easily and the ceramic target is usually good enough if one can optimize the deposition to bombardment rate. Fortunately, the deposition to bombardment rate does not only depend on gas pressure, but also on substrate positioning [**26, 3, 2**]. It was mentioned previously that the thermalizing effect implies that thermal atoms can deposit on any face if the substrate due to their diffusive motion whereas

the energetic bombarding atoms (ions) have a direct line motion from target to substrate. The optimal substrate position can then be found when the deposition to bombardment ratio is maximized. In some cases this position is at the centre of the plasma ring, facing the target plane, while in other situations it may be outside the plasma and at some angle to the target plane. In one specific geometry that utilizes such a position [**33**], two planar targets face each other and the substrates are placed outside the region between the targets. The negative potential at the target implies that only those particles neutralized by stripping in the gas discharge will be able to reach the opposite target as these neutrals will not be influenced by the potential on the target. The natural conclusion of such a geometry is to place a series of targets in a circle or to use a hollow ring-shaped target. This is sometimes known as the hollow cathode sputter system. This particular geometry is of special interest to this investigation as the sputter system being used to deposit the superconducting thin films, called an Inverted Cylindrical Magnetron (ICM), is based on this geometry [**34**]. The preparation of films with the ICM is discussed in Section 3.

Pulsed laser deposition has played a pivotal role in the development of high T_c thin films mainly because it overcomes the many challenges involved in depositing YBCO films. These include the stoichiometric deposition of $Y_1Ba_2Cu_3O_7$ and the ability to work in high oxygen pressures [**14–19**]. The advantages of the laser deposition approach also stems from the ease at which the technique can be used, requiring only a pulsed laser, a vacuum chamber, a heated substrate holder and a YBCO target. In addition pulsed laser deposition is a much faster technique than off-axis sputtering and can be used as a conventional deposition technique for the growth of other components of a multilayered structure. Recently pulsed laser deposition has also been successfully applied to YBCO thin film technology with the development of active Josephson junction devices which are essential ingredients in superconducting circuitry [**35, 36**]. The *in-situ* processing method has been facilitated by the non-equilibrium nature of the pulsed laser deposition process. Although the advantages of this technique have made it popular for the deposition of high T_c films [**37–41**],

understanding the nature of pulsed laser deposition [42–47] relies on the correlation of extensive experimental data. The pulsed laser deposition process is known to be wavelength dependent [41, 48, 49] and the use of a visible wavelength laser (λ = 694nm) in this investigation will enhance the understanding of the ablation phenomena.

1.2 Solid state thermodynamics

Materials consist of phases or a mixture of phases. A phase can be defined as a portion of the system whose properties and composition are homogeneous and which is physically distinct from other parts of the system. A phase has a set of properties including thermodynamic properties, such as entropy, enthalpy and Gibbs free energy. The phase may or may not be in an equilibrium state. The reason why a material undergoes a phase change is because the initial state is unstable relative to the final state. The relative stability of a system is determined by its Gibbs free energy (G). At constant temperature and pressure the change in Gibbs free energy is given by:

$$\Delta G^{\circ} = \Delta H^{\circ} - T\Delta S^{\circ}, \tag{1.1}$$

where ΔH is the change in heat of formation (enthalpy), T the absolute temperature, and ΔS the change in entropy of the system. Enthalpy is a measure of the heat content of a system and is given by $H = E + PV$ where E is the internal energy, P the pressure, and V the volume. The internal energy arises from the total kinetic and potential energies of the atoms within the system. Kinetic energy arises from atomic vibrations in solids or liquids and from translational and rotational energies for the atoms or molecules within a liquid or gas. Potential energy on the otherhand arises from the interactions, or bonds, between the atoms in a given system. If a transformation or reaction occurs the heat that is absorbed or evolved will depend on the change in the internal energy of the system. However, it will also depend on the change in volume of the system, so that at constant pressure the heat absorbed or evolved is given by the change in H. When dealing with condensed phases (solids and liquids) the PV term is usually very small in comparison with E, so that $H \sim E$.

Furthermore, because the term $T\Delta S^\circ$ is usually very small for solid state reactions (ΔS° is only of the order of 0.001 kJ/deg per mole of atoms [50]), the change in enthalpy or heat of formation is a good approximation of the change in Gibbs free energy i.e.

$$\Delta G^\circ = \Delta H^\circ, \tag{1.2}$$

It should therefore be possible to use heats of formation to predict the phase formation sequence when activation or nucleation barriers do not exist, as a system would always want to go to its lowest possible free energy state. It must however be emphasized that during solid-state interaction, phase formation at an interface is a dynamic non-equilibrium process and it is usually found that only one compound phase forms at a particular interface, which is unlike equilibrium systems where formation of a mixture of phases might lead to the lowest free energy state for the system.

1.3 Amorphous alloys

Amorphous alloys have many unique features which mainly arise from the absence of grain boundaries in these materials. The lack of grain boundaries which can act as a fast diffusion path makes these materials good diffusion barriers in the semiconducting industry. In addition, the low magnetic losses exhibited by some amorphous alloys give them improved performance for magnetic recording and the amorphous mix can be used as a starting material to obtain specifically desired crystalline phases without the formation of intermediary phases.

The formation of multilayers (other than YBCO) from an amorphous alloy as part of an integrated structure is considered in this investigation. The alloy is formed by solid-state reaction of two crystalline materials and a basic understanding of the thermodynamics behind alloy formation is worthy of consideration. The foundation of examining the formation of the alloy is the heat of formation, ΔH. Various methods exist to estimate heats of formation when they are not known [50, 51]. Existing techniques are based on using relationships in homologous series, electronegativities, volume changes, heats of solution and packing effects [50]. Oth-

er calculation based techniques use microscopic theory of bonding for equiatomic compounds [**52**] or more exact approximations over the whole composition range for alloys of transition metals [**53, 54**]. Computer programs [**55**] that can calculate, from first principles, heats of formation for solid binary intermediate phases having a cubic crystal structure have been developed. Some of these techniques are however not very reliable and most cover only a relatively small number of compounds, and thus have limited application. However, their partial success strongly suggests that the problem may be solved from a limited set of parameters.

The macroscopic atom model of Miedema [**56**] for calculating heats of formation is a semi-empirical model of alloy cohesion involving essentially only two material constants for each element. Although the model is semi-empirical, these constants are introduced by a consideration of the underlying physical ideas thought to play a role in the cohesion of alloys. This model has proved to be very useful in a wide variety of thermodynamic problems, such as in estimating the enthalpy of formation of vacancies, predicting the crystallization temperature of amorphous alloys and problems concerning metal adsorption on metal substrates [**57**], for example.

The formation of amorphous alloys has been extensively considered in terms of thermodynamics. From the Miedema model [**56**], the formation enthalpy of an amorphous alloy is calculated by:

$$\Delta H^{am} = \Delta H^{chem} + 0.0035\overline{T_m}(kJ/mole), \tag{1.3}$$

in which T_m is the average melting temperature of the solid (in Kelvin). The term T_m reflects the disordered nature of the amorphous phase and compares with the heat of fusion for liquids. The heat of formation of, ΔH^{chem}, may be calculated as a function of concentration where the electron density at the surface of the Wigner-Seitz cell, n_{WS}, and an adjusted value of the work function, ϕ^*, are the material constants.

1.4 Scope of this investigation

This investigation concentrates on two fundamental aspects that are vitally important in considering the growth of thin film superconductors viz. the deposition method used and the substrate used. When considering the deposition method for the growth of (good quality) YBCO thin films, it was noted that virtually all the known thin film deposition techniques could be employed to grow YBCO thin films. A survey of the literature shows that by far the two most successful methods for the growth of YBCO films are single target off-axis sputtering and pulsed laser ablation. This investigation forms the basis of an effort to set up such facilities and analytical techniques for the growth and characterisation of $Y_1Ba_2Cu_3O_7$ thin films at the Van de Graaff group of the National Accelerator Centre. The initiation of a superconductor research programme meant that new facilities and techniques had to be built up. It is for this reason that this investigation details some developmental work that is widely covered in the superconductivity literature. This investigation is also intended as the foundation for future studies in thin film superconductivity at the Van de Graaff Group of the National Accelerator Centre.

Off-axis sputter deposition is a popular method for depositing YBCO thin films, especially as a counter-measure to the film bombardment evident with on-axis sputtering. It is with this consideration that the fairly novel Inverted Cylindrical Magnetron (ICM) sputter deposition technique is used for the growth of YBCO films. The parameters for optimal growth by ICM sputter deposition are determined and the system is used to deposit YBCO films onto a variety of substrates. The major part of this investigation involves films deposited by ICM sputtering. In considering the substrates, the following systems have enjoyed investigation:

- single crystal oxide substrates such as MgO, $SrTiO_3$ and Al_2O_3.
- single crystal Si substrates and,
- silicide substrates.

The composition, thickness, homogeneity and quality of films on all substrates was assessed with Rutherford Backscattering Spectrometry (including ion channeling), Auger electron spectroscopy, X-ray diffraction, resistivity and A.C. susceptibility electrical measurements. The details of the experimental procedures for the growth and characterisation of the thin films is given in chapter 2.

Chapter 3 details the growth and characterisation of $Y_1Ba_2Cu_3O_7$ films on MgO, $SrTiO_3$ and Al_2O_3. The oxide substrates are used in order to provide a means of assessing the efficacy of the deposition systems and as a basis for comparison of films grown by ICM sputter deposition with those grown by other deposition methods. This can be done because of the large amount of literature available concerning the growth of $Y_1Ba_2Cu_3O_7$ films on these substrates.

The interest in the growth of thin film superconductors on Si substrates arises from the numerous potential applications that stem from merging superconductor and semiconductor technologies. A large number of techniques have been described in the literature, to grow YBCO films on Si and mixed results (mostly poor) were found. Likewise, it is seen (chapter 4) that buffer layers are necessary to prevent the Si-YBCO interaction. The growth of buffer layers of MgO, Y_2O_3 and ZrO_2 on Si is described and the subsequent deposition of YBCO films is researched.

Silicides are extensively used as contacts and interconnects in silicon-based devices and the growth of YBCO films on silicides forms part of an integrated approach for the growth of multilayered structures on a single monolithic device. In addition, formation of YBCO on silicides has received little attention and prompted the study of deposition of YBCO films onto $CoSi_2$, $NiSi_2$, PtSi, $CrSi_2$ and PdSi. Once again, the reactivity of Si (in the silicide) with YBCO required the presence of a passivating buffer layer between the silicide and the YBCO layer. The growth of MgO, Y_2O_3 and ZrO_2 onto silicides was therefore examined in chapter 5 and the deposition and characterisation of YBCO films grown on Si/silicide/metal oxide substrates was investigated.

A novel method for the simultaneous formation of a silicide/metal oxide system from an amorphous alloy is also illustrated in chapter 5 by forming a Si<111>/$CoSi_2$/ZrO_2

structure from a Si<111>/α-CoZr structure. The formation of the amorphous alloy via the solid state reaction method of interacting crystalline Co and Zr for long times at temperatures below the crystallization temperature of the Co-Zr alloy is also demonstrated. First phase formation of $CoSi_2$ in this system is considered in terms of thermodynamic factors and the effective heat of formation model is successfully applied to predicting the phase sequence from the alloy. Growth of YBCO films on the Si<111>/$CoSi_2$/ZrO_2 structure is investigated and the electrical properties of such films determined.

The study of laser ablation with a pulsed ruby laser has not received much attention and an investigation into the laser ablation process and the parameters for forming superconducting thin films of $Y_1Ba_2Cu_3O_7$ by pulsed ruby laser ablation is conducted in chapter 6. The fundamental process of laser-solid interaction is also an important issue and the interaction of the pulsed ruby laser with the bulk YBCO target is investigated. Details on the effects of laser energy density, target substrate separation and gas pressure on the laser ablation process are studied. The growth of YBCO films by pulsed ruby laser deposition is investigated and the use of the pulsed ruby laser to create depth controlled damage and to anneal high quality YBCO films is also examined.

CHAPTER 2

Experimental details

2.1 Substrate preparation

MgO<100>, $SrTiO_3$<100> and Al_2O_3<1112> single crystal substrates, used as substrates for $Y_1Ba_2Cu_3O_7$ films, were obtained from KristalHandel Kelpin (cut to our specified dimensions of lengths and thickness, typically 10 x 10 x 0.5 mm) with one face polished. Si<100> and Si<111> single crystal samples (Wacker) were used as substrates for the growth of silicides, metal-oxide films, multilayer films and $Y_1Ba_2Cu_3O_7$ films. The Si substrates were cut from 76.2 mm diameter polished wafers into 10 x 10 mm pieces using a diamond scribe. The Si-wafers were n- or p- doped with resistivity of 1.5 - 2.5 Ω cm. All substrates were sequentially degreased by ultrasonic cleaning in solutions of methanol, acetone and trichloroethylene. The cleaning sequence was then reversed before washing in a deionized (DI) H_2O solution. The removal of the native oxide layer on Si is considered an essential step for obtaining high quality epitaxial films or buffer layers. For the removal of the native oxide layer the Si substrates were etched for 5 minutes in a 20% HF solution. The substrates were then rinsed in water, oxidized in RCA solution (NH_4OH : H_2O_2 : H_2O = 1:1:5) for 5 minutes and subsequently etched in 6% HF solution for 5 minutes. This cleaning procedure is supposed to result in the reduction of the surface native oxide layer (SiO_2) from $\sim$ 2 nm to 0.5 nm, and the Si bonds

at the surface are reportedly terminated with hydrogen so that further oxidation is prevented [58]. MgO and $SrTiO_3$ were annealed at high temperatures (1000°C) in an O_2 flow of more than 1 atmosphere. This leads to the formation of a high density of atomic steps on the surface and desorbs surface contaminants [59, 60].

Due to the high cost of single crystal substrates such as MgO<100> and $SrTiO_3$ <100> we have also investigated the re-use of those substrates onto which film of $Y_1Ba_2Cu_3O_7$ had previously been deposited. This involves etching the $Y_1Ba_2Cu_3O_7$ film from the substrate and then chemically polishing the substrate or sputter etching a few layers off so that a fresh surface may be available for deposition. For the MgO substrates a hot HPO_4 etch was used as a chemical polish and is expected to yield an atomically smooth surface [59]. A mixture of HNO_3 : HF : H_2O = 1:1:2 was used for cleaning the surface of $SrTiO_3$ substrates. A high temperature anneal at 1000° in O_2 or air for 15 hours was used for both MgO and $SrTiO_3$, a procedure that results in the formation of a high density of atomic steps on the substrate surface. Films deposited onto the recycled substrates were not as good as those on virgin substrates and all the results presented in this study were on fresh substrates.

2.2 Laser ablation

A Q-switched pulsed ruby laser (**Fig. 2.1**) with a wavelength of 694 nm and a pulse width (duration) of 30 ns was used for the laser ablation of $Y_1Ba_2Cu_3O_7$. The laser is capable of attaining a maximum peak energy of 1.5 J with the energy density incident on the target being dependant on both the incident energy and the beam spot area at the target. By changing the beam spot area it was possible to vary the energy density on the target up to 35 J cm^{-2} without affecting the quartz window through which the beam passes. The energy of the outgoing pulse is obtained by passing the pulse through a 1% partially reflecting mirror. The reflected beam passes into an energy-meter for calibration of the laser pulse energy. The ruby laser is sensitive to surrounding variations in temperature and is maintained in a temperature controlled environment at 20°C to give reproducible energy values. The

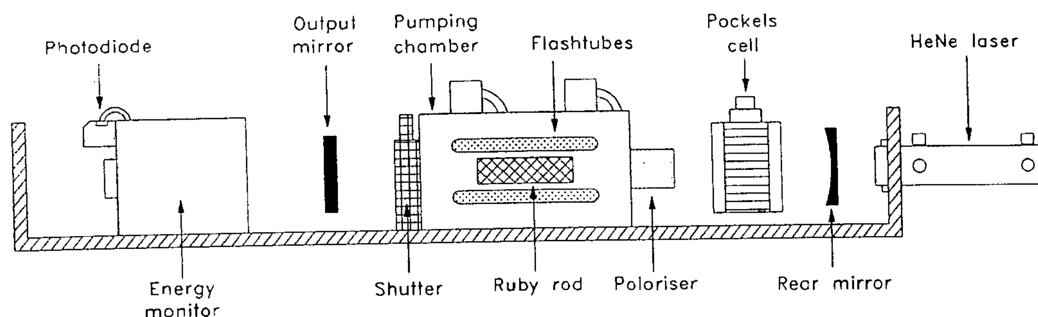

FIGURE 2.1: Schematic illustration of the active components of the Q-switched pulsed ruby laser.

ruby laser beam is aligned with the use of a secondary He-Ne constant wave laser situated at the rear of the ruby laser cavity. The He-Ne laser beam passes through exactly the same optics as the ruby laser pulse itself. The outcoming laser beam is focussed to the required beam size with a pair of lenses that are mounted on an optical track. The beam enters the vacuum chamber through a clear quartz window and impinges on the target at an angle of 45° (**Fig. 2.2**).

The target is a 15 mm diameter, 5 mm thick hot pressed disk of $Y_1Ba_2Cu_3O_7$ (Aldrich Metals) and is bonded to the brass target holder with silver epoxy paint. The target was tested for superconductivity and found to have a transition temperature of 90 K. Rutherford backscattering spectrometry and X-ray diffraction (see later) was used to verify the composition and crystalline state of the target as a superconductor. The bulk targets were maintained under vacuum to prevent degradation of the surfaces by water vapour or CO_2 incorporation. Clean target surfaces for deposition of films could be obtained by removing surface impurities by ablating off a few layers. A shutter was placed over the substrates during the target pre-conditioning to prevent deposition of the unwanted impurities onto the substrate.

The target chamber is evacuated to pressures of better than 10^{-6} mbar prior to deposition. The pumping chamber is designed to work with high gas pressures by using a throttled pumping system: a gate valve between the turbo-pump and the main chamber is closed off and the deposition chamber is evacuated via a bypass tube

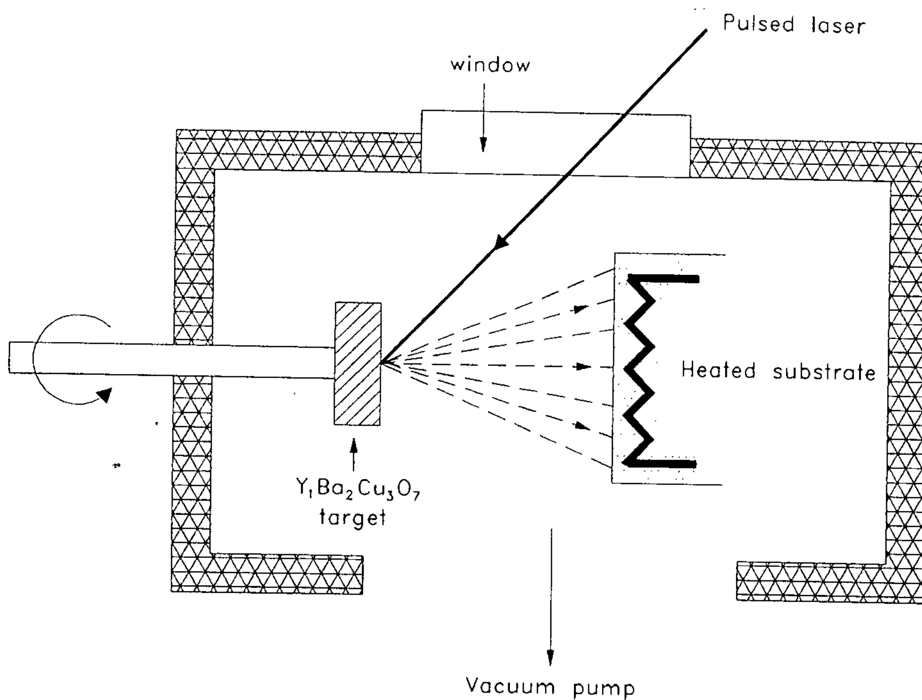

FIGURE 2.2: Schematic illustration of the laser ablation technique for the deposition of thin film superconductors.

that has a considerably smaller opening. This results in a differential in pressure between the turbo pump stage and the deposition chamber and allows for the introduction of oxygen gas (O_2) up to 1 mbar without damage to the turbomolecular pump. All depositions were performed in an oxygen ambient of 10^{-1} mbar

2.3 Sputter deposition

Reactive sputter deposition was used for growing the thin film $Y_1Ba_2Cu_3O_7$ superconductors. The sputtering is reactive in that oxygen is one of of the constituents of the target and is also used as a component of the sputtering gas. This enables oxygen inclusion into the growing film and the sputtered flux while also maintaining the oxygen level in the target. The sputter gun is called an Inverted Cylindrical Magnetron (ICM) gun [34] and is an extension of the commonly use method of off-axis sputter deposition [61]. The $Y_1Ba_2Cu_3O_7$ target is a cylinder of material

mounted on the cathode and the substrates are situated on a heated holder perpendicular to this cylinder and along its central axis. The $Y_1Ba_2Cu_3O_7$ target was tested by X-ray diffraction of a powder sample scraped from the target surface and found to reveal the correct crystalline phase.

Fig. 2.3 is a schematic illustration of the ICM gun. The hot pressed and sintered $Y_1Ba_2Cu_3O_7$ target is mounted as a 5 mm thick and 25 mm high cylinder onto the cathode with thermal solder. The ring magnets and target assembly are attached to a water cooled backing plate that limits heat buildup in the target and magnets. The extremely high temperature of the substrate heater (700°C) can cause decomposition of the target during sputtering and induce variations of sputter rate and deposited stoichiometry. Since the ICM gun is used in the DC sputtering mode, decomposition of the target into non-conducting species will also seriously affect the sputtering process and can cause extinction of the sputter plasma, hence the oxygen flow over the target is required to keep the $Y_1Ba_2Cu_3O_7$ target surface conducting. The oxygen deficient $Y_1Ba_2Cu_3O_6$ is insulating whereas $Y_1Ba_2Cu_3O_7$ is a conductor at room temperature. The ring magnet assembly is adjustable in the vertical direction so that new areas of the target can be used for deposition. The height of the substrate holder is adjustable for maximizing the deposition rate while minimizing the re-sputtering effect.

2.3.1 Substrate heater

The high temperatures and high oxygen pressure used during deposition with the ICM sputter gun has necessitated the design of a reliable substrate heater which can operate for long periods in an oxidizing atmosphere. Radiant heating with filament bulbs has limited use for our application due to the limited lifespan of the bulbs. Non-homogenous distribution of the radiated heat across the substrate area can seriously affect the film quality. Poor thermal transfer also gives rise to thermal lag between the measured and true temperature of the substrate. For instance, Westerheim [62] has shown that radiative heating of $LaAlO_3$ substrates with a radiant heater gives a discrepancy of 200°C between the measured temperature and

the actual surface temperature. The actual temperature was found to be lower because of poor thermal contact. From the work of others [**17, 63, 64**] and as we shall see later (Chap 3), the substrate temperature is of critical importance in forming good superconducting films.

The heater assembly we have designed and constructed consists of a Thermocoax heating element (Thermocoax, Philips) wound into a coiled spiral and sandwiched between two stainless steel plates. The coaxial element has a central Ni/Cr wire core as the heating element enclosed by compacted by MgO powder and isolated from a outer sheath of Alconel . The outer sheath serves to prevent oxidization of the element. The compacted MgO powder gives good thermal transfer from the element to the outer sheath because of the high thermal conductivity of MgO and the compact nature of the powder and also allows for the use of the heater in non-grounded potentials as the potential across the heater core is not affected by substrate biasing or the plasma potential. The stainless steel sandwich is 30 mm in

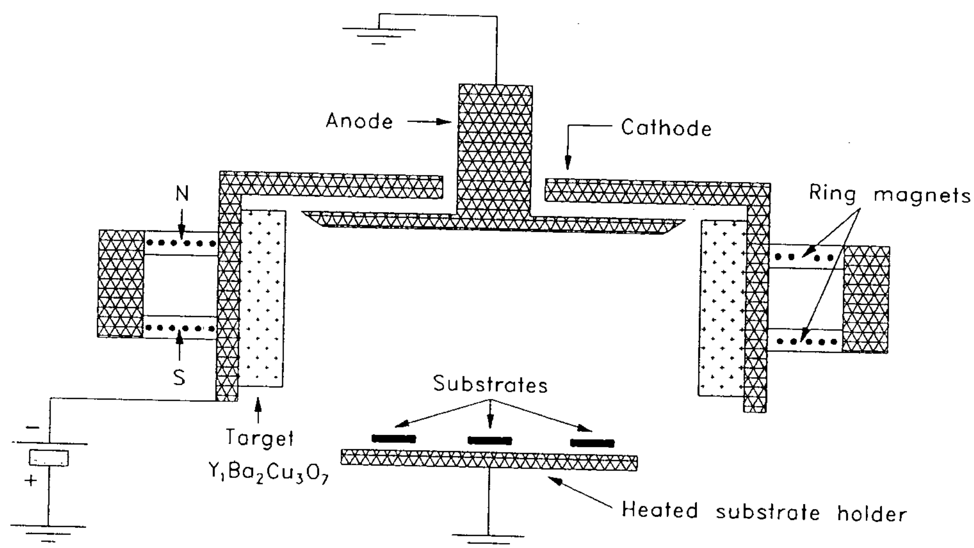

FIGURE 2.3: Schematic of the Inverted Cylindrical Magnetron (ICM) sputter gun. The YBCO target forms a cylindrical ring target with the circular magnet system enclosed behind the target. The anode and cathode (target) are perpendicular to each other and the substrates lie perpendicular to the target.

diameter and consists of two plates 2.5 mm thick and bolted together. The upper plate has a 1 mm recessed groove region to allow for the diameter of the element. The active heating element length is 50cm and tight packing of the coil ensures that there is little chance for the occurrence of "cold" regions in the sandwich. The sandwich gives maximal heat transfer to the substrates while the thickness of the plates is enough to ensure rigidity and flatness of the assembly, even with multiple thermal cycling. To reduce heat loss the heater sandwich has reflective radiation shields on either side. The highly polished thin stainless steel shields completely enclose the lower section of the sandwich whereas the upper shield has openings to allow the sputtered vapour onto the substrate. A water cooled copper shroud for the lower section of the sandwich reduces radiant heating of the chamber walls and fittings, thereby maintaining good vacuum. The water cooling system also assists in controlling the drop in temperature after deposition and can enable quick sample turnaround.

The Thermocoax element has long cold ends i.e. ~1m outside of the 50cm heating region the element wire is a low resistance ZrCu alloy. This portion of element does not heat up as Ni/Cr does and results in a sharp thermal gradient from the hot region at the substrate holder to the electrical power connectors. The thermal gradient enables us to solder the ends of the element to the power connects with ordinary solder and no special cooling or precautions have to be taken for thermally isolating the connectors. The entire heater sandwich with cooling shroud is attached to a thin-walled stainless steel tube that is clamped to the inside of the vacuum flange. Sample turnaround is thus easily brought about by removing the vacuum flange together with the entire heater assembly. Argon and oxygen gas is flowed through the the chamber during sample changing. A type K thermocouple is welded to the surface of the heater assembly. The temperature of the substrate heater is controlled by a Eurotherm temperature controller and powered by a 120 V Variac power supply.

Thermal contact between the heater and the substrates was achieved by painting the back of the substrate with silver paint and curing these at 120°C for 1 hr.

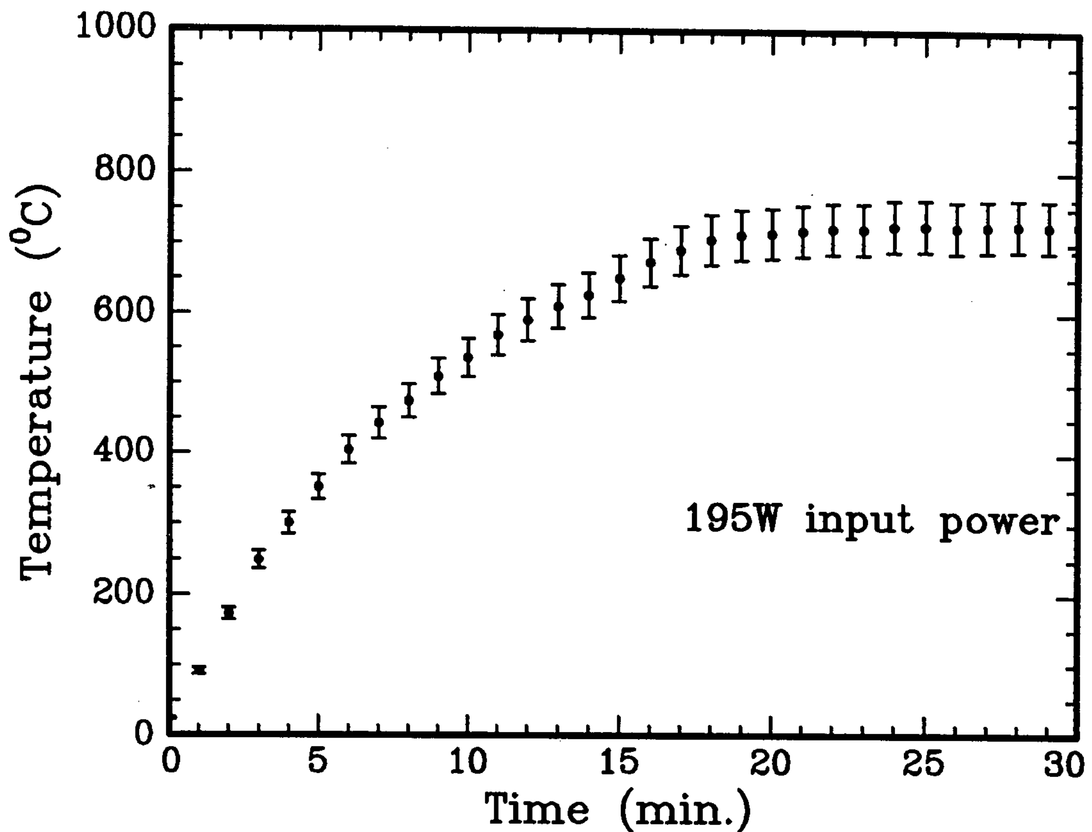

FIGURE 2.4: Temperature profile of the substrate heater performance as a function of time for an input power of 195 W in a gas pressure of 4.5×10^{-1} mbar of Ar/O_2.

The substrates were then attached to the substrate holder with an additional film of silver paint. The excellent thermal transfer achieved with this method has been documented by others [62,65]

Fig. 2.4 shows the rise in temperature with time of the heater for an input power of 195 W in $4.5\text{x}10^{-1}$mbar Ar/O_2 pressure. The heater was tested under conditions that simulate an actual deposition. We can see that it takes roughly 20 minutes to reach the desired temperature level. Higher input powers will result in faster rise times but it was found that rapid heating often results in peeling and blistering of the silver epoxy film, leading to poor thermal contact and lower temperatures at the substrate. The heater assembly has been used for over 100 hours of deposition time and not yet required any maintenance.

2.3.2 System preconditioning

System preconditioning is used to run the sputter system, without deposition onto the substrates, in exactly the same way it would be run during a deposition. This has the effect of outgassing fixtures and target materials, removing the surface layers which may have impurity gases or phases and coating the systems fixtures with the material to be deposited thereby minimizing subsequent contamination of the depositing film [66]. This can be done by removing oxide layers from pure metal targets, outgassing the target and correcting any alterations in surface stoichiometry. The sub-oxides that are sputtered away and contaminants such as H_2O that are broken down in the discharge can cause high discharges currents which decrease as the contaminants are removed. In this sense preconditioning is very important in that the surface oxide or contaminated layer generally has poor electrical conductivity and is very susceptible to spurious electrical activity in the form of sparking and power arcing. A power arc will constrict the centre discharge current into a small cathode spot which moves rapidly over the surface under the effect of the crossed electric and magnetic fields (ExB) motor action. Under these conditions the discharge voltage falls rapidly and the corresponding arc current is greatly increased. High current values can lead to extreme cathode surface arcing, known as "racetrack arcs", in which the arc spot melts the material as it moves along the target surface, leaving a deeply eroded furrow. Such power arcs were controlled by using a current limited power supply. In general presputtering should be carried out so that all deposition conditions (voltages, pressures, temperatures, etc) should be exactly the same as those used during deposition.

2.3.3 Vacuum conditions

The ICM gun is mounted in a double cross-piece vacuum chamber on a standard DN 100 CF flange with a mounting depth of 120 mm. The substrate holder is situated 15 mm from the sputtering head. The vacuum chamber is evacuated by a turbomolecular pump backed by a rotary pump. The vacuum system is separated from the deposition section by a pneumatic gate valve which is bypassed by a

constricted diameter bellows tube with an adjustable flow control valve. This allows for differential pumping on the upper and lower chambers thus enabling the use of the high gas pressures needed during sputtering (up to 1 mbar) without causing damage to the turbomolecular pump. The gate valve is opened during the pump-down stage for fast evacuation of the chamber and kept closed during deposition. High purity Argon and Oxygen gases are fed into the system via the ICM gun and their levels are independantly controlled by a pair of Leybold Leak Valves with a leak range of 10^{-5} mbar $\rightarrow$ 100 mbar. The gas pressure in the chamber is monitored by both Penning and Pirani vacuum gauges mounted into the chamber wall. A glass port window allows for visual monitoring of the deposition process. A schematic of the sputter deposition apparatus is shown in **Fig. 2.5**.

A Heinzinger constant current source was used as the power supply for the ICM gun. The (copper) water cooling tubes are also used for attachment of the sputter voltage supply. At the low operating voltage used during sputter deposition no special means are required to prevent current flow from the target to ground potential via the cooling water. The ICM gun was operated at a current of 500 mA and a voltage of 150 V with an Argon/Oxygen gas mixture in the ratio 2:1 with the total pressure at 4.5×10^{-1} mbar. The Argon/Oxygen mixture is used instead of pure Ar or pure O_2 because for the case of pure Ar, the supplementary oxygen is required to keep the target conducting and provide O_2 to the growing films. The use of pure O_2 is undesirable because energy is required to first break the O_2 molecule and then ionise the two oxygen atoms, resulting in a lower kinetic energy of the bombarding oxygen ions. This results in preferential sputtering and deviation from stoichiometry which is complicated by the ionisation of O_2 molecules which also bombard the target.

2.4 Electron-beam evaporation

Buffer layers and silicides films were prepared using a high power e-beam evaporation system in ultra-high vacuum. The e-gun system consists of a tungsten filament which produces electrons when a high current is passed through it. The cathode

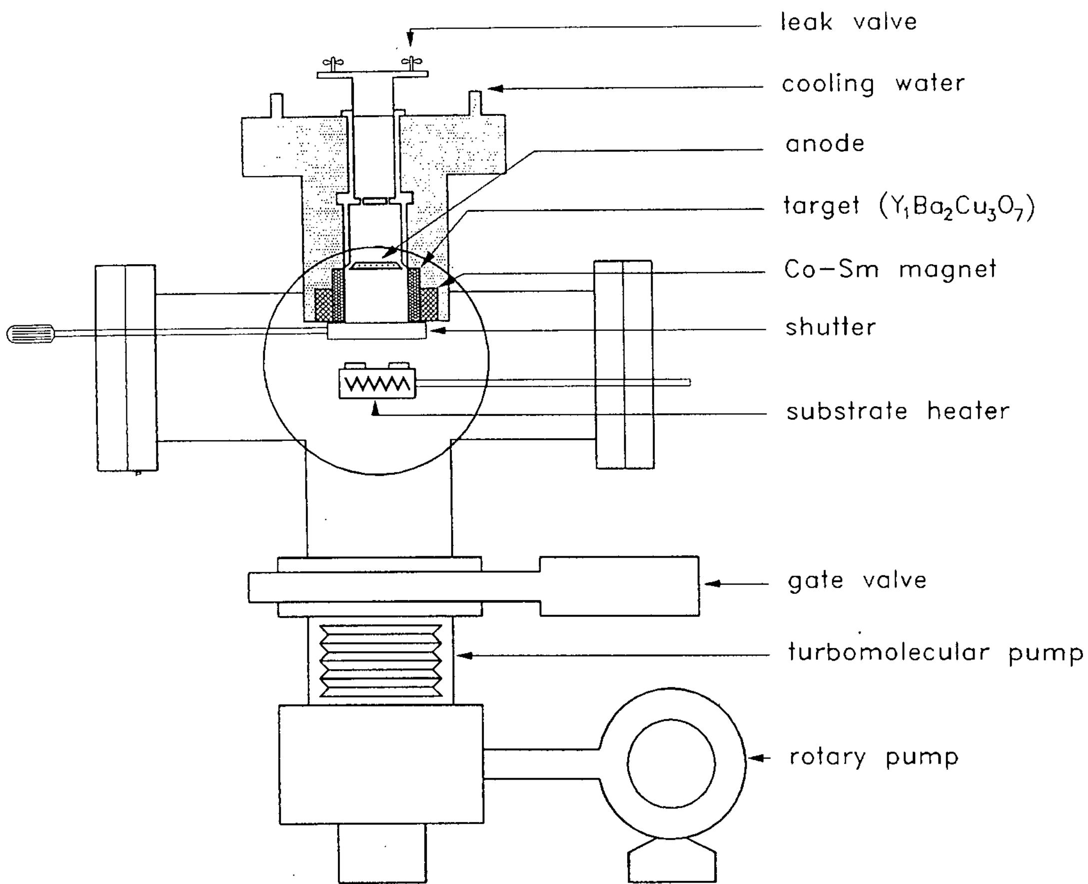

FIGURE 2.5: Schematic of the sputter deposition system showing the ICM gun positioning and the vacuum components. The deposition stage could be isolated from the vacuum pumps with a gate valve and vacuum is maintained by a bypass tube. This allows differential pumping and the use of high gas pressures during deposition.

(filament) is hidden from direct line of sight of the molten pool to prevent erosion by ion bombardment during evaporation and the electrons are steered towards the target material by a combination of electric and magnetic fields. The target material is contained in one of 3 water cooled copper crucibles. The crucibles are thoroughly cleaned between depositions of different materials to prevent possible contamination of the deposit.

The evaporated materials deposits onto substrates situated in a carousel system which allows for deposition onto many substrates. The rate and thickness of material deposited is monitored by an oscillating quartz crystal monitor. The vacuum

system consists of two sections (**Fig. 2.6**), an upper glass bell jar arrangement which is pumped by a rotary and a turbomolecular pump which can bring the pressure of the system down to 10^{-6}Torr. The lower pumping section contains a VacIon sorption pump, a Ti sublimation pump and a liquid nitrogen cooled cryopanel. The lower section can achieve pressures of 10^{-8}Torr, giving a total chamber pressure of $\approx 10^{-7}$Torr. The two sections are isolated by a baffle valve which can be shut during sample turn-around such that a low pressure is maintained in the lower chamber at all times. The substrate holder carousel system can be replaced by a substrate heater for hot depositions and in-situ growth of films. A magnetically operated

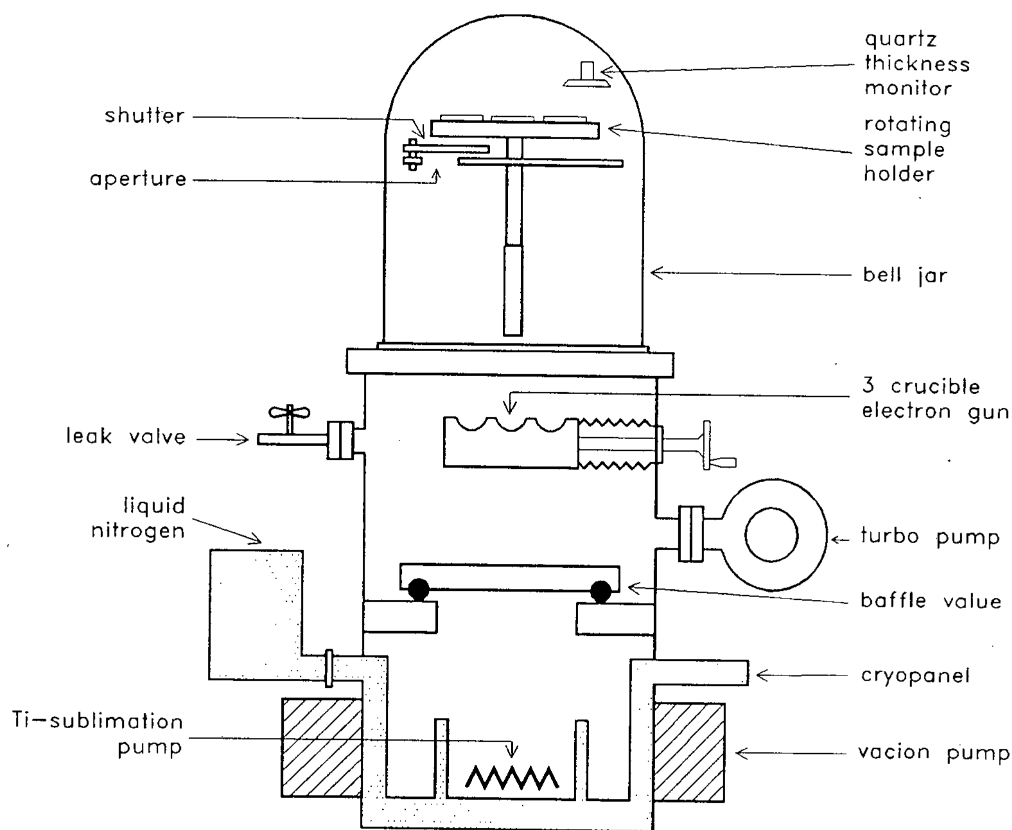

FIGURE 2.6: Schematic illustration of the high vacuum apparatus used for the electron beam evaporation of thin films. The upper section contains the sample holder, thickness monitor and electron gun. The lower section is maintained under vacuum at all times by closing the baffle valve during sample changing.

shutter isolates the substrates during target out-gassing and pre-annealing. The

chamber pressure is continuously monitored by 3 vacuum gauges; two of which are located in the upper chamber and one in the lower chamber.

High gas flow rate in the chamber during deposition can be achieved with a leak valve and the e-gun can operate at pressures of up to 10^{-3} of O_2 before oxidation of the filament occurs. Higher pressure causes scattering of the e-beam and shortens the life of the filament due to erosion by ion bombardment.

2.5 Annealing

Thermal annealing of samples either under vacuum or in an oxidation furnace, was used to crystallize films, enable solid state reaction of multilayers of films or for film-substrate reaction. The furnaces (Lindberg) are equipped with temperature controllers to monitor and adjust the temperature. Both wet and dry oxidation was possible with the oxidation furnace. Dry oxidation was done by flowing dry O_2 gas through the tube furnace during annealing and wet oxidation was achieved by bubbling the O_2 gas through a steam bath before passing it through the furnace. Post annealing of YBCO thin films, in O_2 atmospheres, was done with a microprocessor controlled ramping program on the temperature controller. This enabled us to set slow heating and cooling rates for the YBCO films on various substrates. This was important in light of the thermal mismatch often present between the film and the substrate and the cooling rate is vital in forming continous $Y_1Ba_2Cu_3O_7$ films [**26, 67**]. A typical annealing cycle for a YBCO film on MgO is shown in **Fig. 2.7**.

Silicide films were typically prepared by high temperature annealing of metal overlayers on Si substrates under a vacuum of 10^{-7}Torr and metal-oxide films were prepared by evaporating metal layers in a 10^{-4} mbar oxygen environment. Post-annealing the metallic films under an O_2 flow of > 1 atmosphere in the oxidation furnace was used for complete oxidation and to create dense surface layers and desorb surface contaminants.

2.6 Sample characterization

2.6.1 Rutherford backscattering spectrometry

Rutherford backscattering spectrometry (RBS) was used to determine the thickness, stoichiometry and extent of interaction of the deposited films. RBS was performed at the Van de Graaff Group of the National Accelerator Centre, Faure using the 6 MeV Van de Graaff Accelerator at the VDG to produce 1-4 MeV α-particles. The α-particles are directed onto the target (thin film and substrate) contained in a vacuum chamber and the backscattered α's were detected with a SiLi surface barrier detector at an angle of 165° from the incident beam in order to maximize the energy resolution of the system. The targets were mounted on a motor controlled sample ladder that can hold up to 10 samples. The beam is collimated to a diameter of

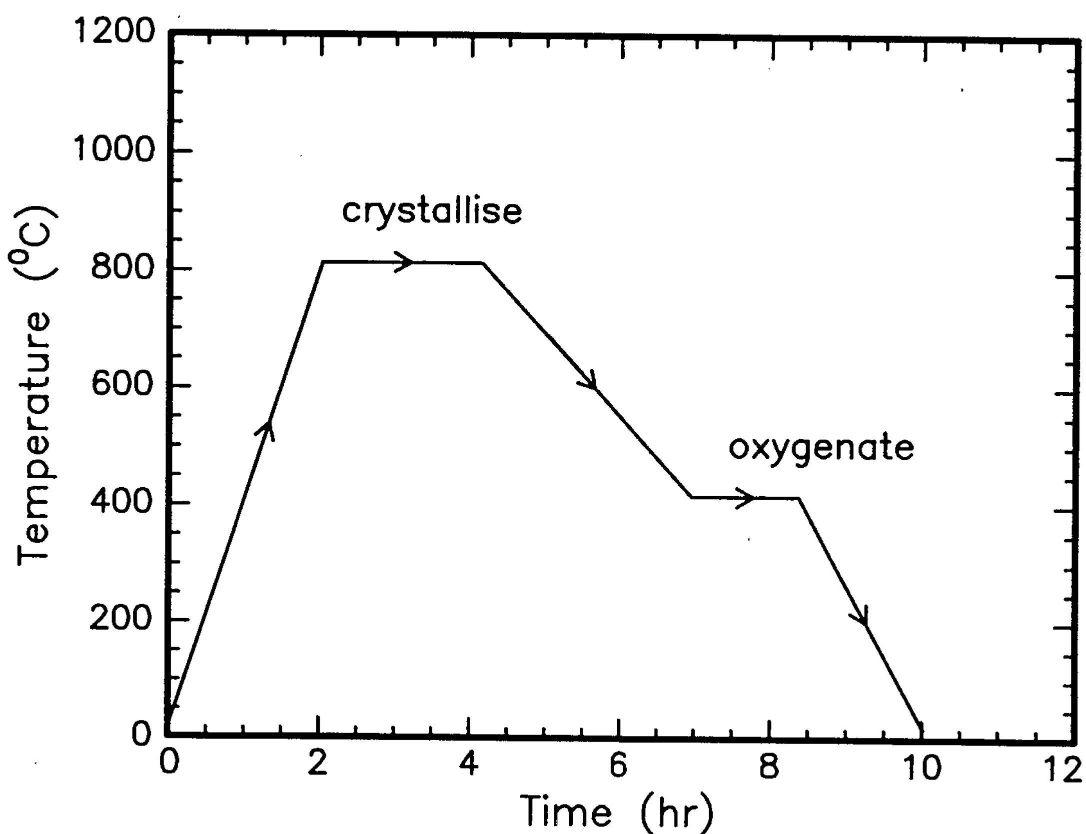

FIGURE 2.7: Temperature-time profile of a typical post-deposition annealing cycle for a thin film of $Y_1Ba_2Cu_3O_7$ on a MgO substrate.

2 mm and the beam current can be varied according to the size of the collimator and the value desired for specific films. For films of YBCO high beam currents can result in permanent film damage so beam currents of 50 nA with a total integrated charge of 10 μC were used. Currents of 150 nA and 20 μC integrated charge were used for silicide and metal-oxide films.

The sample chamber is evacuated to a pressure of better than 10^{-6} mbar during backscattering. The SiLi detector is operated at a bias voltage of +50 V and is connected to an electronics circuit that includes a preamplifier, amplifier and analogue to digital converter (ADC) which feeds the data into the live time data acquisition system SUREAL. Data can be observed on a display monitor and saved on disk for further analysis. The beam current is collected from the chamber wall and accumulated in a current integrator to give the total charge. A schematic of the RBS data acquisition system is shown in **Fig. 2.8**. The experimental setup for ion beam

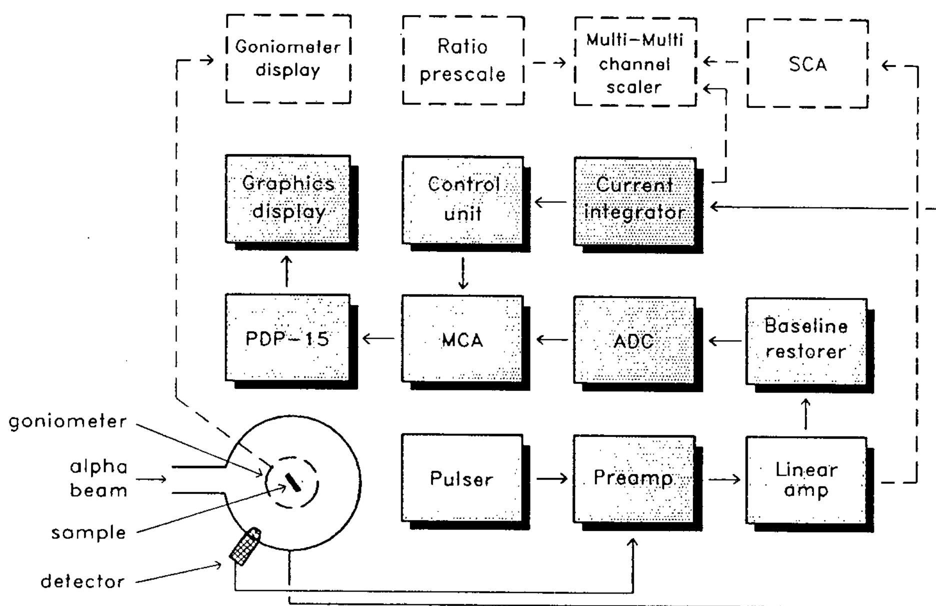

FIGURE 2.8: A schematic of the Rutherford backscattering spectrometry setup and the corresponding data acquisition system. The solid lines indicate the electronics needed for a normal RBS experiment and the broken lines are the additional features required for channeling measurements.

channeling analysis is similiar to that for RBS, with a few exceptions; the target

ladder and 1-dimensional goniometer is replaced by a 3-dimensional goniometer that enables rotation about three axes and allows one to detect the position of minimum backscattered flux; the backscattered spectra are energy gated by a single channel analyser (SCA) such that the backscattering yield at any specific depth of the sample or for any particular element can be selected. Random backscattering spectra were obtained by moving the sample off-axis from any possible position of minimum yield and rotating the sample. Due to possible beam induced damage in the $Y_1Ba_2Cu_3O_7$ films during the determinaton of the channeling position of minimum yield, the sample was laterally translated so that a undamaged spot could be used for the channeled spectrum acquisition.

2.6.2 X-ray diffraction

X-ray diffraction (XRD) analysis is a common method for the determination of the microscopic and morphological structure of material. Thin film analysis by XRD is slightly more complicated due to the small volume of material being probed. However, the high atomic numbers of the constituents of YBCO and the fact that YBCO grows with a high degree of preferential orientation on most of the substrates used means that the diffraction intensity is sufficiently high that standard diffraction techniques and diffractometers can be used. We have employed a Philips Diffractometer with Cu K_α radiation of wavelength $\lambda = 0.15408$ nm. The X-rays were produced with a voltage of 45 kV and a current of 35 mA. The diffractometer operates in the θ-2θ geometry, sometimes known as the Bragg-Brentano configuration. A schematic of the XRD data acquisition system is shown in **Fig. 2.9**. In this geometry only planes parallel to the substrate surface will be detected i.e. some major crystallographic direction is aligned with the surface. This is fortunate in that high quality YBCO films have the c-axis $\perp$ to the surface i.e. the a-b plane parallel to the surface, and this can be detected in the θ-2θ configuration.

The incident beam is collimated and the diffracted beam monochromated with a focussing pyrolytic graphite crystal to select only those peaks due to the Cu K_α line and to suppress the background and random reflections. This configuration

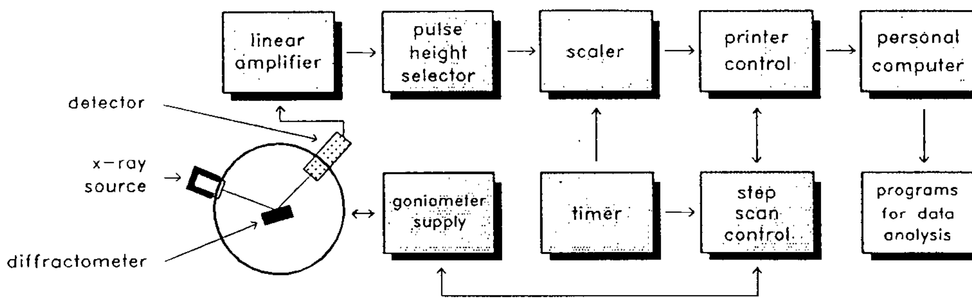

FIGURE 2.9: A schematic of the X-ray diffraction setup.

does away with filters to suppress background and peaks from K_β. The diffracted radiation was detected by a NaI scintillation detector and the intensity of the diffraction lines was correlated with the corresponding diffraction angle 2θ and fed into a personal computer.

2.6.3 Auger electron spectroscopy

Auger electron spectroscopy analysis of some of the film structures investigated in this study was performed at the Materials Science department at the University of Missouri-Rolla. The experimental arrangement for obtaining the Auger spectra is shown in **Fig. 2.10**. Several specimens were mounted on the carousel holder and sequentially rotated into the analysis position. The analysis was carried out with the excitation beam normal to the specimen surface. Argon ion sputtering was used to produce clean surfaces for analysis and for depth profiling. The amplitude of the Auger signal is dependent on the exciting beam energy and current, the amplitude of the modulation voltage, the multiplier gain and the sensitivity setting of the lock-in amplifier. Typical values used in this study are given in **Table 2.1**.

2.6.4 Electrical measurements

The two most important aspects of the electrical measurements is determination of the temperature for the onset of superconducting T_c (onset) and the transition width ΔT (90 - 10%) for the transition from the normal state to the superconducting

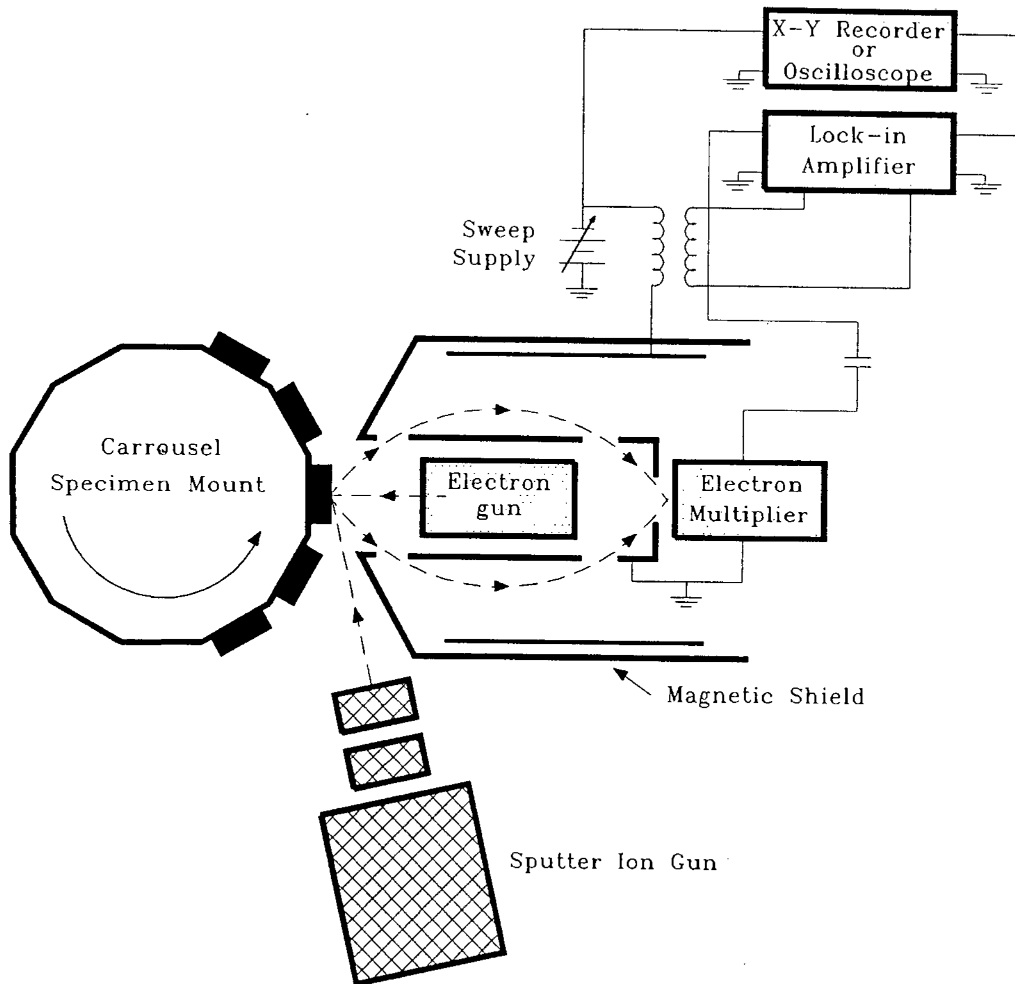

FIGURE 2.10: A schematic of the Auger electron spectrometer setup.

state. We have employed two methods to do this viz:

1. measuring the resistance of the sample
2. Measuring the magnetic susceptibility of the sample to detect the perfect diamagnetism of the superconducting state.

The first method is the one most frequently used as a result of its simplicity. However, the results of resistivity measurements are only meaningful for homogeneous samples for which all parts of the sample undergo the superconducting transition at the same temperature. For non- homogenous samples, the resistance

TABLE 2.1: Parameters for the Auger electron spectrometer settings.

Parameter	Value
e-gun current	1 mA
e-gun voltage	3 kV
modulation	3 eV
gain	10
sensitivity	.001
sputter current	15 mA
sputter voltage	3 kV
sputter rate	2-3 nm/min.

can go to zero when a percolation path is established. This means that only a small sample volume could be superconducting, which is not very useful for many applications and limits the current capabilities of the sample. Moreover, since the sample resistance is zero below the percolation threshold, resistance measurements cannot provide information about changes below the threshold. Hence measurement of the resistive changes alone is inadequate and we have complimented these with magnetic susceptibility measurements which is capable of detecting a transition only if the bulk volume (>40%) of the sample is superconducting [**68**]. The measurement of resistivity as a function of temperature was peformed with a conventional 4-pt probe in the Van de Pauw geometry in a helium closed cycle refrigeration cryostat capable of reaching a temperature of 10 K. The cooling power is generated in a closed loop sealed system filled with gaseous Helium. The samples were positioned on an exchangeable sample holder enclosed by a radiant heat shield and a vacuum shroud. The highly polished radiant shield prevents radiation heating of the sample at low temperatures. The sample compartment is evacuated to 10^{-2} mbar prior to operation of the cooling system. Gold current and voltage contact pads were sputtered through a mask onto the samples. Copper leads for 4-pt measurments were attached to the pads with silver paste. The resistances between 295K and 10 K were measured as the sample was cooled over a period of about 3 hours. A 0.1 μV resolution digital voltmeter was used to continuously measure the resistance of

a calibrated Cryogenics Consultants Rh/Pt thermometer and the resistance of the samples. A thin wire resistive heater is wound around the sample stage to regulate the drop in temperature and to warm the sample up for turn-around. All data was collected by a PC and the resistance and temperature calculations were done almost immediately. Everytime the temperature changed by 1 K or the resistance by more the 1%, a data point was recorded and plotted. In practice about 250 data points per sample were collected.

AC susceptibility measurements on the samples were made using a sensitive resonant frequency circuit based on the design by Xenikos et al [**69**]. Here the sample is placed in close proximity to a pancake shaped coil. This coil forms the inductive component of a resonant parallel LC circuit. The circuit resonates at 2.51 MHz above T_c. The self inductance of the coil is changed, however, by flux expulsion by the film as it goes through the superconducting transition so that the resonant frequency is shifted. The electronic circuitry yields a signal proportional to the resonant frequency and hence to the Meissner state of the film. The typical field generated by the current through the coil is of the order of mG. The coil, sample thermometry and heater is mounted in the cold stage of a liquid nitrogen cooled cryostat that was pumped on to reach a temperature of 50 K. Thermal lag between the sample and the cold stage was minimised by attaching the sample to the stage with a thermally conducting silicone epoxy. Care was taken in all measurments to change the sample temperature sufficiently slowly so as to measure the temperature accurately (better than 0.1K). This was ensured by checking that the hystersis between warming and cooling cycles was minimized. Electrical measurements were performed at the low-temperature laboratories in the Physics departments of the University of the Witwatersrand and the University of Natal and at the Electronic Engineering department of the University of Stellenbosch.

CHAPTER 3

Sputter deposition onto oxide substrates

The use of conventional substrates such as MgO, $SrTiO_3$ and Al_2O_3 is important in testing the viability and effectiveness of the deposition method being used. The ability to judge the quality and to optimize the parameters of deposition that lead to good quality films depends on minimizing the negative effect that the substrate might have on the deposited film. To this end, MgO and $SrTiO_3$ have high temperature thermal stability against interaction with YBCO and have been extensively used as substrates for thin film superconductors [1–7]. The cubic structure of $SrTiO_3$ and MgO have lattice parameters which can accommodate the YBCO lattice. Thermal expansion coefficients which are not greatly mismatched are also essential for the formation of smooth, continuous films free from stress-induced microcracks, which is valid in the case of $SrTiO_3$ [1,70]. In the case of MgO, the good energy separation of alpha particles scattered from the substrate and the thin film in RBS spectra enables accurate determination of thickness and composition of the deposited YBCO film. However, the primary limitation of MgO and $SrTiO_3$ substrates is their inability to be used with any great efficacy in microelectronic and other applications. The poor dielectric properties of $SrTiO_3$ especially, makes its use for microwace purposes very limited. In addition, the high cost of quality

single crystal substrates is a further drawback to possible wide-scale applications. Al_2O_3(sapphire) is, however, a relatively cheap and desirable substrate because of it's low dielectric value and possible use in conjunction with YBCO in microwave devices. The growth of YBCO on Al_2O_3 is therefore of considerable interest from an applications viewpoint.

3.1 Films on MgO

3.1.1 Optimization of deposition conditions

The determination of the ideal parameters for the deposition of good quality superconducting thin films of YBCO is a non-trivial matter due to the large number of parameters that affect such a process and the possible synergistic variation of such parameters. This study relied mainly on the power of RBS for the determination of stoichiometry, thickness and possible interaction to ascertain the empirical values of total pressure, oxygen partial pressure, arc current, arc voltage (sputter power) and substrate temperature that give the best possible films in terms of stoichiometry thickness of the deposit and uniformity through the thickness of the film. While this does not ensure that the deposited films will be superconducting, or that the films will be of good quality, without such an optimization the achievement of good quality films is impossible. The quality of the deposited films depends crucially on other parameters such as the substrate temperature and the substrate surface quality (see 3.1.3 and 3.1.4). MgO substrates have been used for studying the effect of these parameters because of the good separation of substrate and film signal achieved in RBS.

As previously mentioned (see chapter 1 and chapter 2), deviation of the stoichiometry of oxide films such as YBCO from that of the target generally arises due to the presence of negative ions (O^-, BaO^-, O_2^-) [**22, 28**] during sputtering. These energetic negative ions are accelerated towards the depositing film by the electric field and cause compositional changes by preferential re-sputtering or by radiation enhanced surface diffusion. The most useful ways of countering this problem are:

(i) Placing the substrate off-axis so that it does not face the cathode (target) thereby

minimising the ion flux striking the growing film.

(ii) Working at high gas pressures to thermalize the ions and hence prevent energetic ions from striking the film.

(iii) Working with a low discharge voltage to lower the resputter yield.

The first approach has been taken care of by using an Inverted Cylindrical Magnetron [34] which has the off axis sputter geometry (see Chapter 2). It was therefore necessary to concentrate on the variation of gas pressure and discharge voltage to minimise the re-sputtering effect. The pressure and voltage parameters vary synergistically and to a minor extent the effect of substrate temperature must also be taken in account when attempting to minimize the ion damage. In addition, the effect of oxygen partial pressure was investigated in terms of deposited stoichiometry and arc voltages during sputter deposition.

A ratio of 2:1 for the $Ar:O_2$ partial pressures was used as this mixture was found to produce sustained sputter deposition. Variation of oxygen and argon pressure from this value resulted in fluctuating arc voltages at low gas pressures and often caused extinction of the sputtering plasma. **Fig. 3.1** shows the variation of the arc voltage for a range of total pressure values. The arc voltage is very high at low pressures leading to high energy bombardment of the depositing film.

The sputter power (arc voltage $\times$ arc current) at 6×10^{-2} mbar varies non linearly and decreases with increasing arc current implying that in the lower energy ion bombardment region (lower arc voltage), the sputter power cannot be manipulated to increase deposition rate or to correct stoichiometry deviations that may arise in certain power regimes. Also ion implantation may occur under such conditions. The effect of an increase in total pressure causes an immediate alteration in the arc voltage profile. The voltage decreases substantially, suggesting lower ion bombardment of the film, and is nearly constant over a large range of arc current values, meaning that the power level can be adjusted as desired to achieve optimal stoichiometry in the film. This behaviour is seen over a wide range of total pressure from 1.5×10^{-1} mbar to 6×10^{-1} mbar with the arc voltage reaching a minimum

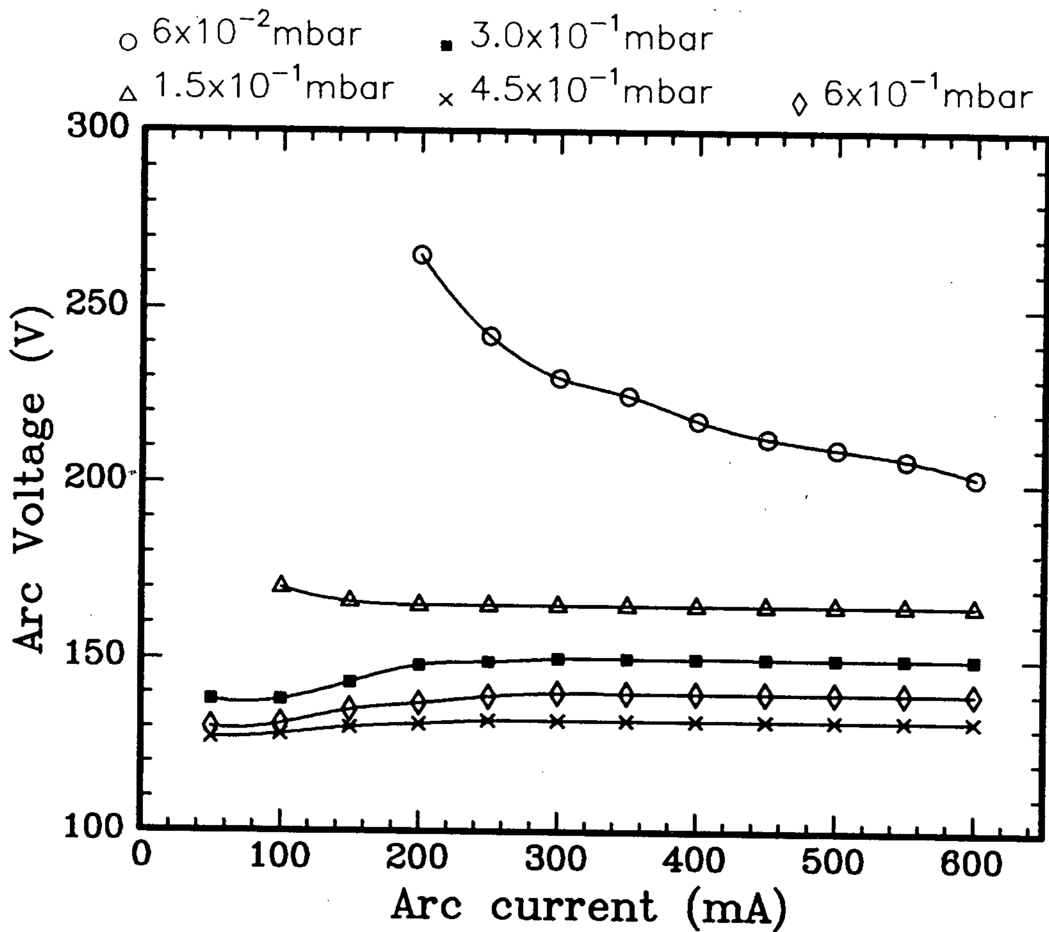

FIGURE 3.1: Variation of the arc voltage and arc current as a function of the total gas pressure in the ICM sputter gun. Low gas pressures result in high arc voltages which mean higher energy ion bombardment. Higher gas pressures lower the ion bombardment energy by thermalisation and give controllable power levels. The Ar/O_2 gas mixture is in the ratio 2/1.

plateau region at 4.5 x 10^{-1} mbar. At higher pressures (6 x 10^{-1} mbar or higher) the arc voltage increases again. This high pressure is very close to the limit that could be sustained with the vacuum pumping system and once again the extinction of the plasma is a problem at these pressures. These very high pressure values can be ignored as it was found that the deposition rate is very low at such pressures due to the large number of collisions the sputtered particles encounter with the gas atoms.

To ensure adequate oxygen incorporation into the depositing film it was necces-

sary to determine the maximum oxygen pressure sustainable while at the same time minimizing the energy of the negative ion bombardment [71]. According to Ahn et al. [72] YBCO decomposes into suboxides at high substrate temperatures and low pressures, demonstrating the need for a relatively high oxygen partial pressure. Since the sputter system operates in d.c. sputtering mode an oxygen flow over the target is required to maintain a conducting target (low O_2 pressure implies no plasma). In addition to oxygen being provided to the target, the formation of suboxides and oxides of the metal constituents leads to increased oxygen provision in the film [18, 29–32]. Direct reaction of the film with oxygen excited by the sputter plasma could also increase the level of oxygen in the film. **Fig. 3.2** shows the relationship between arc voltage (representing ion bombardment energy) and oxygen partial pressure for different arc current values at a constant total pressure of 4.5×10^{-1}mbar. For all three current values, and hence power values, the lowest arc voltage and therefore the minimum negative ion bombardment energy is achieved with an oxygen partial pressure close to 1.5 x 10^{-1} mbar. At higher oxygen partial pressures the negative ion bombardment energy starts to increase again, most likely as a result of the oxygen acting as a sputtering gas. An increase of oxygen partial pressure results in decreasing luminosity of the sputtering plasma. Unlike the case where O_2 is used as a sputtering gas (eg. in the deposition of oxides from metal targets, where an insulating oxide layer forms at the target surface and reduces the sputtering rate [73, 74]), the O_2 in the ICM sputter process helps to keep the target surface conducting. This is so because $Y_1Ba_2Cu_3O_7$ is metallic and conducting in the normal state, at room temperature, whereas the oxygen deficient phase of YBCO, $Y_1Ba_2Cu_3O_6$, is insulating. The luminosity of the plasma decreases because the bright region is more confined to the space within the cylindrical YBCO target when there is O_2 in the sputtering gas. The electrons lose more energy through collisions with an Ar/O_2 mixture than with pure Ar because of the extra energy required to break the O_2 molecule and ionize two oxygen atoms as compared to ionizing an Ar atom. As a result the electrons travel shorter distances in the Ar/O_2 mixture and are more confined to the target surface.

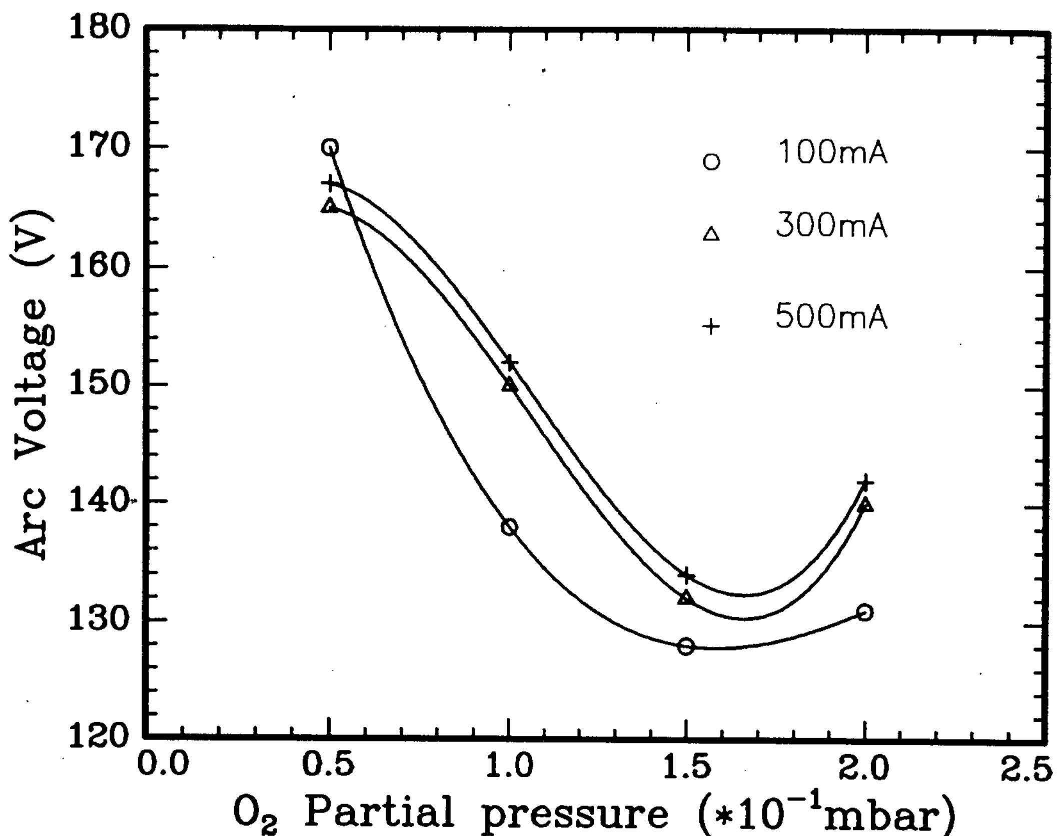

FIGURE 3.2: The effect of oxygen partial pressure on the sputter voltage(ion bombardment) for different values of current and a constant total pressure of 4.5×10^{-1}mbar. The minima at an oxygen pressure of 1.5×10^{-1}mbar represents the lowest energy ion bombardment for maximum oxygen incorporation in the system.

Determination of the stoichiometry of the deposited films as a function of oxygen partial pressure by RBS shows that fairly good metal stoichiometry is achieved at the minimum of the arc voltage (**Fig. 3.3**). The composition of the film was found with a least squares fit between the simulated spectrum and the experimental data under the assumption of homogenous films and the metal compositions were normalised to the Y – content, as this is generally least affected by ion bombardment. Whilst this is not an ideal method for determining stoichiometry of YBCO, it is adequate for the purposes of comparison. At low oxygen partial pressures the deficiency of Ba and an excess of Cu is very evident and is most likely due to the re-sputtering effect of the negative ions. These off-stoichiometric regions correspond to

high arc voltages and confirm that ion-bombardment affects the film composition. At high O_2 pressures the film is closer to the ideal 1:2:3 stoichiometry. Utilising

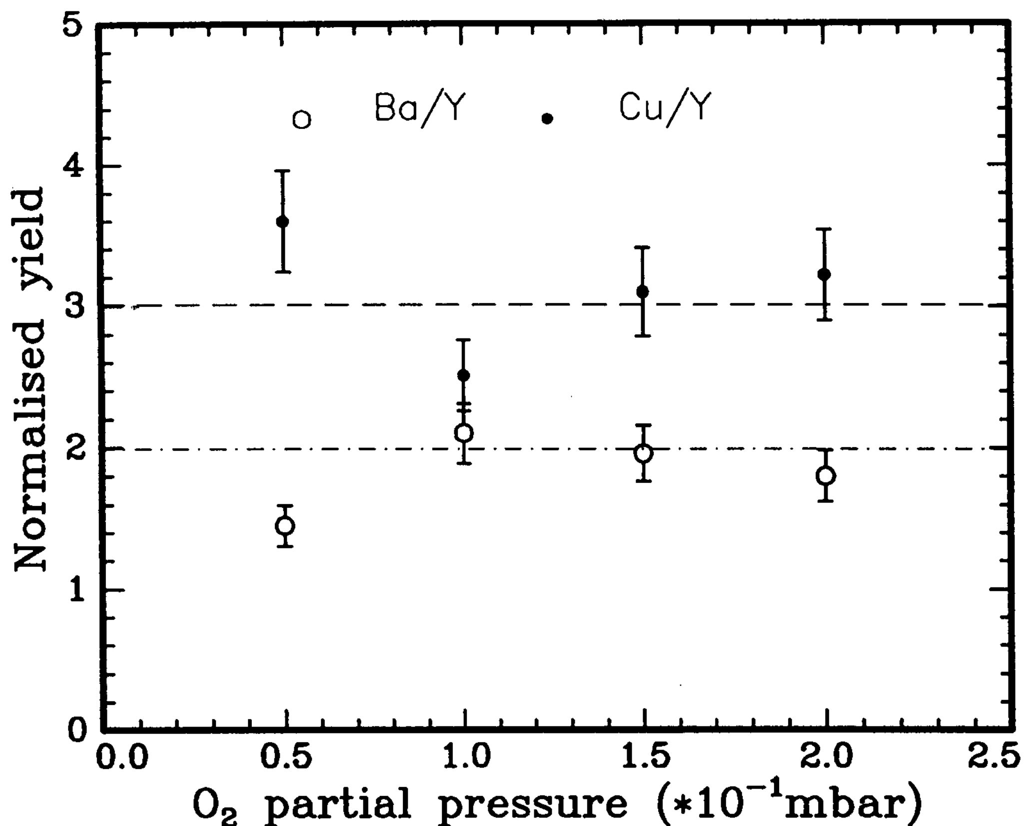

FIGURE 3.3: Stoichiometry of the deposited film, from RBS measurements, as a function of oxygen partial pressure at a constant current of 500 mA and a total pressure of 4.5×10^{-1} mbar. The near stoichiometric values of 1:2:3 for the metal ratios at the minimum of Fig. 3.2 shows that the arc voltage is a good indicator of ion bombardment as the deviation from ideal composition outside the minimum is due to the re-sputtering effect.

the optimized values of total pressure and oxygen partial pressure of 4.5 x 10^{-1} mbar and 1.5 x 10^{-1} mbar respectively, the effect of the variation of sputter power was investigated in terms of the deposited thickness and composition. However, this was hampered by some other factors that had to be taken into account when considering the effect of sputter power. At very low power levels (10-40 W) very little material is deposited, as would be expected from purely kinetic considerations. At

medium power levels (50-80 W) there is a higher deposition rate, however this rate is fairly constant over a large range of power values (50-80 W) which was attributed to the thermalization caused by the high gas pressures. Attempting to increase the deposition rate by raising the power levels to 100 W leads to implantation of Ar in the depositing films which arises from reflection of high energy Ar ions at the hot pressed sintered target towards the film. These reflected particles are not completely thermalized by the high gas pressures used in the optimal settings. At very high sputter powers (>100 W) increased thickness of the deposit is observed. However, this is accompanied by the sputtering of micron sized globules of material from the target due to segregation of the target surface at high powers. The high energies of the incident ions coupled with the small thermal conductivity of the target leads to heat buildup in the surface layers resulting in desorption of clusters of material which are not stoichiometric. Such breakdown of the target surface composition and structure arises from a characteristic "racetrack arc" along the crossed electric and magnetic fields. The racetrack arc is an uncontrolled spark that travels along the target surface and rapidly erodes this surface by spitting out chunks of material. The presence of these globules was detected by optical observation and by scanning electron microscopy. The globules do not have the same structure and composition as the rest of the film and appear to be non-conducting during SEM measurement. RBS of these films display a characteristic tailing off in the film spectra which appears to be interfacial interaction but arises mainly from the granular nature of the film. Such rough surfaces are detrimental to the growth of good quality superlattices and multi-layered structures. The stoichiometry variation in the globules makes it difficult to characterise the effect of sputter power and it was necessary to resort to using the empirically determined medium power level (50-80 W) as the ideal power settings.

3.1.2 Spatial distribution of deposited material

Steep angular distributions in the sputter yield of the constituents is problematic with the use of a planar target sputtering geometry, resulting in considerable in-

homogeneity in the sputtering flux and hence a variation of thickness and possibly composition across the deposited layer [**2**,**4**]. These spatial distributions may result from geometric effects but are also likely to arise from the re-sputtering effect of negative ions. Measurement of the spatial distributions of the deposit was achieved by placing a 2x4 cm^2 rectangular substrate centred on the middle of the substrate holder and in line with the central axis of the sputter gun. RBS measurements were performed along a bisector of the substrate and the beam was translated (scanned) along this bisector to obtain the distribution across the substrate. Circular symmetry of the sputter geometry implied that the maximum deposited thickness would occur in the centre of the substrate holder.

Fig. 3.4 shows the measured variation of thickness across the substrate for a layer of YBCO deposited by ICM sputtering. The thickness values assume a homogenous sample and local variations of density and composition (see later) are folded into the error calculations. The thicknesses were obtained with a least squares fit of the data with the aid of RUMP. Within a radius of 10 mm from the centre of the substrate there is good spatial homogeneity with a thickness variation of roughly 10%. It is assumed that the thickness variation is due to the geometry, where maximum overlap of the deposit is in the central region. Lower substrate temperatures at the outer regions due to increased radiation losses and reduced heater element contact area coverage could also lead to variations in the thickness of the deposit.

The normalised stoichiometry profile across the substrate holder (**Fig. 3.5**), obtained with RBS, also exhibits a deviation of stoichiometry at the edges of the region considered, with a decrease of Cu and increased Ba content noted at the boundaries. Within a radius of 8 mm from the centre it is justifiable to assume both spatial and compositional homogeneity for the deposited films, enabling the deposition of relatively large area high quality films. In addition, the size of the substrates used (10x10 mm^2) means good areal coverage (with ideal composition) over the substrates.

3.1.3 Effect of Substrate Temperature

The deposition of YBCO films onto MgO was investigated as a function of the substrate temperature, which is known to be critical in the formation of good quality superconducting films [**6,63,64,75**]. Films deposited at room temperature, corresponding to zero input energy to the substrate heater, were completely amorphous. It should be noted that even though no power was supplied to the heater, a thermocouple reading of 55-60°C was recorded during deposition, which was attributed to the heat generated during the deposition process by the impingment of energetic species onto the substrate and heater block. However, these films were completely amorphous as the temperature was insufficient to crystallize the film and only the substrate peak was observed with XRD (not shown). These films

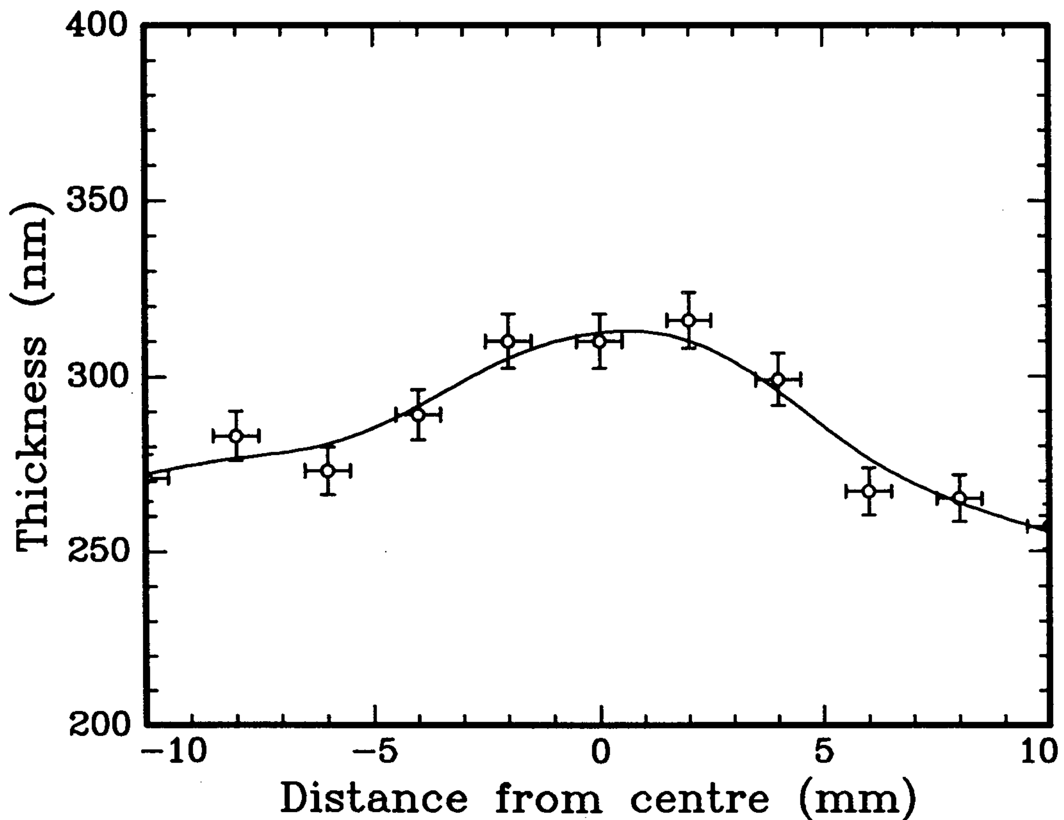

FIGURE 3.4: Variation of the thickness of a YBCO layer deposited by ICM sputtering across the area of the substrate holder.

were insulating. Films deposited at higher substrate temperatures of 400-500°C were subjected to a high temperature post-anneal at 850°C followed by an oxygen intercalation step at 450°C . This procedure produced a film with a degree of c-axis orientation (**Fig. 3.6**). These films were essentially polycrystalline and the (103) (013) orientations of the film are clearly evident. Higher temperature post-annealing at 900°C completely destroyed the superconducting phase in the film, presumably due to film-substrate interaction.

Films deposited at substrate temperatures in excess of 650°C displayed evidence of superconductivity for as-deposited films i.e. the films were of the superconducting phase in-situ. The as-deposited films obtained from sputter deposition

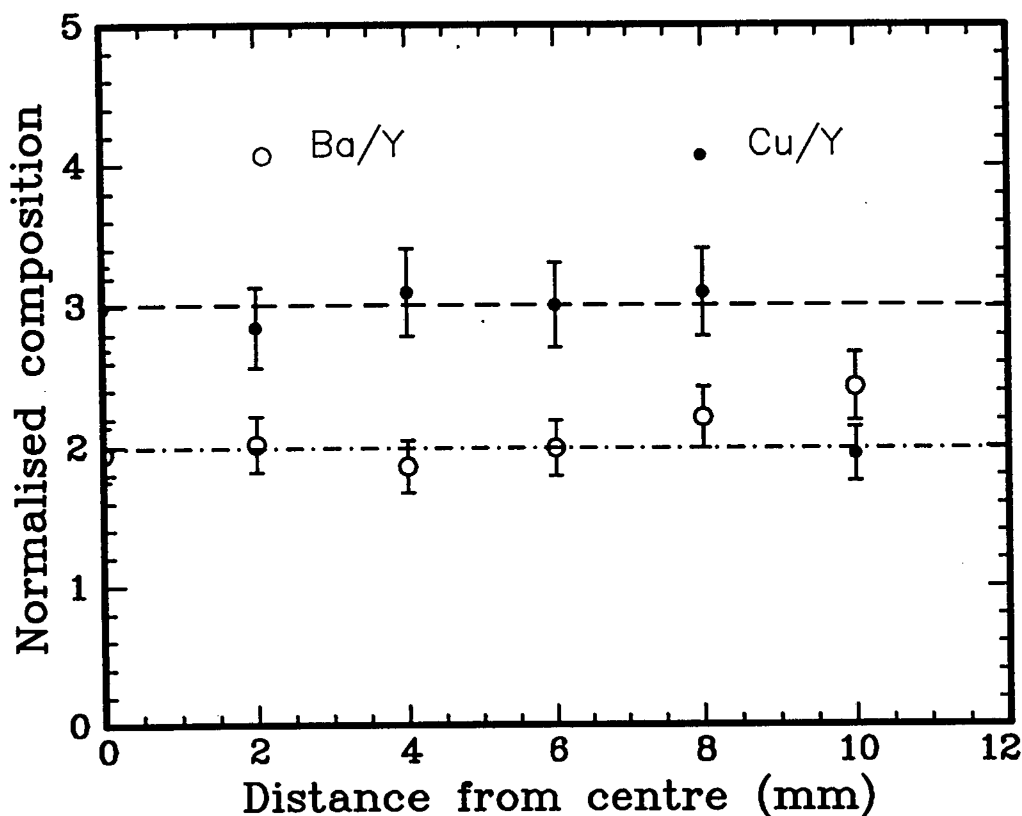

FIGURE 3.5: The composition of the film deposited by ICM sputtering measured as a function of the distance from the centre of the substrate holder to determine the stoichiometry profile across the area of the holder.

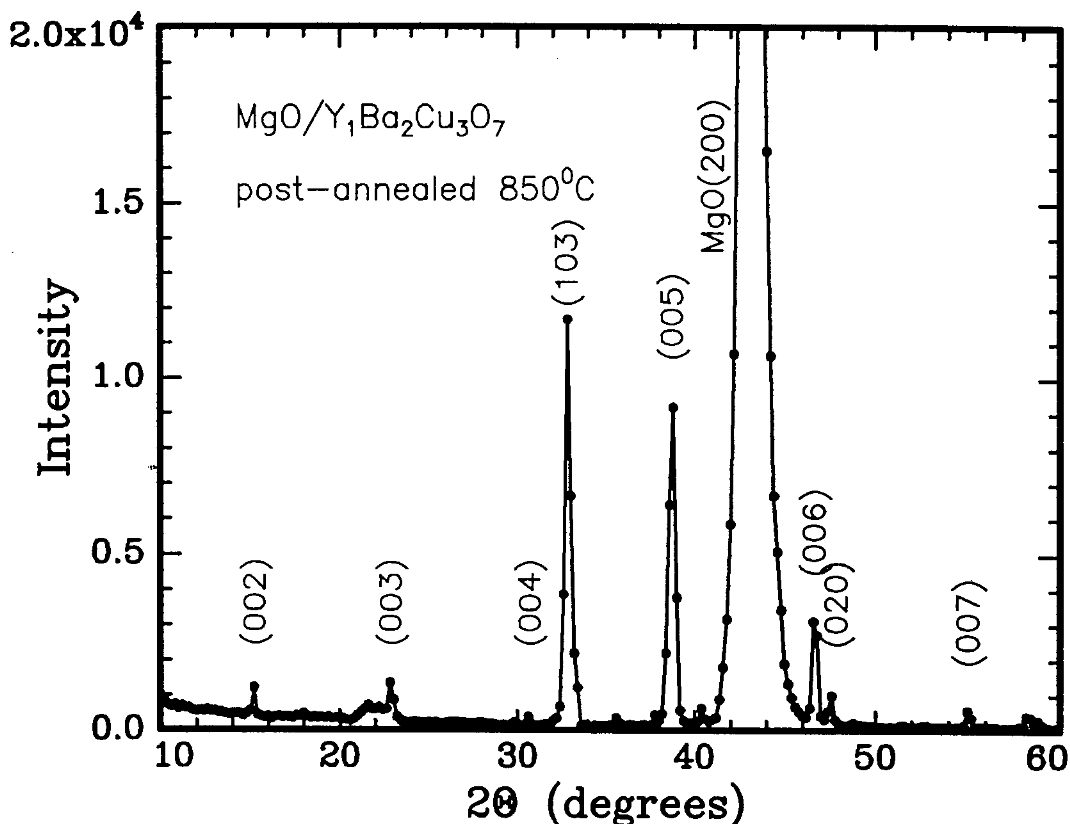

FIGURE 3.6: X-ray diffraction spectrum for a film deposited at 400°C on MgO. The film was subsequently post-annealed at 850°C for 1 hr and oxygenated at 450°C for 30 min. The XRD spectrum reveals peaks for a polycrystalline film withg some preferential orientation in the *ool* direction.

at 650°C were black and shiny with 30 to 100 Ω room temperature resistance values measured with a multimeter. **Fig. 3.7** shows a RBS spectrum for the as-deposited YBCO film on MgO<100>. The compositional ratio of Y:Ba:Cu for the film could be determined from the areas under the respective peaks and the corresponding scattering cross-sections of the respective elements. A homogenous film is assumed in the simulation and the fit has an accuracy of $\approx 5\%$. The solid line in the figure is a simulation of a film of ideal stoichiometry, $Y_1Ba_2Cu_3O_7$ on MgO, obtained with the RBS simulation programme RUMP [76], which emphasises that the film composition is close to ideal stoichiometry through the entire thickness. The film thickness was found to be approximately 500 nm. Information as to possible substrate-film

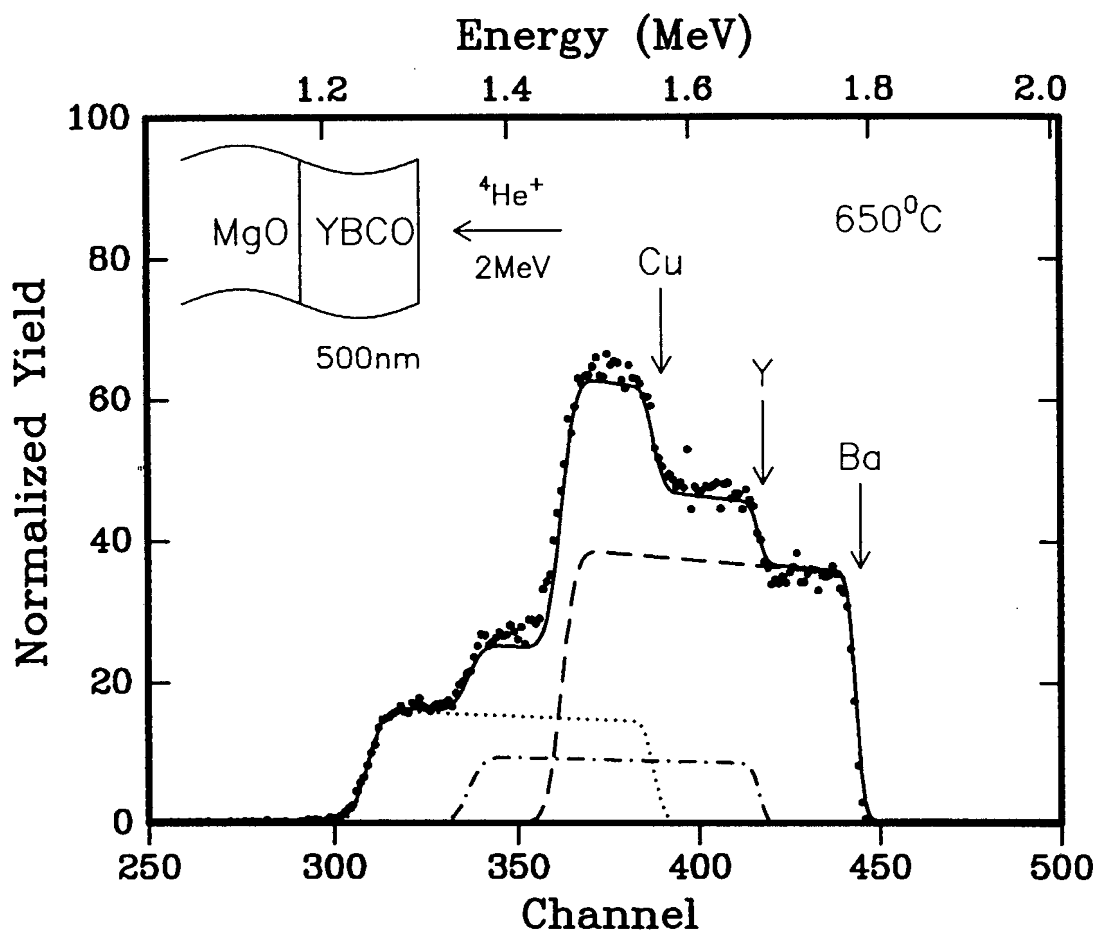

FIGURE 3.7: RBS spectrum of a YBCO film deposited onto a MgO substrate at 650°C . The solid black line is a simulated spectrum of a film of composition $Y_1Ba_2Cu_3O_7$. There is close matching of the experimental and simulated spectra for the metallic elements throughout the film thickness. The surface position of the elements are indicated with arrows and the broken lines denote the relative contribution of the individual elements to the simulation.

interaction at the interface and the dominant diffusing/reacting species can be obtained from the shape and change in shape of the elemental distributions. The sharp edges of the film in the RBS spectrum are proof of uniformity and minimal interfacial reaction.

XRD analysis of the film demonstrated a high degree of c-axis orientation, where the c-axis orientation is defined as normal to the film surface, with no evidence of polycrystalline or non-superconducting phases in the film. The textured nature of

the film contrasted with the XRD spectrum of the target (not shown), which gave a completely random spectrum. However, it is difficult to compare the XRD spectra as the powder sample was taken from the target and the true orientation of the solid target could not be ascertained. The high degree of texturing, however, does not demonstrate epitaxial growth or the absence of polycrystalline material as these reflections may be off-axis i.e. not parallel to the substrate surface and therefore not detectable in the θ-2θ configuration. The average lattice parameter, c, is calculated by plotting the peak position of each diffraction line against the Nilson-Riley function (NRF) [77]. The average lattice parameter, c, is the extrapolation of the least squares fit to NRF=0. This method is helpful in correcting for systematic and random errors. The as-deposited film has a measured lattice parameter c=1.172 nm which is larger than that observed for the bulk superconductor (c=1.168 nm). The expanded c value is most likely due to strain in the film and not an oxygen deficiency effect as a series of oxygenation steps were carried out between 450-600°C after the high temperature deposition stage with no significant change in the lattice parameter. Post-deposition annealing of the film at a high temperature has a direct effect on the lattice parameter c of the as-deposited film. The c-axis lattice parameter decreases with increasing annealing temperature to reach a minimum of 1.167 nm at an annealing temperature of 875°C . Films that were annealed at higher temperatures (900°C) gave a complete loss of preferential orientation and were discoloured presumably due to interaction with the substrate. The absence of significant line broadening of the $(00l)$ lines and the constancy of the variation of the interplanar distance,

$$\Delta d = \frac{\delta d}{d_{hkl}} \tag{3.1}$$

where δd is the normalised variance of the hkl-values from d_{hkl}, implies uniform strain in the as-deposited film. This may be due to a high density of crystal defects, which may have been created during sputter deposition and which are annealed out at high temperatures. This uniform strain will result in the shift in the position of the diffraction peaks as has been observed. **Fig. 3.8** shows the XRD sprectrum of the (003) peak of YBCO for the as-deposited film and for the same film annealed at

high temperature (875°C). The shift towards higher angles means a reduced c-value

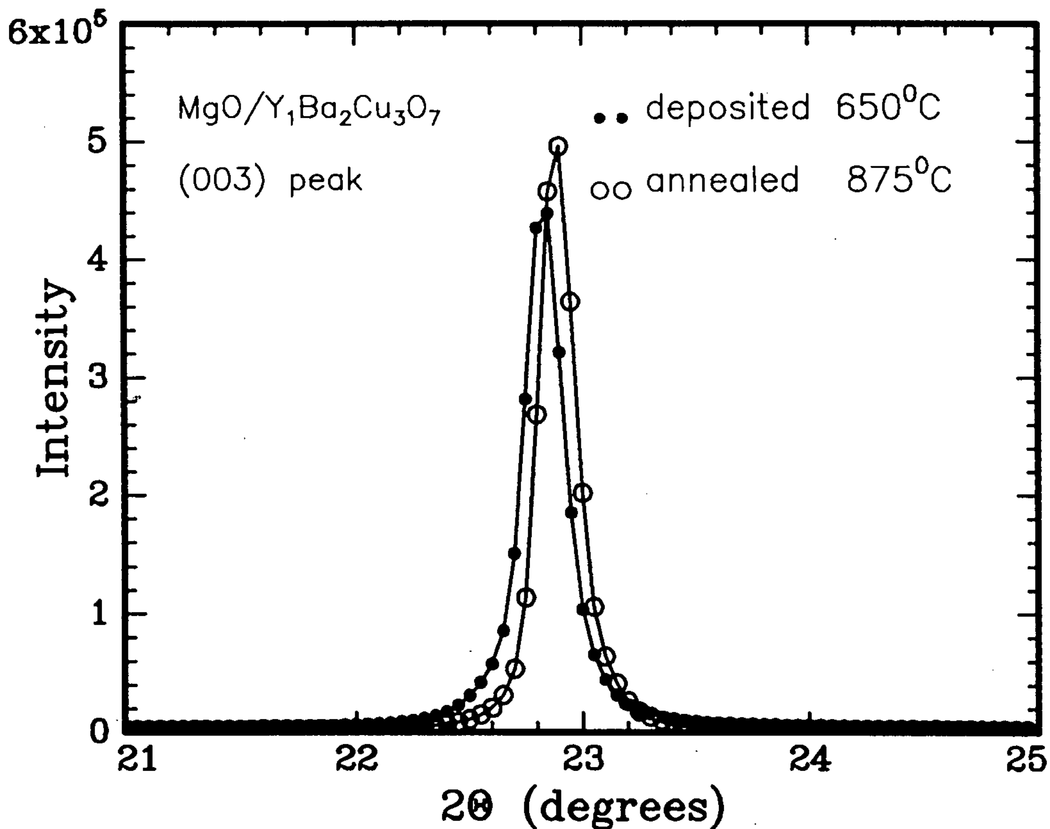

FIGURE 3.8: X-ray diffraction spectra of the (003) peak from a film deposited onto MgO at 650°C . The film has preferential c-axis orientation. The lower angle peak is for the as-deposited film and that at higher angle for the same film annealed at 875°C . The shift towards higher angles implies a decrease in the c-lattice parameter.

and an increase in peak intensity is noted. This increase can be attributed to the conversion of amorphous and non-aligned material to the c-axis orientation. The annealing temperature is high enough to cause a re-crystallization of the film and therefore the film behaves like a post-annealed film with the *c*-value close to that of a bulk superconductor.

Deposition at 700°C resulted in *c*-axis preferentially oriented films with no other orientations or phases detected (**Fig. 3.9**). In addition the c-lattice parameter corresponded closely to the value obtained from bulk material, suggesting an absence of stress factors and high oxygen incorporation into the film. Post annealing

these films at 875°C did not result in any improvement of the film properties as determined by XRD. The deposition at 700°C with the in-situ method gave films

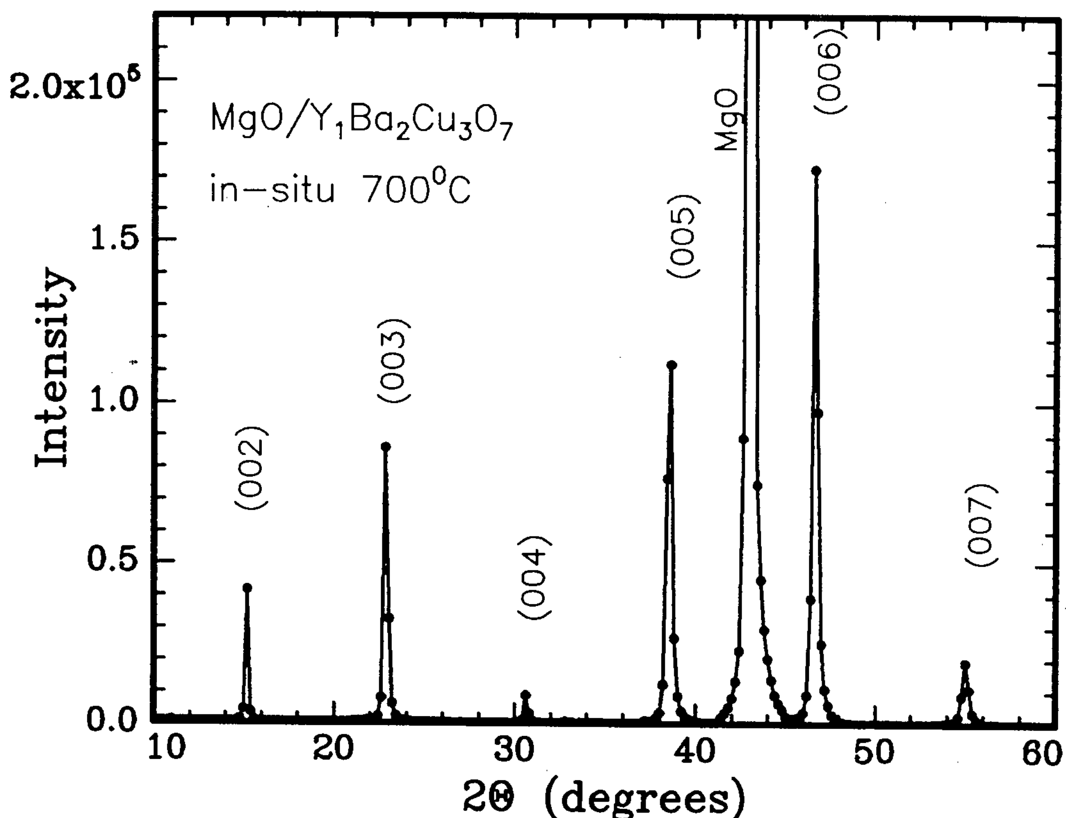

FIGURE 3.9: X-ray diffraction spectrum taken in the θ-2θ geometry of a film deposited onto MgO at 700°C . Only the $(00l)$ lines from the YBCO film were detected implying that the film is preferentially oriented with the c-axis normal to the substrate surface.

with exact stoichiometry and no evidence of interfacial reaction between the film and the substrate as determined by the sharp front and back edges of the substrate and the film in the RBS spectrum (**Fig. 3.10**). These films were also black, shiney and smooth. RBS simulation of the film reveals that there is a uniform distribution of the elements through the entire thickness of the film. Ion channeling measurements on these films gave the best minimum yields of $\chi_{min} = 7\%$ with increased dechanneling evident at the interface of the film and substrate. This dechanneling may be due to misfit dislocations at the interface arising from the relatively large lattice mismatch between YBCO and MgO at the interface.

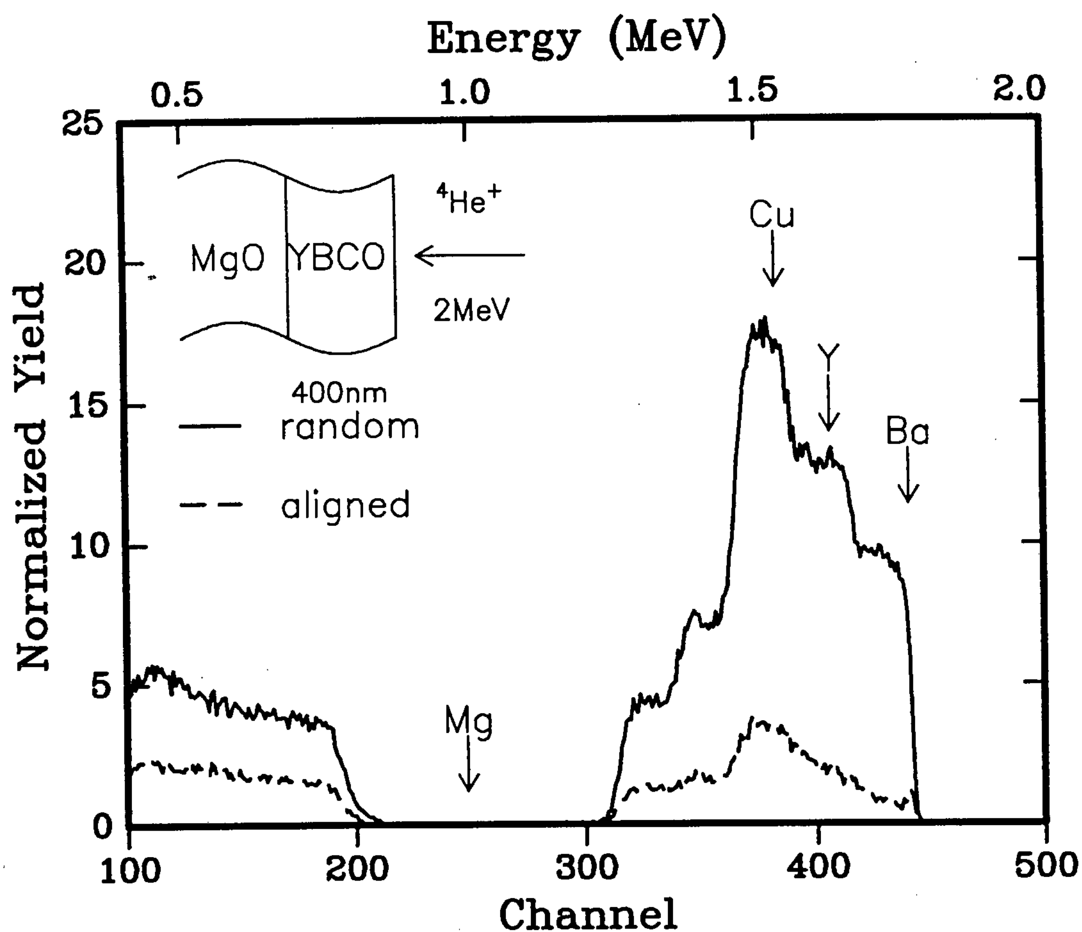

FIGURE 3.10: Rutherford backscattering spectra for a YBCO film deposited onto MgO at 700°C . The spectra are for He ions incident in a random direction and along the aligned [100] direction of the substrate. The reduced yield in the aligned direction gives a minimum yield of $\chi_{min} =$ 7% at the Ba signal with some evidence of dechanneling at the interface.

3.1.4 Effect of substrate surface quality

The effect of the quality of the substrate surface on the deposited film properties was investigated using the optimized conditions discussed previously. Two substrates were used, one of which was degreased in organic solvents and used directly for deposition while the 2nd substrate was subjected to a high temperature anneal at 1000°C in flowing oxygen. XRD spectra are insensitive to the detailed surface structure and both substrates gave identical spectra. Ion channelling measurements on single crystal substrates, however, are sensitive to impurities, defects and surface structure [**78**]. The channelling spectra of the first substrate reveals surface impurity peaks of oxygen and carbon which originates from the degreasing solvents (**Fig. 3.11**). The 2nd substrate, however, displays no evidence of such surface contaminants and a reduced intensity for the surface peak area (SPA) of the Mg peak on the annealed film was observed. The increased SPA is an indication of defects in the unannealed substrate surface, either brought about by the surface contaminants or induced in the surface during the polishing process. The surface quality is therefore improved by the annealing procedure giving a defect-reduced or defect-free substrate surface which is a pre-condition for epitaxial layer growth.

It is expected that the hydrocarbon surface contaminants, which are desorbed by the high temperature anneal in O_2, would deteriorate the film quality on the unannealed substrate. However, a more important function of the high temperature anneal is the formation of a high density of atomic steps on the surface of the substrate that helps to increase nucleation of the YBCO film [**59, 60, 79**]. The YBCO film was grown simultaneously to a thickness of 500 nm on both substrates to ensure identical growth conditions. Thus the principal variable in the films quality and characteristics is the substrate preparation method prior to growth of the YBCO film.

X-ray diffraction measurements of YBCO films grown by the *in situ* deposition method at 700°C on annealed and unannealed substrates reveal c-axis orientation with no significant difference in intensity and FWHM of the diffraction peaks of both films. The c-lattice parameter calculated from these spectra were both c = 1.167nm.

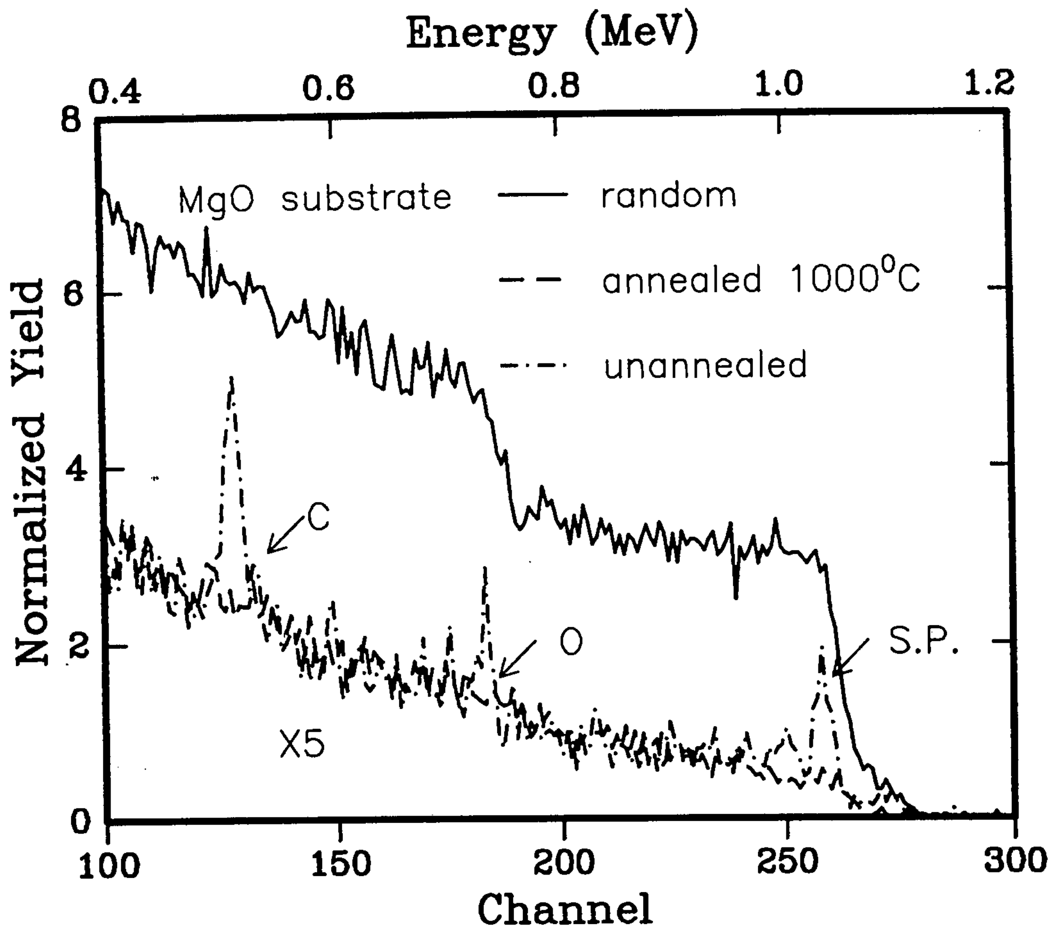

FIGURE 3.11: Ion channeling measurements on the MgO substrates. The lower yield channeling spectrum is for a substrate annealed at 1000°C in O_2. The unannealed substrate displays evidence of organic contaminants on the surface, arising from the cleaning solvents. A reduced surface peak area is seen for the annealed substrate.

Ion channelling of films on these substrates are quantitatively similiar, with little difference observed in the minimum yield. Resistivity measurements for films on annealed and unannealed substrates (**Fig. 3.12**) did not reveal any difference in the transition temperature T_c, the transition width ΔT or the zero resistivity temperature $T_{\rho=0}$. However, the normal state behaviour of the films above T_c differs. The resistivity of the annealed film decreases faster with decreasing temperature, with the normal state resistivity extrapolating to near zero resistivity at 0 K. The unannealed film on the other hand had a slower decrease with temperature

and a larger drop from T_c down to zero resistivity. The normal state behaviour extrapolated to a higher resistivity value at zero kelvin and the resistivity at 100 K was higher than that measured for the annealed film at the same temperature. In addition, the ratio of the room temperature resistivity to the resistivity at 100 K is higher for the annealed substrate, consistent with the sharper decrease in normal resistivity.

It has been mentioned that the transition temperature and transition width were similar for both films. It should be pointed out, therefore, that the resistivity measurement is not sensitive to the bulk superconducting properties and portions

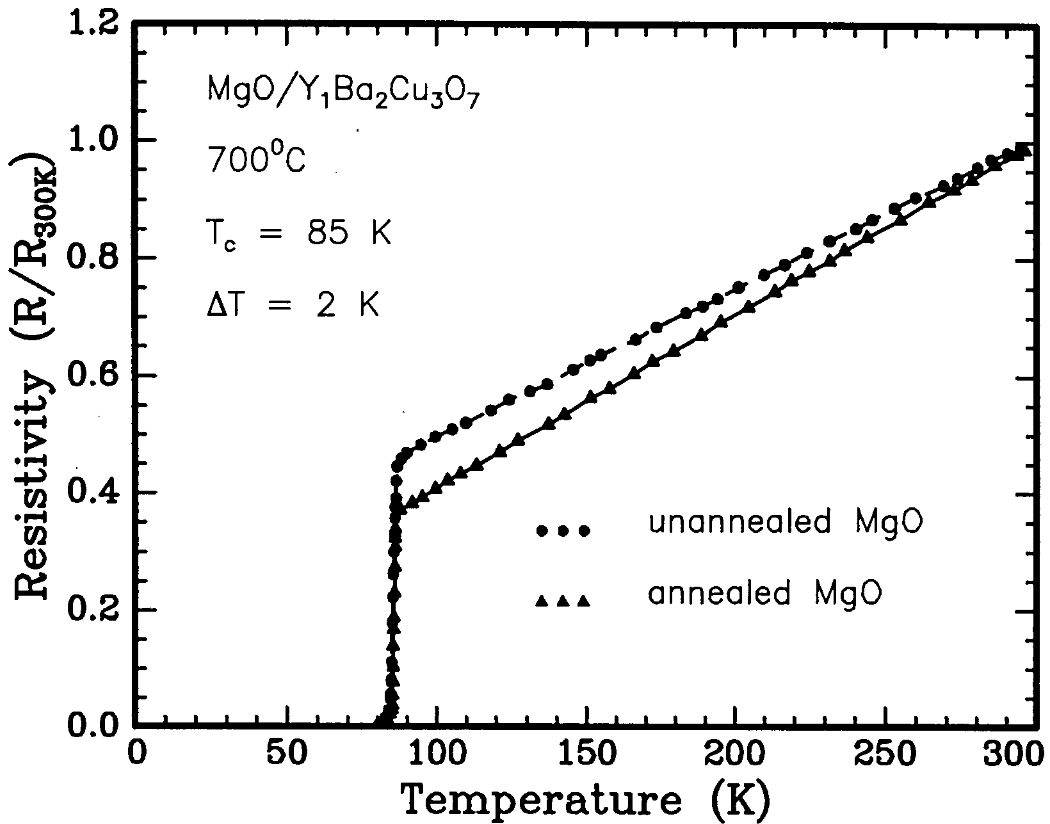

FIGURE 3.12: Resistivity measurements of the $Y_1Ba_2Cu_3O_7$ films deposited onto (a)annealed and (b)unannealed subtrates at 700°C by ICM sputter deposition. Similiar values of T_c(onset) were found for both films but the normal state behaviour of the films differ. The film on the annealed substrate has a greater drop in resistance with temperature in the normal state.

of the films that are similar can result in identical percolation paths giving similar resistive behaviour. A.C. susceptibility measurements, however are more sensitive to the bulk superconducting properties [69, 80] and if the films are nearly identical as these two are, then a measurement of magnetic flux expulsion by the films can be made in order to compare their superconducting properties.

A.C. susceptibility measurements on the film deposited on the annealed substrate displayed a sharp drop in susceptibility at 85 K with a transition width of less than 2 K being recorded (**Fig. 3.13**). This is a manifestation of the homogeneity and good quality of the film. The measurement of the Meissner effect on the unannealed film reveals a similar onset temperature for flux expulsion as for the

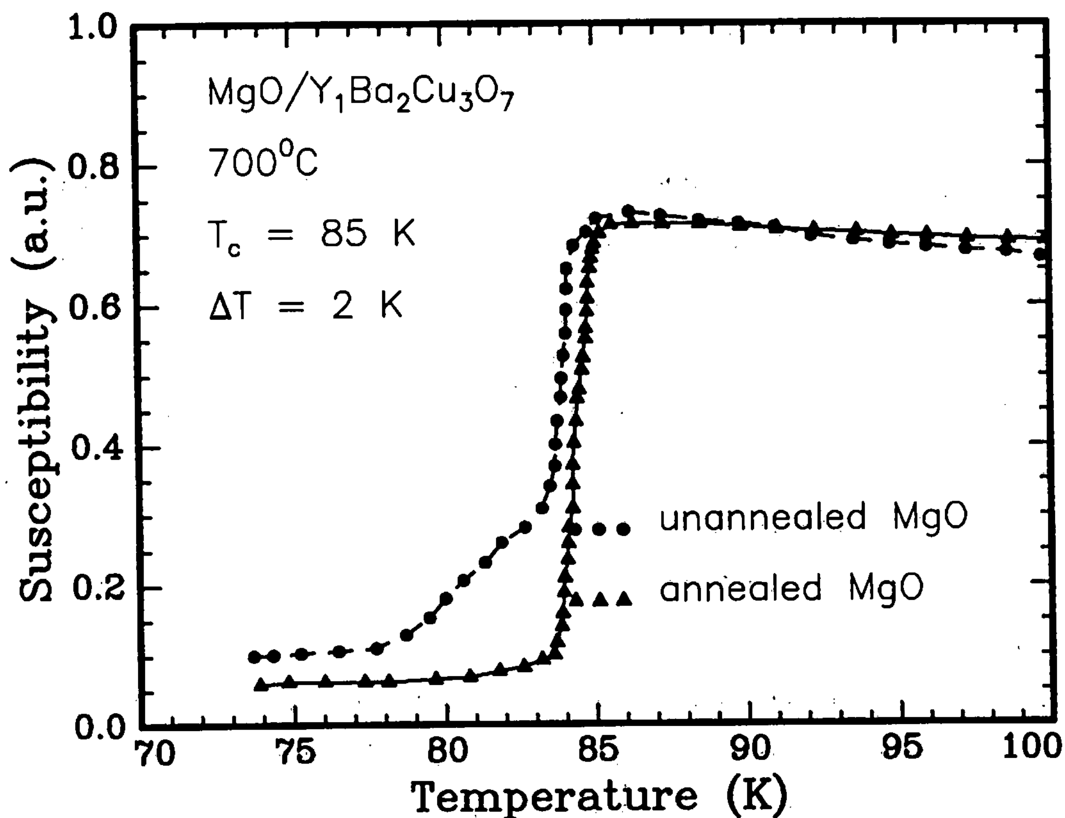

FIGURE 3.13: A.C. susceptibility measurement on the films shown in Fig. 3.12. The difference in behaviour is seen in the foot structure at the end of the transition, which corresponds to the way the film becomes completely superconducting. This discloses a section of the film that becomes superconducting at a lower temperature than the rest of the film. The inhomogeneity in the film on the unannealed substrate is likely to arise from the higher defect density in this film.

annealed substrate. However, the transition width is broader and there is evidence of phenomena occurring below the transition temperature, which is not detectable with the resistivity measurement. The step-like structure at the foot of the transition reveals a region of the film that becomes superconducting very slowly with decreasing temperature disclosing a non-homogenous granular structure in the film. As a result of the wider transition, the effective maximum field expulsion temperature is lower than in the annealed film. It is therefore postulated that a dechanneling interaction or misfit region close to the interface deteriorates the quality of the deposited film and that even though XRD and resistivity measurements are not able to detect any significant difference in film quality, susceptibility measurements of the Meisnner effect reveal superior film quality for substrates pre-annealed at high temperature.

3.1.5 Determination of oxygen content

The critical dependance of the superconducting state of high T_c films of YBCO on the oxygen content in the film makes the quantitative determination of oxygen content an important characterization tool for high T_c thin film superconductors. XRD measurements and resistivity characterization and other methods are often used to indirectly determine the oxygen in YBCO films [**81, 82**]. However, the complicating phenomena of stress in deposited films and small variations in stoichiometry make XRD results ambigous and the possibility of percolation paths in resistivity measurements make the empirical determination of oxygen content with these techniques ambigious.

Conventional RBS techniques in conjunction with ion beam channelling provides a wealth of information about the target material including: composition, depth profiles, lattice damage, impurity lattice location and crystallinity [**83**]. For oxygen analysis, however, the sensitivity of this technique is low, especially when the target material contains other heavy elements, as is the case for YBCO. At energies for conventional backscattering, eg. 2 MeV α-particles incident on the target, the backscattered oxygen signal is overwhelmed by the signals from the substrate. A more suitable method for the direct determination of the oxygen content is achieved

by using the enhanced backscattering yield obtained from the ^{16}O resonance in the $^{16}O(\alpha,\alpha)^{16}O^*$ reaction. This elastic resonant α-scattering at 3.045 MeV is particularly well suited to the purpose of both oxygen concentration determination and depth profiling due to the high sensitivity and narrow width of the resonance [84–86].

Fig. 3.14 shows the RBS spectra of a film of YBCO on a MgO substrate backscattered at 3.067 MeV. The variation in the surface positions of the elements, as compared to previous spectra, is due the increased beam energy (3.067 MeV instead of 2 MeV). The film had c-axis orientation as determined by XRD and was superconducting with a $T_{\rho=0}$ of 84 K. The oxygen peak of the resonantly scattered α-particles rides over the background of non-resonant scattering from oxygen. This background, in turn, sits on top of a continium of elastic scattering by the substrate. The oxygen-content in the film was determined by fitting a theoretical spectra to the observed one by means of a modified version of RUMP [**85**] that takes into account the enhanced cross-section of the resonance. Calibration of the resonance spectra was achieved in two ways: a Ta_2O_5 standard was used to normalise the experimental spectra and the underlying MgO substrate was used as an internal standard to verify the calibration. In addition, the energy of the beam is such that the scattering from the metallic elements is still elastic and the ratio of these can also be determined simultaneously. The simulated fit gave an oxygen value of 6.9, consistent with the XRD data, in terms of the c-lattice parameter, and the superconducting nature of the film.

Depth profiling of the oxygen content in the film is possible by varying the incident energy to sample deeper regions of the film. However, the width of the incident beam and beam straggling effects (into the sample) which broadens the resonance width at greater depths makes determination of the interface and the oxygen depth profile slightly complicated [**86**]. Auger electron spectroscopy (AES) was used to determine the profile of both the oxygen and metallic signals into the substrate. **Fig. 3.15** shows the AES spectrum for the film deposited onto MgO. The depth profile is achieved by sputter removal of material from the surface. The

peak-to-peak height ratios reveal that the metallic and oxygen profiles are constant through the thickness of the film and is evidence of a uniform homogenous film.

3.1.6 Structural analysis by Ion Beam Channeling

The occurrence of lattice strain in the YBCO/MgO system is expected in view of the differing equilibrium lattice constants. Pseudomorphic or commensurate growth can occur when the lattice mismatch and hence the strain is not very large and for fairly thin layers [87]. The lattice parameters of c-axis oriented films have a_1 = 3.83Å, with the lattice constant of the MgO substrate a_2 = 4.21Å. The lattice mismatch is

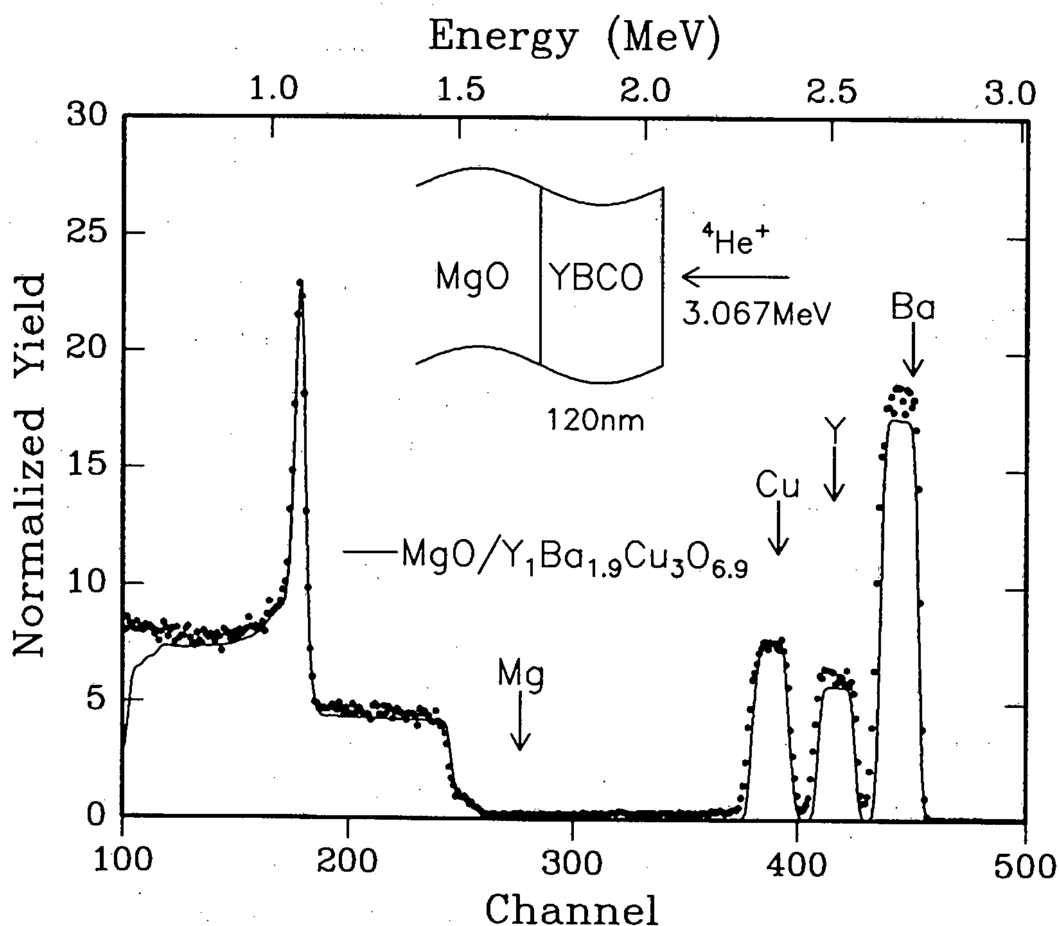

FIGURE 3.14: RBS performed on a YBCO film on a MgO substrate at 3.067MeV. The oxygen resonance is seen as the enhanced yield peak from the oxygen signal that sits on top of the substrate signal. The solid line is a modified RUMP simulation which takes into account the enhanced cross-section of the resonance.

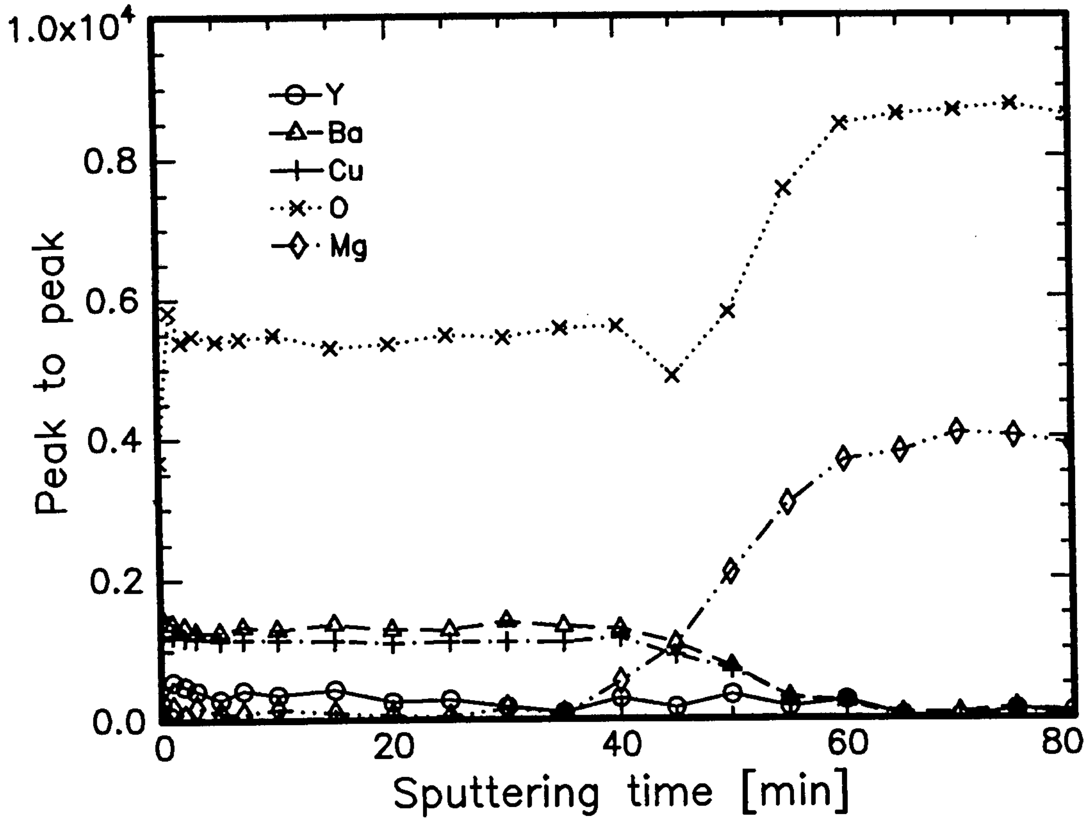

FIGURE 3.15: Auger electron spectroscopy (AES) of a film of YBCO on MgO. The depth profile is obtained by sputter removal of material. The peak-to-peak heights of the oxygen and metal signals is constant through the thickness of the film and display uniformity in the distribution of film elements.

given by:

$$f = 2\left(\frac{a_1 - a_2}{a_1 + a_2}\right) \tag{3.2}$$

having a relatively high value of >9% mismatch between the film and substrate. It is therefore interesting to investigate how highly textured or epitaxial YBCO films are deposited on these mismatched substrates. The lattice parameter of the film (a_1) will tend to expand (in first order) to match the larger substrate lattice constant (a_2). Thus for very thin YBCO films the lattice mismatch is accommodated by coherency strain. The expansion of the a_1 lattice parameters causes compression of the c-lattice parameter by the Poisson effect.

For the edge on edge growth of the YBCO film on MgO, the [100] growth direction maintains straight crystal rows for the film and substrate whereas in the [110] direction of the substrates the [103] direction for the film has a deviation from the substrate direction [87] by the amount:

$$\begin{aligned}\Delta\phi &= arctan(\frac{c/3}{a_1}) - arctan(\frac{a'_2}{a_2}) \\ &= arctan(\frac{c/3}{a}) - 45^o \end{aligned} \quad (3.3)$$

(Where $a'_2 = a_2$ for thick substrates i.e. the strain in the substrate is minimal)

For a thin YBCO layer on MgO the strain is fully constrained to the film and by measuring $\Delta\phi$ the strain can be measured. For such a system the strain in the c direction is given by:

$$\epsilon_c = \frac{(c/3 - a)}{a} \quad (3.4)$$

The strain energy in such a lattice mismatched system increases with increasing film thickness until, at some critical thickness, it becomes energetically favourable for the strain (or part of it) to be relieved by the formation of misfit dislocations near the film-substrate interface. The presence of dislocations (and other defects) at or near the interface, can have profound effects on the quality of the thin films.

Angular scans with ion channeling were performed around the normal and through inclined crystal directions (**Fig. 3.16**). This was done to determine the channeling yield for the film, represented by the Ba yield, and for the substrate, given by the Mg yield in these specified directions. In this way a measurement of the angular deviation $\Delta\phi$ can be made to determine the residual strain present for thick films and to determine to what extent the c-axis of the film is oriented commensurately with the crystal directions of the substrate. Ion channeling measurements at normal incidence were used to probe strain-relieving dislocations near the interface by determining the effect of dechannelling and the occurence of coincidental minima for the angular scans of the [001] and [100] direction of the film and substrate respectively. Coincidental minima for angular scans at inclined directions (45^0) is proof that the assumption of a c-axis oriented film is sound.

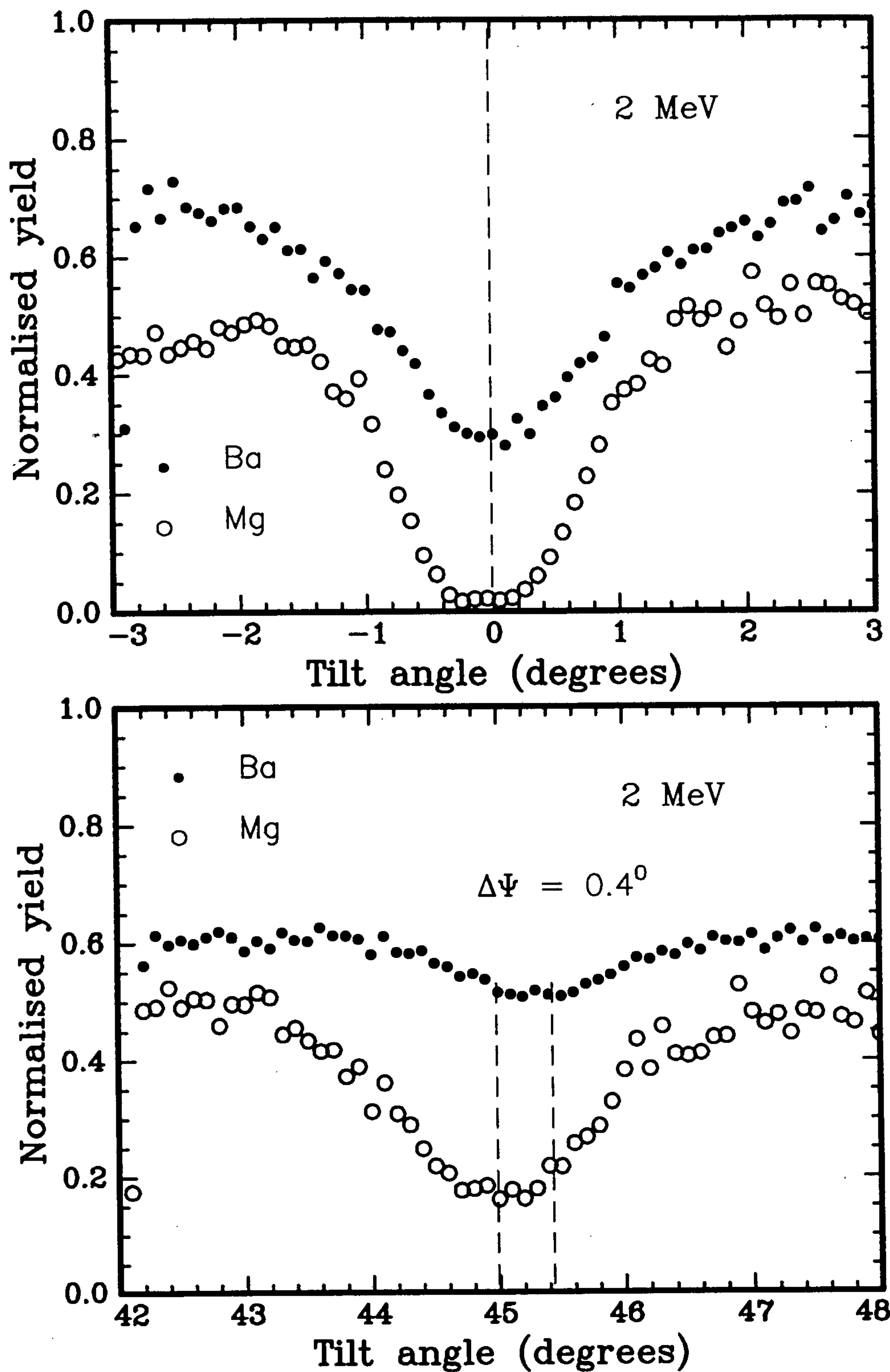

FIGURE 3.16: Angular scan curves for the Ba signal in YBCO and the Mg signal in the substrate in the (a) [100] and (b) [110] directions of the substrate. The coincidental minima of the film and substrate in the normal and inclined directions verifies that the film is c-axis oriented.

Fig. 3.16 shows an angular scan channeling measurement for [100] and [110] scans of the substrate corresponding to [001] and [103] scans in the film. At normal incidence the minimum yield is found at the same angular position for the film and substrate. A slight difference in the minimum of the Ba and Mg signals is noted at inclined incidence. However, this variation is very small $\Delta\psi = 0.4^o$ and is more likely to arise from the deviation of the [103] direction of the film from the [110] direction of the substrate as calculated for an unstrained film **[88]**, pointing to the fact that the strain has been completely relieved for the film, which is what would be expected for a relatively thick film. The occurence of the minimum yield values for the film and substrate at the same angular position for both inclined and normal scans implies that the c-axis of the film is perpendicular to the substrate to within the error of the determination of the minima of the scans (0.1°) and that the assumption of epitaxy is sound.

The effect of the lattice mismatch on the interface structure of a 450 nm thick film was studied using ion channeling at 2 MeV and 4 MeV. **Fig. 3.17** shows 2 and 4 MeV channeling spectra for YBCO in MgO; it can be seen that there is very little increase in dechanneling near the YBCO - MgO interface for the higher backscattering energy, which would occur if strain relieving misfit dislocations were prevelant. The density of defects for a strain-relieved (hetero)epitaxial layer is generally highest near the interface and decreases with distance from the interface. Thus it was observed that at a distance $\sim$500 nm from the interface a minimum yield of 7% can be obtained, proving that even for largely mismatched systems such as YBCO-MgO the density of defects is confined to the near-interfacial region. Direct evidence that thin films of YBCO can grow semi-coherently on MgO was provided by high resolution electron microscopy **[89]**, where it was found that the misfit between the two lattices was accomodated by the formation of periodic dislocations at the interface. The film was heavily faulted at the interface with the film structure becoming well defined as one moved away from the interface, which is confirmed by the ion channeling results. However, the weak energy dependance of the interfacial defects points to a possible mixture of stacking faults and dislocations.

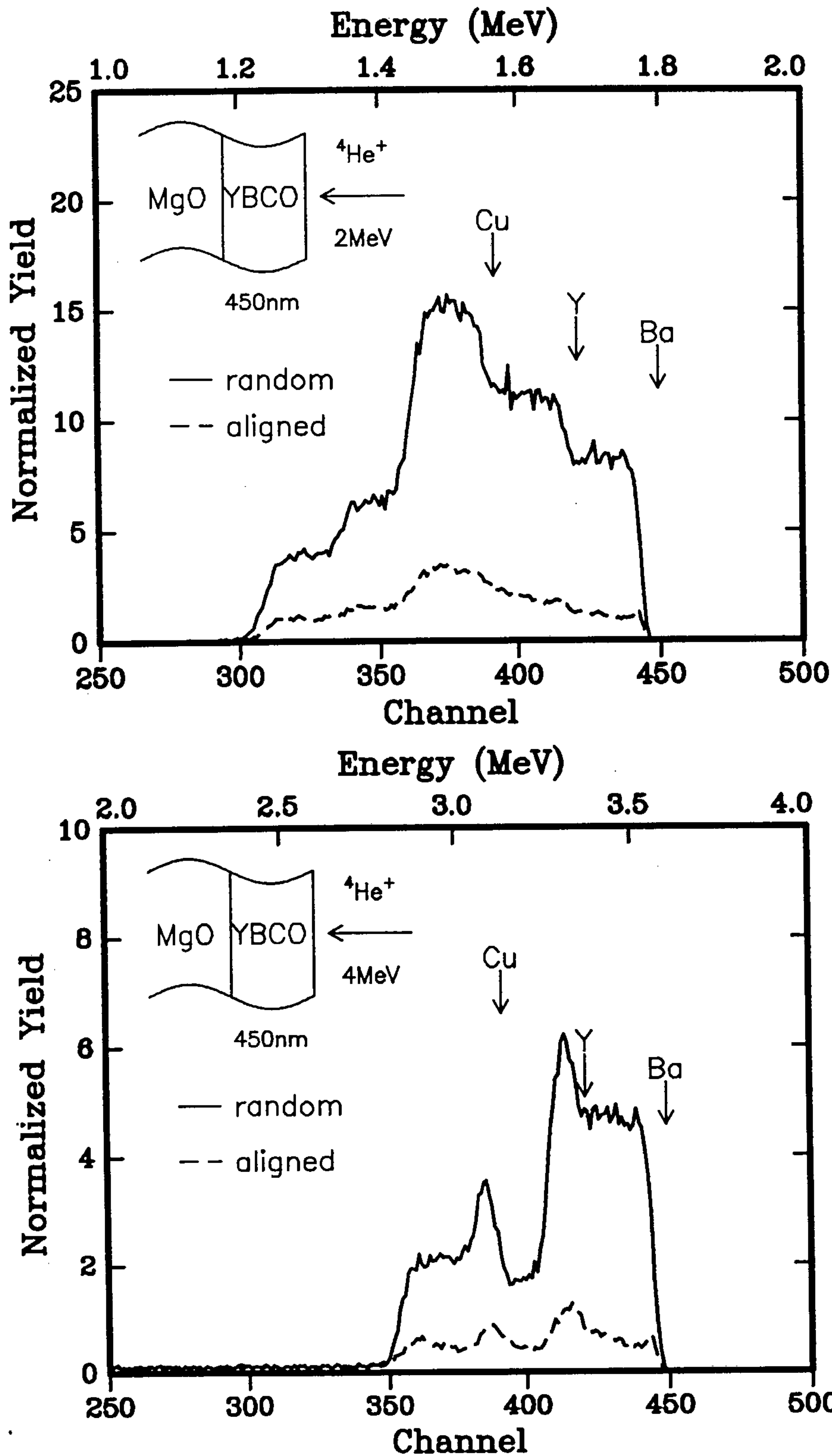

FIGURE 3.17: RBS spectra for a YBCO film on MgO at (a) 2MeV and (b) 4MeV. The aligned spectra were obtained in the [100] direction of the substrate. Increased dechanneling at the interface is evident at the higher energy.

The growth of YBCO on a large lattice mismatched substrate such as MgO renders the film susceptible to developing a mosaic structure [**89, 90**] which consists of subgrains which are c-axis oriented but misoriented with respect to each other by in-plane rotation(s) about the c-axis. For a highly textured material the film may consist of single crystallite grains rather well aligned with the substrate orientation. The standard deviation from the mean growth direction (the [100] axis of MgO) is determined by angular yield measurements [**91**]. The spread in crystallite orientation because of in plane rotation can be determined from:

$$\chi = 1 - \frac{1 - \chi_o}{1 + \frac{\sigma}{\psi^o_{1/2}}^2 ln2} \tag{3.5}$$

where χ is the minimum yield measured for the film, σ is the mosaicity or standard deviation of the crystallite orientations, $\psi^o_{1/2}$ is the angular half width at half maximum and χ_o is the minimum yield for channeling of single crystals. Using the estimated single crystal values and the energy dependence of ψ [**92**] ($\chi_o = 2\%$ and $\psi^o_{1/2} = 1.00°$), the mosaicity is estimated to be 0.22° . The small σ value reveals a mosaic structure with a narrow directional distribution of the crystallites, illustrating the good epitaxial growth quality of films on MgO.

3.2 Films on $SrTiO_3$

$SrTiO_3$ has many properties similar to MgO and is a good substrate for the deposition of YBCO in terms of its close lattice matching to YBCO inducing a very strong texture or even epitaxy. The highest T_c values have been attained with $SrTiO_3$ substrates [**1–3, 5**] because it best fulfills the properties required for a substrate. However, the high cost of producing single crystal $SrTiO_3$ substrates and its extremely high dielectric constant limits its usefulness in widespread applications. As a result of its good lattice match to YBCO it is ideal to be used to compare films deposited by ICM sputtering with those from other deposition methods.

Films deposited at room temperature showed similar behaviour to those deposited on MgO in that they were amorphous as-deposited and required a high temperature post deposition anneal in excess of 850°C to achieve superconductivity in the film. XRD analysis of the post-annealed film indicates polycrystalline film formation (**Fig. 3.18**). Preferential orientation in the form of enhanced c-axis growth is also noted. Films deposited at substrate temperatures in excess of 650°C were superconducting in-situ. However the films deposited at 650°C differed from those on MgO in that both the a- and c-axis orientation could be seen at these temperatures whereas on MgO a strained c-axis oriented film was observed. Growth of YBCO on $SrTiO_3$ with mixtures of a-and c-axis growth have been previously observed [**93**]. The apparent reason for this is the lattice mismatch behaviour of the film and substrate with increasing substrate temperature. The anistropic axial thermal expansion data for YBCO on $SrTiO_3$ [**94**] shows that at low substrate temperatures the c-axis parallel to the substrate (a-orientated film) surface has a lower mismatch while at higher temperatures the c-axis perpendicular texture is favoured, which is consistent with our results. The inherent large lattice mismatch between YBCO and MgO (9% for c-axis oriented films) seems to favour the c-axis orientation. The strong tendency of YBCO to grow with the c-axis orientation because of growth kinetics implies that for lower substrate temperatures where there is no overriding factor of orientational control by the substrate and the deposition rate is slow enough then the surface energy of the depositing film (mobility) can dictate the orientational

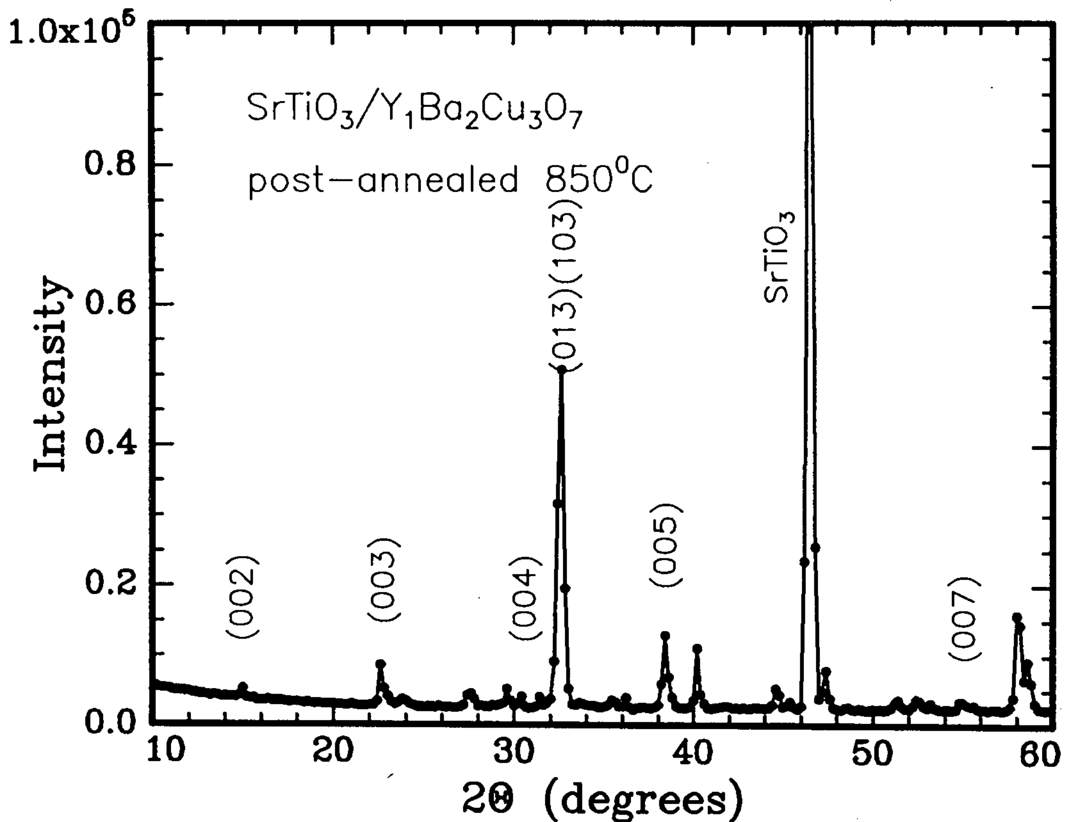

FIGURE 3.18: X-ray diffraction spectrum for a YBCO film deposited on $SrTiO_3$ at room temperature and post annealed at 850°C . The film is poly-crystalline with evidence of some preferential c-axis orientation.

distribution, and it has been found that the c-axis orientation grows an order of magnitude faster than the a-axis orientation [89].

Films deposited at 700°C were c-axis oriented with no other orientations being detected by XRD (**Fig. 3.19**). The strong orientational growth of YBCO on $SrTiO_3$ allows for easy determination of the c-axis parameter, for which a value of c=1.168 nm was obtained. RBS analysis of these films show them to be close to ideal stoichiometry although analysis is complicated by the overlap of the Y and Ba signals from the film with the Sr and Ti peaks from the substrate , making it difficult to determine a possible film substrate interaction. Channeling measurements on these films are interesting when compared with those on MgO. **Fig. 3.20** shows

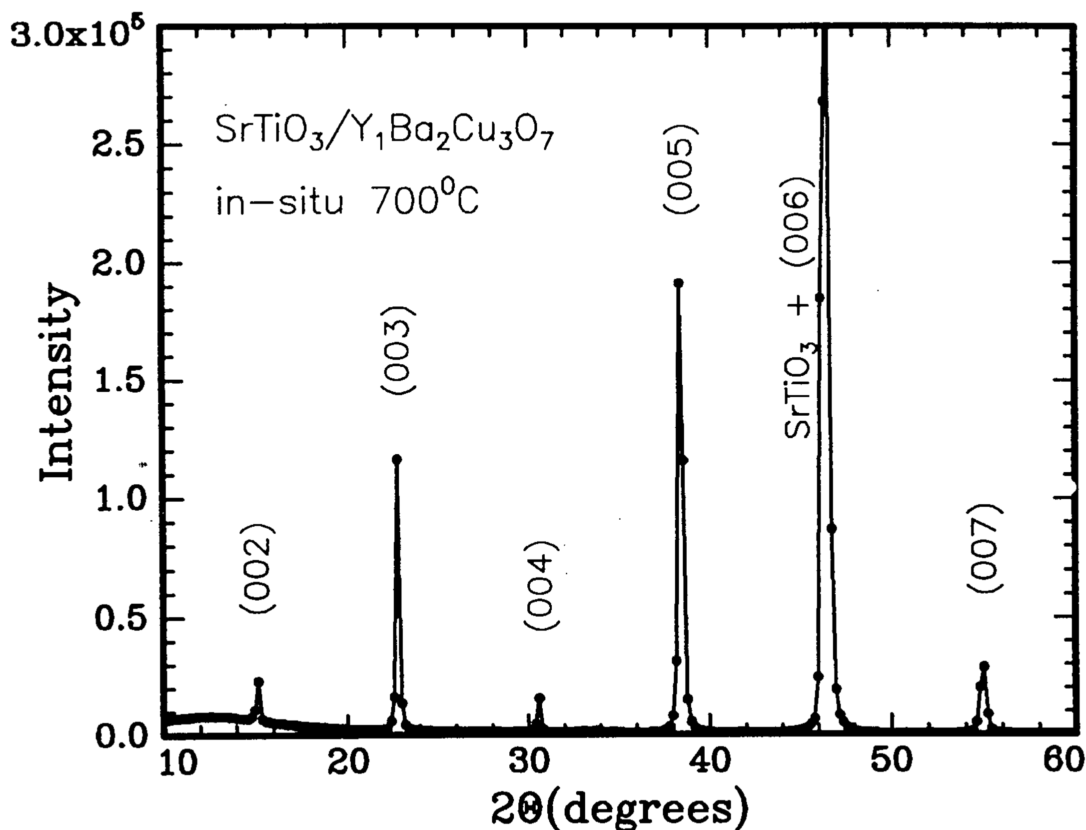

FIGURE 3.19: XRD spectrum of a YBCO film deposited at 700°C onto $SrTiO_3$. The film is superconducting as-deposited and only the c-axis reflections are seen, indicating a highly textured or epitaxial film.

backscattering spectra with the analysing beam in both a random and channeled [100] direction of $SrTiO_3$ for a film deposited at 700°C . The minimum yield measured for the Ba signal is 5.8%, slightly lower than the value measured for the film on MgO (7%). In addition the degree of dechannelling at the interface is much lower. This may be expected in view of the better lattice match between $SrTiO_3$ and YBCO and therefore a lower density of defects occurs at the interface.

The slow increase of the channelling yield from the film surface suggests a smaller number of defects which cause dechannelling of the ions. However, the presence of a dechanneling layer at the interface is due to the finite lattice mismatch and the possibility of a dechanneling interaction layer. This interaction layer may

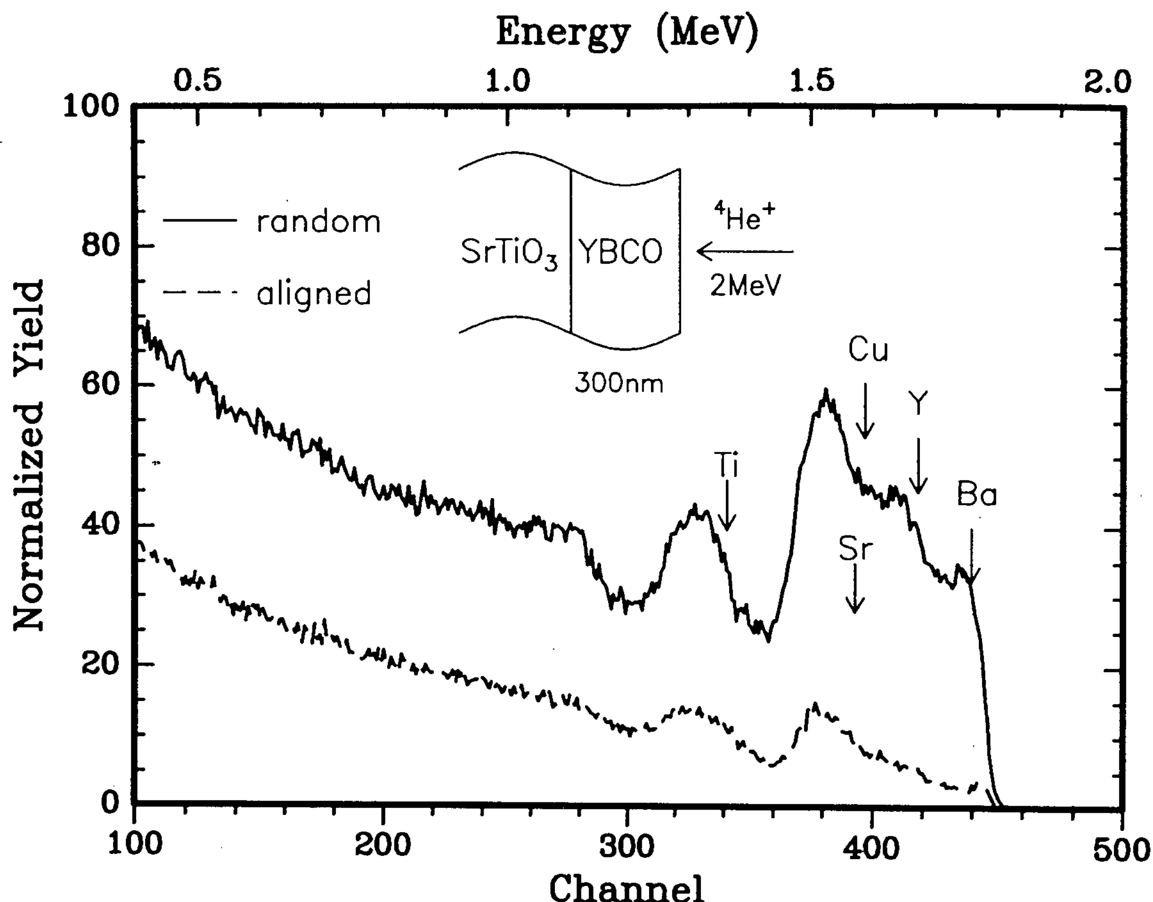

FIGURE 3.20: RBS spectra for the film shown in **Fig. 3.19**. The channeling spectrum was taken for the [100] direction of the substrate. A minimum yield of 6% was measured for the Ba peak in the film.

arise because Sr and Ti have been shown to have a slight tendency (when compared to other substrates) to diffuse into YBCO, mainly by the substitution of Y by Sr [**2, 20, 95–99**].

The angular yield of Ba was measured (from positive to negative tilt angles) and the results are shown in **Fig. 3.21**. A half-angular width at half maximum depth $\Psi_{\frac{1}{2}}$ of 0.9° was measured. Using the full angular width of 2.3° measured on single crystals made at 1.66 MeV, we deduce a full angular width of 2.05° at 2 MeV for single crystals (The $\Psi_{\frac{1}{2}}$ is proportional to $(\frac{1}{E})^{\frac{1}{2}}$ where E is the ion energy [**78**]), which is close to the value we have measured. Due to the large background from

the heavy elements of the substrate viz. Sr and Ti and some overlap with the Ba signal the angular yield for Y could not be determined precisely. As far as can be ascertained the $\Psi_{\frac{1}{2}}$ for Y is close to that of Ba indicating that the assumed c-axis orientation of the film is valid.

The mosaicity of the film was calculated using equation [3.5] and the measured χ_{min} values. The mosaicity σ was calculated to be 0.15° proving that the film has grown nearly epitaxially on the $SrTiO_3$ substrate with a negligible amount of crystallite spread if one takes into account the effect of beam spreading and that the measured spread is close to the limit of detection in the angular scan (0.1^0).

The area under the surface peak of the Ba signal in the channeling spectrum is proportional to the density of atoms on the surface and is a measure of the crystalline

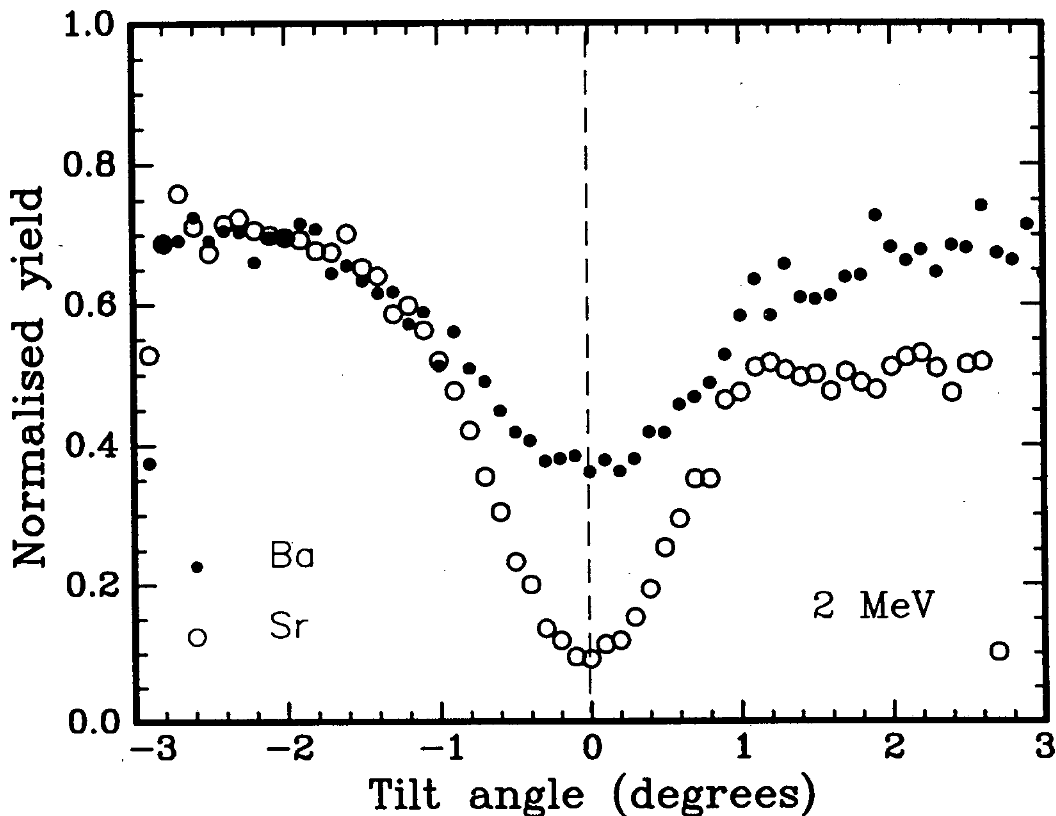

FIGURE 3.21: Angular scan of the minimum yield in the film, represented by the Ba signal, through the [100] direction of the substrate, indicated by the Sr signal.

order at the surface. From the SPA the areal density of Ba atoms in the surface layer, Nt, can be calculated from [**78**]:

$$Nt = SPA.c.\delta E/(H.\epsilon) \tag{3.6}$$

where δE is the energy per channel used for RBS
c is the relative concentration of Ba atoms in YBCO
H is the height of the Ba yield at the surface of the random spectrum
ϵ is the backscattering energy loss factor for He ions scattered from Ba.

Using an idealized composition of $Y_1Ba_2Cu_3O_7$ the extent of disorder at the surface was calculated from equation **3.6** to be a layer of thickness, t, of 1.6 nm. This limitation of the extent of surface disorder is important in the formation of superlattices and multilayered superconducting structures. The disordered surface layer thickness was calculated to be 2.1 nm for the film on MgO.

Superconducting characteristics of the films deposited at 700°C were determined by 4-pt resistivity and a.c. susceptibility measurements (**Fig. 3.22**). The films were black, shiny and displayed metallic behaviour in the normal state, with the resistance dropping with decreasing temperature. The temperature for the onset of superconductivity, $T_c(onset)$, measured at the intercept of the normal state behaviour and the sharp resistive drop, was found to be 87 K. The ratio of the normal state resistance to that at T_c (onset) was 2.7 indicating good film quality. The normal state resistivity line extrapolates to close to zero resistance at 0 K. The resistive drop is sharp with a transition width ΔT (90%-10%) of $\sim$ 1K observed. The a.c. susceptibility measurement is particularly impressive, with a sharp drop in the susceptibility being detected at 87 K. The transition width of $<$2 K is proof that the film is homogenous and does not consist of non-superconducting regions.

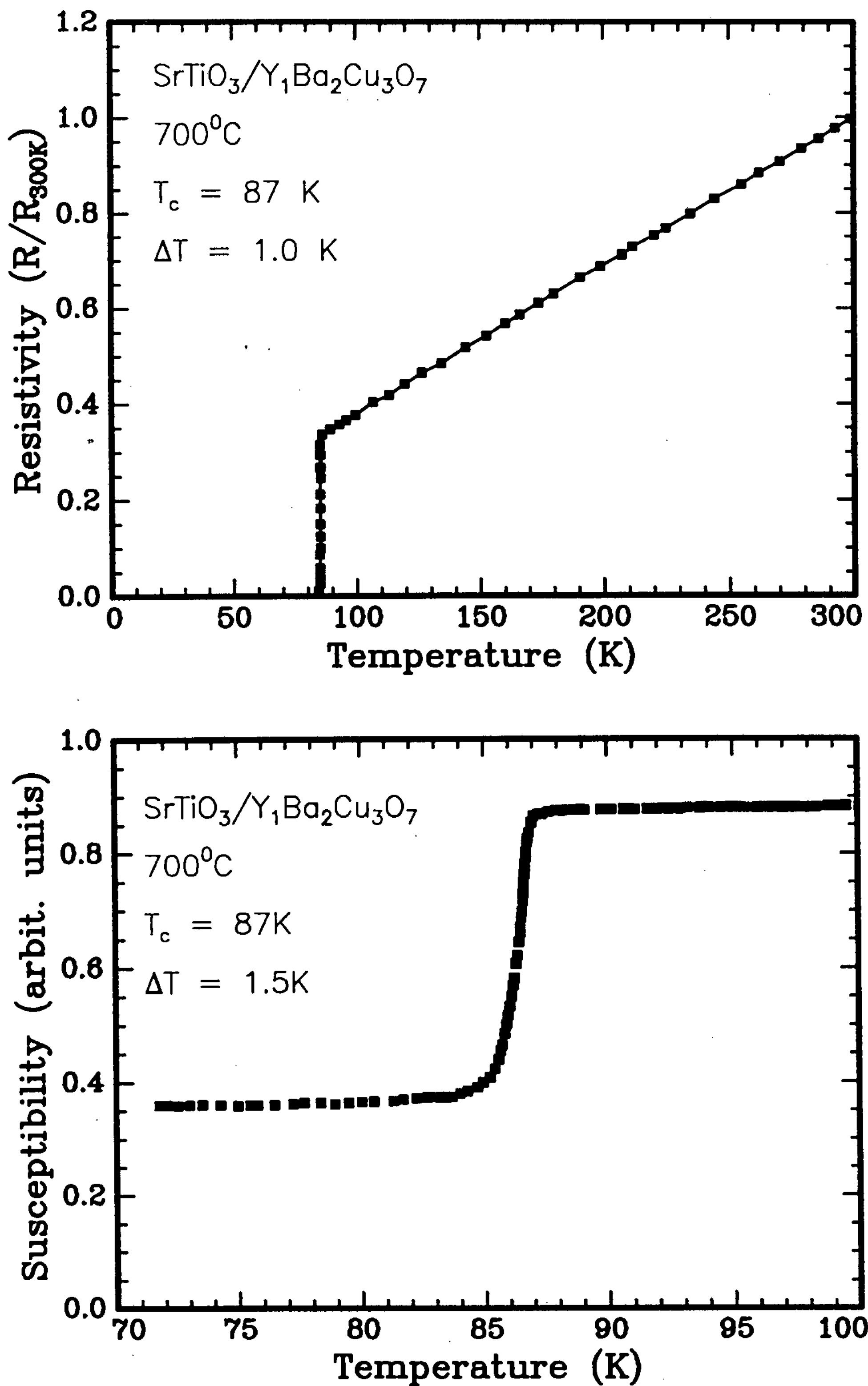

FIGURE 3.22: Electrical properties of the film deposited at 700°C on $SrTiO_3$. Resistivity measurements give a transition temperature of 87 K, with the normal state resistivity extrapolating close to zero resistance at 0 K. The susceptibility measurements confirm these results and indicate that the majority of the film is superconducting.

3.3 Films on Al_2O_3

Aluminium oxide (Al_2O_3) is a highly desirable substrate for the deposition of thin film superconductors because of its wide appeal for use in microwave applications as a result of its good dielectric properties (low dielectric constant) and the ability to make large area Al_2O_3 substrates at relatively low cost.

3.3.1 Direct deposition onto Al_2O_3

Deposition of YBCO onto Al_2O_3 by various techniques have been reported with the quality of the films vacillating with temperature, subtrate and deposition method. A wide range of T_c values have been quoted (20–60 K) [**29,31,100–104**]. It was not possible to deposit good quality films of YBCO onto single crystal Al_2O_3 substrates (1102) using the idealized conditions of the deposition parameters at a substrate temperature of 700°C as used in this study for in-situ deposition of superconducting films on MgO and $SrTiO_3$ substrates. RBS analysis (**Fig. 3.23**) of films deposited at 700°C on Al_2O_3 show a high level of film-substrate interaction which is the reason for the poor film characteristics. The interfacial reaction is shown by the tailing in the elemental distribution of the film and a sloping of the front edge of the Al signal. The formation of $BaAlO_4$ is expected from the reaction of Ba and Al_2O_3 at high temperatures [**2, 105**]. These poor quality films were discoloured and had rough surfaces. Examination of the surface revealed the presence of several micron length cracks. This may be expected in view of the thermal expansion mismatch between Al_2O_3 and YBCO [**1, 103**]. Deposition of YBCO films at room temperature onto Al_2O_3 gave smooth, black and uniform films (**Fig. 3.24**) but these were amorphous with no XRD peaks from the superconducting phase being detected. Normal state resistance of the as-deposited film was of the order of 100-200MΩ. Post-deposition annealing of these films reveals that the film substrate interaction occurs for a temperature as low as 500°C . This illustrates that neither post-deposition annealing nor in-situ deposition will result in good quality superconducting films with the ICM deposition method because of the film-substrate interaction, and although low temperature deposition (540°C) of in-situ superconducting YBCO films by electron

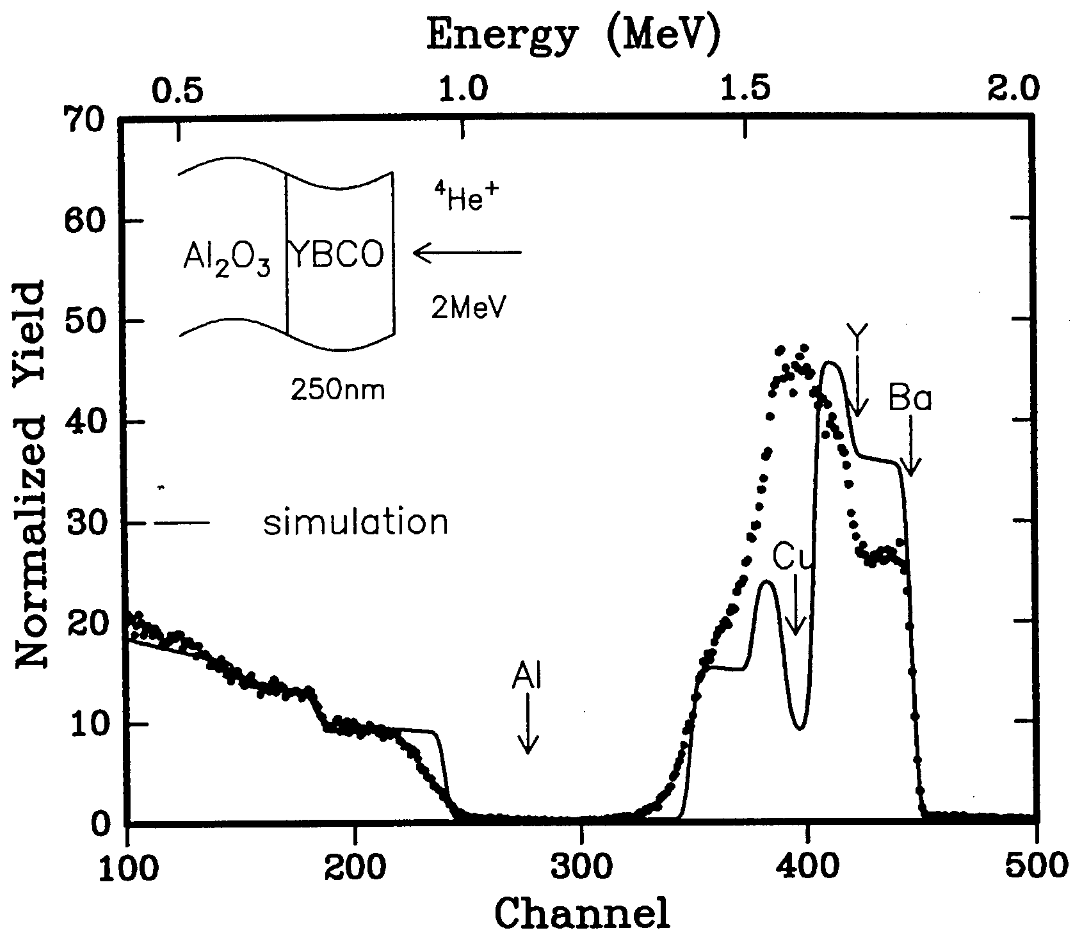

FIGURE 3.23: RBS spectrum for a YBCO film deposited onto Al_2O_3 at 700°C . Strong interaction between the film and the substrate results in the sloping of the signal at the back of the film and at the front of the substrate.

beam evaporation in the presence of plasma excited oxygen have been reported [106], these were also not of good quality - having a transition width of 16 K. This stresses the difference in quality of films that can be achieved with different deposition methods

XRD analysis of the film deposited at 700°C showed evidence of some peaks from the orthorhombic phase of YBCO (**Fig. 3.25**). However, these were for a polycrystalline film and were of very low intensity. These peaks are likely to occur from a surface layer which has not yet been degraded by the interfacial reaction, implying that the reaction occurs slower than the deposition rate of the film and

that for increased deposition rates and/or thicker films the upper part of the film could still be superconducting with the dead layer restricted to the interface. A fairly large critical thickness of 0.35μm was reportedly required for the interaction to be minimised such that the upper layers of the film can be superconducting [67]. The quality and usefullness of such films is however, likely to be less impressive than that of films on MgO and $SrTiO_3$.

The electrical properties of films deposited at 700°C are consistent with the RBS and XRD data. No susceptibility measurements were possible on these films exhibiting the lack of homogeneity in the film. Resistivity measurements displayed

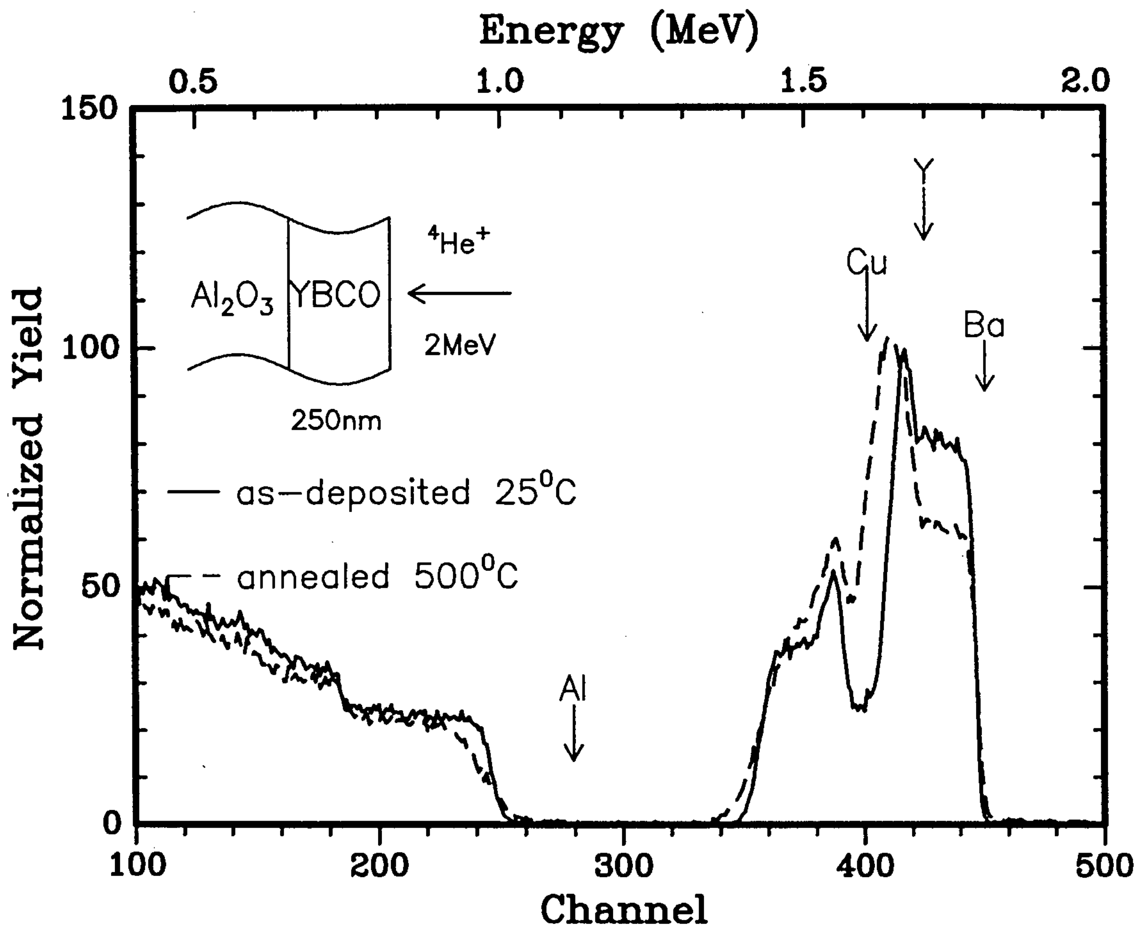

FIGURE 3.24: RBS spectra for a film deposited at room temperature and post-annealed at 500°C . The change in shape of the as-deposited spectrum and the loss of Ba from the surface of the film point to a diffusion of film components.

semiconducting behaviour from room temperature down to the onset transition temperature T_c, with the film resistance increasing with decreasing temperature (Fig. 3.26). At the transition temperature of ~70K, the resistance values drop slowly to below the room temperature resistive level and a zero resistance reading is never recorded. The large transition width is further evidence of a poor quality film. The electrical properties of the film is evidence of a percolative superconducting path in the film which arises from a set of connected superconducting grains. The reproducibility of the electrical properties of the films on Al_2O_3 is poor. This may be attributed to the presence of microcracks in the film that determine the electrical behaviour of individual films. Severe interaction between the YBCO film

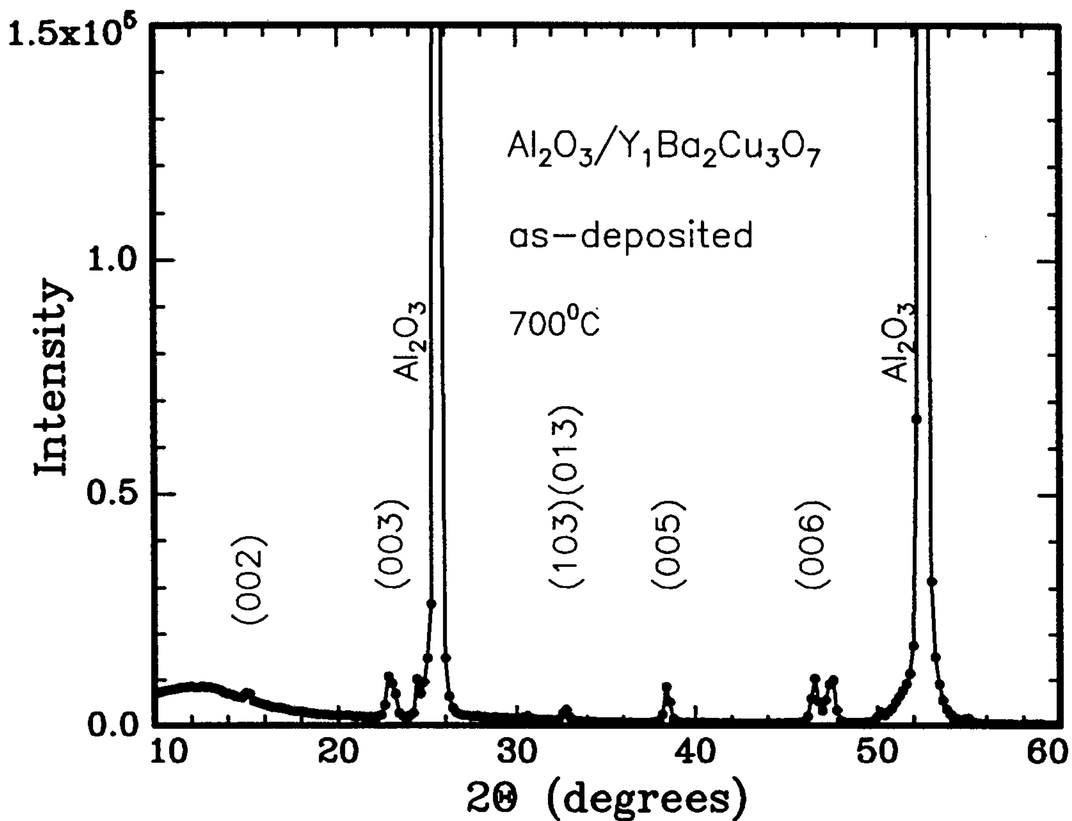

FIGURE 3.25: XRD spectrum for the film in Fig. 3.24. Reflections from the orthorhombic phase of YBCO are detected, but these signify a polycrystalline film and probably arise from a surface region that has not been degraded by the film-substrate interaction.

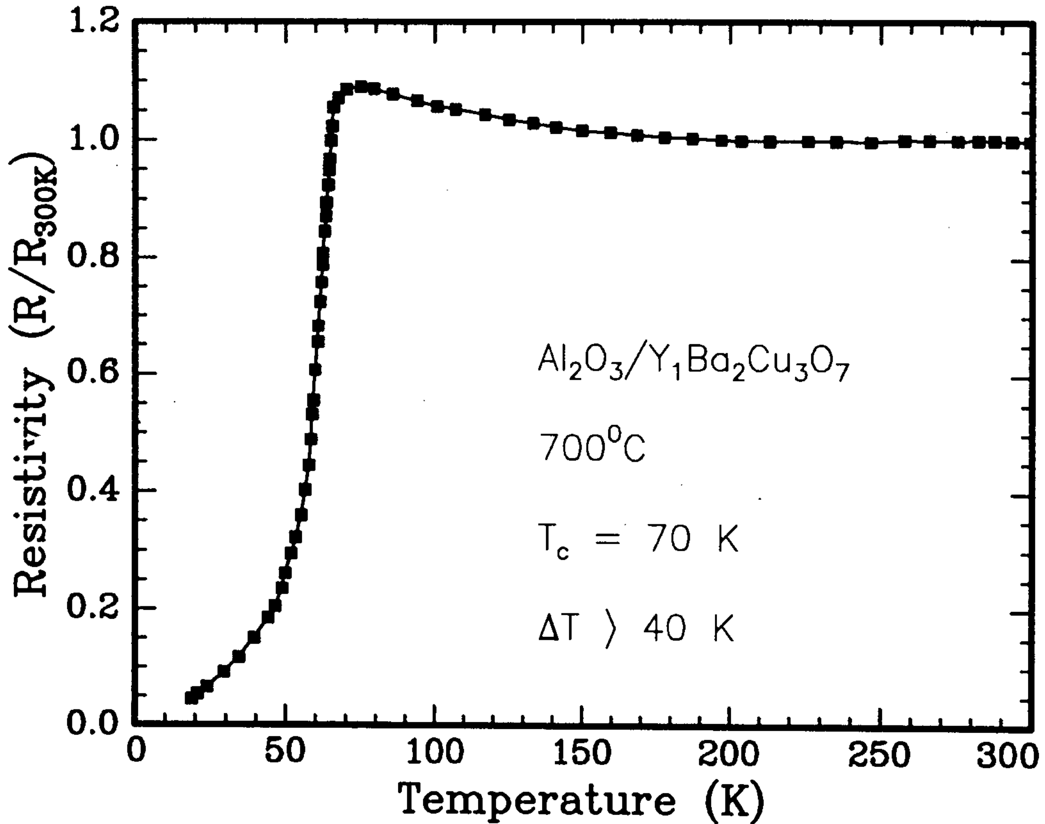

FIGURE 3.26: Resistivity measurement for the film deposited at 700°C . The film displays semiconducting behaviour in the normal state (above T_c) and has a very broad transition to low resistance.

and Al_2O_3 limits the usefulness of the film and the substrate in possible applications due to the degradation of the interfacial region. An additional drawback for the use of Al_2O_3 substrates is the tendency of Al to enhance the formation of the tetragonal phase of YBCO [**107, 108**]. The use of an oxide buffer layer, with reasonable dielectric properties, was therefore investigated. The buffer must prevent the interaction between YBCO and Al_2O_3 while at the same time preserving the nature of the YBCO film and the substrate i.e. the buffer layer itself may not interact with either the substrate or the YBCO film.

3.3.2 MgO buffer layer

MgO was the buffer layer of choice because of its displayed inertness with YBCO for the temperatures used during deposition. The good thermal stability and thermal conductivity of MgO are also important properties when considering a buffer layer. The development of an epitaxial buffer layer such as MgO is important for a number of applications **[109–113]** including compatibility with existing silicon on sapphire (Al_2O_3) technology. Furthermore, MgO on sapphire is expected to yield a very low loss and low dielectric constant for passive microwave circuits. In addition, sapphire substrates are available in large sizes at low cost. Apart from its use as a buffer layer on sapphire, the degree of epitaxy between MgO buffer layers and YBCO **[114]** and the high resistivity of MgO may be exploited for tri-layer superconductor-insulator-superconductor (SIS) junctions.

Fig. 3.27 shows the XRD spectrum of a 500Å MgO layer grown by e-beam evaporation onto a Al_2O_3 <1012> substrate at 450°C . The MgO buffer layer grows with a (h00) preferred orientation as observed by the (200) peaks at 42.8°. The single crystal MgO substrates used in section 3.1 were also (h00) oriented. However, the MgO buffer layer is polycrystalline, consisting of small grains, as evidenced by the relatively broad (200) peak seen for the buffer layer **[115]**. Thus while the MgO buffer provides for some orientational control we can expect that the quality of YBCO films will be inferior to that on single crystal MgO substrates.

The XRD spectrum of a film of YBCO grown on the Al_2O_3 /MgO structure at 700°C is shown in **Fig. 3.28**. The (00l) orientation of the film reveals a highly textured film with the c-axis perpendicular to the substrate surface. No other orientations from the tetragonal phase of YBCO or non-superconducting phases were detected with XRD. The diffraction peaks were sharply defined and of a similar intensity as for a YBCO film on single crystal MgO. RBS analysis of the Al_2O_3 /MgO/YBCO buffered structure (**Fig. 3.29**) shows that the MgO buffer layer is effective in preventing a reaction between the YBCO film and the Al_2O_3 substrate. The sharp edge of the signals from the film and the front edge of the MgO layer illustrate that there is little or no interaction between the film and the buffer

layer. Ion channeling analysis did not show a high degree of single crystallinity which is consistent with fact that the effective substrate for the depositing film is a polycrystalline MgO layer. The growth of YBCO on polycrystalline substrates is known to result in polycrystalline films. For such films the possibility of grain boundary diffusion of film-buffer reaction products or of a buffer-substrate reaction must be taken into account when considering the quality of the YBCO film to be grown. Thus it is expected that the growth of epitaxial MgO layers on Al_2O_3 and on Si will reveal films of the same quality as those on single crystal MgO substrates [111, 112, 116].

The YBCO film deposited onto Al_2O_3 with a MgO buffer layer showed metallic

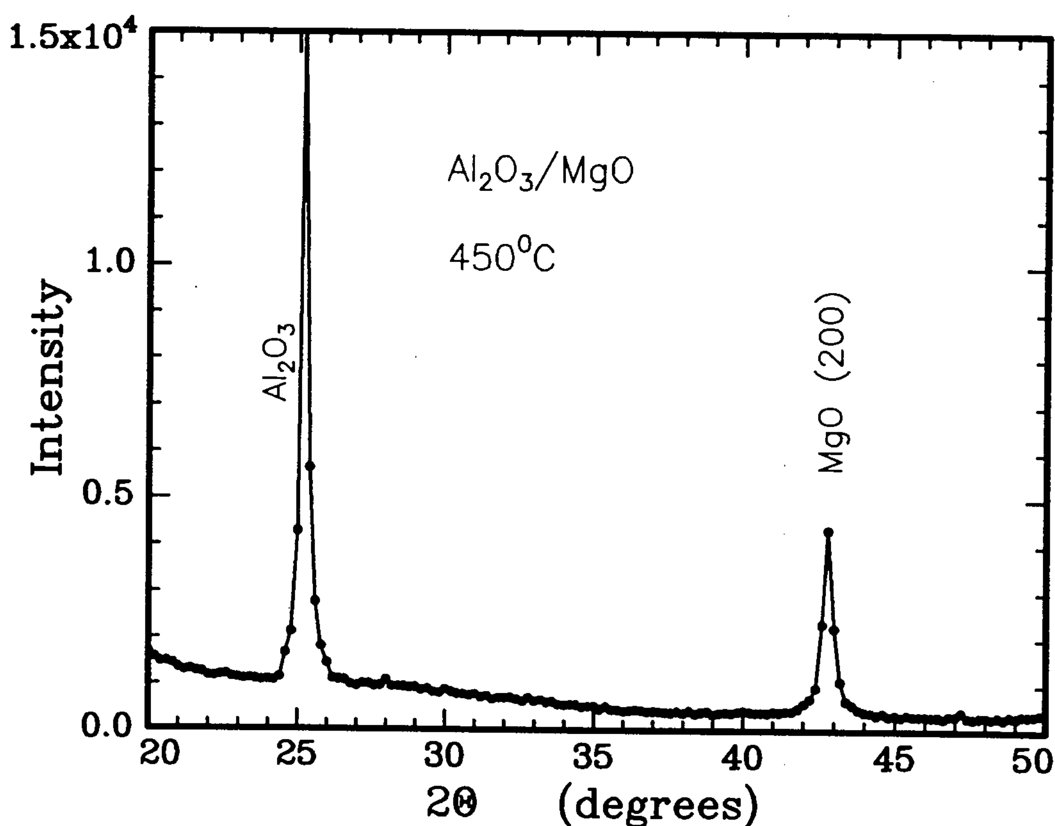

FIGURE 3.27: XRD spectra for a MgO film grown on Al_2O_3 at 450°C . The MgO film is highly textured with only the (200) orientation observed. The small peak height and slightly broadened MgO peak points to a polycrystalline film.

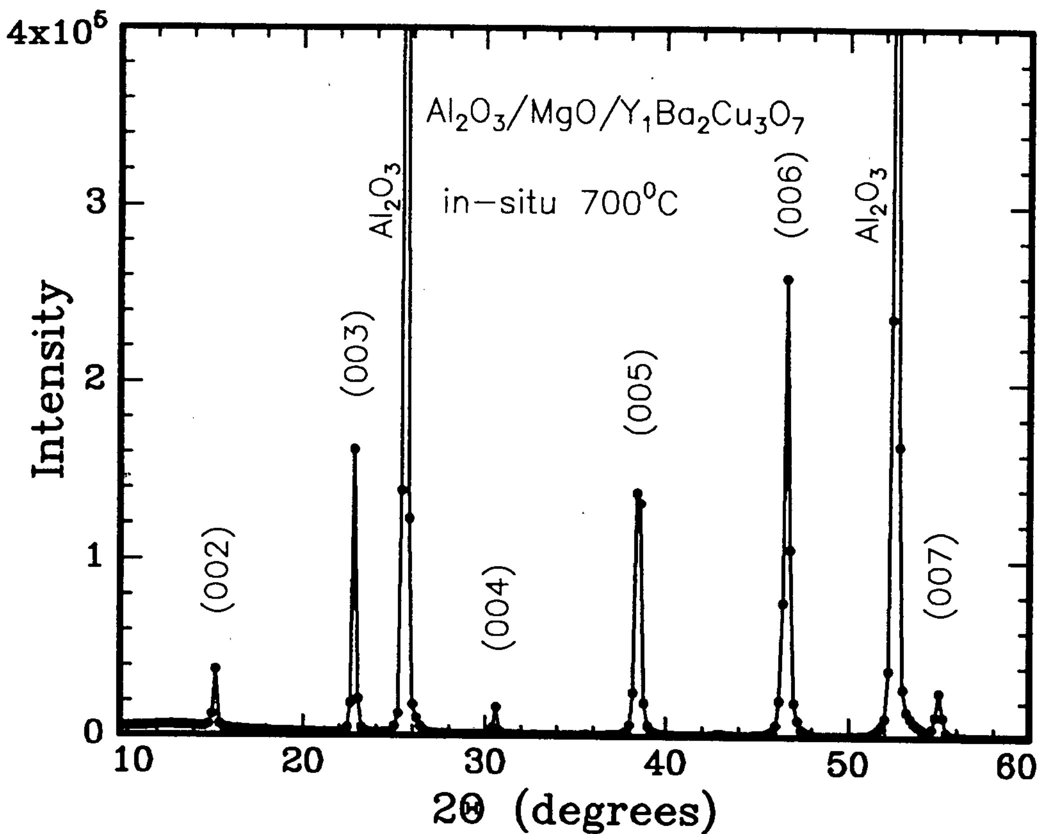

FIGURE 3.28: XRD spectra for a $Y_1Ba_2Cu_3O_7$ film grown on Al_2O_3 with a MgO buffer layer at 700°C . The film is highly textured with the c-axis orientation.

behaviour in the normal state, having a room temperature resistance of 200-400 Ω as measured with a multimeter, as compared to 30-100 Ω for better films. The relatively high resistance value is due to the polycrystalline nature of the film. The resistance values dropped with decreasing temperature, with the onset for superconductivity, T_c, reached at 83 K (**Fig. 3.30**). The transition width to zero resistance is wider than for films on single crystal MgO and the susceptibility measurements are clear evidence of the multigrained structure, with the transition width for the susceptibility measurement being much wider than for the resistivity measurement, which can be explained by multigrained weak link structures in the film.

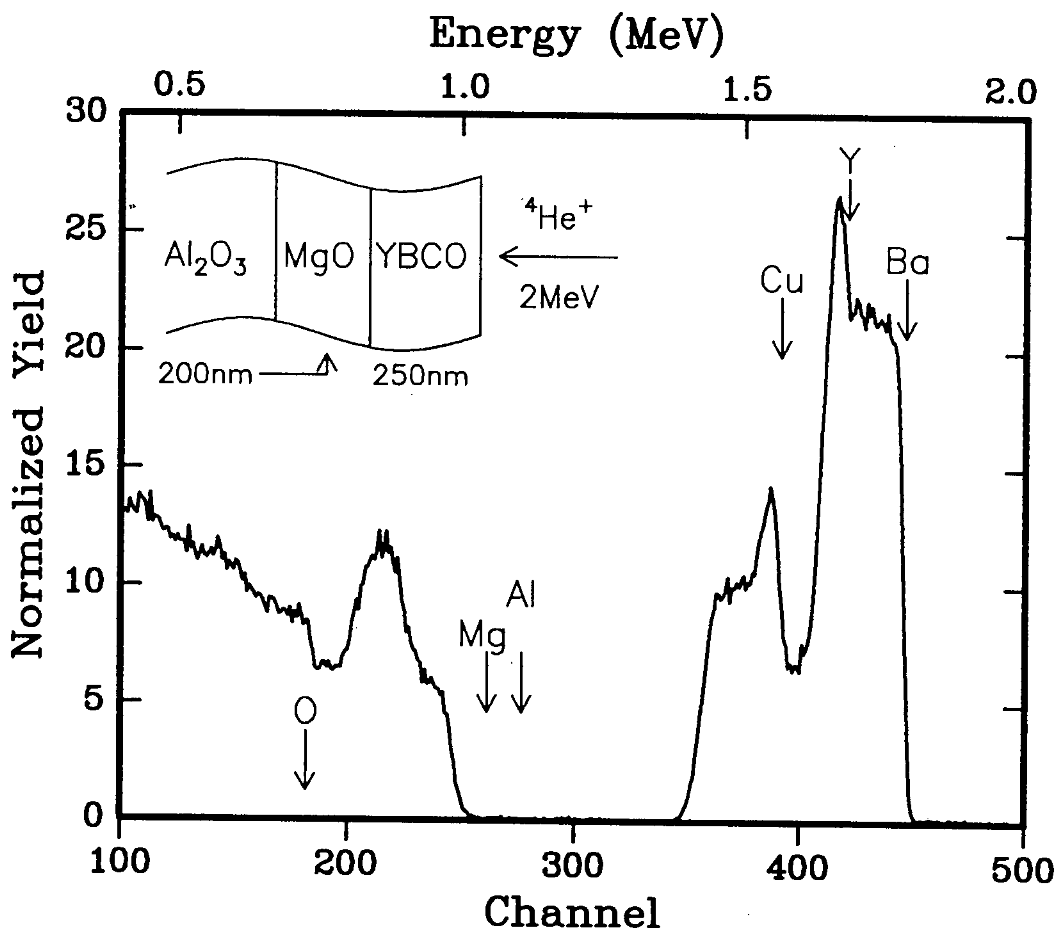

FIGURE 3.29: RBS spectrum of the Al_2O_3 /MgO/YBCO structure. The MgO buffer layer is effective in preventing a reaction between the substrate and superconductor and little reaction between the film and buffer is observed. The YBCO film was deposited by ICM sputtering at 700°C .

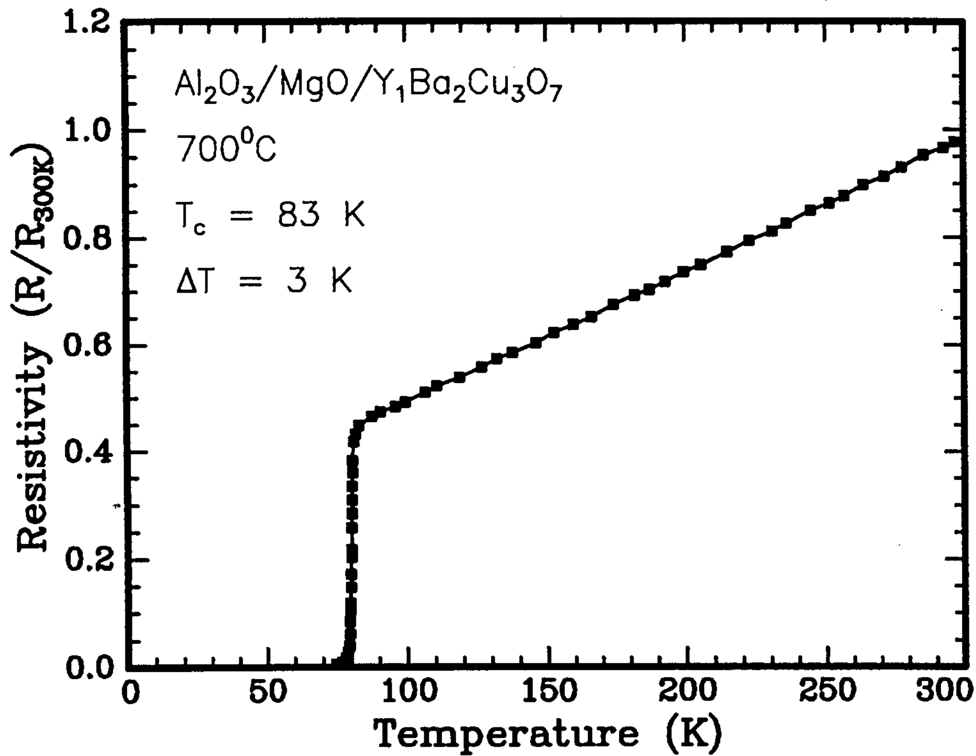

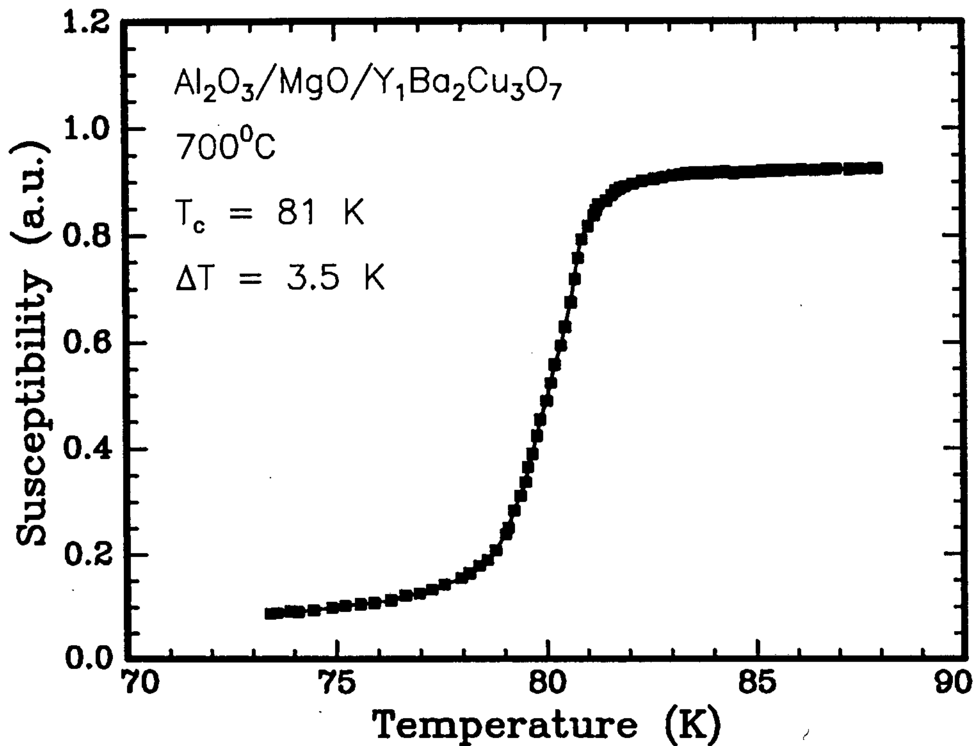

FIGURE 3.30: Resistivity and susceptibility measurements of YBCO films on a Al_2O_3 /MgO structure, grown by ICM sputter deposition at 700°C . The resistivity measurement does not extrapolate to zero in the normal state, with a $T_c = 83\,K$ and a transition width of 3 K recorded. The susceptibility transition starts at 81 K and has a broader transition width of 5 K.

3.4 Summary and discussion

Single crystal substrates of MgO and $SrTiO_3$ were used for the deposition of YBCO thin films in order to test the viability of the deposition method of ICM sputter deposition and to ascertain the necessary deposition parameters for quality films. The quality of such films can be gauged against that of films deposited by others using a variety of deposition techniques onto substrates of MgO and $SrTiO_3$ [1–7].

In the determination of the parameters for growth of YBCO films with adequate thickness and ideal stoichiometry, it was found that the total gas pressure in the deposition chamber and the oxygen partial pressure were of primary importance in influencing the effect of re-sputtering of deposited films. In light of the fact that the deposition system being used is essentially an off-axis sputter geometry that satisfies one of conditions mentioned in Sect. 3.1.3 for reducing the re-sputtering effect by energetic particles [**22, 28**], it was necessary to concentrate on thermalizing the energetic particles by using high gas pressures and on lowering the discharge voltage so that the energy of the particles that cause re-sputtering is reduced. Working with an empirical ratio of 2:1 for the Ar:O_2 gas pressures, it was found that at low total pressures (6×10^{-2} mbar) the arc voltage (and the energy of the bombarding ions) is extremely high. In addition the voltage varies erratically with arc current and a stable arc voltage was never realised for an arc current up to 600 mA. A minimum of arc voltage was seen to occur for a total pressure of 4.5×10^{-1} mbar. This pressure was the value used during all deposition of YBCO films with the ICM sputter gun in this study. The arc voltage has a flat profile which implies that the sputter gun power could be directly controlled by varying the arc current.

Next it was shown that the empirical ratio of 2:1 for the Ar:O_2 partial pressures is in fact the best possible combination. The total pressure was maintained at a constant 4.5×10^{-1}mbar and the partial pressure of oxygen was varied from 0.15×10^{-1}mbar $\rightarrow$ 2×10^{-1}mbar (with a corresponding variation in Ar pressure) to determine the effect of partial pressures on arc voltage (bombardment energy). It was shown that low oxygen partial pressures gave very high arc voltages and a minimum arc voltage was found for an oxygen partial pressure of $\sim 1.5\times10^{-1}$mbar,

which corresponds to an Ar:O_2 ratio of 2:1. This effect was independent of the arc current value used.

Determination of the stoichiometry of the deposited films with RBS confirms that near-stoichiometric films are deposited at a total pressure of 4.5×10^{-1}mbar and oxygen partial pressure of 1.5×10^{-1}mbar. Deviation from ideal stoichiometry is observed at low oxygen partial pressure and this confirms that the arc voltage reading is a good indicator of ion bombardment energy as the assertion that ion-bombardment causes stoichiometry deviation is ratified.

It was also seen that a sputter power of 50-80W is a useful empirical range of operation for the ICM gun. Lower power gives little deposition and higher power results in physical breakup of the target surface and the deposition of globules of material onto the film. Such rough films are detrimental to the growth of good quality superlattices and multilayered structures, besides the fact that compositional variations occur in the globules

From a measurement of the thickness homogeneity across the area covered by ICM sputter deposition, it was demonstrated that thickness variation of less than 10% is observed for a radius of 10mm from the centre of the deposit. Compositional homogeneity within this radius was also observed, pointing to the growth of YBCO films with minimal thickness or compositional gradients. Such planar films are vital in multilayered structures and devices.

Much work on the effect of substrate temperature on the growth of YBCO films [**6, 63, 64, 75**] has shown that low substrate temperatures give amorphous or poor crystallinity films. Low temperature deposition requires high temperature post-anneals to form the superconducting phase and it was found in this investigation that films deposited at low temperatures on MgO and post-annealed at 850°C were poly-crystalline. It was demonstrated that the lowest substrate temperature for which c-axis preferentially oriented films were obtained was 700°C . The stoichiometry of these films was near the 1-2-3 ratio and no film-substrate interaction was observed. The good crystalline quality of these films was proven with ion channeling analysis (fig. 3.10) where it was shown that a minimum yield of $\chi_{min} = 7\%$ could be obtained

for the Ba peak.

In section 3.2 the effect of the surface quality of the MgO substrate on the growth of high quality YBCO film was investigated. It was found that conventional cleaning of the MgO substrates in organic solvents, results in incorporation of carbon and oxygen (and possibly H) into the surface of the substrate and the surface peak of Mg is enhanced pointing to disorder created at the surface. A high temperature anneal (1000°C) in O_2 was used to desorb the contaminants and re-order the surface. Such a procedure is also expected to create a high density of atoms steps at the surface [**59, 60, 79**] which assists in nucleation and growth of the depositing film. Films on annealed substrates had superior electrical properties as compared to films on unannealed substrates. This was explained in terms of the ease of nucleation on the annealed substrate.

The oxygen resonance technique at 3.045 MeV indicated that the YBCO films had high oxygen composition (>6.8), which could be correlated with the superconducting nature of these films as shown in the electrical measurements. Auger Electron Spectroscopy (AES) analysis of a YBCO film on MgO deposited at 700°C by ICM sputtering showed a uniform distribution of the metallic elements and oxygen and indicates a homogenous film.

Ion channeling was used for structure analysis of the growth of high quality films (χ_{min} = 7%, T_c = 85 K, ΔT = 1-2 K) of $Y_1Ba_2Cu_3O_7$ on single crystal MgO<100> substrates at 700°C . In view of the relatively large lattice mismatch between YBCO and MgO it is understandable that true epitaxial growth cannot occur; however, pseudomorphic or commensurate growth can occur for thin YBCO films, where the lattice mismatch is accommodated by stress in the film. Angular scans of the backscattering yields for the film (for the Ba signal) and from the substrate (Mg signal) were taken for both normal incident and for inclined incidence (45°). It was verified that the assumption of c-axis orientation is sound in that coincidental minima were obtained for both normal and inclined angular scans. Although increased dechanneling was observed at the interface it could not be conclusively established that these were due to any specific defects. Ion channeling

experiments at 2 MeV and 4 MeV gave no clear indication of energy dependant behaviour of possible defects. It was found that for large lattice–mismatched systems such as MgO-YBCO, at a distance from the interface the film is well defined with the crystallinity at ~400nm being quite good ($\chi_{min} = 7\%$).

The lattice mismatch also gives rise to the possibility of in-plane rotation of the films i.e. the film develops mosiac structure [**89, 90**]. The mosiacity was of the film was examined using ion channeling and corroborated with data for channeling measurements on single crystals. A mosaic spread of 0.22° was calculated which comes out as a narrow directional spread of the YBCO film crystallites and points to the good (hetero) epitaxial film quality.

In section 3.2 the growth of YBCO films by ICM sputter deposition onto single crystal $SrTiO_3$ <100> substrates was examined. It was found that the growth of YBCO on $SrTiO_3$ is similar to that on MgO; low temperature depositions required high temperature anneals to form the superconducting phase and the films were polycrystallline with some evidence of c-axis orientation. Films deposited at 700°C were preferentially c-axis oriented and showed formation of the superconducting phase in-situ. Examination of these films with ion channeling analysis gave a minimum yield of <6% at the Ba signal. The dechanneling at the interface was lower than for films on MgO and this was explained in terms of the smaller lattice mismatch of YBCO with $SrTiO_3$. Angular scans of the minimum yield of Ba and Sr signals gave coincidental minima for both signals and confirms the c-axis orientation. The measured half-width at half-maximum for the angular scans $\psi_{\frac{1}{2}}$ was deduced to be 0.9° and corresponds well with a value of 1.02° for single crystals of $Y_1Ba_2Cu_3O_7$ [**92**]. Using equation 3.5 the mosaicity of the film was calculated to be 0.15° lower than the 0.22°C found for MgO substrates and proving that the film quality is improved because of the better lattice matching conditions.

The surface peak area (SPA) at the Ba signal was used to calculate the thickness of the disordered layer on the surface of the YBCO film [**78**] and this was found to be a layer of thickness 1.6nm. The surface disorder is an important factor in the growth of multilayers and superlattices and the relatively thin layer found

points to good film growth and stability. Testing the electric properties of YBCO films on $SrTiO_3$ with resistivity and A.C. susceptibility measurements confirms the good quality of the films. The YBCO films were metallic in the normal state i.e. above the superconducting transition, and the drop of resistance with temperature was steep. The transition temperature for the onset of superconductivity, T_c, was found at 87 K and a sharp transition width ΔT (90%-10%) of 1 K was detected. The normal state resistivity extrapolates to zero resistance at zero Kelvin. A.C. susceptibility measurement of the magnetic flux expulsion, i.e. the Meissner effect, gave a transition temperature of 87 K and a transition width of <2 K as proof that the film is homogenous and of good quality. Critical current measurements, in the absence of a magnetic field, gave J_c values of $\approx 10^6$ A cm^{-2} for films on MgO and $SrTiO_3$.

Section 3.3 looked at the growth of YBCO films on Al_2O_3, which is a favoured substrate for microwave applications because of its low dielectric constant and low cost. It turned out that the growth of high quality YBCO films in-situ by ICM Sputter deposition is not viable because of severe interaction between YBCO and Al_2O_3. Ba is expected to react with Al_2O_3 to form $BaAlO_4$ **[2,105]**. These films were poorly crystalline and the resistivity measurements displayed depressed transition temperatures, T_c = 70 K, with a broad transition from the normal state to low resistivity. A zero resistance reading was not obtained and the reproducibility of the results on Al_2O_3 was unsatisfactory. This was attributed to the presence of microcracks in the YBCO film. Investigating the reaction of YBCO and Al_2O_3 by depositing YBCO films at room temperature and post-annealing the structures shows that the interaction between the film and substrate occurs for temperatures as low as 500°C . This illustrates that neither post deposition annealing nor in-situ deposition at 700°C results in good quality YBCO films on Al_2O_3 and necessitated the use of a buffer layer to prevent the film substrate interaction.

MgO was used as the buffer layer because of its inertness with YBCO at 700°C . A MgO layer was grown by e-beam evaporation on a heated Al_2O_3 substrate (450°C) and the MgO ($h00$) orientation was observed. XRD analysis of growth of

a YBCO film by ICM sputter deposition at 700°C established that the YBCO film is highly textured with a prefered c-axis orientation. The RBS spectrum of the Al_2O_3/MgO/YBCO structure confirmed that the MgO is effective in preventing an Al_2O_3-YBCO reaction and it was clear no MgO-YBCO interaction occured. No channeling was observed for the YBCO film, pointing to a polycrystalline film.

The electrical properties of the YBCO film on the buffer Al_2O_3 substrate was substantially different for that on a bare Al_2O_3 substrate in that a high transition temperature for the resistive measurement (T_c=83 K) and a relatively sharp transition width (3 K) was observed. The better film quality was confirmed by A.C. susceptibility measurement. Although a slightly depressed transition temperature and broadened transition width was observed, T_c=81 K and ΔT=5 K, this can be expected for films with weak links between the grains. The weak link behaviour is confirmed by the critical current measurements, for which a J_c value of 3×10^4 A cm^2 was obtained.

Table 3.1 shows some of the results obtained by other workers for deposition onto oxide substrates with various deposition methods. Unfortunately it is not within the scope of this investigation to consider all the results available to deposition of thin film superconductors. As far as possible only those results detailing growth by the *in-situ* method with various deposition techniques are presented. In general this involves substrate temperatures in excess of 450°C . It can be seen from the table that the results obtained by ICM sputter deposition in this study are as good as (or better than) the results from other studies. A comparison with other results obtained from ICM sputter deposition shows that lower deposition temperatures were used in this study. Unfortunately, 700°C is the maximum temperature possible to sustain with the heater used in this investigation. Nevertheless, the results are not greatly affected by the lower deposition temperature and these lower temperatures are more compatible with device processing. The relatively poor results obtained on Al_2O_3 substrates is further validation for the use of buffer layers on these substrates. Note that the other results on Al_2O_3 are at much lower deposition temperatures, and still the $Y_1Ba_2Cu_3O_7$ film properties are degraded. It is unfortunate that transition

TABLE 3.1: A comparison of some results obtained for $Y_1Ba_2Cu_3O_7$ films formed on oxide substrates by various deposition methods. The transition temperatures and widths are for resistivity measurements. The absence of a reading is indicated by a dash (–). The values obtained in this investigation are denoted with an asterisk (*).

Substrate	Deposition Method	Deposition Temperature	T_c (K)	ΔT (K)	Ref.
MgO	Laser ablation	670°C	88	–	[59]
	Magnetron sputter	650°C	82	2.5	[28]
	MOCVD	500°C	90	1.5	[90]
	ICM sputter	780°C	90	–	[34]
	Sputter	650°C	92	6.0	[6]
	ICM sputter	700°C	85	2.0	*
$SrTiO_3$	Laser ablation	650°C	88	5.0	[63]
	e-beam evaporation	540°C	78	8.0	[106]
	Laser ablation	500°C	86	–	[103]
	Laser ablation	650°C	83	–	[31]
	ICM sputter	820°C	90	–	[34]
	ICM sputter	700°C	87	1.0	*
Al_2O_3	Laser ablation	580°C	78	–	[63]
	Laser ablation	500°C	71	–	[103]
	ICM sputter	700°C	70	>60	*
Al_2O_3/MgO	e-beam evaporation	680°C	88	–	[114]
	ICM sputter	700°C	83	3.0	*

widths are not presented for all the quoted reports as one can see that the ΔT values obtained in this study are amongst the smallest values recorded, pointing to good quality films on MgO and $SrTiO_3$. It is also worth mentioning that the T_c values quoted from this study are generally underestimated by 1 or 2 K compared to those quoted by others because the readings in this study are taken at the intercept of the normal-state slope and the slope of the superconducting transition whereas other workers often consider a drop of 5-10% to denote a transition.

The resistivity and susceptibility data for films on $SrTiO_3$ and MgO are very similar, with both showing high T_c and sharp transition widths. Susceptibility

measurements on these films showed homogenous films with the majority of the film having the a superconducting transition at the same temperature. Films on bare Al_2O_3 had low T_c values and broad transition widths to zero resistance. The use of a MgO buffer layer on Al_2O_3 improves the electrical properties of the film considerably. Susceptibility readings for the buffered film denote a polycrystalline film with some inhomogeneity in the YBCO film as seen in the transition to zero resistance.

CHAPTER 4

Thin film superconductors on silicon

The deposition of thin films of $Y_1Ba_2Cu_3O_7$ onto oxide substrates such as $SrTiO_3$ and MgO have been shown by this and other investigations [**63, 64, 75, 101, 103**], to yield good quality films with high T_c values and sharp transition widths. From a technology point of view the challenge is, however, to incorporate these superconducting thin films into useful structures and devices. The integration of semiconductor and superconductor microelectronic technology holds great promise for potential applications, especially in the use of silicon(Si) semiconductor technology. Silicon is the favoured substrate of use due to the advanced processing techniques and numerous device capabilities that exist for Si. The basis of the merger will be the ability to deposit superconducting thin films onto silicon and silicon based substrates. However, it has been established that the reaction and interdiffusion of YBCO with silicon is severe [**10, 24, 117**]. This causes YBCO thin films on Si to have reacted interfaces or diffusion poisoned films that has limited the growth of high quality thin films on silicon substrates. The undesirable reaction at the interface also results in poor film substrate adhesion [**95, 118**]. In addition, single crystal substrates of Si have large mismatch of the lattice parameters and the thermal expansion coefficients when compared with YBCO and this can result in film cracking and poor orientational control of the superconducting film [**1**]. The highly reactive nature of the YBCO film on Si substrates makes even in-situ deposition

difficult as temperatures of 650-700°C are required for the deposition of good quality films.

Limited reports of good quality films by direct deposition onto Si at relatively low substrate temperatures are to be found with, for example, T_c values of 81 K [**119**], 86 K [**120**] and 63 K [**121**] being reported. Two methods have been used to enable successful growth on Si: *in situ* growth of YBCO films and the use of buffer layers as diffusion barriers. Both of these techniques have been employed in the present study. *In situ* growth of YBCO films at relatively low temperatures (lower than the post-annealing temperatures) can be used to avoid or reduce the interaction between film and substrate. It can also improve the films surface smoothness and morphology, structure and density [**122**]. High quality thin films have been successfully grown by *in situ* deposition with laser ablation [**101**], magnetron sputtering [**3, 26, 61, 122**] (and **Chap. 3**), e-beam evaporation [**123**] and molecular beam epitaxy [**124**]. Buffer layers have been used to prevent the Si/YBCO reaction and preserve the superconducting properties of the YBCO film [**8–13**]. Diffusion barriers between Si and YBCO films can also improve lattice constant and thermal expansion matching between film and substrate. Good quality YBCO films have been grown on Si buffered with MgO [**113**], ZrO_2 [**24**], RuO_2 [**125**], indium-tin-oxide(ITO) [**13**] and bilayers of $MgOAl_2O_4/BaTiO_3$ [**126**], $MgOAl_2O_4/SrTiO_3$ [**127**], ZrO_2 (Y)/Y_2O_3 [**128, 129**] and multilayers of $SiO_2/ZrO_2/Y_2O_3$ [**129, 130**].

4.1 Direct deposition onto silicon

A RBS spectrum of a thin film of YBCO grown on a single crystal Si substrate by ICM sputter deposition at a temperature of 700°C is shown in **Fig. 4.1**. The severe interaction between the film and substrate is apparent. The stoichiometry of the deposited layer was assessed by using a MgO substrate as a control specimen such that the films on the control and on the Si substrate were deposited during the same run. The stoichiometry in the control specimen was in the nominal ratio 1:2:3 for the elements Y:Ba:Cu. The Si substrate specimen showed a deficiency in the Ba signal at the surface of the film, which is attributed to diffusion of Ba into the Si

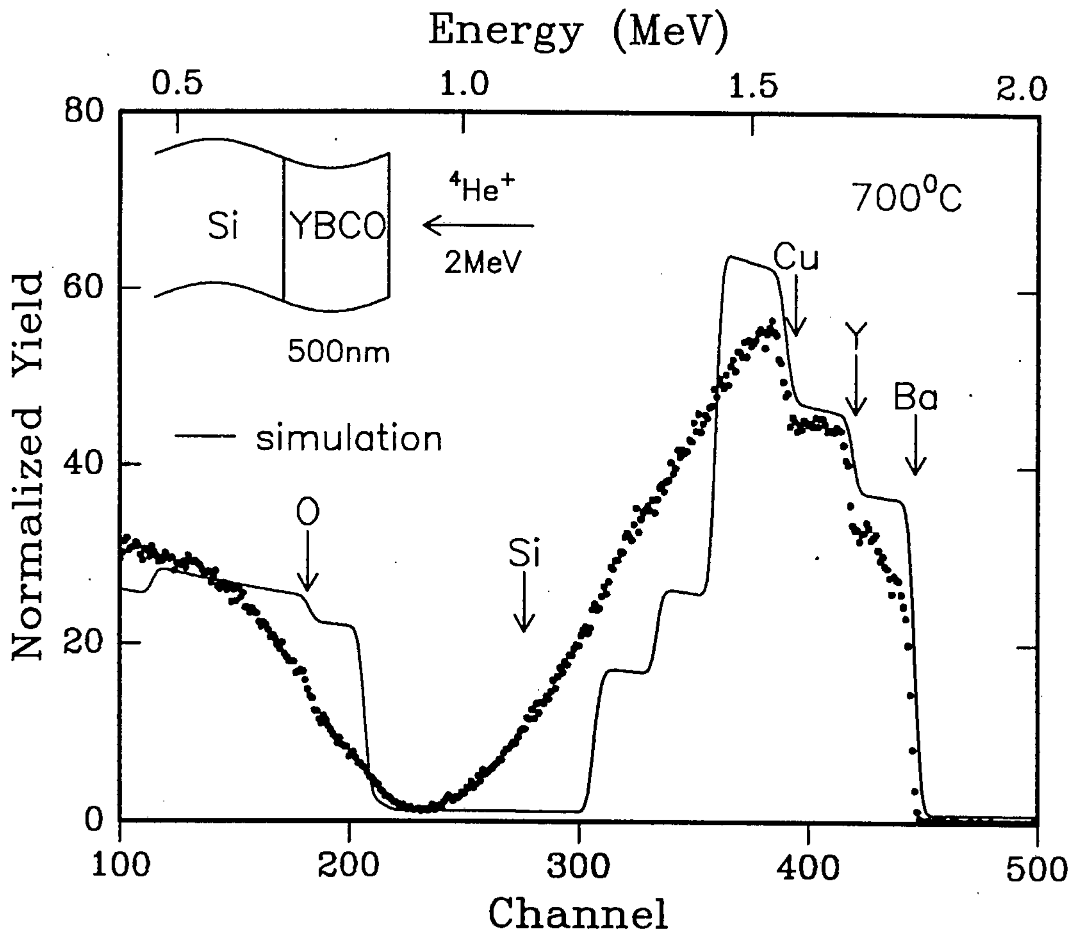

FIGURE 4.1: RBS spectrum for a thin film of YBCO deposited onto a bare Si substrate at 700°C by ICM sputtering. A severe reaction between the film and the substrate occurs, as seen by the loss of height in the Ba signal, the loss of thickness in the Cu signal and the sloping of the back edge of the film signals and the front edge of the Si signal.

substrate, and a loss of thickness in the Cu signal. The reaction of Ba with the Si substrate is known to result in the formation of Ba_2SiO_4 [**9, 121**] and the diffusion of Cu into Si, given by the characteristic tailing in the back edge of the film signal, has been previously reported for YBCO films on Si [**99, 118**]. The interfacial reaction not only produces a dead layer between the film and substrate but the diffusion of Ba and Cu from the YBCO film causes excess buildup of segregation products in the film thereby affecting the quality of the film.

Thin films of YBCO on bare Si displayed semiconducting behaviour in the

normal state i.e. above the transition to superconductivity the resistance increases with decreasing temperature (**Fig. 4.2**). The increase of resistivity with decreasing temperature is reminiscent of the behaviour of a YBCO film on Al_2O_3 (see section 3.3). The resistivity measurements confirm that the Si-YBCO reaction has seriously affected the film characteristics. The film resistance increases with decreasing temperature and only starts to drop at 50 K. The superconducting transition is broad and a zero resistance reading is never achieved denoting the poor quality of the film. No susceptibility transition was observed, pointing to an inhomogenous film with poorly connected grains.

The results for direct deposition on Si concur with other results in which

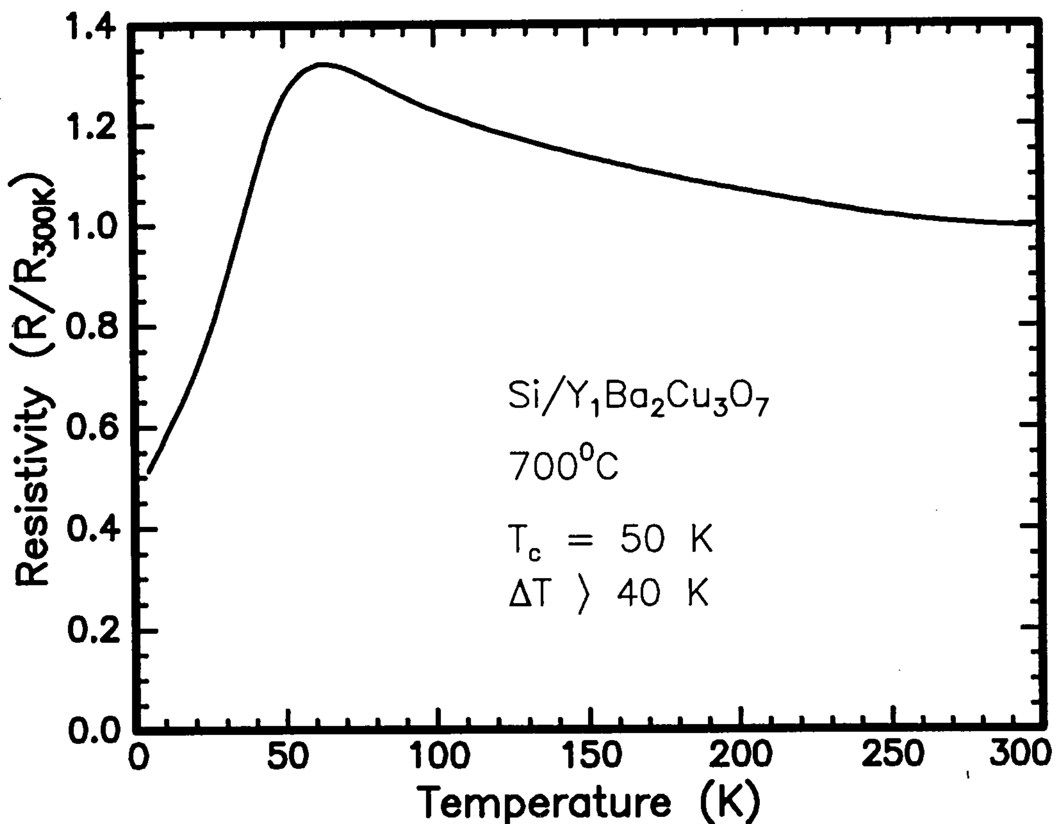

FIGURE 4.2: Resistivity measurements of a YBCO film deposited onto bare Si at 700°C . The film displays semiconducting behaviour, with an increase of resistance with decreasing temperature observed. The film has low T_c and a zero resistance reading is never achieved.

attempts to form good superconducting films directly on Si were largely unsuccessful [**93, 131**]. Elemental depth profiling confirms that severe interdiffusion and rearrangement of the constituents of YBCO cause the poor film properties [**131**]. Understanding the reaction of Si with YBCO is of paramount importance if one is to attempt to successfully incorporate the two disparate systems. This understanding rests on the determination of the reaction between Si and YBCO and how this reaction can be prevented or minimised. It has been empirically found that the substrate temperature is crucial in determining the extent of reaction and good quality films have been deposited onto bare Si at low temperatures [**119, 120**]. The method of deposition has also been a factor in achieving good films. This can be understood in terms of the reaction of Si-YBCO not being solely dependant on the reaction rates of the individual elements of YBCO with Si but that in different deposition systems the arrival of oxides, suboxides, clusters of YBCO, neutral particles, ionised species and energetic particles will have varying influence on the reaction. Thus we can expect variation in the Si-YBCO reaction with laser ablation, e-beam evaporation, and the numerous sputter deposition techniques. The identification of the Si-YBCO reaction process and its products also has implications for the choice of buffer layers to be used in the Si-YBCO system as such buffer layers must not only prevent the Si-YBCO reaction but must themselves not react with YBCO.

Differing results on the reacting species in the Si-YBCO interaction have been reported. As a general rule these can be classified as those that arise from the reaction of Ba with Si [**9, 10, 132**] with the formation of a Ba_2SiO_4 layer and those from the reaction of Cu with Si [**99, 118, 133**]. The question as to which of these reactions proceed first (or whether they are simultaneous) has not been adequately addressed. X-ray photoelectron spectroscopy (XPS) analysis of Si-YBCO interfaces revealed Cu and Ba reaction with Si resulting in the formation of a mixture of Ba and Cu-silicates [**134**]. The reaction of both Ba and Cu is also alluded to by the RBS spectrum in Fig. 4.1. The reaction of Cu with Si was reported by Nakajima [**99**] and Chourasia et al. [**133**] found that the breaking of the Cu-O bonds by

Si was the primary cause for interaction. In all available Si-YBCO reaction data the reaction of Cu or Ba with the film is either by diffusion of these elements or by diffusion of Si into the film. The absence of data in the literature detailing the reactivity of Y in YBCO with Si is noteworthy. The small peak height of Y in the RBS spectrum and the overlap with the Ba and Cu peaks prevents an assessment of the behaviour of Y during the interaction of YBCO with Si but XPS probing of the reaction interface of Si and YBCO showed no distortion of the Y3*d* peak shape **[134]**. This displays the inert nature of Y which arises from the highly oxidizing nature of Y and the high thermal stability of Y_2O_3 (see section 4.3).

4.2 Si/YBCO interactions

The interaction of single crystal silicon with thin films of Cu and Ba was investigated by RBS. Thin films of Cu and Ba were evaporated onto Si in a vacuum of $2x10^{-7}$ mbar. Due to the highly oxidizable nature of Ba **[30, 93]** we found that the as-deposited Ba films contained oxygen. The reaction of these films with Si was investigated by annealing the films at 700°C and 850°C for 30min and ascertaining the extent of reaction with RBS. These temperatures were used as they correspond to those used during ICM sputter deposition and a commonly used post-annealing temperature respectively. Annealing was carried out under flowing O_2 ($>$ 1 atmosphere) to simulate the presence of oxygen gas during sputter deposition.

4.2.1 The Si-Cu system

Fig. 4.3 shows the results for a thin film of Cu deposited on a single crystal silicon substrate and subsequently annealed at 700°C and 850°C in O_2 for 30min. The experimental RBS spectra were fitted with simulated spectra generated by the simulation program RUMP. The simulation reveals that at an annealing temperature of 700°C the Cu film seems to have reacted with the Si substrate to form a silicide of nominal composition Cu_3Si. However, it should be noted that islanding of the copper or copper-silicon compounds on the surface of the Si can also lead to such a spectrum. Evidence for the formation of Cu_3Si at relatively low temperatures has

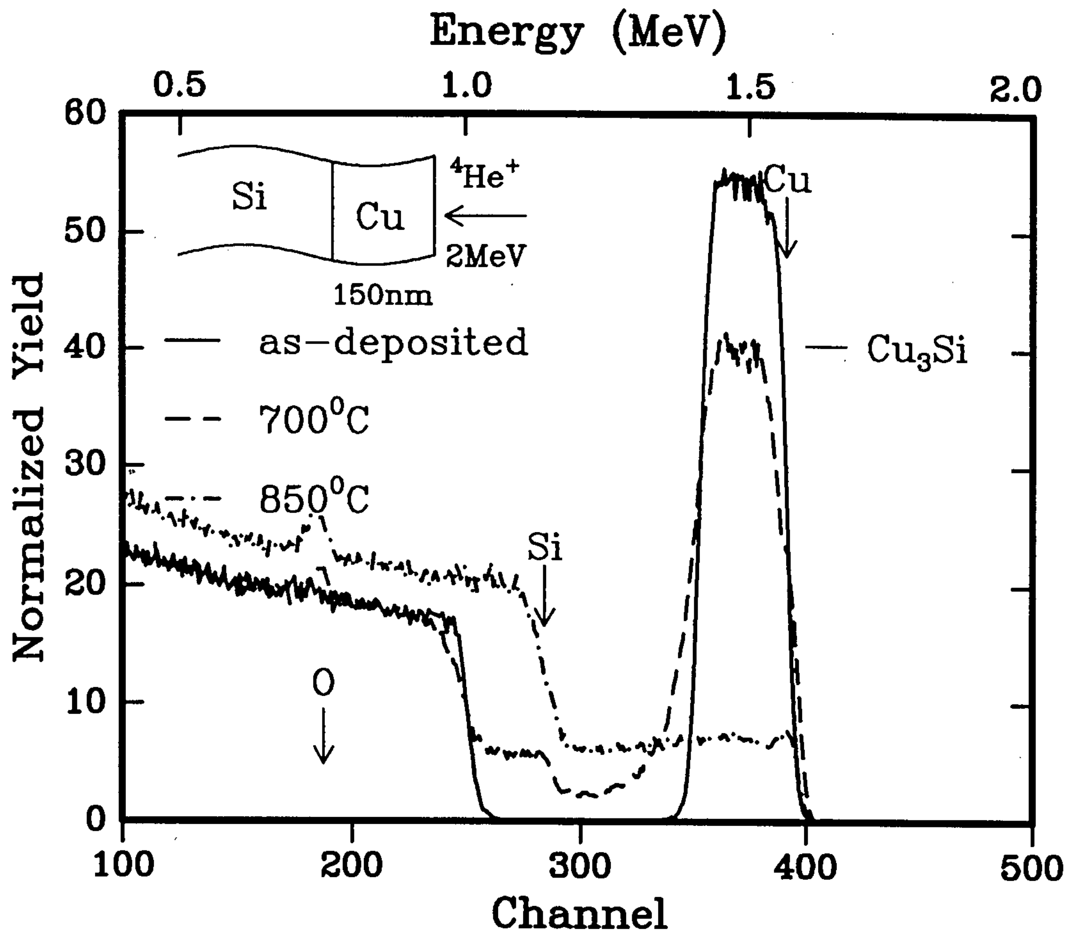

FIGURE 4.3: RBS spectra for a thin film of Cu deposited onto a Si substrate and post-annealed at 700°C and 850°C in O_2 for 30 min. The spectra suggest the formation of a Cu_3Si layer at 700°C and this is transformed into a silicon rich $CuSi_5$ solution at 850°C .

been found by Hong et. al. [**135**]. Although it has been postulated that Cu_3Si is highly oxidizable [**135**], it is seen by the thickness of the oxygen signal that only the surface contained significant levels of oxygen. This does not preclude the presence of trace amounts of oxygen in the silicide. This may result in the formation of Cu-silicates [**133**], but we have not found any evidence to suggest that the Cu-Si compound is a silicate.

At the higher annealing temperature of 850°C , further reduction in the Cu peak height demonstrates the presence of a Cu-silicon compound with an increasing proportion of Si. This is also alluded to by the loss of the Si shoulder. No

interfacial roughening effects and surface features such as tailing effects are seen in this spectrum and the Cu has completely dissolved into the Si to form a solid solution. Simulation of the observed spectrum shows that the Cu-Si solution extends to depth greater than 1μm. This result fits well with the Cu-Si binary phase diagram where a eutectic for the Cu-Si mixing in the liquid state is found at 802°C . Oxygen was still present at the surface. The flat top of the Cu peak is proof that the Cu-Si composition is constant through the thickness of the layer. The nominal composition of this layer was estimated to be $CuSi_5$ but it is pointed out that this not a Cu-Si compound but a solution of the two elements.

4.2.2 The Si-Ba system

The vacuum deposition of Ba onto Si resulted in a highly oxygen rich Ba layer as seen in the as-deposited spectrum (**Fig. 4.4**). Ba has a large affinity for oxygen and apart from Ba-oxides, the formation of Ba-carbonate and Ba-hydroxide is also possible [**1, 136**]. Upon annealing at 700°C the Ba peak height increases and the thickness of the Ba-oxide layer decreases. The amount of Ba in the film remains constant as measured by the peak area, pointing to the desorption of oxygen and impurities during the anneal, mainly carbonates. The movement of the leading edge of the Si signal towards higher backscattering energies is a consequence of the decrease of the thickness of the surface layer and not due to the formation of a Ba-silicon compound. At 850°C the Si has moved to the surface and the simulation of the backscattered spectrum reveals a Ba-silicate layer on the surface. The tailing in the Ba peak and the specular reflectivity of the film surface denote a combination of interfacial roughening and surface roughness. Simulation of the observed spectrum with RUMP shows that the silicate compound has a composition of Ba_2SiO_4. These results are similar those for a BaF_2 film on Si annealed in O_2, where Ba reacts with Si to form Ba_2SiO_4 [9].

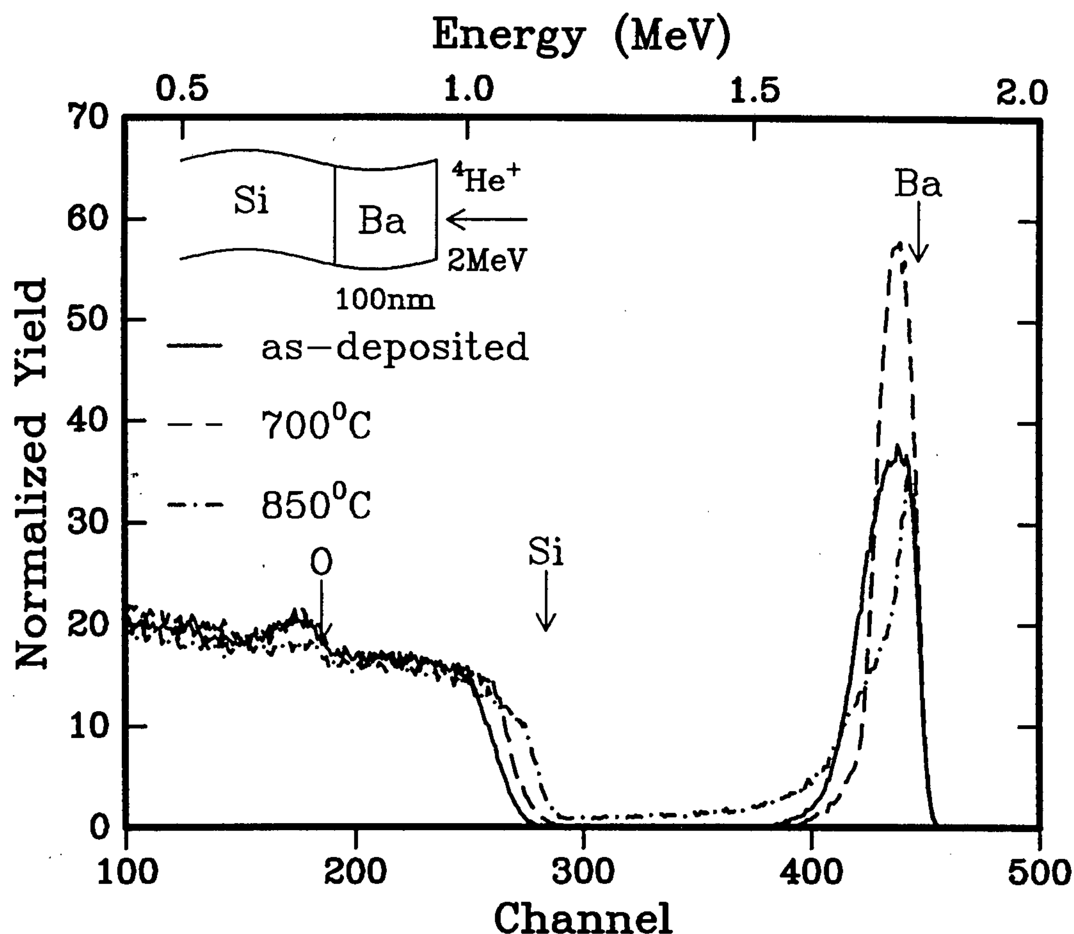

FIGURE 4.4: RBS spectra for a film of Ba deposited onto a Si substrate and post-annealed at 700°C and 850°C in O_2 for 30 min. The as-deposited Ba film had a high concentration of oxygen, which is likely to be in the form of hydroxides and carbonates. Annealing at 700°C leads to desorption of the hydroxides and carbonates but no Si-Ba reaction was seen. At 850°C a Ba-silicate layer (Ba_2SiO_4) was formed.

4.2.3 The Si-Cu-Ba system

Sequential evaporation of a layer of Cu and a layer of Ba was carried out to investigate the behaviour of this combination of elements at high temperatures. Fig. 4.5 shows the RBS spectra for the above combination as-deposited and annealed at 700°C and 850°C . At 700°C the interaction of Cu (closest to Si) with Si is the same as that for the Si-Cu system (see 4.3.1) with the possibility of Cu_3Si forming. However, the interesting aspect of this spectrum is that the Si signal appears at its

surface position and the simulation reveals the formation of Ba_2SiO_4 at the surface. This means that the Si has reacted with the Ba at the lower temperature of 700°C . The peak at the foot of the leading edge of the Cu signal at 850°C suggests the formation of a Ba-Cu-O compound, of which $BaCuO_2$ is the most probable [137]. The oxygen peak is restricted to the Ba layer and oxidation of the Cu layer is not observed. At 850°C the Cu forms a solid solution with the Si substrate as

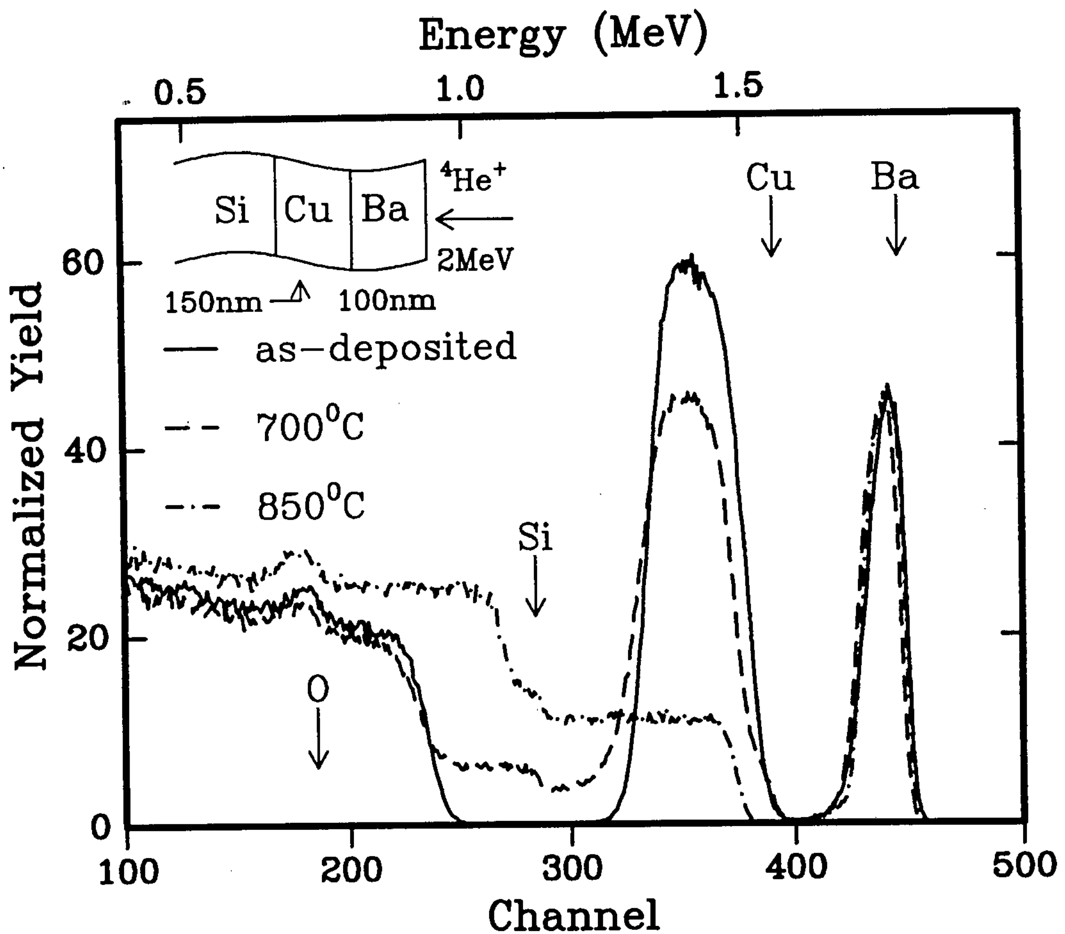

FIGURE 4.5: RBS spectra for a Si-Cu-Ba structure. Annealing at 700°C in O_2 for 30 min points to the formation of Cu_3Si and Ba_2SiO_4. Higher temperature annealing at 850°C caused the Cu to dissolve into the Si but no further reaction of the Ba was observed.

was seen in the Si-Cu system and Ba_2SiO_4 is still observed at the surface. The disappearance of the Cu-Ba reaction peak means that all the Cu has reacted with

the Si. The movement of the Cu signal towards lower backscattering energies points to a possible SiO_2 layer formation between the Cu and Ba layers. The formation of a Ba-silicate at the lower temperature of 700°C is due to the reaction of Cu with Si which releases Si from the tightly bound structure in the single crystal and makes it available for reaction with Ba to form the silicate at lower temperatures. The retention of the Si-Cu-Ba level structure is also of importance as will become clear in section 4.3.3. Whereas for the Cu-silicide formation it is difficult to determine whether Si or Cu is the diffusing species. From the results of Hong et al. [**135**], where it was demonstrated that Cu is the mobile species, it is reasonable to assume that the high mobility of Cu means that it is the diffusing species during silicide formation.

4.2.4 The Si-Ba-Cu system

Fig. 4.6 gives the RBS spectra for a thick layer of Cu deposited onto a BaO_x layer which was previously deposited on the Si substrate. The peak on top of the broad signal arises from the overlap of the RBS signals from the thick Cu layer with that from the BaO_x layer. Annealing at 700°C proves that the Cu is very mobile, with the entire Cu layer moving through the Ba layer. If Si was the diffusing species then the Cu–Si interaction would have occurred on top of the Ba layer and the Ba signal would not appear at its' surface position. The complete diffusion and reaction of the Cu layer suggests the high mobility of Cu and points to the Cu-Si reaction occuring at some lower temperature than used in this study. Simulation of the composition with RUMP shows that the Ba layer has also reacted to form the silicate Ba_2SiO_4, in line with the results for the Si-Cu-Ba system. The loss of area of the Ba peak points to the spreading of the Ba signal and some interaction with the Cu as it diffuses through the Ba layer. Using the assumption of Cu diffusion, the inversion of the layers brings the system characteristics back to that of the Si-Cu-Ba system. The roughening of interfaces between the different layers is noted and is consistent with the identical phenomena observed in the Si-Ba and Si-Cu spectra. The hump at the rear of the Cu signal which coincides with the Ba signal from the as-deposited

sample does not arise from Ba but is due to the overlap of the silicon signals from the silicide and the silicate with the Cu signal. Elevating the annealing temperature to 850°C has little effect on the structure except for an increased silicon signal observed at the Cu-silicide/silicon interface.

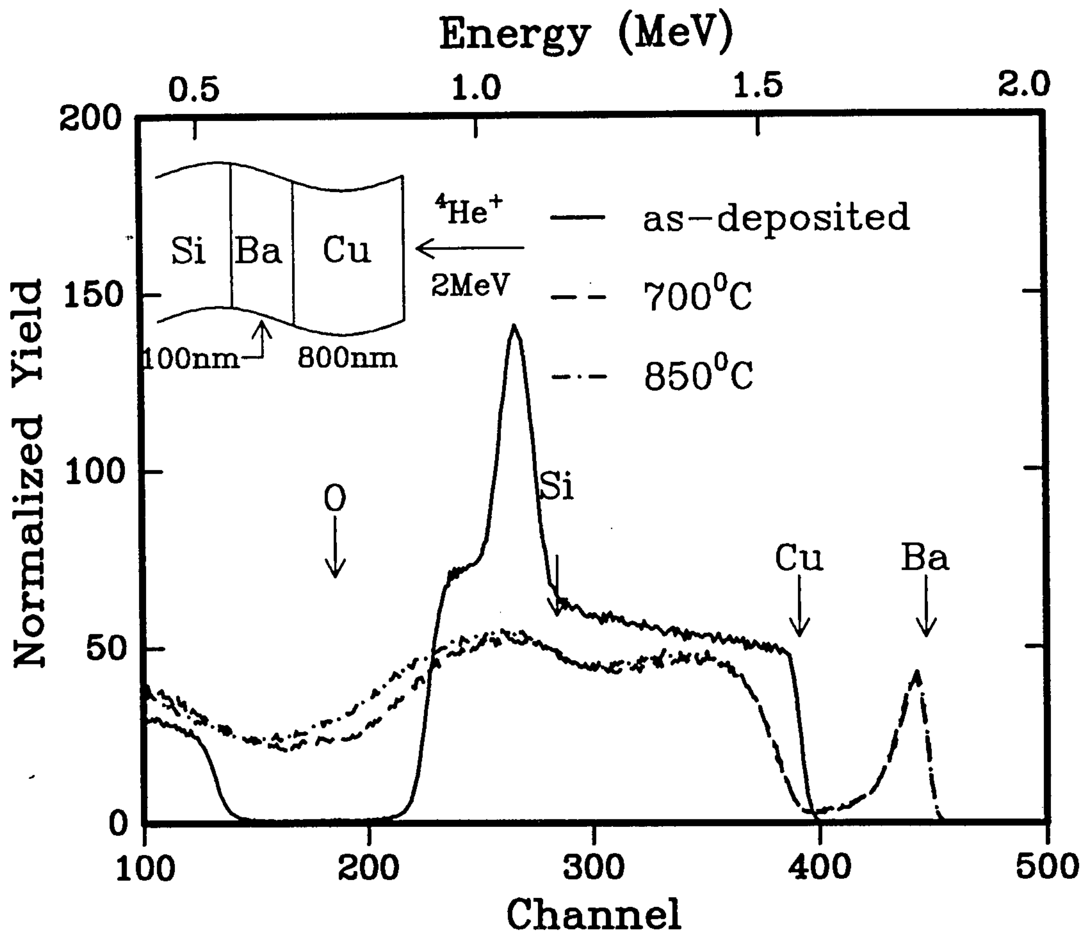

FIGURE 4.6: RBS spectra for a Si-Ba-Cu structure. Annealing at 700°C for 30 min leads to an inversion of the level structure and the spectrum points to the formation of Cu_3Si and Ba_2SiO_4. Higher temperature annealing at 850°C does not significantly affect the Si-silicide-silicate structure.

4.3 Oxide buffer layers

Buffer layers of MgO, ZrO_2 and Y_2O_3 were used in an attempt to prevent the reaction between Si and YBCO and retain the deposited YBCO film properties. The

possibility of growing epitaxial oxides on Si has important technological applications that include semiconductor-insulator-metal structures. The structures formed in this study (semiconductor-insulator-superconductor) have been created with the aim of finding new buffer materials and possible structures that accommodate the high T_c superconductors and as a precursor to possible devices. The investigation of the growth of YBCO films on Si/buffer systems by ICM sputter deposition at 700°C is also important. An extended set of epitaxial oxide materials on Si is also desirable because of the increased design choices for device fabrication. Furthermore, such oxide layers are promising for compatibility with existing silicon on sapphire technology and as an alternative to SiO_2. An investigation of the properties of the semiconductor/buffer structure was also conducted as the issue of the diffusion of Si into the buffer or of elements of the buffer into Si has received little attention thus far. The importance of this issue is very obvious since the introduction of trace elements into Si can seriously affect the electrical properties of the semiconductor and hence of devices containing Si/buffer structures. This is especially so since the deposition and treatment of YBCO films are often performed at elevated temperatures.

An intriguing aspect of the growth of YBCO on buffer layers is the possibility of obtaining highly textured (though not single crystal) films on buffer layers which are polycrystalline. This arises from the strong tendency that YBCO has to align itself with the c-axis perpendicular to the substrate surface, which results from the strongly two-dimensional growth of this material. The growth rate within the a-b plane has been observed to be an order of magnitude higher than along the c-direction [**138**]. Thus even on polycrystalline substrates a preferred orientation of the c-axis perpendicular to the substrate has been observed [**139**]. However, the lack of a template for in-plane orientational control can result in a polycrystalline YBCO film due to in-plane disorder [**140, 141**]. As a result of the lack of in-plane epitaxial alignment, high angle grain boundaries can occur in such films. Therefore, for single crystalline YBCO films the formation of epitaxial buffer layers is imperative. For films of moderate crystalline quality, the surface smoothness of the substrate seems to be more important than the crystalline perfection of the buffer layer.

4.3.1 MgO buffer layers

MgO has several interesting properties such as high transparency, high electrical resistivity, good chemical resistivity, thermal stability and thermal conductivity. MgO buffer layers 100 nm thick were grown, by e-beam evaporation of MgO pieces in an oxygen flow of 10^{-4}mbar, onto Si substrates heated to 450°C . The employment of reactive evaporation techniques for the deposition of oxides is widely reported [**13,30,142,143**]. The oxygen presence is used to compensate for oxygen lost during the evaporation of MgO. Efficient oxygen incorporation during the evaporation step was also important in forming a stoichiometric and dense MgO layer [**114, 144**]. Buffer layers formed at low oxygen pressures gave YBCO films of poor quality and post-annealing of the Si/MgO structures in O_2 did not improve the quality of the deposited YBCO films. XRD measurements for the Si/MgO system showed that the buffer layer grows with a (h00) orientation which is similar to the growth of MgO films on Al_2O_3 (see 3.4). A small, strongly broadened peak for MgO suggests that the buffer layer consists of a polycrystalline fine-grained structure, as was the case on Al_2O_3.

The thermal stability of the MgO layer on Si was investigated by RBS. Samples of Si/MgO were annealed under flowing oxygen ($>$ 1 atmosphere) for 1 hour at temperatures of 700°C and 850°C . The RBS spectra for the as-deposited sample and the subsequently annealed stages are shown in **Fig. 4.7**. It is evident that the barrier oxide has high thermal stability and no breakdown of the buffer layer was seen for the high temperature anneals.

Although the Mg and Si signals overlap, the sharp slope of the Si front edge and the Mg back edge implies little interfacial reaction between buffer and substrate. X-ray diffraction of the post-annealed samples showed no change in the orientation of the buffer layer. Thermal stability of a Si/MgO structure has been previously reported with a mixed oxide of MgO-SiO_x only being detected for annealing temperatures of 900°C or higher [**145**]. The slight change in the spectrum at the surface alludes to a possible reaction but the resolution of the RBS system prevents us from detecting the presence of a small interfacial layer formed during the high

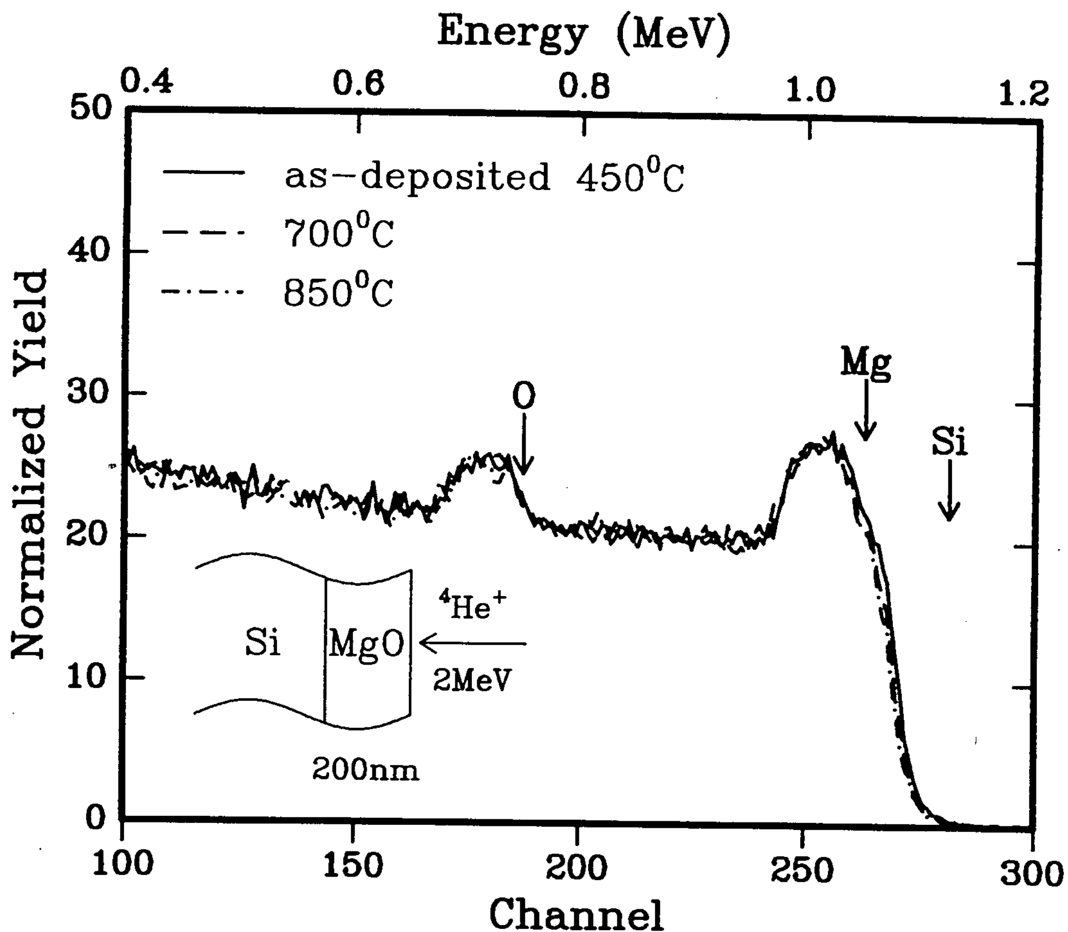

FIGURE 4.7: RBS spectra for the MgO film deposited onto Si at 450°C and subsequently annealed in oxygen at 700°C and 850°C for 1 hour. No decomposition of the buffer layer or interaction of the MgO film with the underlying Si was observed at these temperatures.

temperature anneal. The annealing of MgO in O_2 is important for the desorption of contaminants such as hydroxides and for the formation of a dense microstructure (see **Chap. 3**). Ion channeling measurements of Si/MgO gave minimum yields of 80-90%, confirming the polycrystalline nature of the buffer.

YBCO films formed on the Si/MgO structures were smooth, shiny and black. The RBS spectrum of a YBCO film grown on a Si/MgO structure by ICM sputter deposition at 700°C is shown in **Fig. 4.8**. There is no evidence for interaction between the film and buffer and the MgO layer has been effective in preventing a

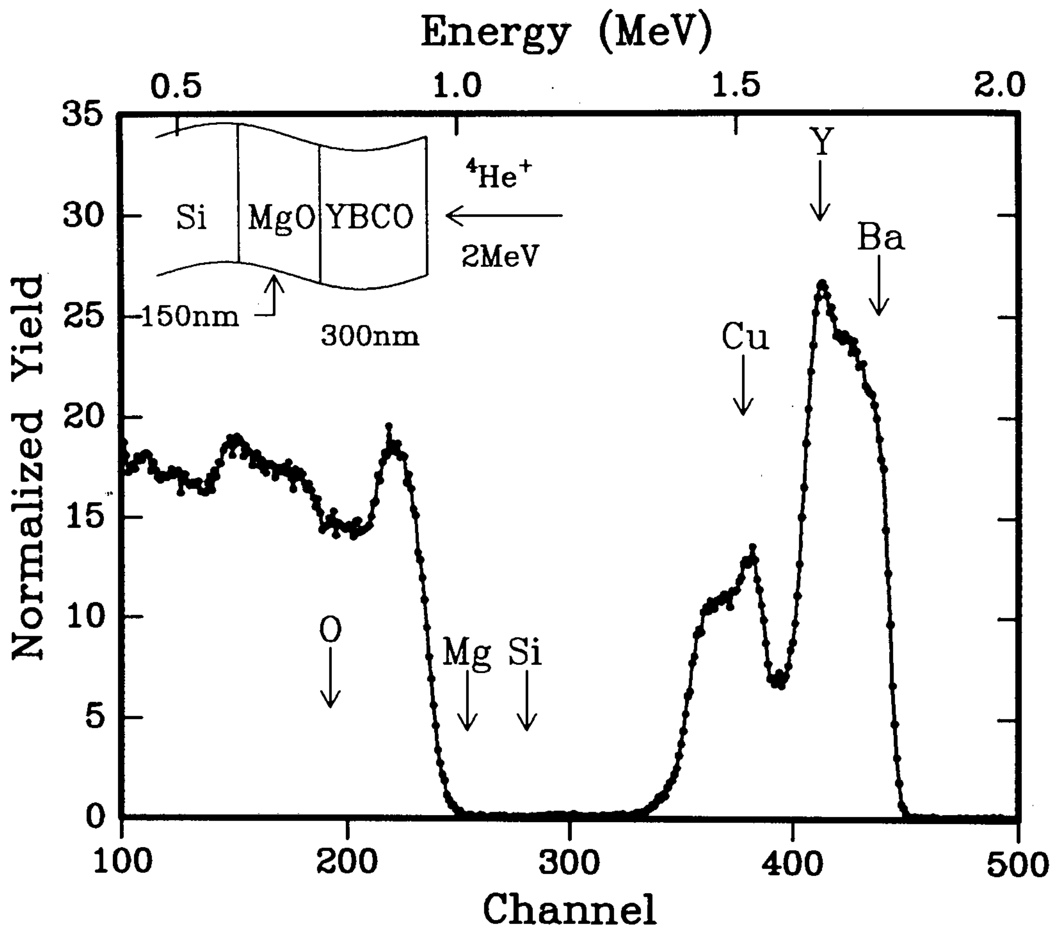

FIGURE 4.8: RBS spectrum for a YBCO film deposited at 700°C onto the Si-MgO structure by ICM sputter deposition. The MgO buffer layer is effective in preventing a Si-YBCO interaction. A comparison of the RBS spectrum with that in **Fig. 4.1** illustrates the effectiveness of the buffer layer.The sharp edges of the YBCO and buffer signals illustrate the absence of reaction.

reaction with the Si substrate. The efficacy of the buffer layer is demonstrated by comparison of **Fig. 4.8** with that of a film deposited on bare Si (see **Fig. 4.1**). The sharp edges of the buffer layer and of the components of the film and the retention of stoichiometry in the film are indicators that the MgO layer has performed well as a barrier. As a result of the lack of in-plane epitaxial alignment, high angle grain boundaries are generally present in such films which detrimentally affect the quality of the films [**140,141**]. The XRD spectrum for the film grown *in situ* on the buffer layer revealed a highly textured film with c-axis orientation and no evidence for non-superconducting phases (**Fig. 4.9**). The diffraction peaks are sharp and well

defined with the fwhm of the (003) peak measured to be 0.15°, only slightly larger than the value obtained for films on single crystal MgO substrates (0.12°). The broad peak at low angles is from the perspex sample holder.

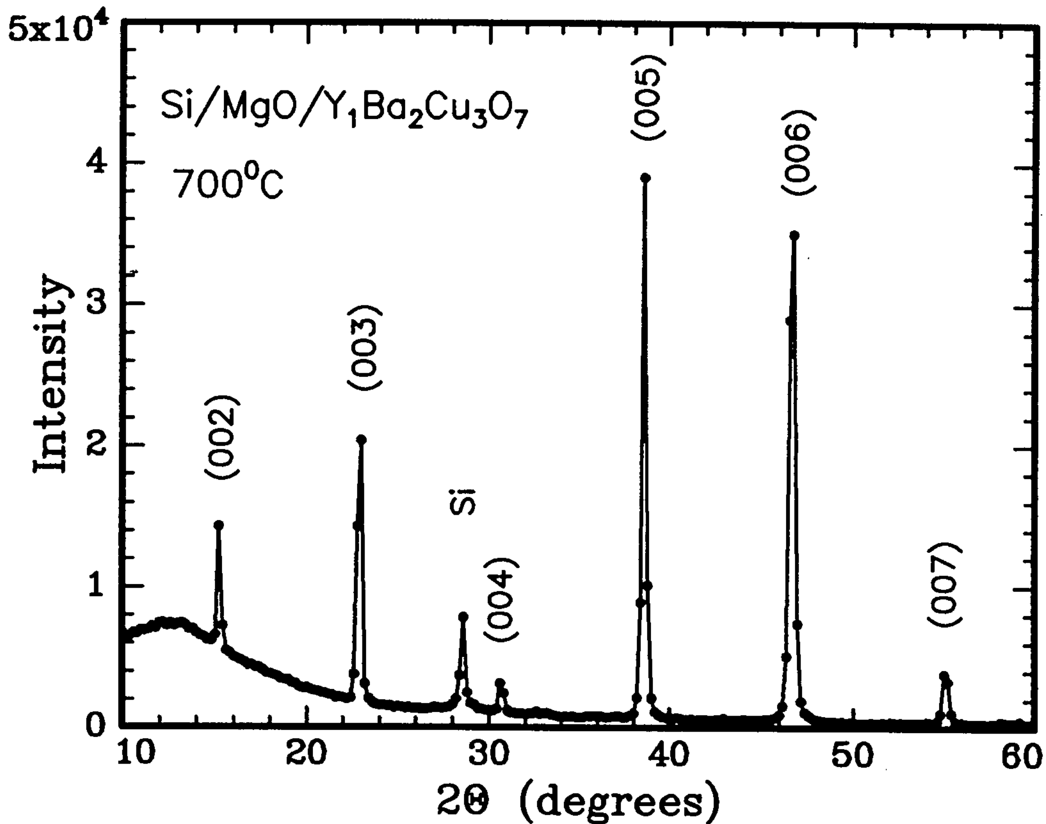

FIGURE 4.9: The XRD spectrum of the YBCO film deposited onto the Si-MgO structure at 700°C . The film is preferentially c-axis oriented and the XRD spectrum is similar to that of YBCO on single crystal MgO.

4.3.2 Y_2O_3 buffer layers

Y_2O_3 is extremely well suited as a dielectric gate oxide material on Si because of its high dielectric value [**143**] which is about 4 times larger than that of SiO_2. In addition Y_2O_3 displays high thermal stability and good high frequency performance [**146**]. The high oxygen affinity of yttrium gives it the ability to reduce most other oxides and Y_2O_3 has only one stable structure (b.c.c.) below 2200°C . Y_2O_3 has

been used as a tunnel barrier in YBCO/Y_2O_3/YBCO heterostructures [**142, 147**] and in conjunction with yttria stabilised zirconia ($ZrO_2(Y)$ or YSZ) as a buffer layer on Si [**128–130**]. Single crystal Y_2O_3 has also been used as a substrate for YBCO film growth [**148**].

Y_2O_3 films were deposited by evaporating Y metal in a 10^{-4}mbar oxygen atmosphere onto substrates heated to 100°C . Takayi [**149**] has shown that good quality metal oxide layers can be grown in this way and the use of such reactive evaporation techniques for the deposition of oxides is widely reported [**13, 30, 142, 143**]. The highly oxidizable nature of Y means that the evaporating flux will pick up oxygen from the ambient and form oxides upon deposition. Oxygen inclusion into the deposited film can also occur. This method is prefered to the e-beam evaporation of oxide targets because of the ease of evaporating the metal as compared to the oxide [**143**]. Even with the use of oxide targets it has often been found that an oyxgen flow during evaporation is required to give better stoichiometry control of the deposited films [**145**]. The thermal stability of the Y-oxide buffer layer on Si was investigated by annealing the system, $ex-situ$, in flowing O_2 (> 1 atmosphere) at 700°C and 850°C for 1 hour. **Fig. 4.10** shows the RBS spectra for the as-deposited and annealed samples. The as-deposited sample had high oxygen content, but there seems to be an increase of oxygen for the 700°C anneal as seen by the slight decrease in the height of the Y peak. Higher temperature annealing causes a decrease in the height of the Y peak, pointing to a possible Si-Y reaction at high temperature. To ensure a highly oxygenated buffer layer and to desorb possible contaminants such as hydroxides the as-deposited buffer samples were annealed at 700°C $ex-situ$ for 2 hours prior to deposition of the YBCO film. This procedure also assists in forming a dense surface structure. In spite of the relatively low formation temperature of yttrium-silicide, YSi_2 (300°C), the Y-Si reaction was not observed either during the formation of Y_2O_3 or in the post-deposition anneals. This is an indication of the high thermal stability of the Y-oxide compound. The crucial factor that determines whether or not a Y-silicide will form might be the amount of oxygen present during the deposition step. The polycrystallinity of the Y_2O_3 films was confirmed by the

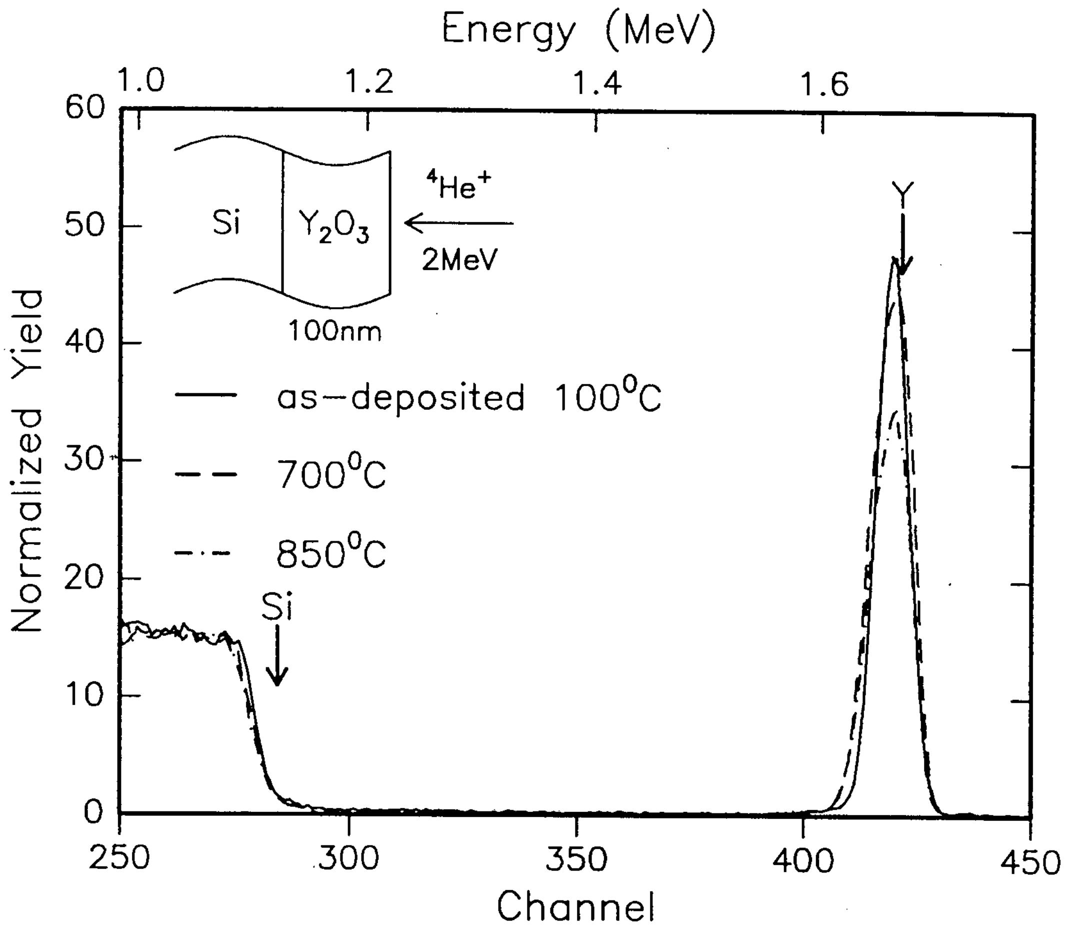

FIGURE 4.10: RBS spectra for a Y-oxide layer deposited onto Si at 100°C and post-annealed at 700°C and 850°C in oxygen for 1 hour. A substrate-buffer reaction was noted at 850°C by the drop in the Y-peak height.

absence of ion channeling by these films.

The Y_2O_3 layer is relatively effective in preventing a reaction between the film and the substrate as seen by RBS (**Fig. 4.11**). There are indications that the Y_2O_3 layer has not prevented all interaction between the YBCO film and substrate. The tail in the film+buffer signal and the rounding of the leading edge of the Si signal point to the diffusion of Cu into the buffer layer and possibly into the Si substrate as well. This may arise from the reduction of Cu-O by Y and the freeing of highly mobile elemental Cu. The formation of a Y-Cu-O compound may also occur, with $Y_2Cu_2O_5$ the most probable phase to form [**137**]. Bardal et al. [**128**] have shown that a Ba layer exists at the Y_2O_3 - YBCO interface.

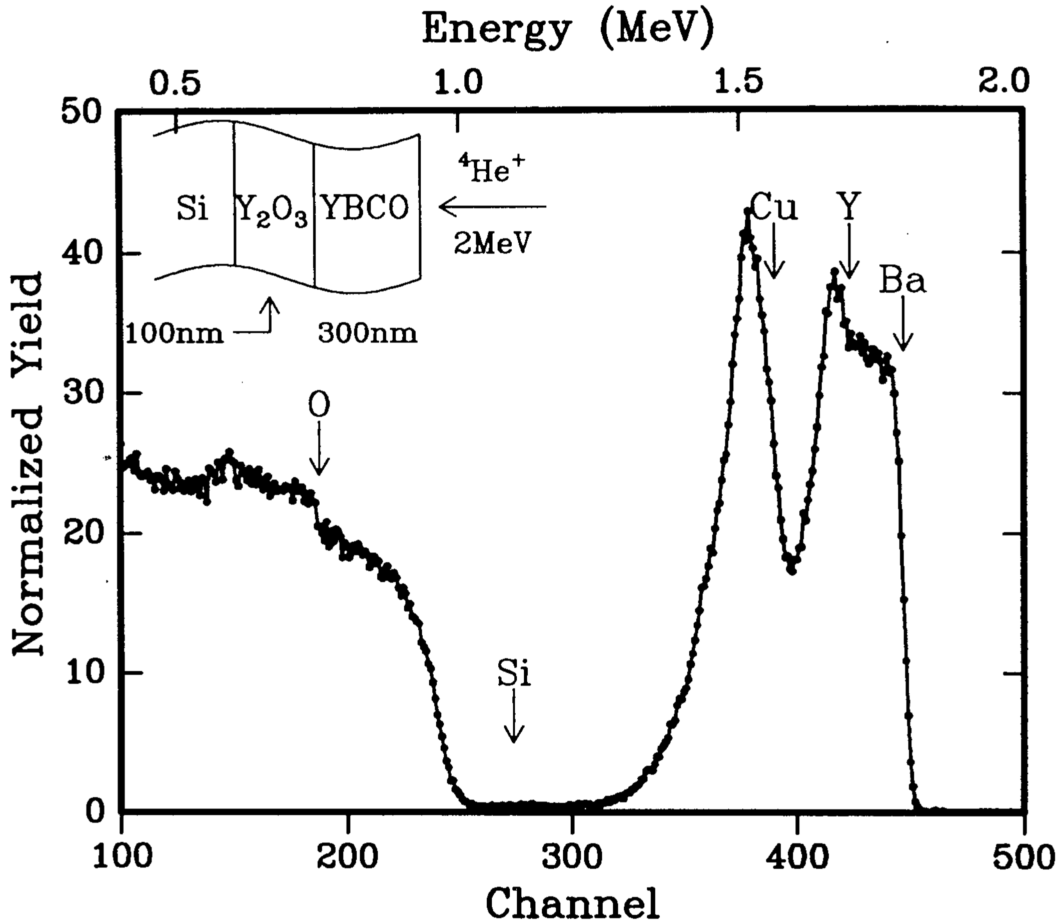

FIGURE 4.11: RBS spectrum for a YBCO film deposited at 700°C onto the Si-Y_2O_3 structure. The buffer layer prevents large scale Si-YBCO interaction although the rounding in the leading edge of the Si signal point to the possibility of some interaction with the buffer or the YBCO film.

XRD analysis of YBCO films deposited on Si with Y_2O_3 buffer layers by in-situ ICM sputter deposition at 700°C (**Fig. 4.12**) showed the film to be highly textured with a preferred c-perpendicular orientation. A small peak from the (103) orientation at 32.4° indicates that the film is polycrystalline.

4.3.3 ZrO_2 buffer layers

ZrO_2 is another member of the class of oxide materials that have suitable properties as gate oxide materials. Yttria stabilized zirconia (YSZ) ZrO_2-Y_2O_3 has

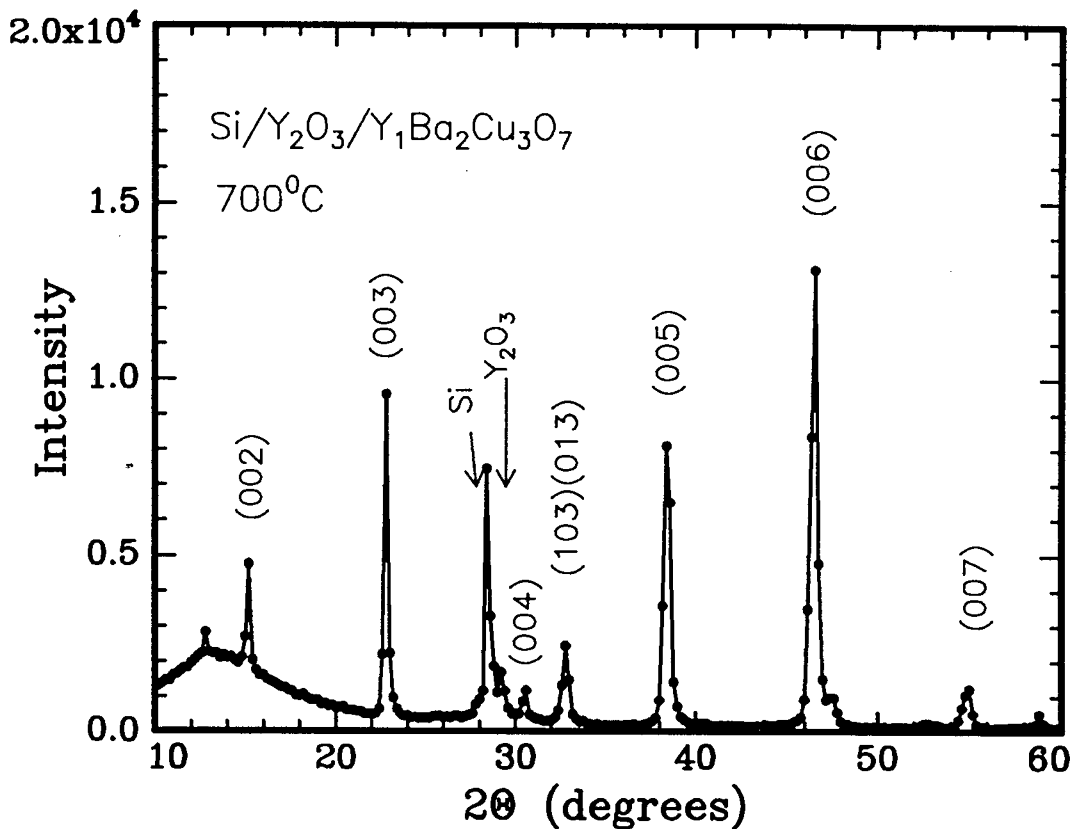

FIGURE 4.12: XRD spectrum of a YBCO film deposited at 700°C onto a Si substrate buffered with Y_2O_3. The highly textured nature of the film is demonstrated by the c-axis orientation although the presence of peaks from other orientations indicate a polycrystalline film.

been used extensively as a buffer layer for the growth of good quality YBCO layers on Si [**11**, **141**, **10**, **8**]. However, the high temperatures (800°C) required for the growth of good quality YSZ buffer layers often lead to the formation of interfacial SiO_2 layers and some reaction of YSZ and YBCO has been observed [**141**, **9**].

ZrO_2 layers (100 nm) were formed by the evaporation of Zr in an oxygen ambient of 10^{-4} mbar onto substrates held at 100°C . This is the same method used for the deposition of Y_2O_3 layers. The stability of the buffer layer was checked with RBS (**Fig. 4.13**). Post-deposition annealing of the Si-ZrO_2 system demonstrates the high thermal stability of ZrO_2. No change in the height of the Zr signal was observed at 700°C or 850°C pointing to the complete oxidation of the buffer at

deposition and high stability of ZrO_2 on Si. The absence of any Si-Zr reaction up to 850°C was also noted. These results are in accordance with XPS results detailing the unreactive nature of ZrO_2 on Si [**134**]. No ion channeling was observed for the ZrO_2 films, showing that they were polycrystalline.

The RBS spectrum of a YBCO film deposited at 700°C onto the Si-ZrO_2 structure is shown in **Fig. 4.14**. The sharp interfaces and good stoichiometry of the YBCO film show that the ZrO_2 buffer helps to prevent any Si-YBCO reaction. There was no evidence to suggest the reaction of Ba with ZrO_2 which results in the formation of $BaZrO_3$ [**141**]. Although the XRD spectrum of this film (**Fig. 4.15**)

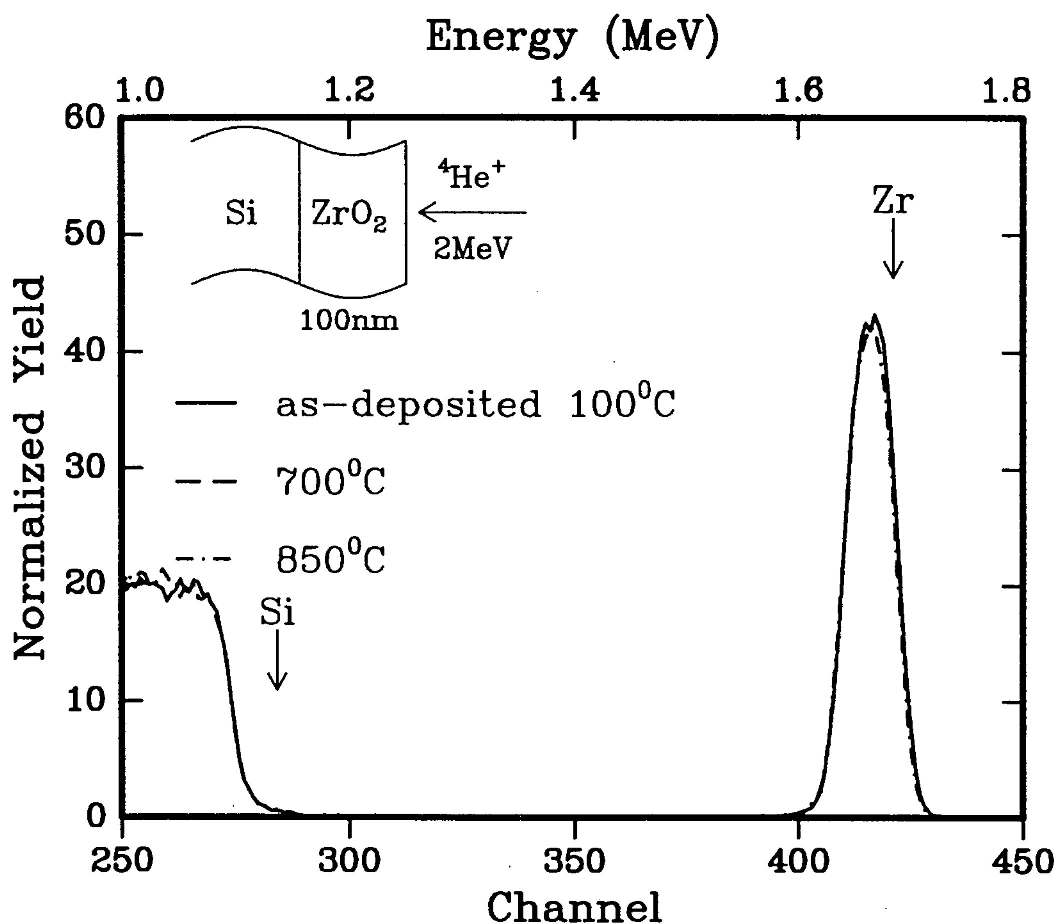

FIGURE 4.13: RBS spectra for a ZrO_2 layer deposited onto Si at 100°C in an oxygen ambient of 10^{-4}mbar. Post annealing for 1 hour at 700°C and 850°C in O_2 did not affect the Zr peak height, demonstrating the stability of ZrO_2 as no substrate-buffer interaction was seen.

showed it to be preferentially c-axis orientated, a large background is observed from the sample holder as seen by the broad peaks in the spectrum. The c-axis orientation of the YBCO film and the relatively good RBS spectrum point to little interaction at the film-buffer interface.

4.3.4 Electrical properties

The superconducting electrical characteristics of the films on Si with oxide buffer layers were determined with 4-point resistance and a.c. susceptibility measurements (**Fig. 4.16**). YBCO films on all the oxide buffer layers were superconducting with

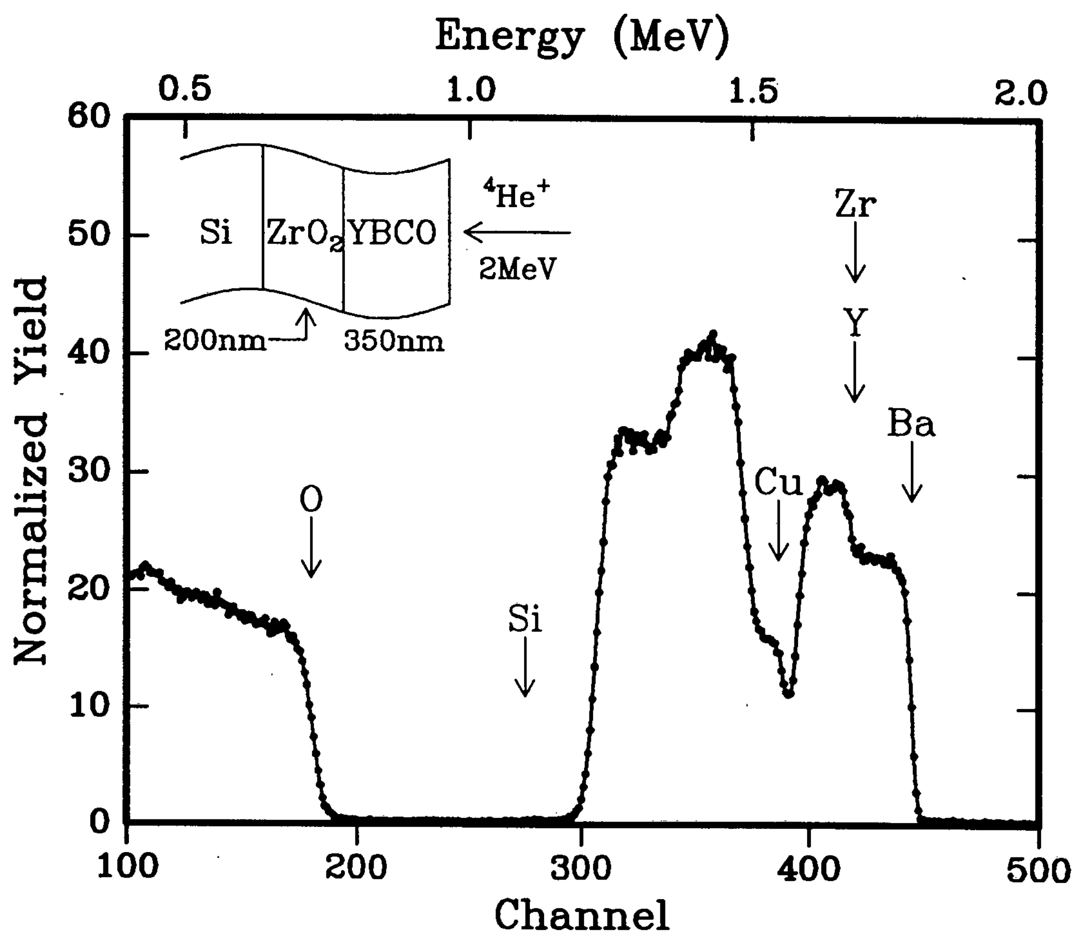

FIGURE 4.14: RBS spectrum for a film of YBCO deposited onto a Si-ZrO_2 structure at 700°C . The ZrO_2 layer prevents the reaction of the film and substrate. The YBCO film has ideal stoichiometry and is uniform through its thickness.

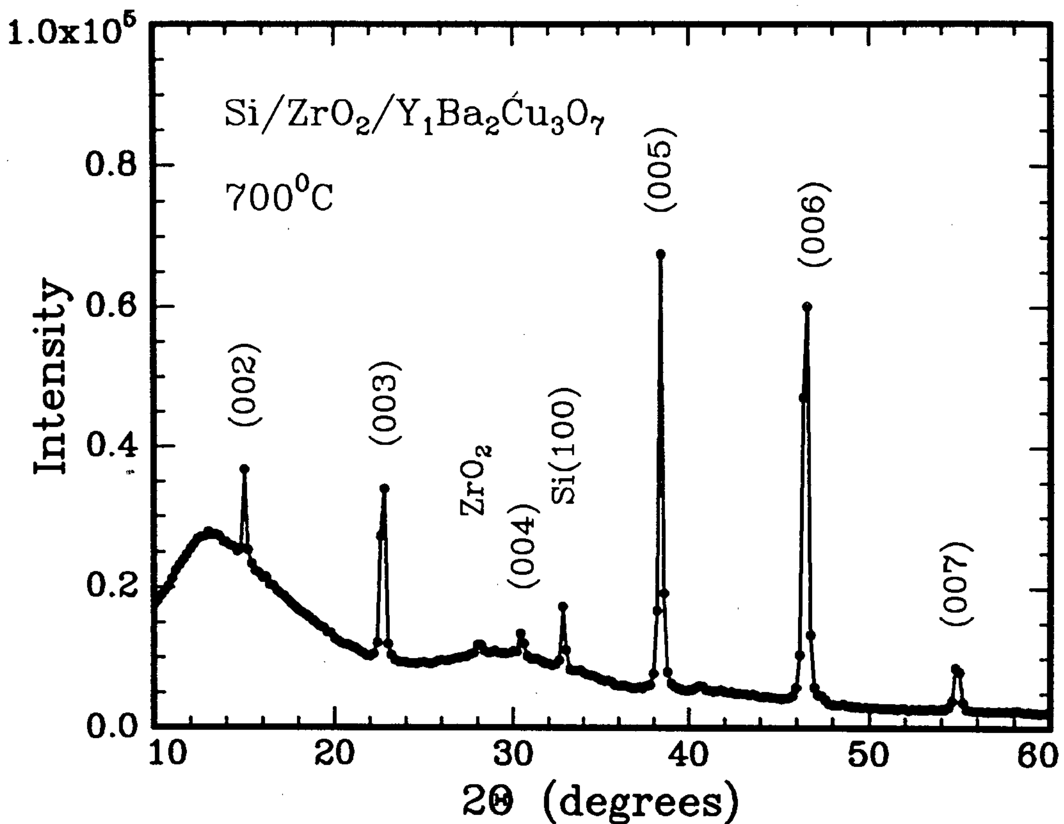

FIGURE 4.15: XRD spectrum for a YBCO film deposited on Si-ZrO_2 at 700°C . The film had preferential c-axis orientation, The large, broad background, especially at low angles arises from the perspex sample holder used in the XRD setup.

high transition temperatures T_c. Room temperature resistance values of the films varied, with the highest resistance values consistently measured on Y_2O_3 buffered substrates. The normal state behaviour of the films also differed with the sharpest drop in resistance with decreasing temperature being recorded on the Si/MgO substrate. Similar values for the transition temperature and the transition width were recorded. The measured T_c values were 83 K, 81 K and 81 K for films on MgO, Y_2O_3 and ZrO_2 buffered films respectively. The transition widths were in the range 5-7 K.

A.C. susceptibility measurements showed a complete transition only for the film on Si/MgO ie.the magnetic field expulsion by the sample reaches some con-

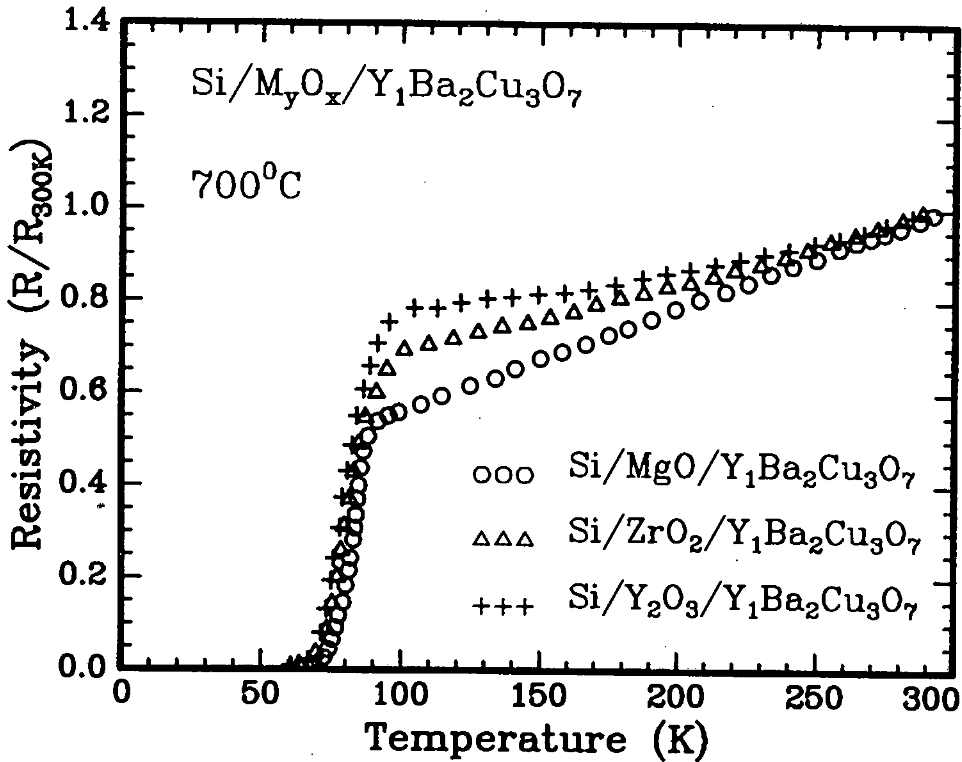

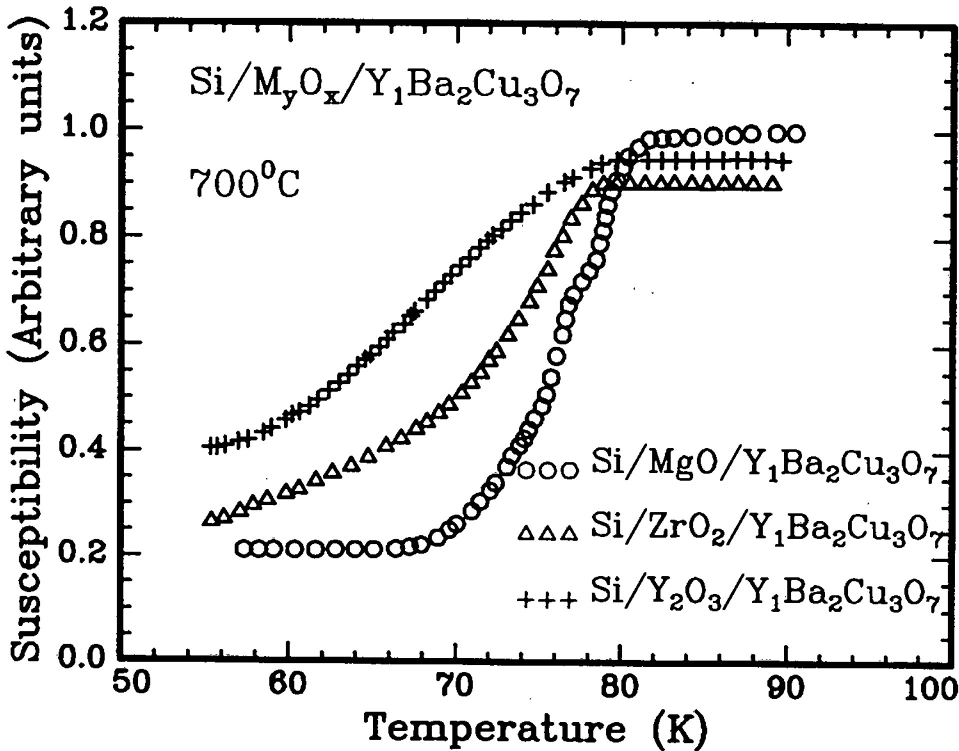

FIGURE 4.16: (a)Resistivity and (b)Susceptibility measurements for the YBCO films deposited onto Si with MgO, Y_2O_3 and ZrO_2 buffer layers. The highest transition temperatures and sharpest transition widths were obtained on a MgO buffer layer.

stant level. This generally implies that the entire sample has become completely superconducting and no portion of the sample still has to make the transition to the superconducting state. The broad, multi-levelled transition illustrates a non-homogenous transition observed on the Si/MgO system is caused by sections of the film becoming superconducting at various temperatures. The width of the complete field expulsion transition was found to be 11 K. Films on Si/ZrO_2 and Y_2O_3 had broadened transitions and a complete field expulsion was never achieved down to 55 K. Readings were not recorded below 55 K. The large transition width(>25 K) observed on these systems may be due to poor connectivity of the grains of the film, possible interaction in the case of the Y_2O_3 buffer layer and inhomogeneity in the films. The critical current values confirm that the films are polycrystalline, with the MgO buffer layer giving the highest current density. **Table 4.1** summarises the electrical properties of thin film $Y_1Ba_2Cu_3O_7$ superconductors formed in this study on Si substrates with oxide buffer layers. Critical current measurements are obtained at 77 K.

TABLE 4.1: Electrical properties of thin film $Y_1Ba_2Cu_3O_7$ superconductors on silicon with oxide buffer layers.

Substrate	Resistivity		Susceptiblity		Critical current
	T_c(K)	ΔT(K)	T_c(K)	ΔT(K)	J_c(A.cm^{-2})
Si	50	40	–	–	–
Si/MgO	83	5.5	81	11	4×10^4
Si/ZrO_2	81	6	79	>24	5×10^3
Si/Y_2O_3	81	7	78	>23	2×10^3

4.4 Summary and discussion

The merging of superconductor and semiconductor technologies on a single integrated device is extremely attractive for device purposes. However it was found that severe reaction between single crystal Si and YBCO occurs upon deposition of a YBCO film by ICM sputtering at 700°C . This was despite the fact that the in-situ deposition method was used and the deposition temperature is below that commonly used for post-annealing YBCO film [≥850°C]. The reaction of YBCO with Si is similar to that seen by others [**10,24,117**] although the poor film adhesion caused by the reaction of YBCO with Si previously reported [**95, 118**], was not observed in this study. The peeling of films may depend on the extent of reaction, the thickness of the film and the reaction temperature and was not always observed in some other studies during the reaction of Si with YBCO. The deposition of good quality films directly on Si have relied on the use of lower substrate temperatures, higher oxygen pressures, the use of activated oxygen during deposition or rapid thermal annealing [**119–121**]. Even with these novel techniques, the YBCO films are generally not as good as films on oxide substrates such as MgO and $SrTiO_3$ This shows that direct deposition on Si is still a problem with the use of conventional deposition techniques. Although the reaction of Si and YBCO severely dampened the electrical performance of the YBCO film a superconducting transition was still noted. This arises from the relatively large thickness of the YBCO film (500nm) in which the upper layers are less degraded during the interaction. However, the transition was at a low temperature (T_c = 50 K), had a broad drop to low resistance, and a zero resistance value was not achieved above 10K. This is a confirmation of the poor film quality.

Conflicting reports exist on whether Ba reacts with Si [**9, 10, 132**] or whether Cu reacts with Si [**99, 118, 133**]. A recent report detailed the reaction of both Ba and Cu from YBCO with the Si substrate [**134**]. The RBS spectrum pointed to a reaction of both Ba and Cu with the substrate at 700°C . It was with this in mind that the Si-YBCO interaction was studied (Sect. 4.2) by investigating the reaction of the systems Si-Cu, Si-Ba, Si-Cu-Ba and Si-Ba-Cu at different annealing

temperatures in an O_2 flow. The O_2 was used to simulate the presence of oxygen during deposition.

It was illustrated in Sect. 4.2.1 that elemental Cu is extremely reactive with Si. A Cu_3Si compound phase formed at 700°C and was transformed into a Cu-Si solution at 850°C . The Cu_3Si phase has been previously observed for Cu films annealed on Si substrates [**135**] and the low eutectic of the Cu-Si system (802°C) means that a solution of Cu and Si can form above this temperature. The liquid solution is quenched to a solid solution upon cooling, giving a nominal composition of $CuSi_5$. The long range diffusion of Cu into the Si was confirmed by the RBS spectra where Cu is seen at depths in excess of 1μm. Annealing in O_2 had little effect on the reaction as a surface oxide layer was formed and extensive oxygen incorporation was not observed. This is in disagreement with the high oxidizable nature of Cu_3Si reported by Hong et al. [**135**].

The reaction of Ba with Si was investigated in Section 4.2.2. The as-deposited Ba had carbonate and hydroxide impurities that were desorbed by annealing at 700°C . These impurities are likely to be incorporated during evaporation and also be adsorbed by the Ba layer during transfer of the samples from the evaporator to the furnace. The Ba layer reacts with the Si to form a Ba_2SiO_4 compound at 850°C . This agrees with the results obtained by annealing at BaF_2 layer on Si in O_2 where a Ba_2SiO_2 layer was also observed [**9**].

The Si-Cu-Ba and Si-Ba-Cu structures were also analysed (Section 4.2.3 and 4.2.4) and it was shown that when the Cu reacts with Si at 700°C to form Cu_3Si it also enables the Ba to react with Si to form Ba_2SiO_4 at 700°C . It was proposed that the reaction with Ba occurs at the lower temperature because of the increased mobility of Si in the silicide Cu_3Si as compared to in the single crystal state. The high mobility of Cu was demonstrated in the Si-Ba-Cu system in which a thick Cu layer diffuses through the Ba layer to form the silicide Cu_3Si at the interface while Ba forms a Ba_2SiO_4 layer at the surface.

Although these interaction investigations cannot simulate exactly the reaction of Si with YBCO, it has been demonstrated that Cu and Ba in combination react

vigorously with the Si substrate. The presence of oxygen during the deposition of YBCO and the nature of the depositing species also affect the interaction with Si. It is expected that the presence of mixtures of Y, Ba, Cu and O will affect the reaction rate. The effect of atomic species, clusters and ionic species during deposition is a possible explanation for the varying reaction rates seen with different deposition methods.

The use of oxide buffer layers on Si was considered in Section 4.3. The thermal stability of MgO, Y_2O_3 and ZrO_2 buffers was first assessed and it was established that the as-deposited oxide layers were stoichiometric and stable at the sputter deposition temperature of 700°C . At a temperature of 850°C reaction between the Y_2O_3 layer and the Si substrate was observed. The Si-MgO and Si-ZrO_2 systems did not display any interaction at 850°C and no apparent silicide formation was noted. The interaction of Y_2O_3 on Si arises from the vacancy structure of Y_2O_3 **[150,151]**. These vacancies lie along the (111) direction of Y_2O_3 and the oxygen ions have high mobility in this direction. The Y_2O_3-Si reaction will form a Y-silicate which has been seen for Y_2O_3 layers on Si **[93]** indicating that an intact Y_2O_3 layer exists over a reacted silicate $YSiO_4$ layer. The stability of Si-MgO and Si-ZrO_2 systems is in agreement with the inertness of these structures as observed by others **[134, 145]**. The stability of all 3 oxide buffer layers on Si at the temperature used for in-situ sputter deposition (700°C) justifies the use of these layers as buffer materials on Si.

Thin film superconductors were grown on the Si-metal oxide structures by ICM sputter deposition at 700°C . The RBS data displayed the passivating behaviour of the buffer layers and the severe interaction observed for direct deposition of YBCO on Si was absent for the buffered substrate. In addition, there was little evidence to prove large scale interaction of the YBCO film and the oxide buffer. Some interaction was observed for the Y_2O_3 buffer layer. In all cases the stoichiometry of the YBCO films was close to the ideal composition of $Y_1Ba_2Cu_3O_7$ and the surface of the films appeared smooth, black and shiny. The good quality of the YBCO films was verified by the X-ray diffraction spectra, in which preferential c-axis orientation was seen in all the Si/metal oxide/YBCO systems. Whereas in the case of Si buffered with

MgO and ZrO_2, only the c-axis peaks ((00l) reflections) were detected, for the Y_2O_3 buffer layer the polycrystalline nature of the YBCO film was clearly illustrated by the presence of reflections from other orientations of YBCO. This is attributed to the reaction of Y_2O_3 and YBCO seen with RBS spectrum. Even though these films were c-axis oriented it is expected that the lack of an orientational template (the buffer layers are polycrystalline) will prevent the growth of epitaxial YBCO films. This was confirmed by the absence of ion channeling by these films. The highly textured nature of the YBCO film on polycrystalline substrates stems from the anisotropic growth parameters, with the a-b plane growing an order of magnitude faster than the c-axis [**139**].

The resistivity and a.c. susceptibility measurements confirmed that the film quality of YBCO deposited onto buffered Si is better than that of direct deposition onto Si. For all metal oxide buffer layers, the YBCO films were metallic in the normal state (above T_c), had high transition temperatures (T_c) and relatively small transition widths (ΔT). The a.c. susceptibility measurements are more reliable tests of the superconducting quality of the film as it is not dependent on the presence of a single percolation path in the film but relies on the films bulk properties in terms of the density of percolation paths to assess the diamagnetic state of the YBCO film. Muller [**80**] has estimated that a complete susceptibility transition only occurs if >66% of the sample is superconducting.

A.C. susceptibility readings on thin films are not commonly quoted and the determination of both the resistance and magnetic behaviour of the YBCO film in this investigation assists in obtaining a better understanding of the superconducting electrical properties. It was often seen that the transition temperature observed from the susceptibility assessment was lower than that of the resistivity evaluation. This stems from the possibility of perlocation paths in the sample showing superconducting behaviour at higher temperatures whereas Muller [**80**] has shown that the onset of magnetic field expulsion in the sample only occurs when approximately 30% of the sample is superconducting. Magnetic flux lines cannot penetrate a superconducting path. Hence the motion of the magnetic flux lines through the

sample is unimpeded until superconducting percolation paths are set up and the flux is increasingly impeded as the density of the superconducting paths increase. However it can be energetically favourable for the flux lines to break through the superconducting paths at weak points in the path if the strength of the magnetic field exceeds a local critical field. Such events give rise to the broadened transition to a complete field expulsion. As the temperature decreases the amount of magnetic flux in the sample decreases and the strength of the weak link increases and a stage is reached when the flux cannot penetrate the sample at all. This corresponds to the flattening of the susceptibility transition and what is termed a "complete field expulsion transition". If portions of the sample become flux-repellant at different temperatures then the multi-stepped transition occuring in some of the susceptibility measurements is observed. When complete field expulsion does not occur it implies that the weak link density is high and even lowering the temperature does not cause complete field expulsion.

A comparison of results obtained by others for depositions onto Si, either directly or with buffer layers is shown in **Table 4.2**. The results for direct deposition onto Si are amongst the best results available in the literature. It can be seen from the table that although some researchers report high T_c values for films grown on Si, the large transition widths obtained for these films points to the poor quality. These large transitions arise from the reactivity of Si with YBCO. It can therefore be confidently stated that direct deposition onto Si does not result in good quality YBCO films and it was demonstrated in this study and in others that the Si-YBCO reaction destroys the superconductivity. The use of buffer layers is validated by the vast improvement observed for the transition of YBCO films on Si with buffer layers. Note in particular that the result for the $ZrO_2(Y)$ buffer is particularly impressive. This is because the buffer layer in that study (Ref.[**120**]) is close to single crystalline. It is also noteworthy that most of the good results with buffer layers have been obtained with the laser ablation method. Two reasons for this are the possibility of growing good epitaxy buffer layers with ablation and the *in-situ* growth of both the buffer layer and the YBCO film in the same deposition chamber,

with minimal contamination of the surface of the buffer layer. The multi-step, multi-chamber deposition used for the growth of structures in this study is therefore less than ideal. It should be emphasized that the T_c values quoted in this study, both

TABLE 4.2: A comparison of some of the results obtained for $Y_1Ba_2Cu_3O_7$ films on Si substrates with various deposition methods. The lower half of the table show the results obtained with buffer layers on Si. The transition temperatures and widths are quoted for resistivity measurements. The values obtained in this investigation are denoted with an asterisk (*).

Substrate	Deposition Method	Deposition Temperature	T_c (K)	ΔT (K)	Ref.
Si	Sputter	650°C	87	11	[117]
	Sputter	700°C	80	35	[117]
	Laser ablation	600°C	75	25	[10]
	evaporation	550°C	84	22	[121]
	ICM sputter	700°C	50	40	*
Si/ZrO_2	Laser ablation	600°C	90	10	[10]
$Si/ZrO_2(Y)$	Laser ablation	750°C	87	1.0	[120]
Si/ZrO_2	ICM sputter	700°C	81	5.9	*
Si/MgO	Laser ablation	700°C	86	2	[12]
Si/MgO	ICM sputter	700°C	83	5.4	*
$Si/YSZ/Y_2O_3$	Laser ablation	650°C	89	1.0	[129]
$Si/YSZ/Y_2O_3$	Laser ablation	680°C	92	6.0	[130]
Si/Y_2O_3	ICM sputter	700°C	81	7.0	*

for the resistive and magnetic measurements are determined at the intercept of the normal state behaviour and the slope of the superconducting transition. Whilst this is a more accurate determination of the transition temperature, it is generally lower than the T_c values obtained by noting the onset of a change in the normal behaviour, a method frequently used by other researchers to determine the T_c value. Thus while the T_c values in this study may appear to be lower in comparision to other reports, they are generally more accurately determined and the results present are more consistent as this method is used for all samples.

CHAPTER 5

Thin film superconductors on silicides

The continuous increase in packing density and minimum feature size in bipolar and metal oxide semiconductor (MOS) integrated circuits leads to an increase in the switching speed of the transitors. Simultaneously, however, the delay of signal propagation through the interconnects increases due to the increase in length (larger circuit complexity and size) and the increase of interconnect resistance and specific capacitance (thinner layers, smaller lateral size). These opposing influences on the device access or switching time eventually leads to a so-called interconnection limited current. A MOS device not only degrades in performance with downscaling because of increasing delay times in the interconnects, but also because of increasing device series resistance. This series resistance is composed of two major contributions: the contact resistence of the metal-semiconductor contacts in the source and drain, and the sheet resistance of the source and drain regions.

These problems necessitate the use of new high temperature stable contact and interconnect materials with a lower resistivity. Silicides are particularly suited for these applications [**152, 153**]. Since the supply of Si is practically unlimited in a Si-based device, the most thermodynamically stable silicides are generally the Si-rich ones [**154**]. The fundamental criterion for choosing a particular silicide is that it should have as low a resistivity as possible. In addition good high temperature stability and adhesion to the underlying Si is also desirable. Other criteria depend

on the particular application. In the last decade there has been much interest in epitaxial silicides grown on silicon both from a fundamental and from an applied point of view [**152–157**]. Technologically, epitaxial metal-semiconductor structures have potentially interesting applications. This is especially so for silicides that have good electrical conductivity and long electron mean free paths, such as is found with $CoSi_2$ [**154**]. These properties make these silicides possible candidates for high speed devices such as metal base transistors (MBT) and permeable base transistors (PBT).

Thin film superconductors grown on silicides form part of an integrated approach for merging semiconductor and superconductor technologies. The metallic silicides used in this study have a variety of applications ranging from contacts and interconnects to active device components. The pulsed laser deposition technique has recently been successfully employed to grow $Y_1Ba_2Cu_3O_7$ films onto Si substrates buffered with a $CoSi_2$ layer [**158, 159**]. The growth of semiconductor-silicide-superconductor and semiconductor-silicide-insulator-superconductor structures (section 5.3) have potential applications in 3-D micro-electronic devices and as field effect devices and detectors. Understanding the mechanism of growth of such multilayered systems is also important from a fundamental point of view i.e. the interface between the layers, growth dynamics, microstructure and epitaxy of such systems are of considerable importance.

5.1 Direct deposition of YBCO onto silicides

Metal-silicide films were formed by electron-beam deposition of metal overlayers onto single crystal silicon substrates (Si$< 111 >$ or Si$< 100 >$) in a HV system (see Section 2.4), followed by vacuum annealing at 800°C for an hour. The high temperature anneal is expected to produce the silicon rich silicides, PtSi, $CrSi_2$, $NiSi_2$ and $CoSi_2$. Pd_2Si was formed by annealing at 750°C . Formation of silicides in this way is widely reported [**152–157, 160**]. Films of the superconductor $Y_1Ba_2Cu_3O_7$ were then deposited onto these silicides by ICM sputter deposition at a substrate temperature of 700°C (see Section 2.3). The YBCO films on silicides displayed similar behaviour to that of YBCO films on silicon (see Chap. 4) in that severe interaction between the

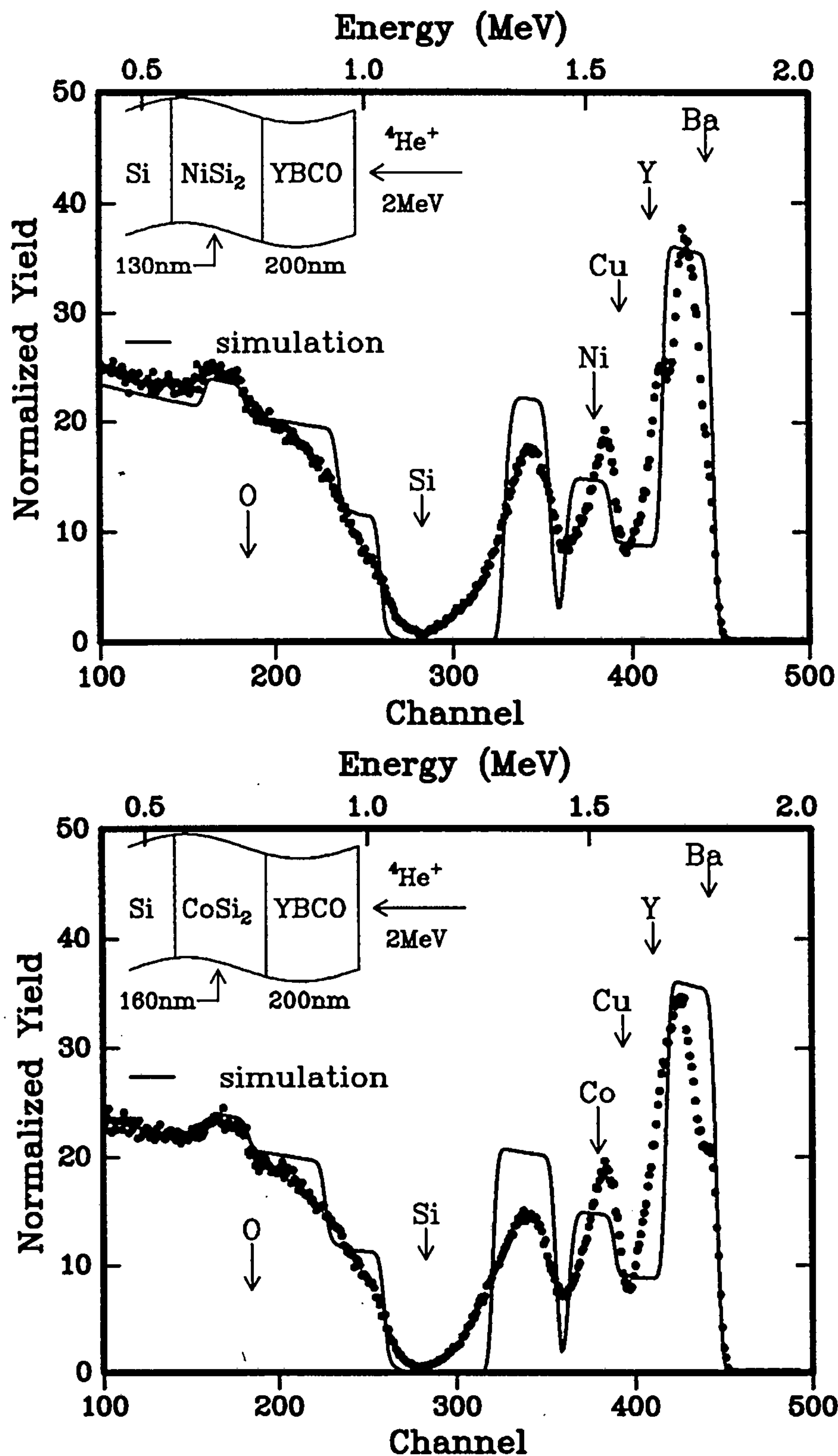

FIGURE 5.1: RBS spectra for $Y_1Ba_2Cu_3O_7$ thin film superconductors deposited directly onto $CoSi_2$ and $NiSi_2$ at 700°C . The film and the silicide interact strongly and superconductivity is lost in the YBCO layer. Diffusion of Cu and Ba into the silicide is seen from the RBS spectra. The behaviour of Y cannot be assesed because the small Y peak is overwhelmed by the Ba signal.

film and the silicide was observed. RBS spectra (**Fig. 5.1**) for YBCO films deposited onto $CoSi_2$ and $NiSi_2$ display the interaction between film and substrate. The diffusion of Ba and Cu towards the silicon substrate was illustrated by comparing the RBS spectrum for a thin film of YBCO deposited by ICM sputter deposition at 700°C with a simulation for an ideal Si-silicide-YBCO system. The thicknesses of the silicide layer and the YBCO film used in the simulation are from an RBS spectrum of the silicide on silicon (without YBCO) and from a YBCO film on MgO deposited during the same deposition. The MgO substrate serves as a control specimen for the thickness determination as accurate thicknesses cannot be determined on the silicide substrate due to the interaction. The drop in the Ba peak height at the surface and a corresponding increase towards the YBCO-silicide interface is noted while the copper signal also shows spreading of Cu into the silicide. No indication as to the behaviour of the Y in YBCO can be seen from the RBS spectrum because of the small peak height of Y and the overlap with the Ba and Cu signals. However, other diffusion studies of YBCO on various substrates indicate that Y is not very reactive [**105**]. The drop in the height of the metal signal in the silicide also points to intermixing of elements of YBCO with the silicide layer. The strongly smeared RBS spectra point to granular non-homogenous films with irregular interfaces at the Si-Silicide-YBCO junctions and a possible non-uniform YBCO surface. This phenomena was seen for all of the silicides studied and is attributed to the reaction between silicon in the silicide and YBCO. This interaction leads to the destruction of superconductivity in the YBCO films and none of the YBCO films on silicides investigated in this study displayed any evidence of superconductivity. No XRD peaks of the superconducting orthorhombic phase of YBCO could be detected and resistivity measurement displayed semiconducting behaviour, with the resistance increasing with a lowering of temperature. No transition to the superconducting state was observed. This suggests that the interaction with the silicides is even more severe than that with single crystal silicon, in which case some evidence of superconductivity was found, when comparing samples deposited under the same conditions (see Chap. 4). Analysing the reaction between the silicides and YBCO is

complicated by the breakdown of the silicide and the YBCO layer at the deposition stage (700°C) and the possible interaction of the metal from the silicide with the components of YBCO at elevated temperatures **[161–163]**. However, from the results in Chapter 4, in which it was found that the reaction between single crystal silicon and YBCO is severe, it is expected that the reaction between the Si in the silicides and YBCO is equally if not more intense, due to the higher mobility and greater availibility of Si in the silicide than in the single crystal form.

A possible mechanism for the increased reaction level of YBCO with silicides as compared to YBCO with single crystal silicon can be suggested. During deposition of the YBCO layer at 700°C, the oxidizing nature of the deposition conditions (oxygen, gas, ionized oxygen and energetic oxygen) provides the silicide layer with a means to form a surface oxide layer. For the silicides that were used in this investigation the oxide layer will be an SiO_2 layer. It has been found that Si and SiO_2 are equally reactive with YBCO **[121, 134, 133]**. Chourasia et al. **[133]** and Tsukamoto **[121]** showed that a SiO_2 layer forms on the Si surface during deposition of YBCO and that destruction of the YBCO layer results because Ba reacts with SiO_2 to form $BaSiO_4$. Frampton et al. **[164]** have shown that the oxidation of most silicides, including PtSi, Pd_2Si, $CrSi_2$, $NiSi_2$ and $CoSi_2$, results in the formation of SiO_2 much faster, and at lower temperatures than the oxidation of single crystal silicon. They demonstrated that a 20 nm thick SiO_2 layer grows on a $CoSi_2$ film when it was oxidized for 2hr at 700°C at atmospheric pressure, whereas less than 5 nm grew on a single crystal silicon substrate. The increased SiO_2 layer thickness found on silicides, as compared to single crystal silicon, is expected to affect the reaction rate with YBCO because of the reaction of Ba with SiO_2, but more importantly the reason for the increased oxide production is the higher mobility of the silicon in the metallic silicide than in the semiconducting single crystal **[164, 165]**. This means that a reaction between YBCO and Si can proceed faster with silicides than with single crystal silicon, and hence the observed enhanced reaction. The dependence of the kinetics of reaction on the electronic properties of the surface has also been discussed previously **[164–166]**, where it was demonstrated that semiconducting

silicides exhibit oxidation rates comparable to silicon whereas metallic-like silicides oxidize more rapidly and it was also shown that if the oxidation process is sufficiently slow the silicide layer remains intact but buried beneath the oxide cap. This was not observed for the deposition of YBCO on silicides (this investigation). No distinction between the reaction of different silicides with YBCO was noted pointing to the Si-YBCO reaction as the primary reaction path.

5.2 Silicon/silicide/metal oxide structures

The severe interaction between silicides and YBCO has prevented the deposition of thin superconducting films directly onto silicides and necessitated the use of buffer layers to preserve the film quality and prevent degradation of the silicide and superconductor film properties. Metal oxide buffer films (MgO, ZrO_2 and Y_2O_3) were used as buffer layers in our investigation. Motivation for the use of these buffer layers is to be found in Chap.4. There is little information available on the study of semiconductor-silicide-metal oxide- superconductor (SSMOS) multilayered structures (see for example the work by de Reus [**167,168**] and Aarnink [**169,170**]). The distinctive current carrying capacities of the superconductor YBCO and its excellent field expulsion capabilities in the superconducting state make the use of the SSMOS structures for unique field effect devices, switching devices and as detectors very attractive. Other applications include the dielectric isolation of different devices on a single semiconducting substrate and the fabrication of 3-D epitaxial heterostructures. The SSMOS system is a complex multilayer structure and in order to understand more clearly what transpires in such a system it was neccessary to first examine (separately) the semiconductor-silicide-metal oxide subsystem to determine its' thermal stability as a substrate for the deposition of YBCO films.

5.2.1 Formation and characterisation

Buffer layers of MgO, ZrO_2 and Y_2O_3 were deposited onto the silicides by e-beam evaporation in the same way as for the growth of oxide layers on Si (see section 4.3). For the growth of ZrO_2 and Y_2O_3 layers on silicides (111) oriented films are

expected to occur [**149**]. However, the (111) reflections of both ZrO_2 and Y_2O_3 are small and overlap with the large Si(111) peak. To ensure that the buffer is not amorphous the silicide/oxide structure was annealed at 700°C and no change in the XRD reflections were observed. The absence of other reflections for the oxide buffers points to the overlap of the (111) orientations of the oxide buffer with the Si peak. Ion beam analysis of the silicide/ZrO_2 and silicide/Y_2O_3 systems did not reveal any channeling in the oxide layers. MgO buffer layers deposited onto the silicides PtSi, Pd_2Si, $CrSi_2$, $NiSi_2$ and $CoSi_2$ were polycrystalline as ascertained by XRD. The preferred orientation of the films varied, with (200) preferentially oriented films found on PtSi. On $NiSi_2$ and $CoSi_2$ the MgO film orientation was (111); this looked promising as an epitaxial layer on the (111) oriented $CoSi_2$ and $NiSi_2$ layers. However, ion beam analysis did not display channeling for the oxide layers and confirmed that the small, broadened XRD peak observed is due to a fine grained polycrystalline film. On Pd_2Si a mixture of (111) and (200) orientation was observed for the MgO layer but these were very low intensity reflections and poorly developed, pointing to poor crystallinity of the film. This effect is not fully understood. No clear diffraction peaks were observed for the MgO layer on $CrSi_2$. Post-annealing the $CrSi_2$-MgO structures in O_2 at 700°C for 1 hour did not cause any change in the XRD spectrum. The use of rapid thermal annealing (RTA) at high temperatures has been successfully employed to improve the crystalline quality of insulators on silicon and on silicides [**171, 172**] without destruction of the underlying layer. Although in those cases the insulator was CaF_2, the RTA treatment of oxide buffer layers on silicides might be a route to use to improve the crystalline quality of the oxide buffer layer. Unlike the situation in Chapter 3 where improved surface quality was achieved by annealing single crystal MgO substrates at high temperature, with MgO buffer layers on silicides the high temperature anneals (1000°C for single crystal MgO) affects the nature of the underlying silicide layer (see 5.2) and higher temperatures than those used during deposition are not beneficial to the stability of the multilayers or to improving the epitaxy of the layers.

5.2.2 Thermal stability

The thermal stability of semiconductor-silicide-metal oxide multilayer structures was assessed by annealing at 700°C and 850°C under flowing O_2 at atmospheric pressure in a similair fashion as was done on Si substrates. Reaction between the silicide and oxide layers is likely to lower the chemical inertness of the oxide buffer layer and reduce its' efficacy in preventing the YBCO film from reacting with the silicide layer and/or with the buffer layer itself. Reaction of the silicide with the underlying Si can also occur at high temperatures.

An investigation of the thermal stability of the oxide buffers MgO, ZrO_2 and Y_2O_3 on the silicides PtSi, Pd_2Si, $CoSi_2$, $NiSi_2$ and $CrSi_2$ reveals that all of the Si/silicide/metal oxide structures are stable up to annealing temperatures of 700°C for 1 hour. At 850°C , a reaction of the Y_2O_3 layer was observed with all the silicide layers, with $CrSi_2$ showing the least reactivity with the Y-oxide. This may due the possible formation of an inert Cr-oxide at the surface of the $CrSi_2$ layer. RBS spectra for Y_2O_3 layers on PtSi, $CoSi_2$, $CrSi_2$, Pd_2Si and $NiSi_2$ (**Fig. 5.2**) shows that at 850°C the Y signal height drops and the tailing in the Y signal denotes spreading of Y. The shifting of the leading edge of the metal signal, from the silicide, points to the formation of an interfacial layer. For example, the $CoSi_2$ spectrum is reminiscent of oxidation of $CoSi_2$, where the silicide is buried under a SiO_2 layer - implying that the interfacial layer is possibly SiO_2.

The lower peak heights for both the Y in Y_2O_3 and the metal signal from the silicide layers means a lower backscattering yield from these elements due to intermixing of elements of the silicide and oxide layers. The formation of a Y-silicate during the high temperature annealing of Y_2O_3 on the silicides can cause the breakdown of the Y_2O_3 buffer layer [**143**]. Y_2O_3 has an incomplete fluorite structure (CaF_2), with oxygen atoms occupying three-quarters of the fluorine positions and the remaining quarter "occupied" by vacancies. The Y-ion is 6-coordinate while the O-ion is 4-coordinate. This vacancy structure is required for charge neutrality of the Y^{3+} and O^{2-} ions. Fukomoto [**151**] found higher χ_{min} values for ion channeling in the (111) direction as a result of defects induced by the incomplete crystalline

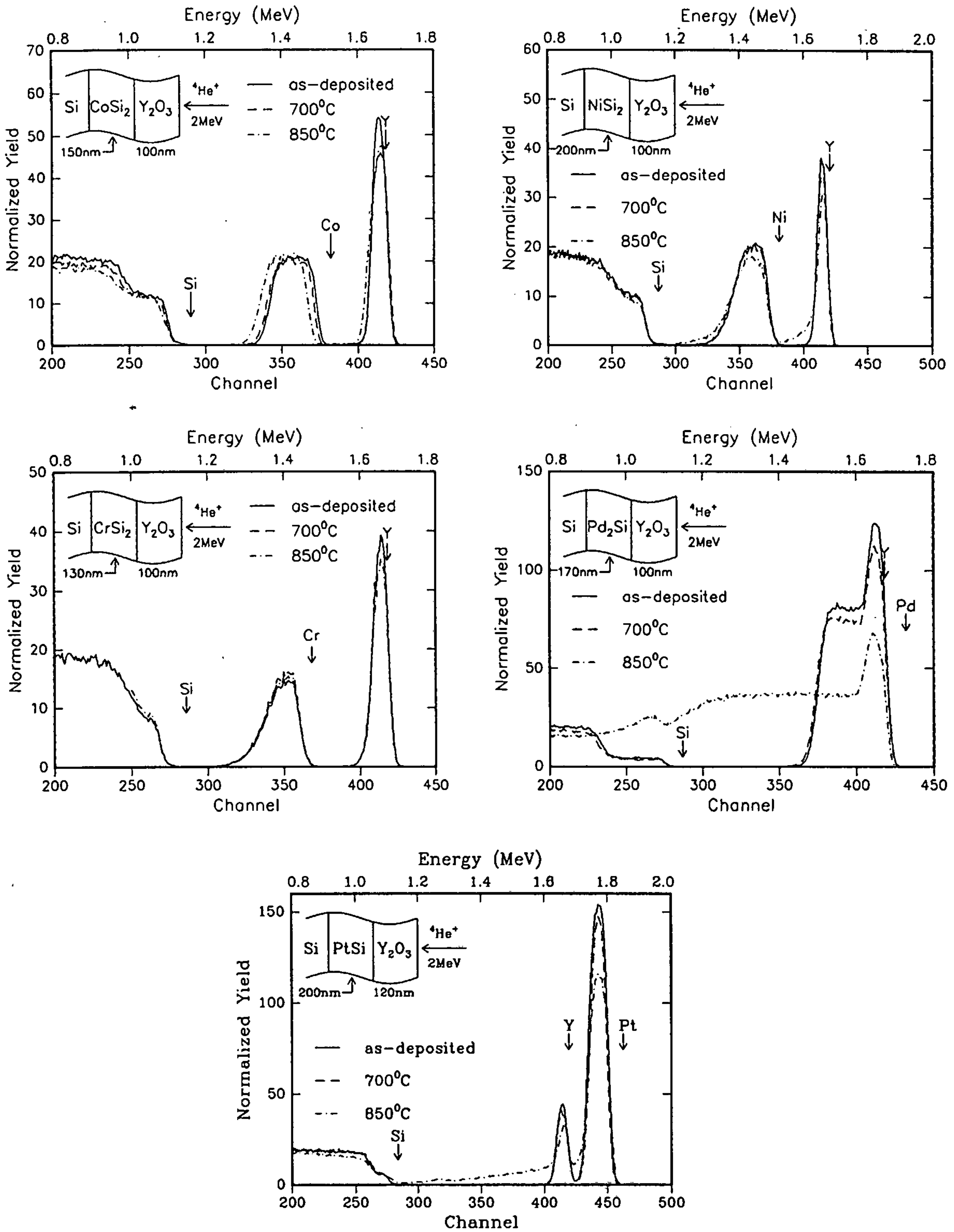

FIGURE 5.2: RBS spectra for a Y_2O_3 layer on PtSi, $CoSi_2$, $CrSi_2$, Pd_2Si and $NiSi_2$. The spectra shows the effect of annealing these structures at 700°C and 850°C . The silicide-metal oxide systems are stable at 700°C but a segregation of the Y_2O_3 layer occurs at 850°C and intermixing with the silicide is observed.

structure. Onisawa [**150**] has shown that the poor dielectric properties observed along the <111> direction of Y_2O_3 is caused by the vacancies lying in this direction and the mobility of ions is high for (111) oriented grains due to the higher density of diffusion paths in this direction. The vacancy structure permits oxygen diffusion through the yttria layer and the high temperatures allows the diffusing oxygen to react at the silicide-yttria interface and form SiO_2 or Y-silicate. The diffusion of oxygen ions can also explain why the $CrSi_2$ is not as reactive as the other silicides; Cr can also oxidise and the Cr-oxide prevents the the formation of the SiO_2 or Y-silicate layer. The presence of (111) oriented grains in our Y_2O_3 films and the incomplete structure means that a reaction is likely to occur at high temperature in order to form a more stable crystal structure. The mobility of Si at high temperatures is expected to result in a $YSiO_4$ reaction layer [**143**] but the thin reaction layer could not be detected by XRD analysis or in the RBS spectra. The Pd spectrum show that at 850°C the Pd "flows" into the Si. This was attributed to the reactivity of the Y_2O_3 layer and the melting eutectic of the Pd-Si system, which is close to 800°C . However, it should be pointed out that the melting will only occur if the Pd and Si in Pd_2Si are broken up - as would occur if reaction with the Y_2O_3 layer is present.

In comparison, ZrO_2 showed relatively good thermal stability up to 850°C , although slight interaction is suggested in the $CrSi_2/ZrO_2$ and $NiSi_2/ZrO_2$ spectra. **Fig. 5.3** shows the RBS spectra for a ZrO_2 buffer layer on the silicides. The Si/silicide/MgO spectra are shown in **Fig. 5.4**. Surprisingly, both systems do not display the severe breakup of the Pd_2Si layer observed previously, implying that the stability of the oxide determines the behaviour of the underlying silicide. Little reaction between the oxide buffer layer (MgO) and the silicide layers was observed at high temperatures. $CoSi_2$ and $NiSi_2$ showed thermal stability up to 850°C in line with other results detailing the thermal stability of such disilicides [**160, 173, 174**], but a downwards shift of the Ni signal was noted. Spreading of the Cr and Pt signals was also observed.

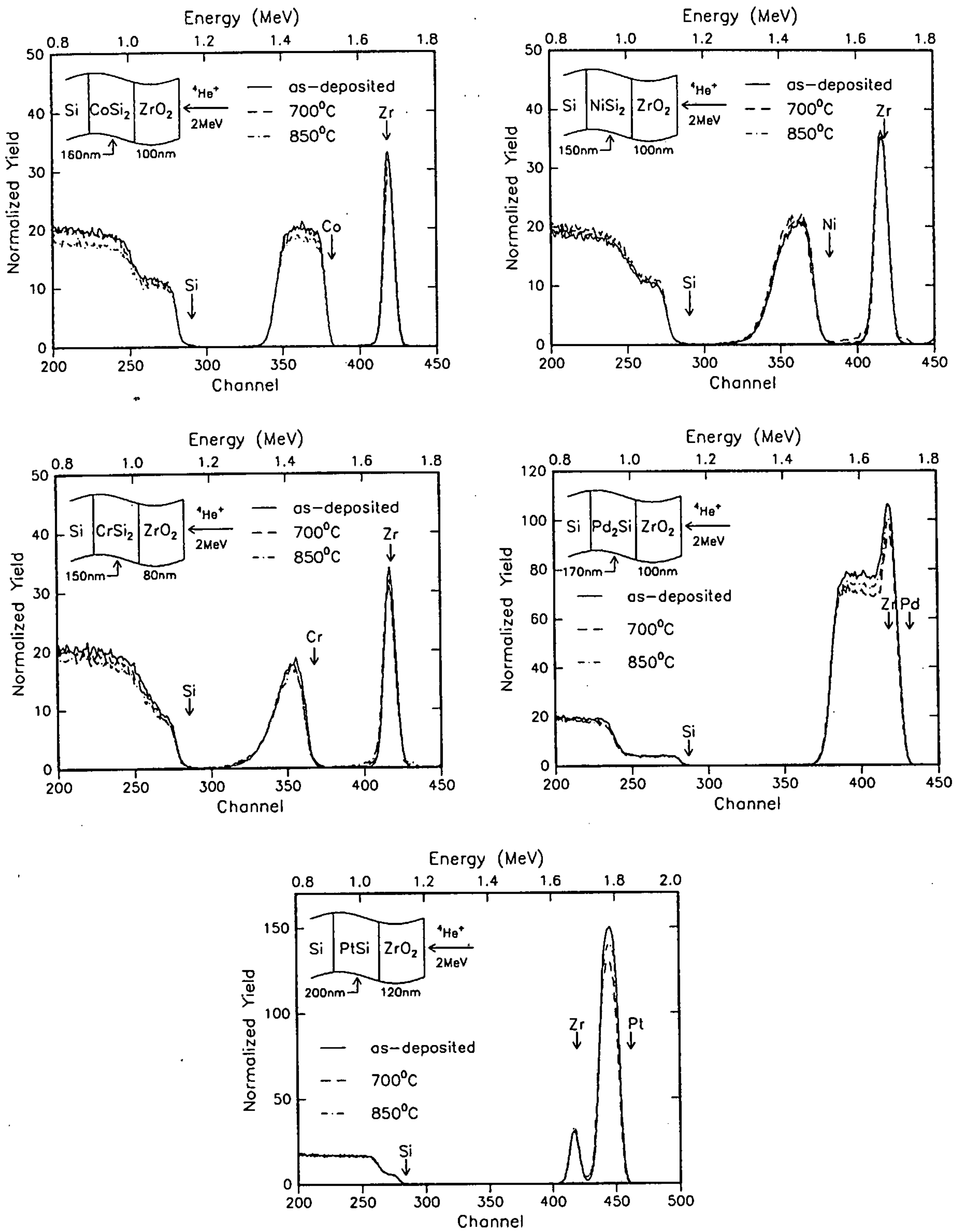

FIGURE 5.3: RBS spectra for a ZrO_2 buffer layer on silicides. The thermal stability of the ZrO_2 layer is noted by the absence of interaction up to 850°C. Comparison of these RBS spectra with **Fig.5.2** demonstrates that ZrO_2 is more stable than Y_2O_3 at high temperature.

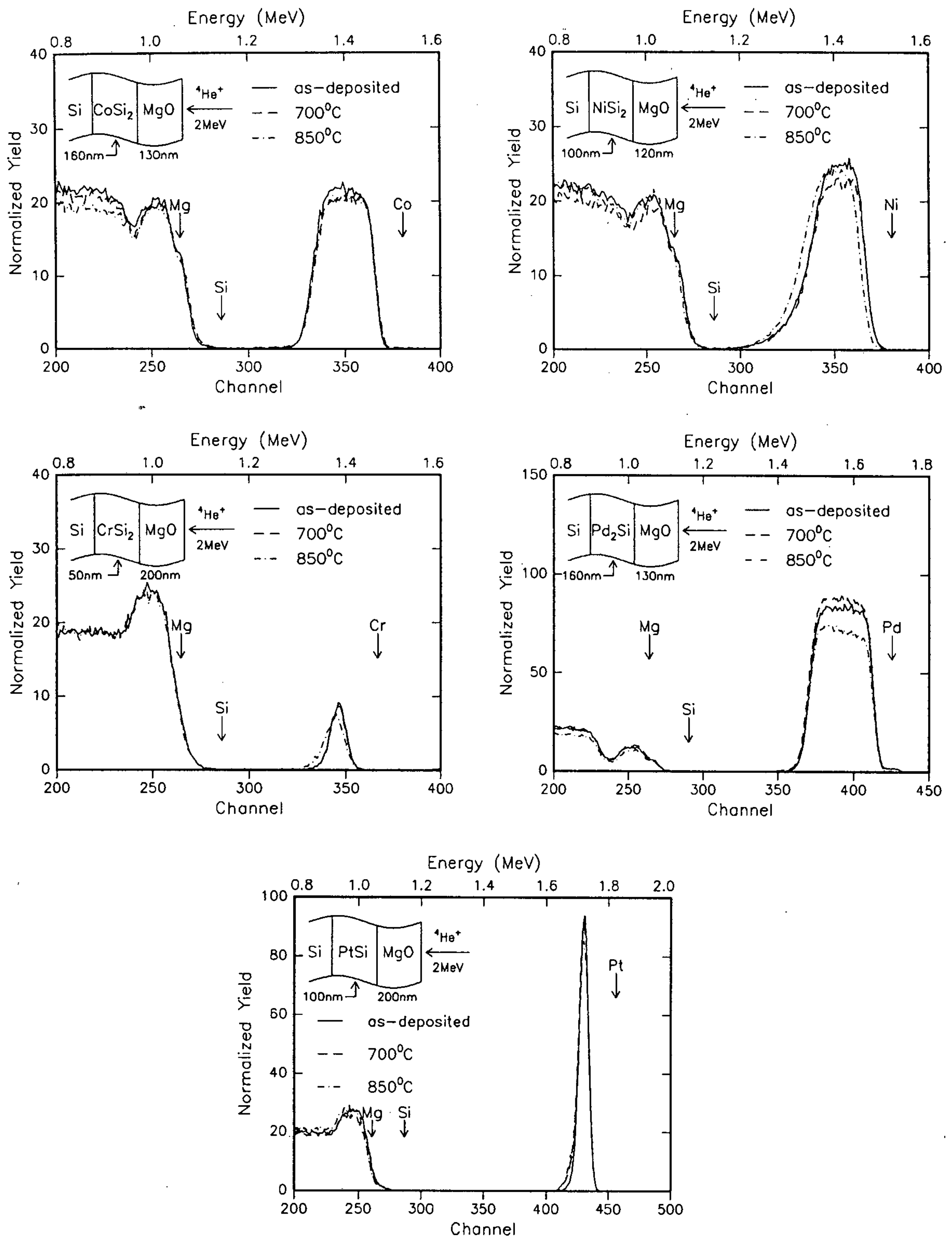

FIGURE 5.4: RBS spectra for a MgO buffer layer on silicides. The thermal stability of the MgO layer is noted by the absence of large scale interaction up to 850°C but the movement of the leading edge of the metal signal (from the silicide) points to the formation of an interfacial layer. Some interaction at the silicon-silicide interface is noted for all the silicides at high temperature.

5.3 Formation of YBCO on silicides with buffer layers

The use of oxide buffer layers for the growth of $Y_1Ba_2Cu_3O_7$ films on single crystal silicon was demonstrated in Chap. 4. As a result of the severe interaction between silicides and YBCO it was again necessary to resort to the use of these buffer layers (MgO, Y_2O_3 and ZrO_2) to prevent the silicide-YBCO interaction. In section 5.2 it was demonstrated that the silicon/silicide/metal oxide structures used in this investigation are stable at the temperatures used during ICM sputter deposition (700°C). This is a promising result for the growth of thin film YBCO superconductors onto silicides.

Ideally, the growth of epitaxial silicides with a further epitaxial oxide buffer layer would be expected to yield the best quality superconducting films. However, the relatively poor vacuum conditions for e-beam evaporation (10^{-6} - 10^{-7} Torr) available in this investigation, do not satisfy the stringent conditions for multilayer epitaxial growth. For example, the epitaxial growth of the insulator CaF_2 onto an epitaxial $CoSi_2$ film on Si<111> was achieved with Molecular Beam Epitaxy at a pressure of 10^{-10}Torr [**171, 175**]. Added to this, the demonstration of the ability to deposit fairly good quality high T_c films on polycrystalline oxide buffer layers (Chap.4 and [**139**]) means that good quality textured films can be grown on the buffers and the growth of the multilayer structure can be assessed without the restrictively stringent conditions for multiple epitaxy. Epitaxial oxide layers on silicides have not been intensively investigated and to date the only similiar work has been by Phillips et al. [**171, 175**] and Fathauser [**176**] detailing the growth of an epitaxial silicide capped with an epitaxial insulator. In all these studies the insulator was CaF_2. The epitaxial growth of a Si/metal/insulator/metal structure was recently demonstrated [**177**]. Aluminium metal was used as the conductor and CaF_2 as the insulator. CaF_2 was not used as a buffer in our investigations due to the high reactivity of CaF_2 with YBCO [**178**].

5.3.1 MgO buffer layers

Thin films of YBCO were deposited onto the silicide-MgO structures by ICM sputter deposition at 700°C . All films were black and conducting as-deposited but reflectivity of the surface differed, with films on $CrSi_2$/MgO and Pd_2Si/MgO being dull and specular, indicating a roughened surface, whilst films on $NiSi_2$/MgO, $CoSi_2$/MgO and PtSi/MgO were shiny and highly reflective (mirror-like).

The RBS spectra for YBCO films on silicide/MgO structures are shown in **Fig. 5.5**. The MgO layer was effective in preventing the interaction between the superconductor YBCO and silicides, seen in section 5.1. Simulation of the observed spectrum shows that the YBCO film is close to the ideal $Y_1Ba_2Cu_3O_7$ composition. The interfaces between the YBCO film and the MgO buffer is sharp and no interaction at this interface is observed. The simulation reveals roughening of the silicon-silicide interface but the multilayer structure is intact. The roughening effect is due to an irregular silicon-silicide interface which occurs during the formation of the silicide. Although no interaction between YBCO and Si (or silicide) was also noticed for YBCO films on $NiSi_2$/MgO, $CoSi_2$/MgO and PtSi/MgO, an interaction between the MgO buffer and YBCO was found to occur for films on $CrSi_2$/MgO and Pd_2Si/MgO. It is not clear how the thickness of the silicide affects the stability of the buffer (and ultimately that of the YBCO film) as the reactive films were found on the thinnest silicide layers. In both these systems the diffusion of Cu into the MgO layer occurs. The foot-like ledge at the rear of the film signal denotes the interaction of the film and buffer. Comparing the observed spectrum with a simulation with exact composition $Y_1Ba_2Cu_3O_7$ shows that the Cu signal in the film is lowered. This arises from the YBCO-MgO interaction. The reaction of YBCO with MgO at high temperature has been documented **[168]**. It is postulated that the poor crystallinity of the MgO film on $CrSi_2$ and on Pd_2Si makes the MgO layer less stable against reaction with Cu than the crystalline MgO buffer. As an example, no Cu-MgO reaction was seen for $Y_1Ba_2Cu_3O_7$ films on Al_2O_2/MgO and Si/MgO substrates (see Chap. 4), and YBCO films on $CoSi_2$/MgO, PtSi/MgO and $NiSi_2$/MgO do not display the foot-like structure, at the rear of the film signal. de Reus **[167]**

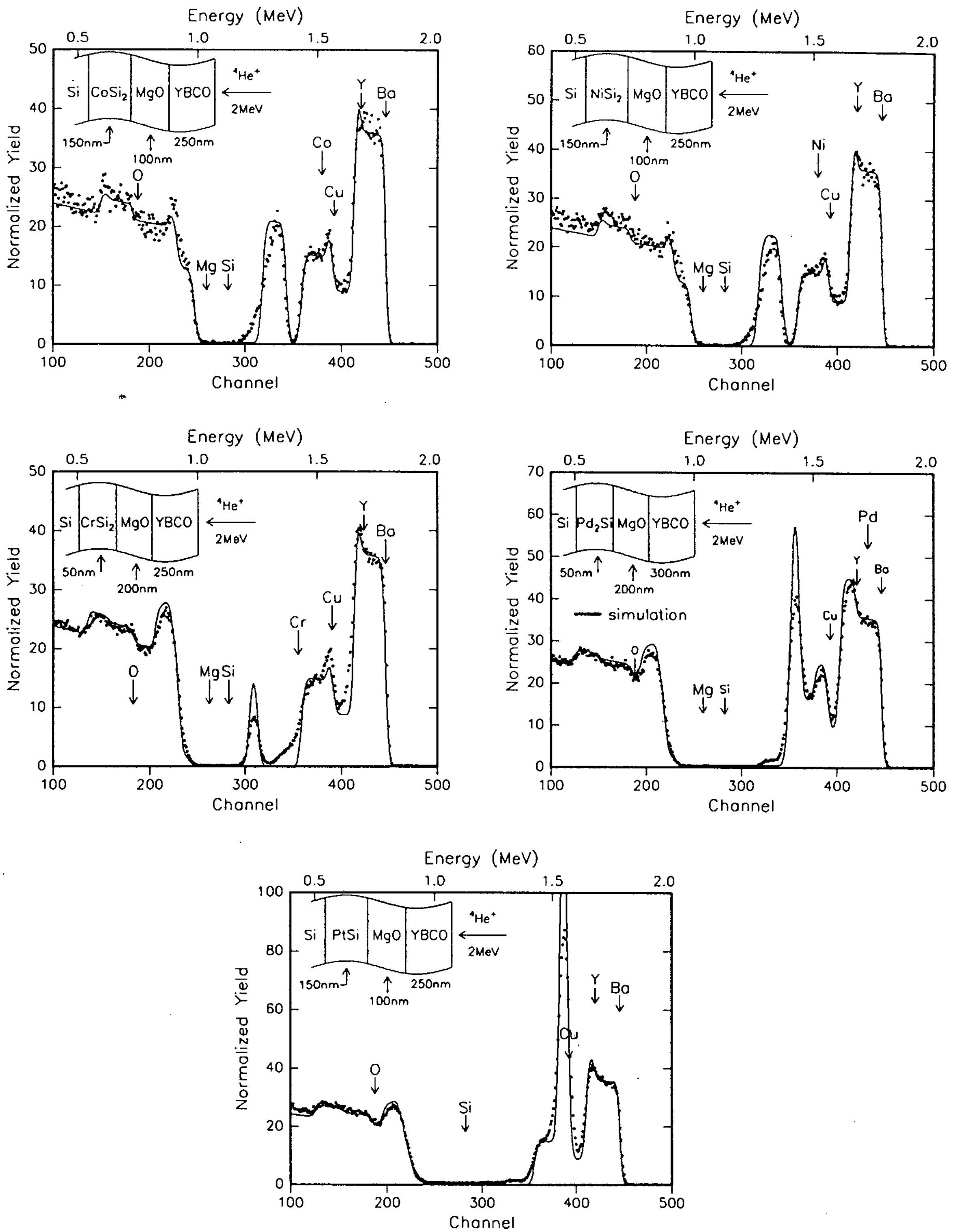

FIGURE 5.5: RBS spectra for $Y_1Ba_2Cu_3O_7$ thin film superconductors deposited onto silicides buffered with MgO at 700°C . Very little interaction can be seen between the $Y_1Ba_2Cu_3O_7$ film and the silicide for $CoSi_2$, $NiSi_2$ and PtSi and the sharpness of the film and buffer signals and the retention of stoichiometry in the film illustrate that film-buffer interaction was avoided. For $CrSi_2$ and Pd_2Si significant reaction between YBCO and the MgO layer was observed by the foot at the rear of the Cu-signal. The solid lines are from the RUMP simulation.

has reported the growth of poor quality YBCO films on MgO buffer layers. No data was presented on the crystallinity of the MgO layer in those studies but the room temperature deposition of MgO reported by de Reus **[167]** most likely gave amorphous MgO which is the reason for the MgO-YBCO interaction. Even with the Cu-MgO interaction seen in the $CrSi_2$/MgO/YBCO and Pd_2Si/MgO/YBCO systems, the YBCO film still has a near uniform distribution above the reacted layer and is close to ideal stoichiometry.

X-ray diffraction of a YBCO film on $CoSi_2$ with a MgO buffer gave the best XRD spectrum and revealed a preferential c-axis orientation for the YBCO film (**Fig. 5.6**). The textured orientation of the $CoSi_2$ layer was also observed. No non-superconducting phases were seen. Preferential orientation was also observed for films on $NiSi_2$ and PtSi. Even though the XRD data points to c-axis oriented films, ion channeling analysis indicated that these films were polycrystalline, with the best minimum yield of 85% obtained on a Si/$CoSi_2$/MgO/$Y_1Ba_2Cu_3O_7$ multilayer. The highly $(00l)$ textured YBCO film is surprising since the MgO film is polycrystalline and shows that the texture of the film on polycrystalline substrates is more dependent on factors such as surface smoothness and growth dynamics of the c-axis orientation than matching of the lattice parameters. This corresponds with the results of Norton **[139]** where it was found that the large anisotropy of the growth kinetics of $Y_1Ba_2Cu_3O_7$ can result in c-axis oriented films on randomly oriented polycrystalline substrates. On $CrSi_2$ some c-axis orientation was detected but the intensity of the c-axis reflections were very small and the YBCO films were polycrystalline as the presence of peaks from other orientations of YBCO was observed. The peak intensities were also smaller than for films on $CoSi_2$, $NiSi_2$ and PtSi. Films on Pd_2Si were completely randomized with the strongest peak occurring for the (110)(103)(013) set of reflections at $\sim 32.6°$. This reflection is also the strongest reflection for bulk or powder YBCO samples.

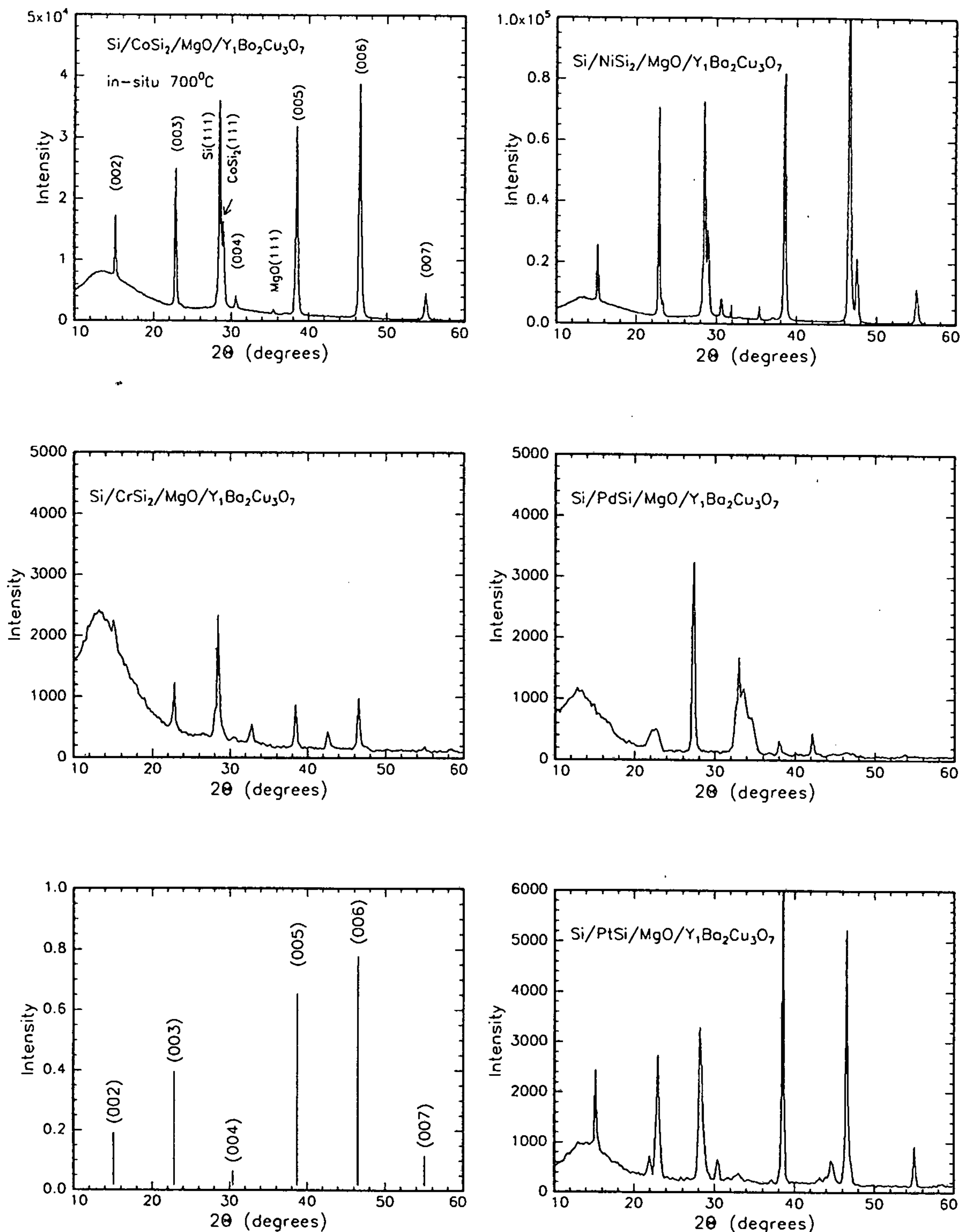

FIGURE 5.6: XRD spectra for $Y_1Ba_2Cu_3O_7$ thin film superconductors deposited onto silicide/MgO structures at 700°C . The $Y_1Ba_2Cu_3O_7$ film is preferentially c-axis oriented on $CoSi_2$/MgO, $NiSi_2$/MgO and PtSi/MgO. The small MgO peak is swamped by the intensity of the other reflections. The line diagram illustrates the position and relative intensity of the (00*l*) reflections for a highly textured $Y_1Ba_2Cu_3O_7$ film.

5.3.2 Y_2O_3 buffer layers

Y_2O_3 buffer layers on silicides of PtSi, $NiSi_2$, $CoSi_2$, Pd_2Si and $CrSi_2$ were successful in preventing large scale reaction between YBCO and the silicide (**Fig. 5.7**). However, reaction between the superconductor and the Y_2O_3 buffer was observed for $NiSi_2/Y_2O_3$/YBCO, Pd_2Si/Y_2O_3/YBCO and $CoSi_2/Y_2O_3$/YBCO structures. For most of the systems, rough Si-silicide interfaces were seen. The RBS spectra (**Fig. 5.7**) depict a reduction of the Y peak height and a tailing at the rear of the Ba signal for some structures, which points to an interaction between Ba and Y, with the possible formation of $BaYO_2$. The existence of a Ba-rich layer at the Y_2O_3 - YBCO interface was also observed by Bardal et al. [**128**] in YBCO–Y_2O_3–YBCO heterostructures. This interaction is limited to the interfacial region and the film maintains good stoichiometry above this region. The interaction of Y_2O_3 with YBCO is likely to diminish the quality of the YBCO films. X-ray diffraction results show that all the YBCO films are polycrystalline (**Fig. 5.8**). Little evidence of c-axis preferential orientation was seen for the YBCO films on silicide/Y_2O_3 structures.

5.3.3 ZrO_2 buffer layers

ZrO_2 buffer layers on silicides also displayed some reactivity with YBCO. The formation of $BaZrO_3$ from the reaction of Ba and ZrO_2 has been noted [**141**]. The ZrO_2 layer was in all cases successful in preventing a reaction of YBCO with the silicides, but a drop in Zr peak height was observed for the ZrO_2 buffer layer denoting ZrO_2 - YBCO interaction (**Fig. 5.9**). The tailing in the Ba - signal and the loss of Ba height alludes to the formation of $BaZrO_3$. The reaction appeared to affect the Zr - peak the most for $CrSi_2$ and Pd_2Si samples. The Pd_2Si sample showed the spreading of Pd observed previously and the silicide layer was Si - rich. Rough Si-silicide interfaces are suggested, but these are compounded by the overlap with the tailing YBCO signal. The YBCO films on ZrO_2 were polycrystalline with preferential c-axis orientation seen on $CoSi_2/ZrO_2$ and $PtSi/ZrO_2$ (**Fig. 5.10**). The reaction of YBCO with the buffer layer (mainly Y_2O_3 and ZrO_2) does not appear to depend critically on which of the silicides is the underlying layer.

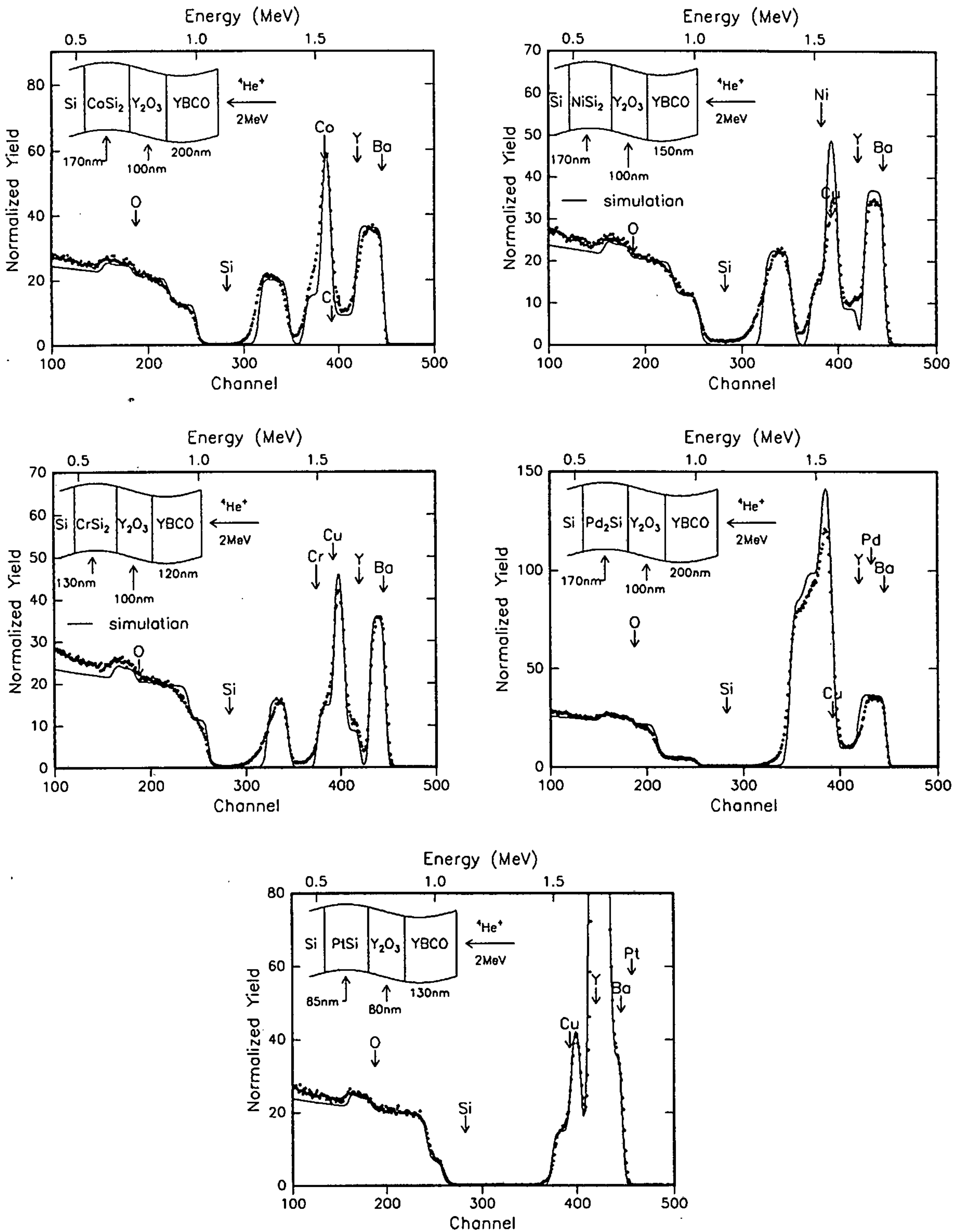

FIGURE 5.7: RBS spectra for $Y_1Ba_2Cu_3O_7$ thin film superconductors deposited onto silicide/Y_2O_3 systems at 700°C . The film-silicide interaction is prevented by the Y_2O_3 buffer layer but reaction between the YBCO layer and the Y_2O_3 layer is seen on the $NiSi_2$ and $CoSi_2$ samples as a reduction in the peak height of the Y signal and the appearance of a small peak at the rear of the Ba signal. The Pd_2Si sample shows smearing of the Pd-signal. The solid lines are RUMP simulations.

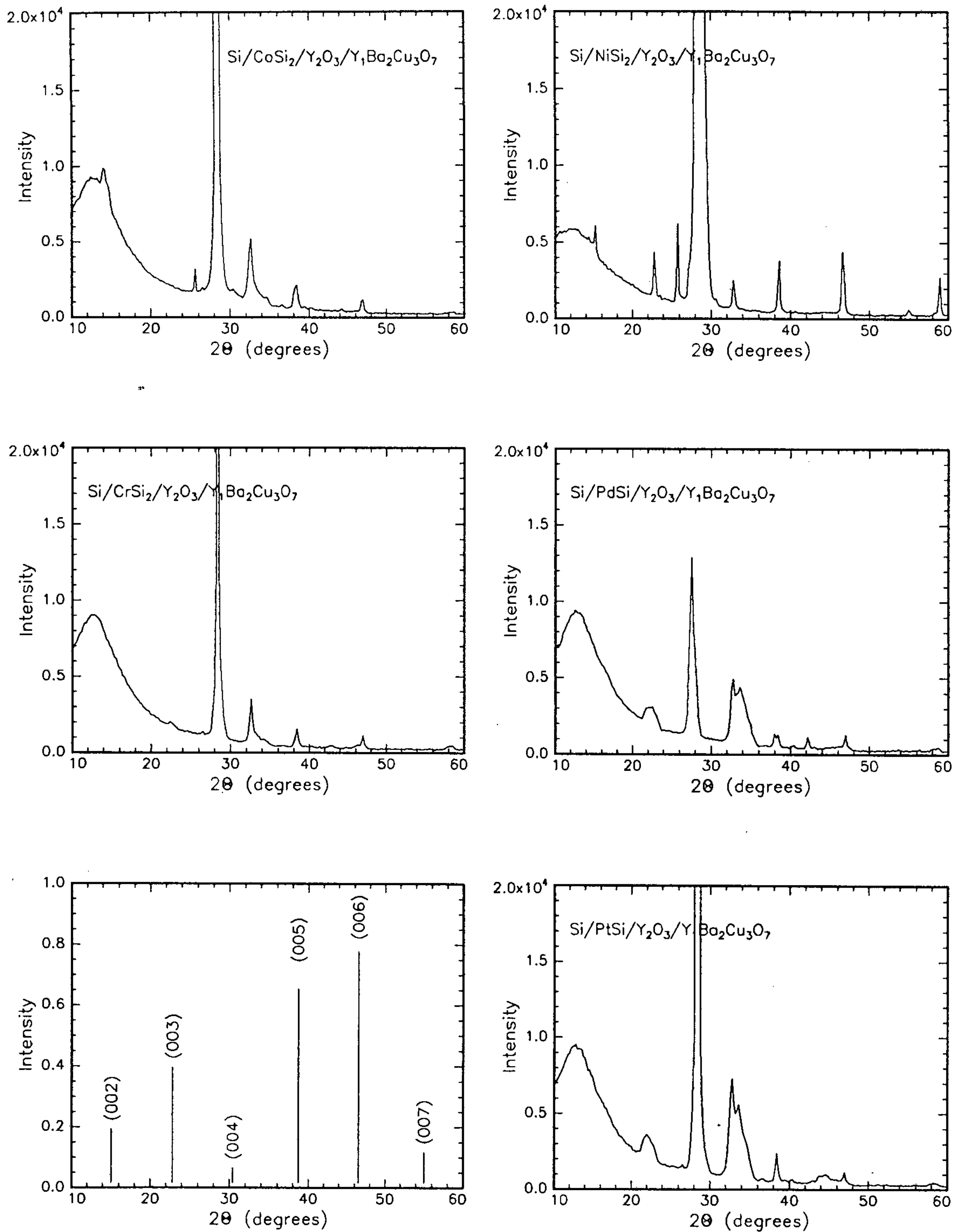

FIGURE 5.8: XRD spectra for $Y_1Ba_2Cu_3O_7$ thin film superconductors deposited onto silicide/Y_2O_3 structures. The $Y_1Ba_2Cu_3O_7$ film is preferentially c-axis oriented on $CrSi_2/Y_2O_3$ but the intensity of the c-axis reflections is small. The Y_2O_3 reflection overlaps with the Si(111) reflection. The line diagram illustrates the position and relative intensity of the $(00l)$ reflections of a highly textured $Y_1Ba_2Cu_3O_7$ film.

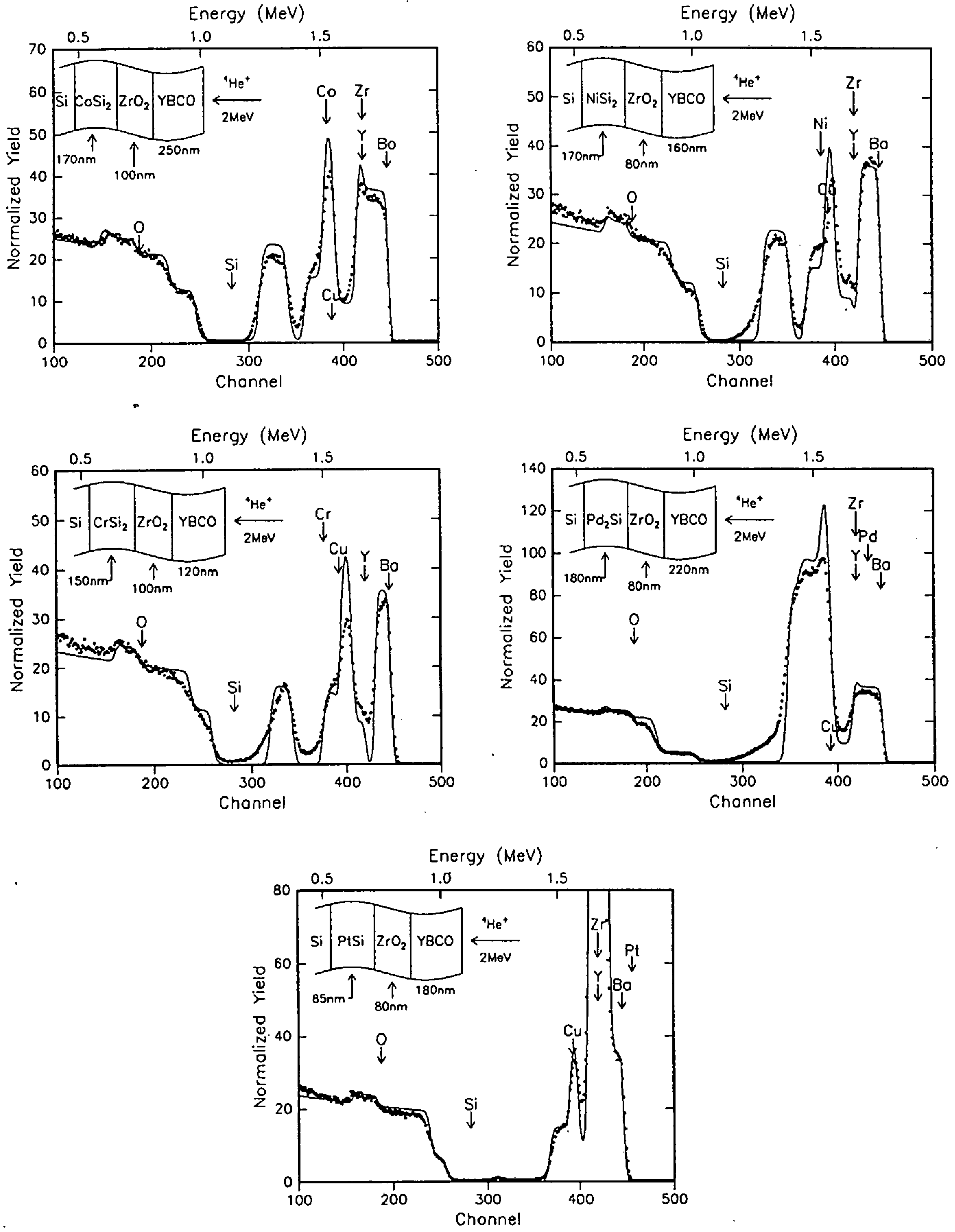

FIGURE 5.9: RBS spectra for a $Y_1Ba_2Cu_3O_7$ thin film superconductor deposited onto silicide/ZrO_2 systems. The film-silicide interaction is prevented by the ZrO_2 layer but reaction of the ZrO_2 buffer and the YBCO layer is alluded to by the Zr peak height drop and tailing of the Ba signal. The solid lines are RUMP simulations.

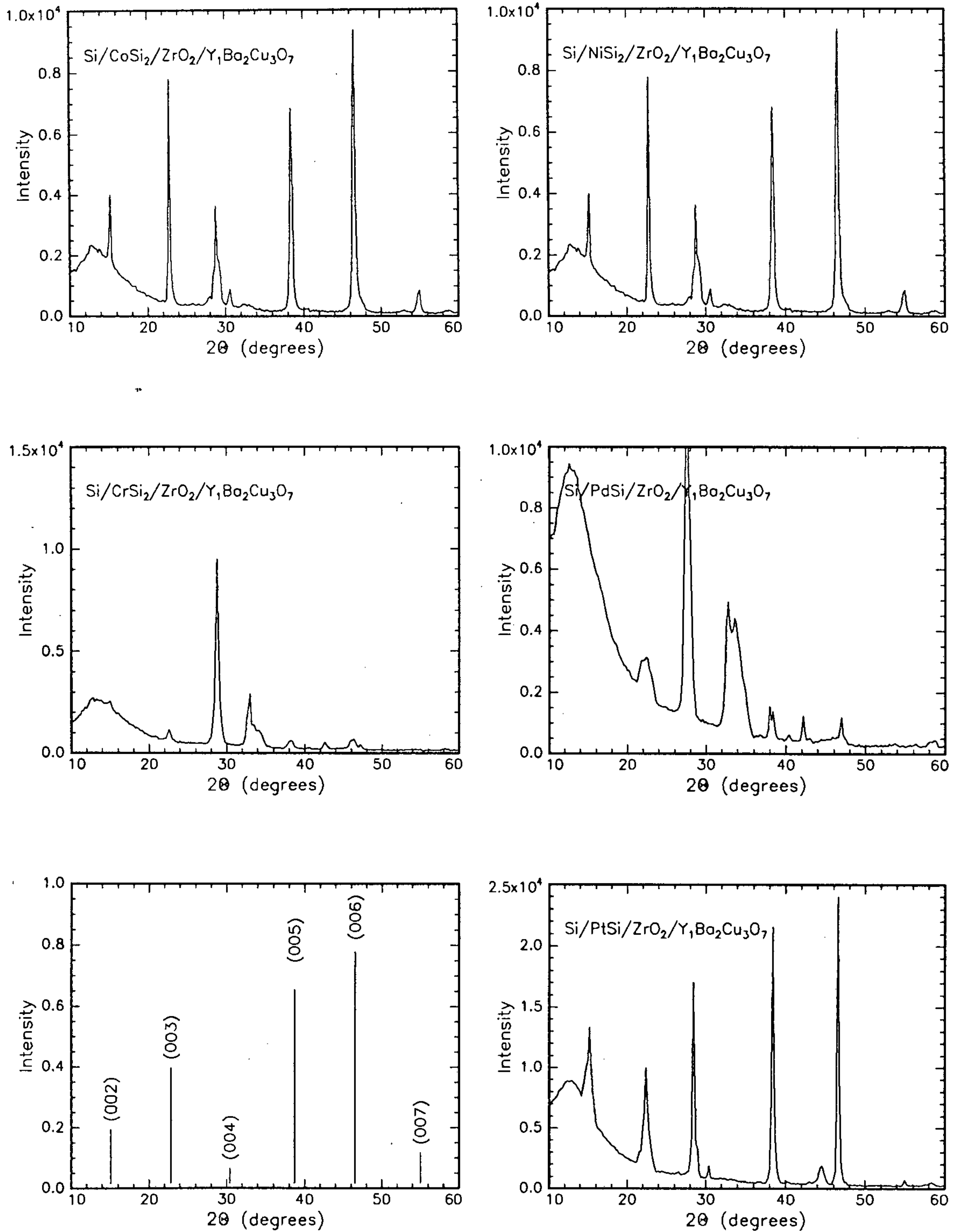

FIGURE 5.10: XRD spectra for $Y_1Ba_2Cu_3O_7$ thin film superconductors deposited onto silicide/ZrO_2 structures. The $Y_1Ba_2Cu_3O_7$ film is preferentially c-axis oriented on $CoSi_2/ZrO_2$. The ZrO_2 peak is swamped by the intensity of the Si(111) substrate reflection. The line diagram illustrates the position and relative intensity of the $(00l)$ reflections of a highly textured $Y_1Ba_2Cu_3O_7$ film.

5.3.4 Electrical properties

Electrical resistivity and a.c. susceptibility as a function of temperature of the thin film superconductors on silicides with oxide buffer layers was determined with a 4-pt probe resistivity evaluation and a diamagnetic susceptibility measurement as described in the experimental details. The resistivity versus temperature curves (R-T curves) and a.c. susceptibility curves were grouped together for common buffer layers. The results for YBCO films deposited on silicide-MgO structures are shown in **Fig. 5.11**.

On MgO buffer layers the highest transition temperatures T_c and the sharpest transition widths ΔT were obtained for films on $CoSi_2$, $NiSi_2$ and PtSi. All YBCO films were conducting in the normal state (above T_c) but the resistive behaviour from room temperature to T_c differed. Films on Pd_2Si and $CrSi_2$ showed slow decreases of resistivity with temperature. The increase of resistivity with decreasing temperature for the film on Pd_2Si points to a mixture of conducting and semi-conducting grains in the YBCO film. In the normal state, above T_c, semiconducting behaviour is displayed ie. the resistance increases with decreasing temperature. At T_c the superconducting grains dominate when a percolation path is set up. For $CrSi_2$/MgO a long transition to zero resistivity was observed. Zero resistivity was never achieved for the film on Pd_2Si/MgO demonstrating that the film quality was poor. This tallies with the RBS results which showed a reaction between YBCO and the MgO buffer by the diffusion of Cu (from YBCO) into the buffer layer. Segregation products that act as impurities in the YBCO film and degrade the superconducting transition by contaminating the grain boundaries and reducing the current capabilities and the transition to superconductivity lead to the poor transition seen in the R-T curves for films on Pd_2Si/MgO and $CrSi_2$/MgO.

Complete A.C. susceptibility transitions, in which the magnetic field expulsion stabilises to a constant value, were only recorded for films on $CoSi_2$/MgO and $NiSi_2$/MgO. On PtSi/MgO and $CrSi_2$/MgO the transition extended to below 55 K, below which point readings were not recorded. No susceptibility transition was observed for the film on Pd_2Si/MgO. The weak link behaviour of the YBCO films

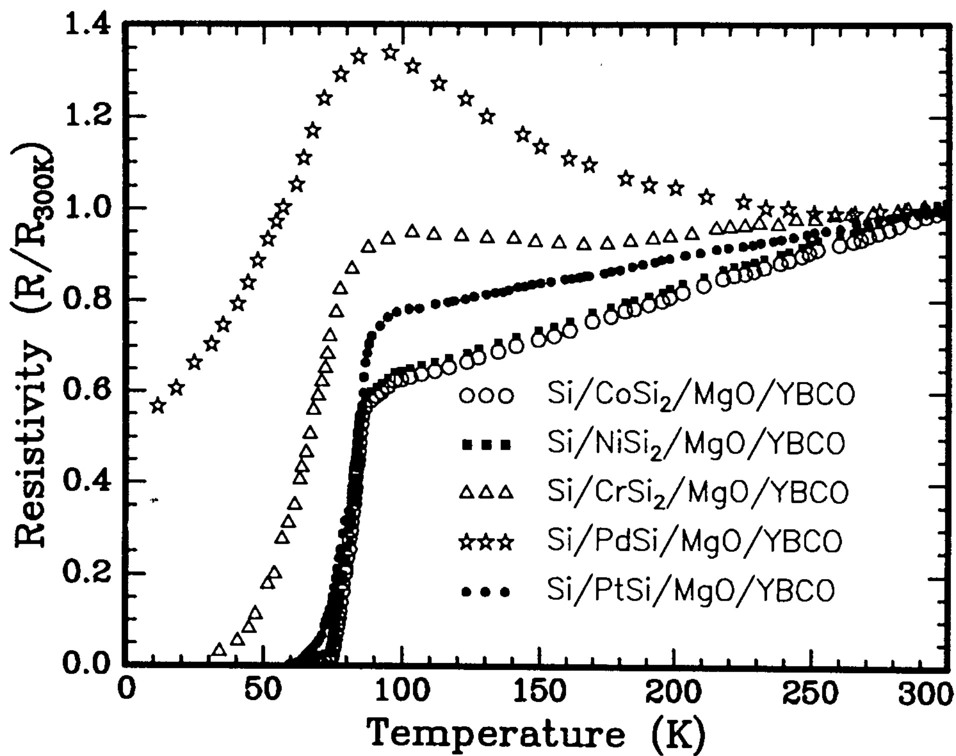

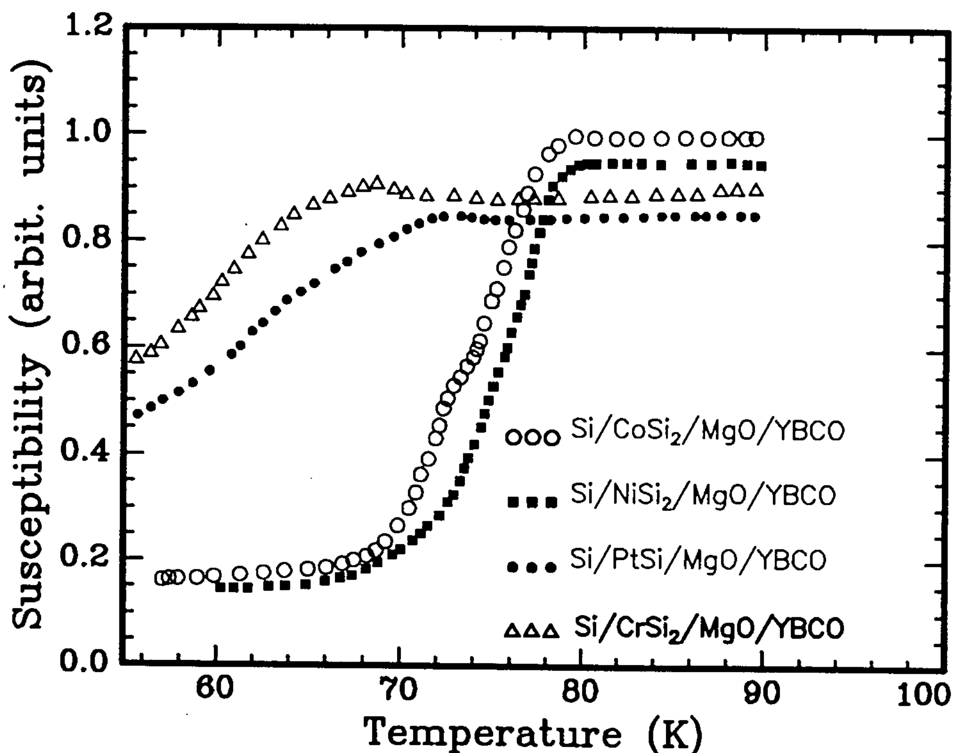

FIGURE 5.11: (a) Resisitivity and (b) susceptibility data for the thin films of $Y_1Ba_2Cu_3O_7$ grown on silicides with MgO buffer layers. The varying electrical behaviour arises from the crystalline state of the $Y_1Ba_2Cu_3O_7$ film and its reaction with the buffer.

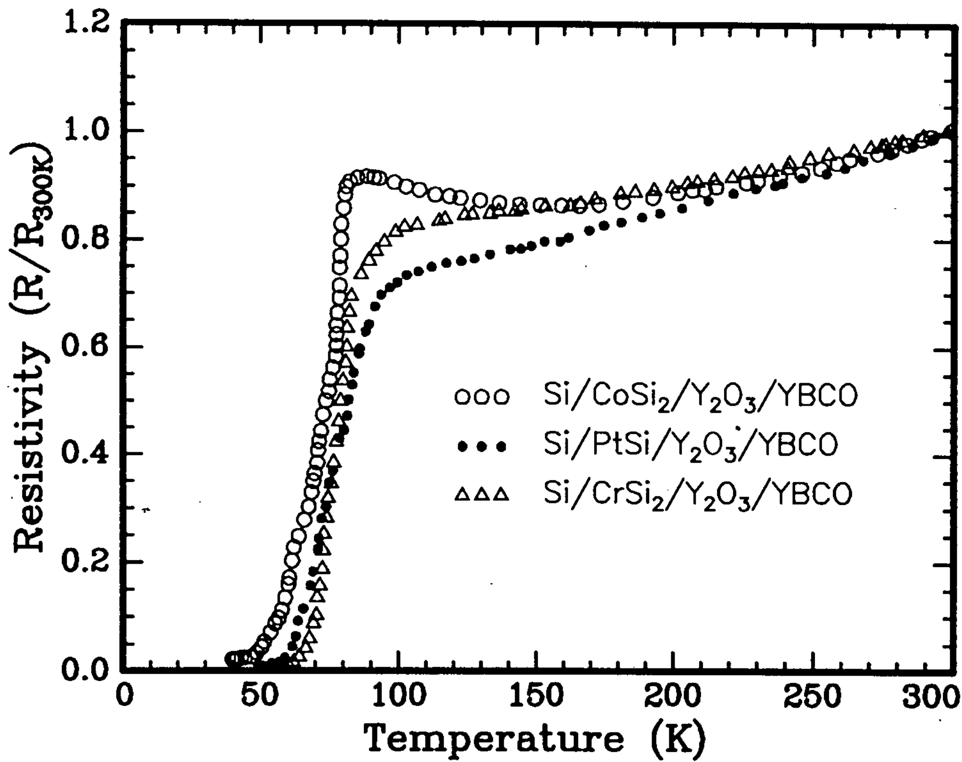

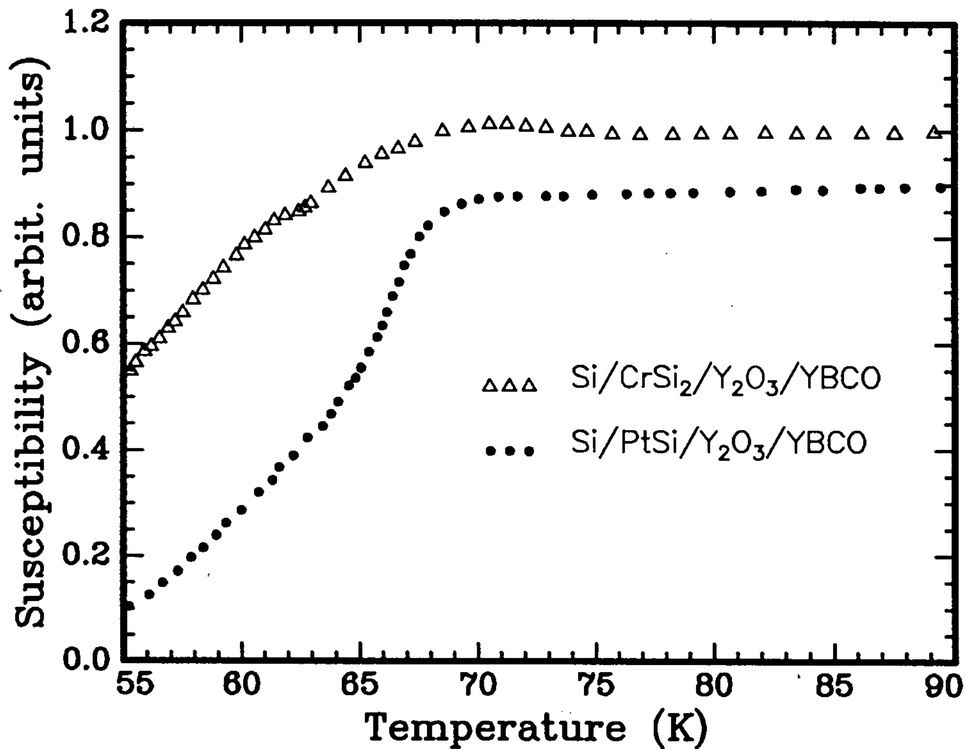

FIGURE 5.12: (a) Resisitivity and (b) Susceptibility data for the thin films of $Y_1Ba_2Cu_3O_7$ grown on silicides with Y_2O_3 buffer layers. Not all the YBCO films on Y_2O_3 were superconducting, illustrating that the YBCO-Y_2O_3 interaction seen with RBS has destroyed the superconductivity.

on silicon-silicide-metal oxide substrates is indicated by the broad transitions to complete field expulsion, implying that different sections of the film become superconducting at different temperatures.

For the silicion-silicide-Y_2O_3 system thin film superconductors on $PtSi/Y_2O_3$ and $CrSi_2/Y_2O_3$ gave the highest transition temperatures and sharpest transition widths (**Fig. 5.12**). The resistive drop from room temperature to T_c was not as sharp as for films on MgO and a poor transition was observed for films on $CoSi_2/Y_2O_3$. No resistive transition was observed for films on $NiSi_2/Y_2O_3$ and Pd_2Si/Y_2O_3 which can be attributed to the YBCO-Y_2O_3 reaction seen in the RBS spectra. The A.C. susceptibility measurements gave depressed transition temperatures and broad transition widths.

For ZrO_2 buffer layers, YBCO films on $CrSi_2/ZrO_2$ and $PtSi/ZrO_2$ films were the poorest, the best resistivity results being obtained on $CoSi_2/ZrO_2$ (**Fig. 5.13**). The reaction of Ba with ZrO_2 to form $BaZrO_3$ as seen by the RBS spectrum is expected to deteriorate the YBCO film quality and is the reason behind the relatively poor film quality on $CrSi_2/ZrO_2$, $NiSi_2/ZrO_2$ and Pd_2Si/ZrO_2. The best susceptibility results were found for YBCO deposited on $CoSi_2/ZrO_2$. **Table 5.1** summarizes the electrical behaviour of thin film YBCO superconductors on silicides with oxide buffer layers. From the table it is clear that the best results were obtained with MgO buffer layers and ZrO_2 also performs well as a buffer layer, showing that the ZrO_2 - YBCO interaction observed in the RBS spectra is limited to the interface and does not degrade the electrical properties severely, although preventing this reaction should improve the YBCO film quality. The Y_2O_3 layer was the poorest buffer layer as seen from the electrical measurements. In terms of the silicides, $CoSi_2$, $NiSi_2$ and PtSi gave the best results. The growth of single crystal buffer layers will not only improve the electrical properties of the YBCO layer by providing a template for epitaxial growth, but will also reduce the possibility that elements of the silicide will diffuse along the grain boundaries of the buffer layer and contaminate the YBCO layer.

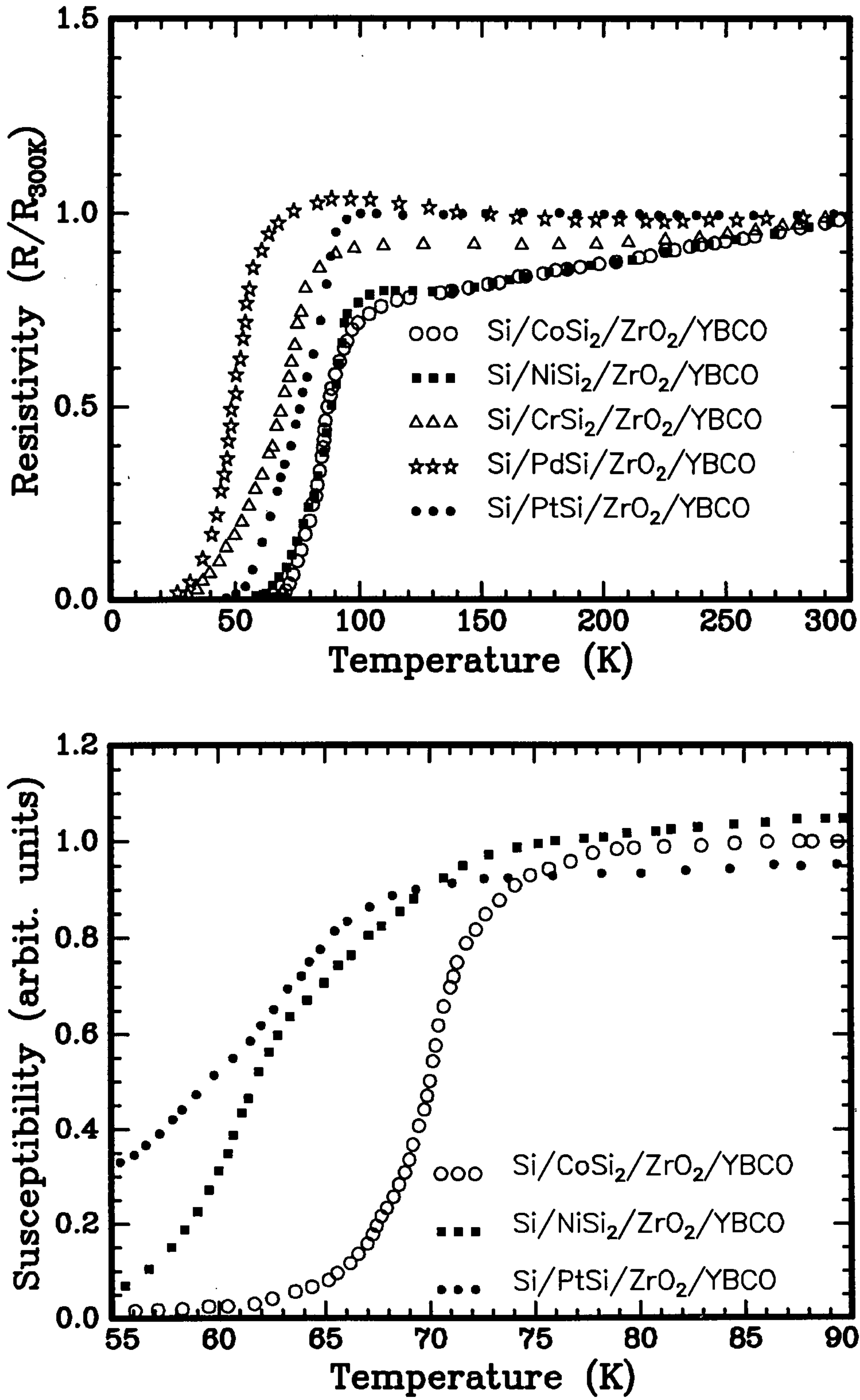

FIGURE 5.13: (a) Resisitivity and (b) Susceptibility data for the thin films of $Y_1Ba_2Cu_3O_7$ grown on silicides with ZrO_2 buffer layers.

TABLE 5.1: Electrical properties of thin film $Y_1Ba_2Cu_3O_7$ superconductors on silicides with MgO, Y_2O_3 and ZrO_2 buffer layers. The absence of a superconducting transition is denoted by a dash (–).

Buffer	Silicide	Resistivity		Susceptiblity	
		T_c(K)	ΔT(K)	T_c(K)	ΔT(K)
MgO	$CoSi_2$	81	4	78	9
	$NiSi_2$	81	4	79	10
	$CrSi_2$	75	19	68	>13
	Pd_2Si	76	>70	–	–
	PtSi	79	4	71	>16
Y_2O_3	$CoSi_2$	70	17	–	–
	$NiSi_2$	–	–	–	–
	$CrSi_2$	75	8	65	>>15
	Pd_2Si	–	–	–	–
	PtSi	76	15	68	>10
ZrO_2	$CoSi_2$	80	4	72	11
	$NiSi_2$	79	7	65	12
	$CrSi_2$	73	13	–	–
	Pd_2Si	60	11	–	–
	PtSi	79	18	63	>>15

5.4 Formation via amorphous CoZr alloys

The Co-Zr multilayer system is an interesting demonstration of the formation of a silicide/oxide bilayer structure grown simultaneously from an amorphous CoZr alloy. The formation of the alloy is based on the solid state amorphization reaction in multicomponent metallic systems [**179–181**] in which metallic elements **A** and **B** are reacted with each other at temperatures below the crystallisation temperature of the alloy $\mathbf{A}_x\mathbf{B}_{1-x}$. The realization of amorphous inter-metallic materials has many potential application for microelectronics [**182–184**]. Recent advances in the use of alloys include the work by Rozgonyi et al. [**183**], where an ultra thin $NiSi_2$ layer was formed by NiCr/Si interaction through a segregated semi-permeable amorphous Cr-rich membrane. Dass et al. [**184**] reported the growth of a $CoSi_2$ epitaxial layer covered by TiN on Si(100) by annealing a layered Si/Ti/Co structure in N_2 ambient

[184]. Hong et al. [182] formed epitaxial cobalt disilicide through solid state interaction in a multilayered Si/Ti/Co/Ti/Co/Ti/Co system. The simultaneous formation of an epitaxial $NiSi_2$ layer and a capping ZrO_2 layer formed by annealing an amorphous NiZr layer in O_2 was reported by de Reus et al. [168]. In our investigation the concurrent formation of an epitaxial $CoSi_2$ layer on Si(111) and a polycrystalline ZrO_2 capping layer from an amorphous CoZr alloy is reported. The starting structure was a multilayer Si(111)/Zr/Co/Zr system. Amorphous CoZr alloys have been extensively studied because their soft magnetic properties are desirable in the fabrication of thin film recording heads [185–189].

5.4.1 Formation of Si/$CoSi_2$/ZrO_2 structures

Sequential evaporation of Zr/Co/Zr was done in a vacuum of 10^{-6} - 10^{-7} Torr. The thickness of the films on the Si substrate in the sequence Si/Zr/Co/Zr was 8 nm/15 nm/15 nm respectively. The substrate was held at room temperature to avoid any reaction during the evaporation. After deposition was completed the uppermost Zr layer was oxidized by annealing in-situ at 100°C in a 10^{-4} Torr oxygen flow for 1 hour. Oxidation of the uppermost layer has several purposes. de Reus [168] has shown that oxidation of underlying layers is prevented by an oxidized Zr capping layer. It is believed that the capping ZrO_2 layer prevents oxidation of Co in the α-CoZr layer, which would hamper the formation of $CoSi_2$ at relatively low temperature [190]. The reaction of Co with the Zr in the upper layer, at low temperatures, is prevented by the rapid oxidation of the Zr and the inertness of the ZrO_2 layer formed. In addition, Zr can diffuse into the ZrO_2 layer at high temperatures when segregation of the α-CoZr alloy occurs, the ZrO_2 capping layer thereby acting as a sink for the mobile Zr.

The second step in forming the $CoSi_2$-ZrO_2 bilayer structure is the intermixing of the underlying Co and Zr layers to form an amorphous CoZr alloy. The solid state amorphization reaction follows the route taken by Samwer [181] in which the metallic layers were annealed at a temperature below their crystallization temperature ($\approx$400°C) for a long period (24-36 hours). The reaction temperature for

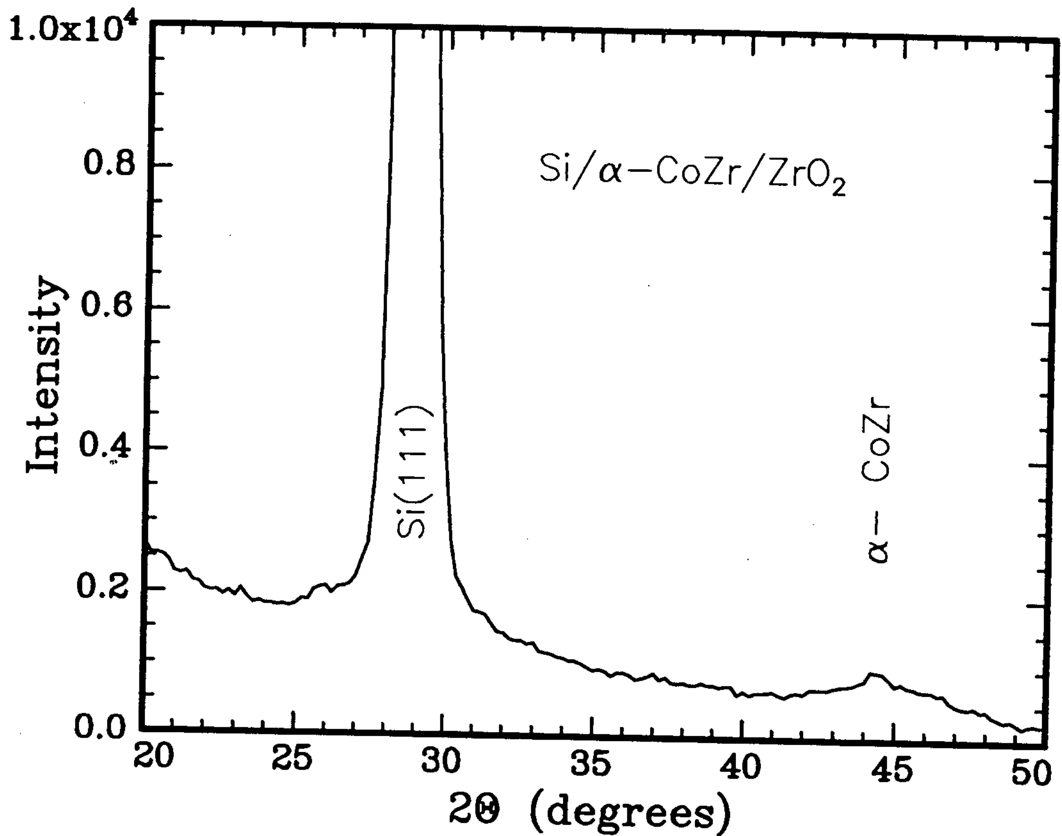

FIGURE 5.14: XRD spectrum for the amorphous CoZr alloy. The broad maxima at 2θ ≈45° denotes the amorphous alloy. The large peak at 28° is the reflection from the Si<111> substrate.

amorphisation was 280°C and the intermixing was carried out in-situ for a reaction time of 24 hrs. Higher reaction temperatures are more likely to form a crystalline CoZr phase at an early stage. The reasons for using an amorphous CoZr alloy rather than crystallline CoZr will be explained later. The diffusion of some oxygen into the α-CoZr alloy (from or through the ZrO_2 layer) does not hamper the formation of the amorphous alloy and may even be beneficial to amorphisation as it has been reported that the amorphisation process is retarded in ultra-high vacuum deposition ($\ll 10^{-11}$ Torr) [191] and the presence of impurities (such as O_2) is expected to enhance the amorphisation. XRD analysis of the annealed structure revealed a small broad hump at $2\theta \approx 45°$ which is evidence of the formation of an amorphous

Co-Zr mixture (**Fig. 5.14**). Simulation of the experimentally determined RBS spectrum with RUMP gives the nominal Co:Zr ratio as 60:40. Longer annealing times (up to 36 hrs.) did not influence the reaction composition significantly. In accordance with the results from Ni-Hf bi-layers [**192**] and the work by Samwer on Co-Zr alloys [**181**], the crystalline Co starting layer diffuses more rapidly than the Zr in forming an alloy (i.e. Co diffuses into Zr). This means that of the two crystalline starting layers (Co and Zr), the Co layer is depleted quickest. Hence the amorphous CoZr alloy is very Co rich. This contrasts with the $Co_{45}Zr_{55}$ composition found by Schroder [**193**]. However, the composition of the amorphous layer is expected to be dependant on the preparation conditions of the crystalline starting layers, the amount of material available for alloying and the time and temperature of amorphisation. The diffusion of Co into crystalline Zr is known to be extremely fast [**179**] and the amorphisation process is thought to arise from the fast diffusion of the late transition metal (Co) into the crystalline reaction partner (Zr). The basis of the formation of the amorphous alloy rather than the crystalline phase is the asymmetric mobilities of the two reactants, and has been demonstrated in marker experiments and electrical conductance measurements [**181, 192–194**] where, for example, it was found that in the formation of α-NiZr from bi-layers of Ni and Zr only Ni was the mobile species. Annealing at higher temperatures enhances the mobility of both species and leads to crystallisation.

Subsequent annealing of the Si<111>/α-$Co_{60}Zr_{40}/ZrO_2$ structure at 650°C , either in vacuum or in O_2, results in the simultaneous bi-layer formation of an aligned $CoSi_2$ layer and a thicker capping Zr-oxide layer. In the case of oxygen annealing the Zr-oxide layer has the composition ZrO_2, while vacuum annealing prevents the formation of the dioxide and the capping layer will be of the form ZrO_{2-x}, where x is some small number. The RBS spectrum of the CoZr alloy and the formation of a $CoSi_2$-ZrO_{2-x} bi-layer upon vacuum annealing is shown in **Fig. 5.15**. The movement of cobalt towards the silicon substrate is denoted by the movement of the Co-signal to lower backscattering energies in the RBS spectrum. The increase in height of the Zr signal is due to the increased Zr-content on the surface layer

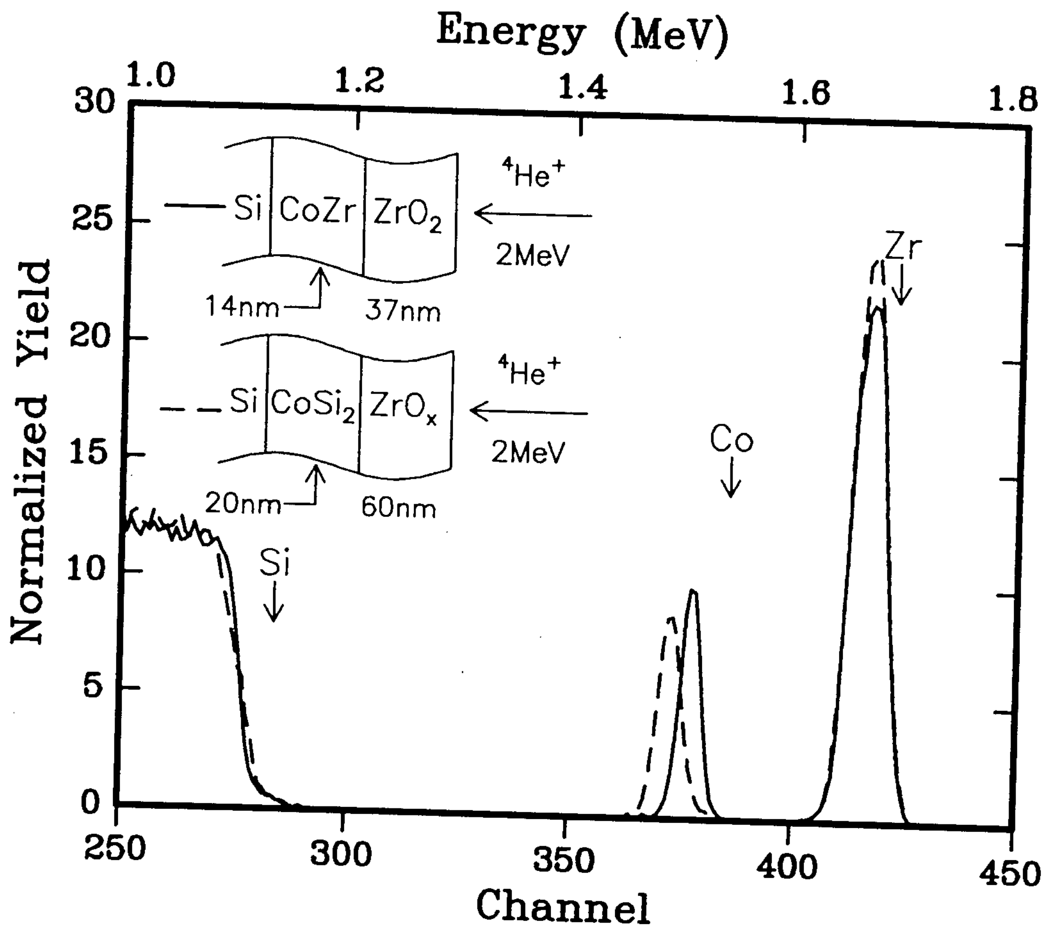

FIGURE 5.15: RBS spectra for the α-CoZr alloy and the bi-layer formed after annealing the alloy at 650°C in vacuum. The movement of Co to lower backscattering energies is due to diffusion of Co into Si to form $CoSi_2$. This is confirmed by the change in shape of the Si interface signal. The Zr peak height increases because of increased Zr content in the ZrO_2 layer due to the segregation of the alloy and the increased signal height of Zr in ZrO_2 than in CoZr.

caused by the separation of the α-CoZr layer (no extra O_2 is available to react with the Zr from the alloy but it can share the oxygen already in the ZrO_2 layer). Post-oxidation of the vacuum annealed films results in complete oxidation of the capping layer to form ZrO_2. The change in shape in the silicon surface signal results from the formation of $CoSi_2$. The formation of a $CoSi_2$(111) layer could not be determined with XRD due to the overlap of the $CoSi_2$ (111) peak with the large Si(111) peak from the substrate, but the disappearance of the broad maxima at ≈45° denotes the

break-up and segregation of the α-CoZr layer. Ion beam channeling along the (111) direction of the Si substrate confirmed that the Co is present in the form of epitaxial $CoSi_2$ (**Fig. 5.16**). The drop in yield of the Co-signal implied a channeling yield of 30-40%. The actual crystallinity of the $CoSi_2$ layer is better than was observed as dechanneling of the α-particle beam by the thick ZrO_2 layer above the $CoSi_2$ causes spreading of the incident beam which will increase the minimum yield values in the $CoSi_2$ layer. The effects of the oxidation anneal and the diffusion of Co and Zr on the crystallisation of the CoZr alloy is beyond the scope of theis investigation. Since the annealing temperature is above the crystallisation temperature (400°C) it is expected that some crystallisation will occur.

It was found that below 650°C , no detectable reaction occurs, which leads one to speculate that a Zr-oxide layer exists on the surface of the Si substrate. The Zr-oxide could arise from the reduction of the native oxide layer (SiO_2) by Zr. Matthee et al. [**129**] have found that Zr cleans up the SiO_2 layer to form a Zr-oxide. It is thus postulated that the 650°C anneal is required to break through the thin surface oxide layer. This means that ultra-clean surfaces (such as is attainable in vacuums of better than 10^{-10} Torr) might result in even lower temperature formation of epitaxial $CoSi_2$. de Reus [**167**] has also shown that with an amorphous NiZr alloy on Si(111), no reaction occurs until a temperature of 600°C is reached, whereas the use of an amorphous Si layer on the Si(111) substrate lowers the reaction temperature to 350°C . Tung [**195, 196**] has shown that epitaxial $CoSi_2$ on silicon will form at low temperatures if a sequential deposition and annealing of Co monolayers was achieved. In this study the Co from the amorphous alloy can form a silicide layer before the Zr can, due to the higher mobility of Co as compared to Zr in the α-CoZr alloy. The presence of oxygen in the CoZr alloy could also possibly prevent the Zr from reacting with Si at low temperatures. At higher temperatures a mixture of Co and Zr silicides may be expected because of the increased mobility of Zr and Si. For the $CoSi_2$-ZrO_2 formed by annealing in O_2 no interaction between the silicide and the metal oxide overlayer was observed for annealing temperatures up to 850°C . This is in accordance with the results of section 5.2 where ZrO_2 was

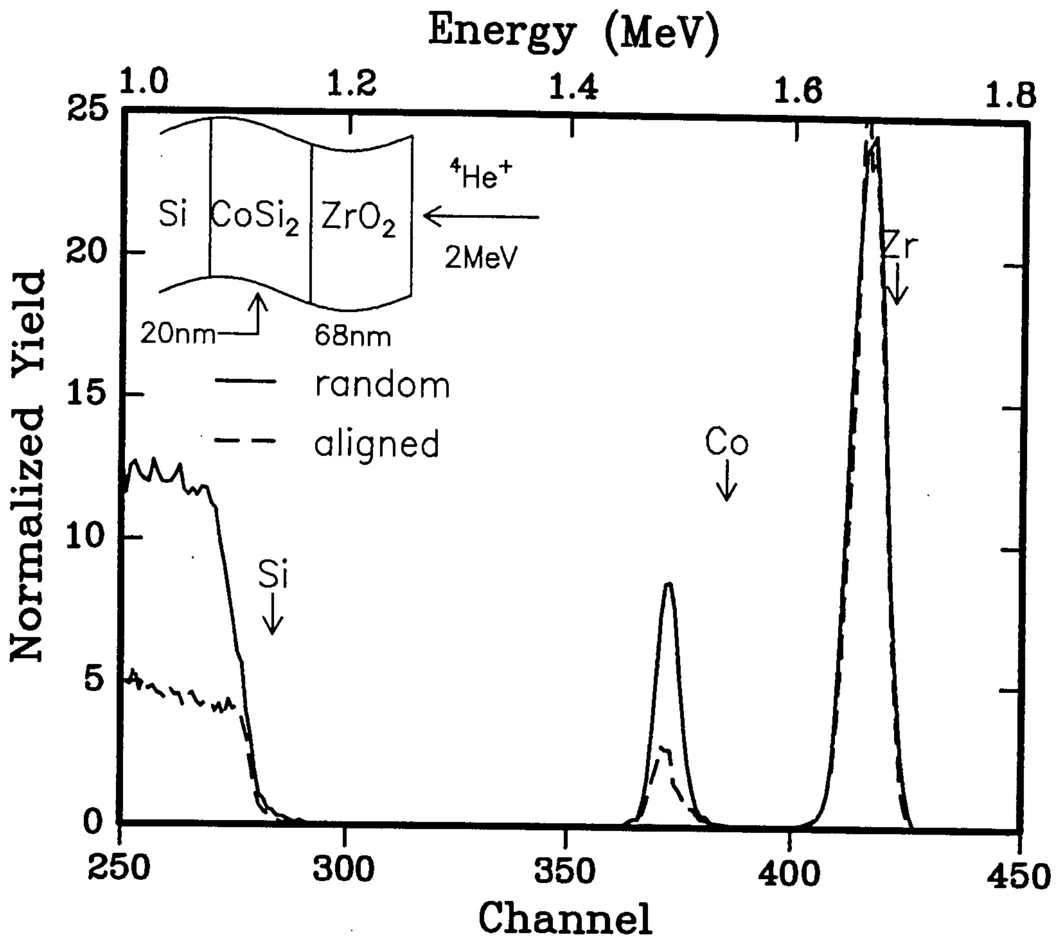

FIGURE 5.16: RBS spectra of the Si/$CoSi_2$-ZrO_2 structure formed from the α-CoZr alloy. The spectra were taken for a random backscattering direction and in the (111) channeling direction of the Si substrate. The reduced yield in the Co signal depicts the channeling in the $CoSi_2$ layer. In view of the dechanneling of the incident beam by the capping ZrO_2 layer, it is expected that the true channeling yield of the $CoSi_2$ layer is lower than that shown.

stable on $CoSi_2$ for annealing temperatures of 850°C in O_2. However, if the bi-layer formation is brought about by vacuum annealing the alloy at various temperatures then a reaction occurs at 850°C . Below 850°C the bi-layer formation observed at 650°C occurs. The RBS spectrum (**Fig. 5.17**) shows the presence of mixed silicides at 850°C and silicon is found at the surface. Movement of Co towards the surface is also noted. The formation of mixed silicides and the instability of the bi-layer in vacuum annealing at 850°C is due to the reduced stability of the suboxide ZrO_{2-x}

as compared to ZrO_2 and the increased mobility of both Si and Co. The excess Zr in the capping layer is not completely constrained by the oxygen atoms and can react with the mobile Si to form a silicide (or a silicate). The presence of O_2 during the oxidation annealing stabilises the capping layer by restricting the Zr to form ZrO_2. The use of the ZrO_2 capping layer is validated by the stable separation of the $CoSi_2$ and ZrO_2 layers up to a temperature of 850°C in vacuum annealing. de Reus [168] did not use a ZrO_2 cap and found mixed Ni and Zr silicides at temperatures as low as 650°C during vacuum annealing. This is due to the increased mobility of Si at

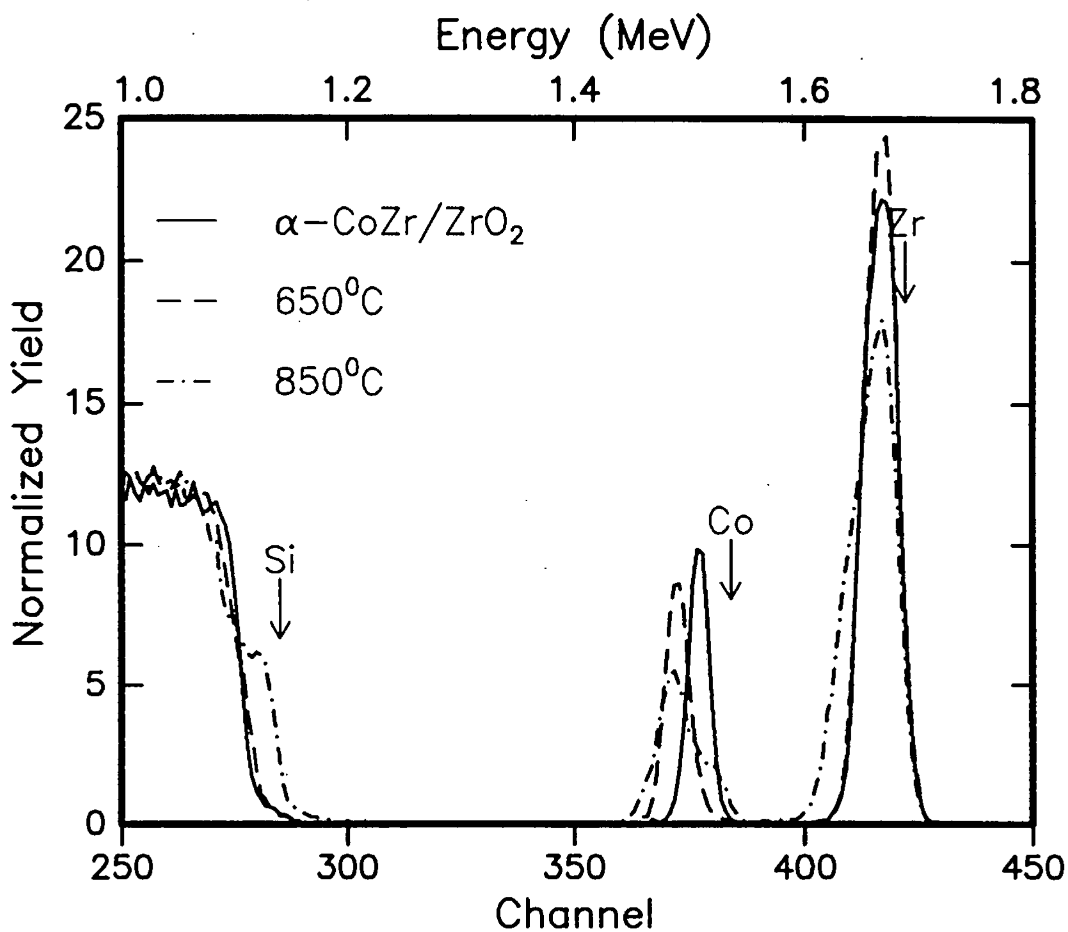

FIGURE 5.17: The formation of mixed silicides from the amorphous Co-Zr alloy occurs upon vacuum annealing at high temperature (850°C) in vacuum. This is due to the increased mobility of Si and Zr at these temperatures. The stability of the bi-layer is maintained if the structure is annealed at the same temperature in O_2. This occurs because ZrO_2 is stable against reaction with Si at 850°C whereas the suboxide ZrO_{2-x} is not.

these temperatures and the absence of an oxidized Zr layer which is stable against reaction with the silicide (see 5.2). The ZrO_2 capping layer also serves as a sink for the Zr and prevents the reaction of Zr with Si in $CoSi_2$ up to 850°C .

5.4.2 YBCO on $Si/CoSi_2/ZrO_2$ formed via a CoZr alloy

Thin films of $Y_1Ba_2Cu_3O_7$ were deposited onto the $CoSi_2$-ZrO_2 bilayer structures (formed as described in section 5.4.1) by ICM deposition at 700°C . The films were smooth and mirror like and RBS analysis demonstrated that no interaction had occurred between YBCO and the substrate and that the ZrO_2 acted as an efficient buffer layer (**Fig. 5.18**). The YBCO film was preferentially c-axis oriented. These results are better than those found for YBCO films grown on $CoSi_2/ZrO_2$ formed by sequential deposition of $CoSi_2$ and ZrO_2 (section 5.2) where some interaction between YBCO and ZrO_2 was observed and the YBCO films on silicide/ZrO_2 structures were not strongly textured. This points to good quality oxide buffer growth in the bi-layer formation from an α-CoZr alloy. Although the ZrO_2 layer is not single crystal (see ion channeling spectra **Fig. 5.16**), it is seems that the slower growth of ZrO_2, by in-situ annealing at low temperature and during the "slow" formation of $CoSi_2$, results in a denser and more stable ZrO_2 layer. The slow growth of a metal-oxide layer was also reported by Takayi [**149**], who showed that an epitaxial metal oxide layer could be grown in this manner. The presence of a smooth ZrO_2 surface, due to the slow growth dynamics, is also imperative for the formation of the c-axis oriented YBCO film and is an additional factor influencing the good quality growth of YBCO films on the $CoSi_2$-ZrO_2 bi-layer structure.

The electrical properties of the YBCO film on the bi-layer (**Fig. 5.19**) verified that the quality of the buffer layer is a crucial factor in determining the film quality. The film was superconducting at high T_c (81 K), had a relatively sharp transition width (3K) and the drop in resistivity in the normal state was sharp. A.C. susceptibility measurements confirmed the good transition temperature assessed by the resistivity method, although a slightly broadened transition width was observed. The multistep transition to complete field expulsion points to a weak-link granular

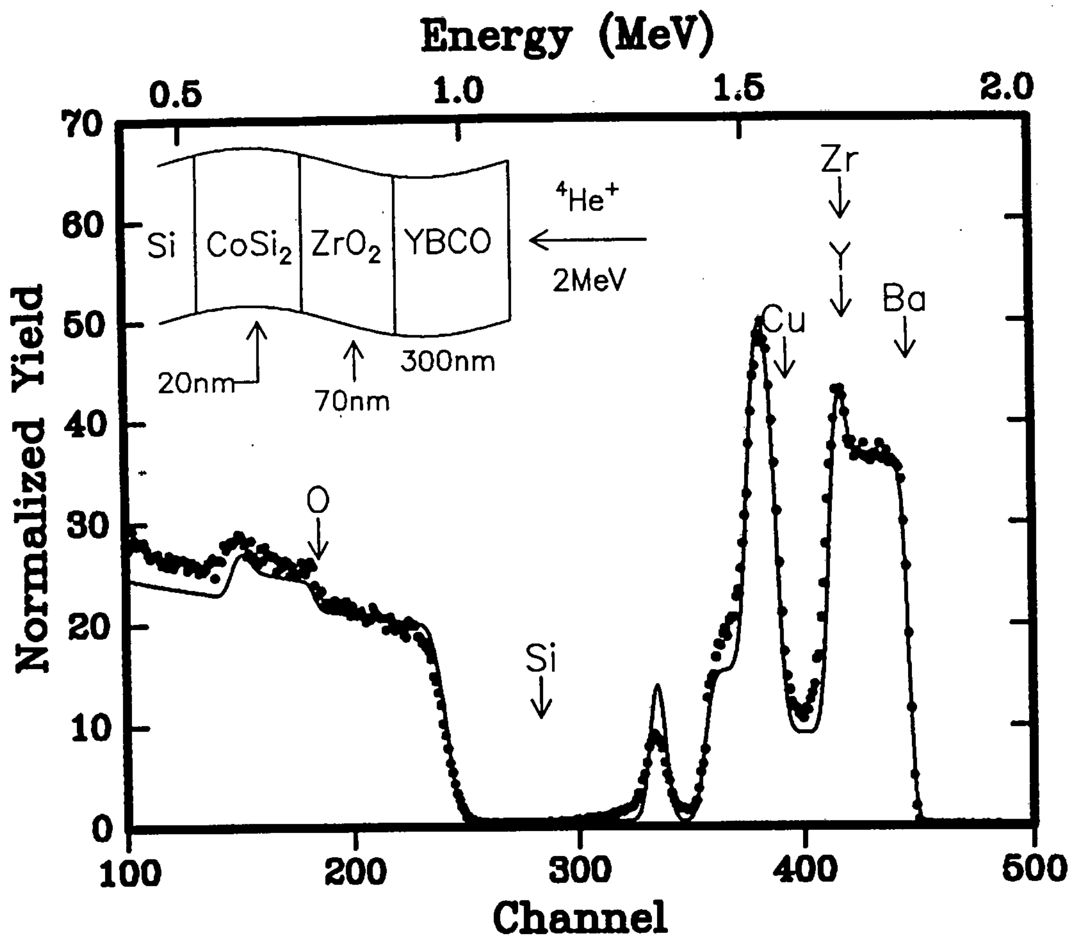

FIGURE 5.18: RBS spectra for a YBCO film grown on the $CoSi_2$-ZrO_2 bi-layer by ICM sputter deposition at 700°C . The bi-layer is formed by annealing an amorphous CoZr alloy at 650°C in O_2. No interaction between YBCO and the silicide or the oxide layer is observed. The solid line is a RUMP simulation.

structure.

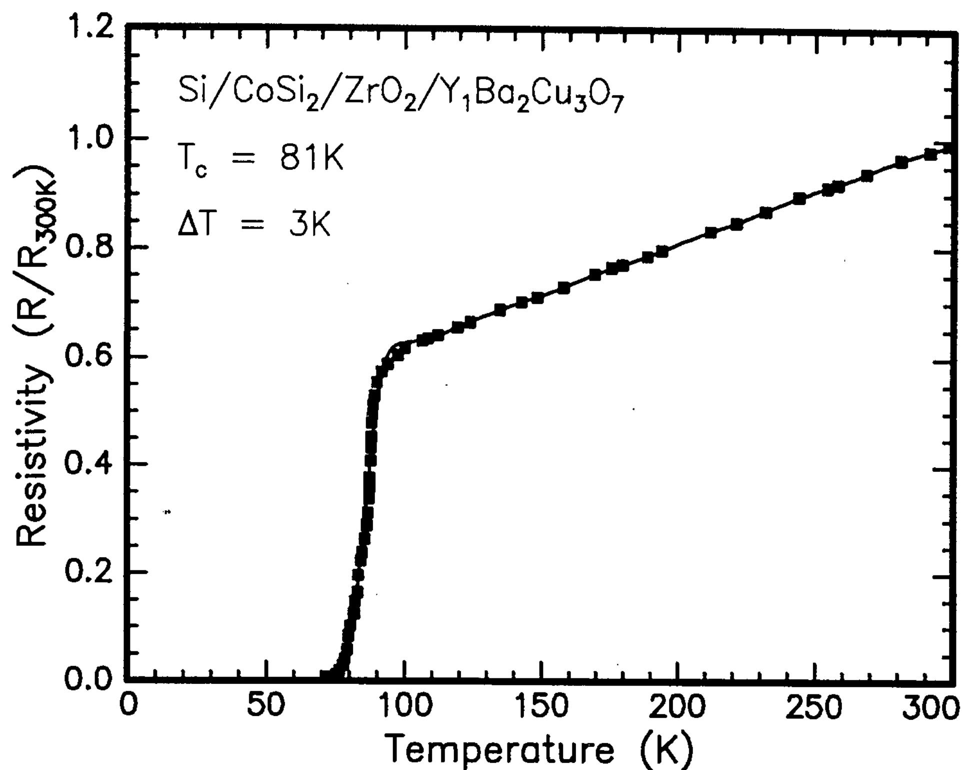

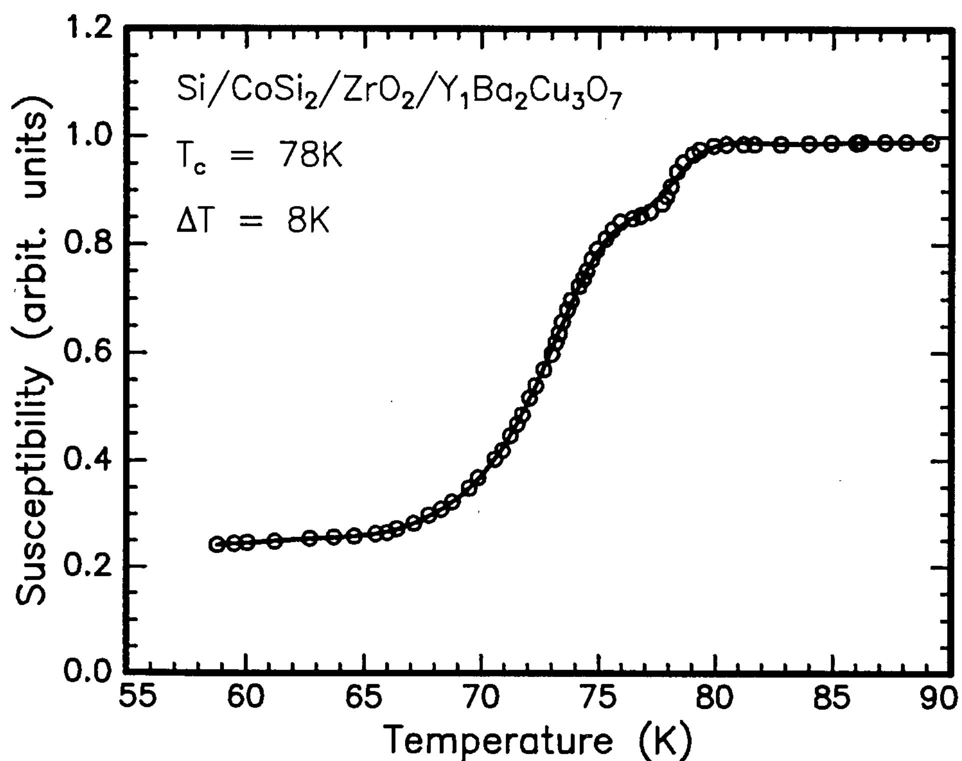

FIGURE 5.19: (a) Resisitivity and (b) Susceptibility data for the thin films of $Y_1Ba_2Cu_3O_7$ grown on the $CoSi_2$-ZrO_2 bi-layer. The resistive drop in the normal state is gradual while and the transition width is sharp but the susceptibility measurements indicate that inter-granular weak links in the $Y_1Ba_2Cu_3O_7$ film broaden the susceptibility transition.

5.5 Summary and discussion

The growth of thin film superconductors such as YBCO on silicides forms part of an integrated approach to combining superconductor and semiconductor devices on the same monolithic chip. Metal-silicides have been extensively researched **[152–157]** and are attractive for use as contacts and interconnects on Si devices as a result of the low resistivities and the intimate contact possible with silicon wafers. The growth of semiconductor-silicide-superconductor and semiconductor-silicide-metal oxide- superconductor (SSMOS) structures was investigated. The development of such systems not only have potential applications in 3-D devices and detectors but a consideration of the fundamentals of growth of such multilayers is also important for determining the properties of, for example, the superconducting layer. Using the pulsed laser deposition technique Luo **[158]** and Kumar **[159]** have recently demonstrated that textured thin films of $Y_1Ba_2Cu_3O_7$ could be grown onto Si substrates with $CoSi_2$ buffer layers.

The growth of YBCO films by ICM deposition onto the silicides PtSi, Pd_2Si, $CrSi_2$, $NiSi_2$ and $CoSi_2$ was attempted in Section 5.1. However, it was found that the YBCO layer reacts severely with all of the silicides and superconductivity in the YBCO layer was destroyed. Unlike the case for the deposition of YBCO onto single crystal Si, where some superconducting was observed (albeit poor) no evidence for superconductivity was found for the YBCO films on silicides, demonstrating that the YBCO-silicide interaction is more severe than that of YBCO with single crystal Si. The reaction between YBCO and silicides was explained in terms of the components of YBCO (especially Cu and Ba) reacting with elemental Si.

A possible mechanism for the enhanced reaction between YBCO and silicides was suggested in terms of the increased mobility of the silicon in the silicide as compared to silicon in the single crystal form. This proposed phenomenological model of interaction drew on the work of Frampton **[164]**, who showed that silicides oxidize faster than single crystal Si and at a lower temperature. It is expected that an SiO_2 layer will form on the surface of the silicide. The reaction between YBCO and SiO_2 is known to be similar to that between YBCO and Si and is also

detrimental to the superconducting film. Chaourasia [133] and Tsukamoto [121] showed that an SiO_2 layer forms on the surface of Si during deposition of YBCO and the destruction of the YBCO layer results from the reaction of Ba with SiO_2 to form Ba_2SiO_4. It was proposed that the increased mobility of Si in the silicides means enhanced reactivity and hence the complete loss of superconductivity which was observed for the YBCO film. It is worth noting that even with the successful deposition of textured YBCO films onto $CoSi_2$ [158, 159], a reacted zone was seen between the YBCO film and the $CoSi_2$ layer. Luo [158] postulates that the reacted layer is an SiO_2 layer that shows some reaction with Ba from the YBCO film.

The severe interaction between silicides and YBCO prevented the deposition of YBCO films directly onto silicides and necessitated the use of buffer layers to preserve the film quality of the superconductor and silicide layers. MgO, ZrO_2 and Y_2O_3 buffer layers were used in this study. The oxide buffer layers were analysed by ion beam channeling and found to be polycrystalline. The semiconductor-silicide-metal oxide-superconductor (SSMOS) multilayered structures have not been extensively studied. The complexity of the SSMOS system required that an initial examination of the thermal stability of the semiconductor-silicide-metal oxide subsystem be conducted to assess the suitability of such structures for the deposition of YBCO films. The thermal stability of the subsystem Si/silicide/metal oxide was assessed by annealing the multilayer structures at 700°C and 850°C under flowing O_2 (> 1 atmosphere) for 1hr.

It was found (section 5.2.1) that the Si/silicide/metal oxide structures were stable at the annealing temperature of 700°C for all the metal oxide and silicide layers. This is also the temperature used during ICM sputter deposition and the thermal stability of these structures validates their use as "substrates" for sputter deposition. At the higher temperature of 850°C interaction between the Y_2O_3 layer and the silicides was observed (to varying degrees). The instability of the Y_2O_3 structure at high temperature was explained in terms of the incomplete fluorite structure which result in vacancies in the lattice [150, 151]. As a result of these vacancies, the mobility of ions in the structure is high at elevated temperatures. The

reactivity of Y_2O_3 at high temperatures corresponds well with the result of Gurvitch [143] where a Y-silicate ($YSiO_4$) was found during high temperature annealing of Y_2O_3 on Si. MgO and ZrO_2 layers showed good stability up to 850°C and no significant deterioration of these layers was observed. This fits in well with the observed thermal stability of MgO [145] and ZrO_2 [134]. The Pd_2Si/Y_2O_3 film showed agglomeration, or balling-up, of the Pd-signal at elevated temperatures but this was not observed with the other oxide buffers.

An evaluation of the suitability of silicides (from those used) from the literature would point to the use of $CoSi_2$ and $NiSi_2$ as the most likely candidates for a silicide-buffer-superconductor structure. $CoSi_2$ and $NiSi_2$ are thermally stable at high temperatures [160, 173, 174] and have excellent electrical transport properties with low resistivity values [197]. In addition they have small lattice mismatch with single crystal Si and have been epitaxially grown on Si<111> [198] and Si<100> [199, 200]. These features have led to these silicides becoming leading candidates for the next generation of materials to be used as contacts, gates and interconnects in very large scale integration and vertical integration technologies [153].

In a comparison of the thermal stability of silicon/silicide/metal oxide structures of MgO, ZrO_2 and Y_2O_3 on $NiSi_2$, $CoSi_2$, $CrSi_2$, PtSi and Pd_2Si this study shows that MgO and ZrO_2 are the most stable buffer layers. Of the silicides used $CoSi_2$, PtSi and $NiSi_2$ were the most stable, with poor results for Pd_2Si and $CrSi_2$ showing intermediate behaviour.

Section 5.3 describes the results obtained for the growth of YBCO films on the silicon/silicide/metal oxide structures by ICM sputter deposition at 700°C . For MgO buffer layers, the best YBCO films were grown on $CoSi_2$/MgO, $NiSi_2$/MgO and PtSi/MgO. The RBS spectra for these systems and YBCO showed little interaction between the YBCO film and the buffer and X-ray diffraction results gave preferential c-axis orientation for these films. The RBS spectra of $CrSi_2$/MgO/YBCO and Pd_2Si/MgO/YBCO showed reaction of YBCO with the MgO layer. Although these films demonstrated some c-axis orientation, the polycrystalline nature of the film was evident from the presence of peaks from other orientations of YBCO. The growth

of highly textured YBCO films on polycrystalline buffer layers was attributed to the anisotropic growth of YBCO, where the a-b plane grows an order of magnitude faster than the c-axis direction. These results agree with those of Norton **[139]** where it was found that the anistropy of the growth kinetics can result in c-axis oriented films on randomly oriented polycrystalline substrates.

Y_2O_3 buffer layers were successful in preventing large scale reaction between the YBCO film and the silicides but a reaction between the YBCO layer and the buffer was observed for the $NiSi_2/Y_2O_3$/YBCO and Pd_2Si/Y_2O_3/YBCO systems. X-ray diffraction analysis showed that the YBCO films on silicide /Y_2O_3 structures were polycrystalline and the intensity of the c-axis peaks were not as strong as for film on MgO buffer layers. The poor preferential orientation was attributed to the reaction between YBCO and Y_2O_3 and to the possible diffusion of oxygen through the Y_2O_3 layer which arises from the vacancy structure of Y_2O_3. Similarly on ZrO_2 buffered structures, the buffer layer prevented the YBCO film from reacting with the underlying silicide, but some reaction between the YBCO film and the ZrO_2 buffer layer was observed for the $CrSi_2/ZrO_2$/YBCO and Pd_2Si/ZrO_2/YBCO structures. The YBCO films were polycrystalline on all silicides, with varying degrees of c-axis orientation noted. The strongest c-axis texturing was seen on the $NiSi_2/ZrO_2$/YBCO structure. It appears as if the c-axis orientation will grow if there is minimal reaction at the buffer-YBCO interface.

The electrical properties of the YBCO films were measured by 4-pt probe resistivity and A.C. susceptibility measurements. A summary of the transition temperatures and transition widths is contained in **Table 5.1**. In terms of the electrical measurements, Y_2O_3 performed worst as a buffer layer and not all the samples with Y_2O_3 buffer layers displayed superconductivity. It is assumed that this arises from the reaction of YBCO and Y_2O_3 seen in the RBS spectra and the low level of prefered texture. Also, those systems that do superconduct (with Y_2O_3 buffer) had depressed transition temperatures and broadened transition widths. A complete field expulsion state, in which the magnetic field expulsion attains a constant value, was never achieved in susceptibility measurements of films with Y_2O_3 buffers. The

best results were obtained on MgO buffer layers with intermediate results for ZrO_2 buffer layers. This is reasonable if one considers that ZrO_2 is more likely to react with YBCO than MgO [**105**]. It was thus proved that the reactivity of the buffer layer determines both the extent of preferential orientation of the YBCO films and ultimately the electrical properties of those films.

The work on the use of an amorphous Co-Zr alloy to simultaneously form an epitaxial $CoSi_2$ layer buried beneath a capping ZrO_2 layer is unique to this study and is extremely promising as a method of forming epitaxial silicides at temperatures which are more compatible with device fabrication. Due to the fact that the evaporation system employed for the deposition of thin films is limited to single element evaporation, it was not possible to form the amorphous alloy by co-evaporation of Co and Zr. The co-evaporation route to form the alloy was used by de Reus [**168**] who demonstrated the bi-layer formation of epitaxial $NiSi_2$ and a capping ZrO_2 layer from an amorphous NiZr alloy annealed in O_2. In this study the formation of the alloy is based on the solid state amorphization reaction in multicomponent metallic systems in which the elements Co and Zr are reacted with each other at a temperature below the crystallization temperature of Co-Zr. A schematic of the formation sequence of the bi-layer structure is shown in **Fig. 5.20**.

The starting structure consisted of a layer of Co sandwiched between two Zr layers on a Si(111) substrate [Si(111)/Zr/Co/Zr]. The system was annealed *in- situ* at low temperature in O_2 to oxidise the uppermost Zr film and form a capping ZrO_2 layer. It was shown that the ZrO_2 layer prevents oxidation of the underlying layers [**168**] during the long thermal reaction [24 hrs] to amorphise the underlying layers. Use of the Si/Zr/Co system [no cappping Zr] did not result in mixing of the Zr and Co layers and it was assumed that oxidation of the Co layer [at 280°C for 24 hrs] prevents the mixing. The formation of a Co-oxide at the relatively poor vacuum of 10^{-6}Torr is one of the reasons that the capping ZrO_2 layer is required and oxygen in the Co is expected to hamper the formation of $CoSi_2$ at low temperature [**190**]. The mixing of Co with the upper Zr layer is prevented at low temperatures because of the rapid oxidation of Zr and the relative inertness of ZrO_2. The formation of the

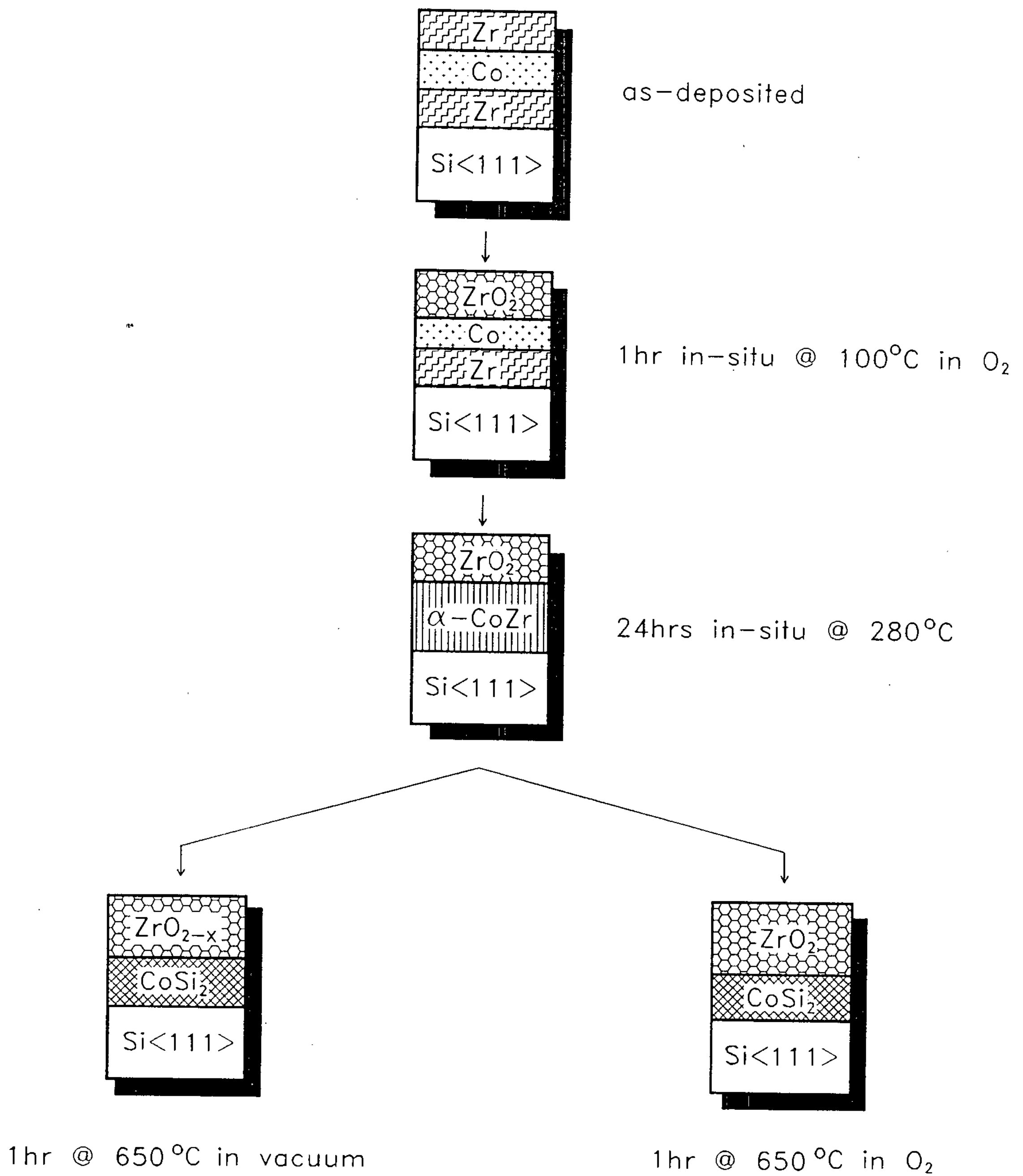

FIGURE 5.20: Schematic illustration of the formation sequence of the Si<111>/$CoSi_2$/ZrO_2 structure from an amorphous Co-Zr alloy. The initial structure was a multilayer sandwich of Zr-Co-Zr.

amorphous Co-Zr underlayer was brought about by annealing the samples *in-situ* at 280°C for 24 hours. The temperature was chosen to be below the crystallization temperature of CoZr (400°C) and also lower than the formation temperature of Zr-silicide. The solid state reaction formation of amorphous alloys is similar to the work done by Schwarz **[179]**, Herd **[180]** and Samwer **[181]**. XRD analysis showed the formation of an amorphous alloy and RBS simulation of the observed spectrum gave a nominal composition of $Co_{60}Zr_{40}$ for the alloy. Annealing the sample (Si/α-CoZr/ZrO_2) either in vacuum or in O_2 at 650°C gave a Si/$CoSi_2$/ZrO_{2-x} structure, where x=0 for annealing in O_2. Ion channeling analysis of the $CoSi_2$ layer shows that it grows with an epitaxial alignment on the Si<111> substrate.

The growth of $CoSi_2$ <111> onto Si<111> at relatively low temperatures in the Si/α-CoZr/ZrO_2 system without the formation of the intermediary silicides Co_2Si and CoSi was considered in terms of the Effective Heat of Formation model **[201–204]**. The EHF model predicts the first phase formation of silicides according to the following rule:

"The first silicide compound to form during metal-silicon interaction is the congruent phase with the most negative effective heat of formation ($\Delta H'$) at the concentration of the liquidus minimum (lowest temperature eutectic) of the binary system." The effective heat of formation is derived from the standard heat of formation ($\Delta H°$) as:

$$\Delta H' = \Delta H^\circ \times \left(\frac{\textit{effective concentration limiting element}}{\textit{compound concentration limiting element}}\right) \qquad (5.1)$$

where $\Delta H°$and $\Delta H'$are expressed in kJ per mole of atoms. The definitions of the effective concentration and compound concentration of the limiting element are given in **[201–204]**.

The effective heat of formation diagram for the Co-Si system is shown together with the binary Co-Si phase diagram in **Fig. 5.21**. From the phase diagram one can deduce that the lowest melting eutectic lies on the metal-rich compound side, and the largest effective heat of formation change is seen for the Co_2Si phase. The model thus predicts the formation of Co_2Si as the first phase and this has been the phase experimentally observed to form first **[206]**. After all the Co has been

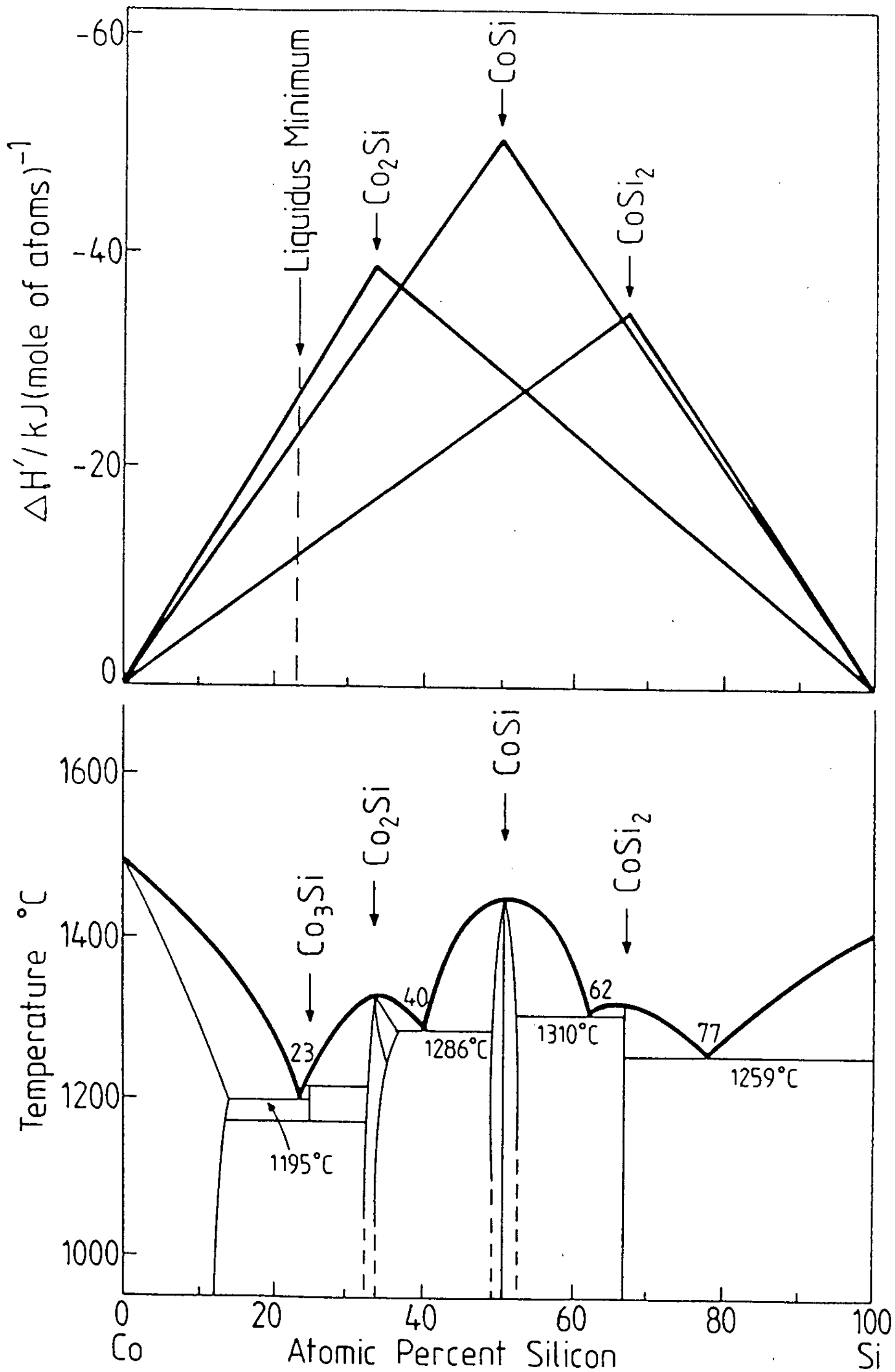

FIGURE 5.21: The effective heat of formation diagram and the binary phase diagram for the Co-Si system [205]. The first phase predicted to form is Co_2Si. Subsequent to the complete reaction of Co to form Co_2Si (Co < Si), the effective concentration moves to the Si-rich side, leading first to the formation of CoSi and then $CoSi_2$. The amorphous CoZr alloy reduces the effective Co-concentration and pushes the first phase formation to the Si-rich side, resulting in the formation of $CoSi_2$.

consumed (Co < Si due to Co thin film on thick Si substrate) for the formation of Co_2Si, the effective concentration moves to the Si-rich side (no more Co to react but Si still available) leading first to CoSi formation and then to $CoSi_2$. Measurements indicate that this is the observed phase sequence [**206–208**]. The Co_2Si and CoSi transform to $CoSi_2$ at temperatures above 500°C [**209–211**]. The direct growth of the $CoSi_2$ phase epitaxially at 650°C from the amorphous Co-Zr alloy is surprising as epitaxial $CoSi_2$ is usually formed at temperatures in excess of 800°C .

In the case of the α-CoZr alloy, formed from a Si<111>/Zr/Co/Zr structure, two aspects are important: firstly the Zr layer on the Si substrate strips off the surface oxide and provides a clean surface for epitaxial growth. The direct contact between the α-CoZr alloy and the Si substrate facilitates epitaxial growth. Secondly, the concentration of Co in the α-CoZr alloy is lower than in elemental Co, thereby reducing the effective concentration of Co available for reaction and it is the slow release of Co from the CoZr alloy to form $CoSi_2$ which pushes the effective concentration towards the silicon rich side, where the EHF model predicts that $CoSi_2$ formation will lead to the largest free energy change. The epitaxy of the $CoSi_2$ layer also arises because of the slow diffusion of Co from the alloy. The diffusion of Co from the alloy into Si causes a diffusion gradient in the alloy and the movement of Co along this diffusion gradient feeds the growth of the epitaxial $CoSi_2$ layer. The diffusion of Co from α-CoZr is retarded with respect to elemental Co diffusion due to the absence of grain boundaries in the amorphous alloy. The slow diffusion of Co through an α-CoZr layer has been confirmed by cross-sectional TEM [**181**]. The diffusion mechanism in the amorphous phase is not fully understood. If the supply of Co is sufficiently slow so that there is enough time for the formation of $CoSi_2$ and its epitaxial alignment with the substrate before the next Co layer is supplied to the interface, then the new $CoSi_2$ layer can also grow epitaxially.

It is believed that the EHF model not only explains the formation of epitaxial $CoSi_2$ from an amorphous Co-Zr alloy but also accounts for the low formation temperature (390°C) of $CoSi_2$ seen for Co layers deposited onto a thin Au layer on Si [**212**]. The model can also be used to explain the results for an amorphous Co-

W alloy [**213**] which gave epitaxial $CoSi_2$ films at low temperautres (600°C) and the formation of a $CoSi_2$ epitaxial layer covered by TiN resulting from annealing a Si/Ti/Co layered structure in N_2 [**184**]. The work of de Reus [**167, 168**] and Rozgonyi [**183**] for the first phase formation of epitaxial $NiSi_2$ layers also fits in well with the model.

It was also demonstrated that annealing the α-CoZr layer at high temperatures (850°C) in vacuum results in the formation of mixed silicides. This was attributed to the increased mobility of both Si and Zr at the high temperatures which can react to form mixed silicides. Interestingly if this anneal (850°C) was conducted in an O_2 flow (> 1atmosphere) the bi-layer structure ($CoSi_2$-ZrO_2) was intact and no mixed silicides were observed. This is attributed to the stability of ZrO_2 against reaction with the $CoSi_2$ layer, which was also demonstrated in Section 5.2. The formation of mixed silicides during vacuum annealing occured as a result of formation of the suboxide ZrO_{2-x}, which is less stable than the fully oxygenated form ZrO_2. The use of the ZrO_2 layer over the Co-Zr alloy is emphasised by the stability of the formation of the $CoSi_2$-ZrO_2 bi-layer up to 850°C for vacuum annealing.

Thin films of YBCO deposited onto the Si/$CoSi_2$/ZrO_2 structures by ICM sputter deposition at 700°C were superconducting as-deposited. RBS analysis denoted the absence of reaction between YBCO and silicide or YBCO and ZrO_2 (Fig 5.17). The films were preferentially c-axis oriented. Electrical measurements gave high T_c values (81 K) for the resistivity readings. A depressed susceptibility measurement of 78 K was found (Fig 5.18) and a broadened transition width observed. Comparing the electrical properties (**Table 5.2**) of the films grown on an Si/$CoSi_2$/ZrO_2

TABLE 5.2: Comparison of electrical properties of thin film $Y_1Ba_2Cu_3O_7$ superconductors on Si/$CoSi_2$/ZrO_2 structures formed sequentially and from an amorphous Co-Zr alloy.

Method	Resistivity		Susceptiblity	
	T_c(K)	ΔT(K)	T_c(K)	ΔT(K)
Sequential	80	4	77	11
Alloy	81	3	78	8

structure formed from an amorphous alloy with those grown on the sequentially formed $Si/CoSi_2/ZrO_2$ structure shows that the electrical measurements are slightly better for formation via the alloy. This is attributed to the "slow" formation of the ZrO_2 layer during the bi-layer formation which is expected to produce a dense film microstructure with a smooth surface.

CHAPTER 6

Pulsed ruby laser ablation of $Y_1Ba_2Cu_3O_7$

In-situ processing of high T_c superconducting thin films has been facilitated by the non-equilibrium nature of the laser deposition process [**14–19**]. The main advantages of the laser ablation method for depositing thin films is the ease with which films of $Y_1Ba_2Cu_3O_7$ can be produced, and the stoichiometry retention properties of the ablation process. In terms of the ease of deposition, all that is required for deposition is a vacuum chamber with a window, a bulk target, a substrate heater, an O_2 supply and a pulsed laser. The intrinsic advantage for the deposition of $Y_1Ba_2Cu_3O_7$ films is the excellent stoichiometry retention in the films, and the external positioning of the laser allows for relatively high oxygen pressures during deposition, which assists in forming the superconducting phase at low substrate temperatures. Although the advantages of this technique have made it popular for the deposition of high T_c superconducting thin films, understanding the nature of the deposition process requires extensive experimentation for a comprehensive picture of laser ablation to be compiled [**42–47**]. The wavelength dependence of the ablation process [**41, 48, 49**] means that as wide a range of wavelengths as possible should be used in order to get a complete understanding of the ablation process. When this study commenced, as far as could be ascertained, no reports

were available on the deposition of thin films of the superconductor $Y_1Ba_2Cu_3O_7$ by a pulsed ruby laser. Modelling of the interaction between the laser pulse and the bulk solid $Y_1Ba_2Cu_3O_7$ target in terms of the one dimensional time dependent heat flow equation is presented. Experimental results in terms of the composition and thickness dependence of the deposited film on the incident pulse energy density are given. The influence of target-substrate separation distance and increasing oxygen pressure during deposition was also investigated and the angular spread of the ablated material is compared with that of conventional thermal evaporation.

6.1 Modelling of heat flow

The dynamics of melting and ablation for the deposition of high T_c YBCO films by pulsed ruby laser ablation and the interaction of the pulsed ruby laser with bulk targets of $Y_1Ba_2Cu_3O_7$ were investigated in terms of a one-dimensional heat conduction equation [**214**] using the program HEATUP [**215**]. The thermal effects of interaction of nanosecond laser beams with semiconductors and metals has been dealt with extensively in the literature [**216,217**], and excellent agreement between the theory and experimental results has been obtained [**217**]. Modelling of the interaction of excimer lasers with $Y_1Ba_2Cu_3O_7$ was reported previously [**218**]. The heat diffusion equation can be written as:

$$\frac{dT}{dt} = \frac{1}{\rho C_p}\left[\frac{d}{dx}\left(\kappa\frac{dT}{dx}\right) + \alpha I(x,t)\right], \tag{6.1}$$

where κ is the thermal conductivity of YBCO ($W.cm^{-1}.K^{-1}$), C_p the specific heat ($J.g^{-1}.K^{-1}$), ρ the mass density ($g.cm^{-3}$), α the absorbtion coefficient for the laser light in YBCO and T the temperature (K). The source term $I(x,t)$ describes the laser power density at a depth x and time t and is governed by the mechanism of laser-solid interaction and the time shape of the laser pulse. The laser pulse is assumed to be Gaussian. The fundamental heat flow equation was solved numerically using the finite element method to estimate the time evolution of temperature, the time change

and the depth of molten layer thickness for different incident laser energy densities. The temperature profile as a function of depth, x, in the sample was also computed. From these calculations inferences can be made as to the threshold incident laser energy density necessary for melting and ablation at the target surface. Details of the numerical simulation have been presented previously **[215]**. The calculated results are compared with experimental results of laser induced melting and ablation to see how well the thermal model can explain the laser interaction with YBCO. One deficiency in the model is that the effect of the heat of vaporization and the energy loss factor due to material removal is not included in the simulation.

In the present simulation a pulsed ruby laser of wavelength $\lambda = 694$ nm and FWHM 30 ns was used to irradiate a bulk $Y_1Ba_2Cu_3O_7$ target (5 mm thick). The ruby laser operates at a frequency of 0.1 Hz and the beam diameter was 6mm. The optical and thermal properties for the YBCO superconductor have been studied by many researchers for ablation by excimer lasers **[14, 37, 41, 48, 219]** and the wavelength dependence of the reflectivity and absorption coefficient allows for assumptions to be made as to these values for interaction of $Y_1Ba_2Cu_3O_7$ with the light from the pulsed ruby laser. The values of the parameters used in this simulation are found in **Table 6.1**. The simulation ignores the enthalpy of the liquid-gas phase transition. The simulation assumes that at the initiation of the laser pulse, time t=0 and the depth x=0 at the surface of the target and the ambient temperature at the surface is 300 K.

Profiles of the temperature distribution in the YBCO target irradiated at 0.2 J cm^{-2} at times of 50 ns, 100 ns, 150 ns and 200 ns after the start of the laser pulse are given in **Fig. 6.1**. The temperature profiles show that the surface of the sample attains a maximum temperature of 1900 K, which is above the melt temperature for YBCO (1500 K) but below the vaporization temperature (2500 K). The pulse width of the laser is only 30 ns, meaning that the evolution of temperature at the longer times is due to thermal conduction of heat into the sample. This is verified by the observation that layers deeper in the sample have higher temperatures at later times. A complete description of the temperature into the sample is provided

TABLE 6.1: Parameters for the simulation of heatflow in the $Y_1Ba_2Cu_3O_7$ target used in the programme HEATUP [218, 219].

Parameter	Symbol	value
Melt temperature	T_m	1573 K
Vaporization temperature	T_{vap}	2500 K
Density	ρ	$5.82\ g.cm^{-3}$
Specific heat	C_p	$0.45\ J\,g^{-1}K^{-1}$
Thermal conductivity	κ	$e^{0.377 log(T+273)-2.32}\ W.cm^{-1}K^{-1}$
Latent heat of fusion	H_m	$300\ J\,g^{-1}$
Reflectivity	R	0.15
Absorption coefficient	α	$1.55 \times 10^5 cm^{-1}$

by a temperature-time profile at different depths of the sample for incident energies of $0.2\,J\,cm^{-2}$ and $0.5\,J\,cm^{-2}$ (**Fig. 6.2**). The surface layer temperature rapidly increases and attains a maximum of 1900 K (for $E=0.2J\,cm^{-2}$) at a time 55 ns after the start of the laser pulse. The surface layer then cools due to energy loss via thermal conduction into the bulk of the sample which acts as a heat sink. The flat ledge at the front and rear of the temperature profiles denote the latent heat of melting and solidification respectively. For the melting stage energy is rapidly absorbed (from the fast laser pulse), whereas in the solidification process heat is released slowly by thermal conduction, hence the asymmetry in the time lengths of the two processes. The energy density of $0.20\,J\,cm^{-2}$ is clearly sufficient to melt the surface of the film ($T>T_{melt} \approx 1500\,K$). The temperature profiles of the underlying layers depend on the thermal conductivity of the material and on the coupling of the laser energy within the absorption depth, α_t^{-1} [**42, 45, 220**]. When the absorption depth of the laser α^{-1} is much smaller than the thermal diffusion distance $(2D\tau)^{\frac{1}{2}}$,

$$\frac{1}{\alpha} \ll (2D\tau)^{\frac{1}{2}}, \tag{6.2}$$

the intense energy of the laser is absorbed within a short distance and the temperature evolution of the interior of the sample depends on the thermal conduction of the heat energy into the sample. On the other hand for long absorption length and where thermal diffusivity does not play any major role e.g. in the ablation of

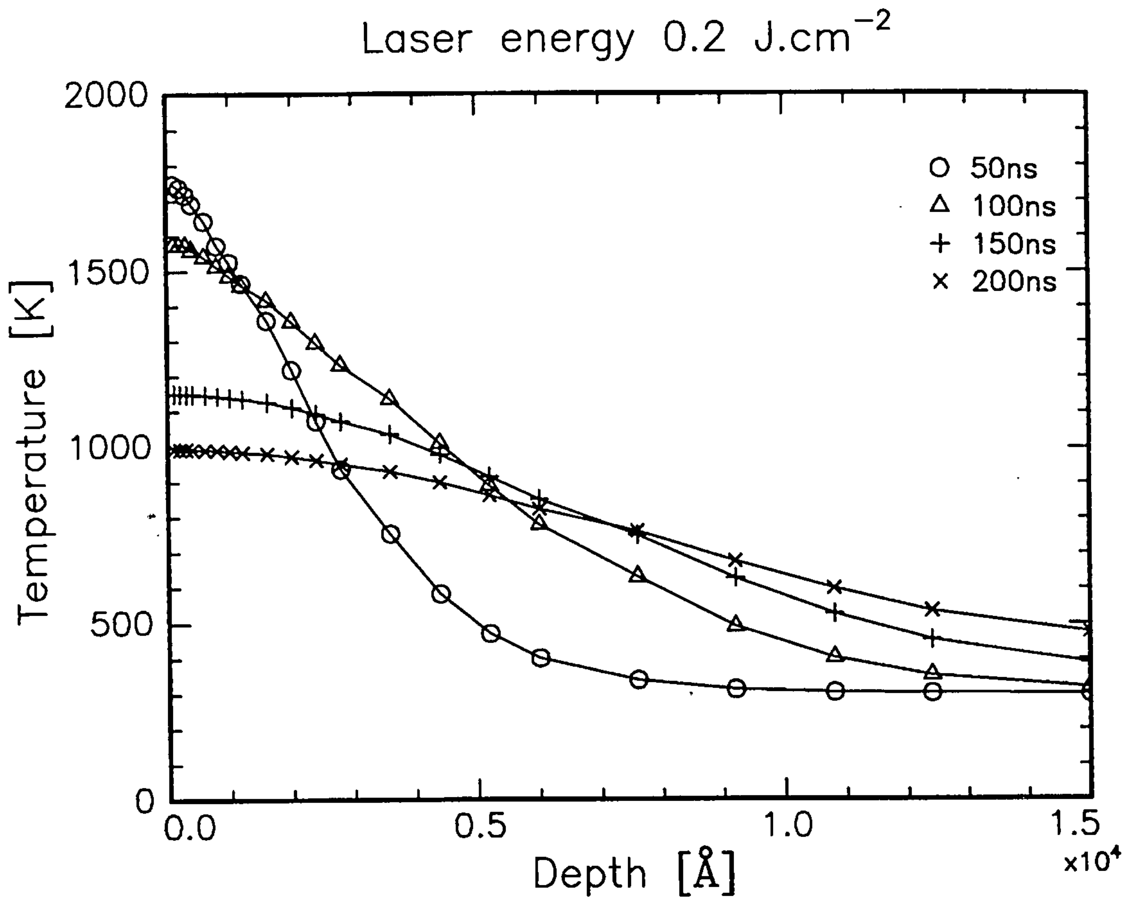

FIGURE 6.1: Simulated temperature profiles in a $Y_1Ba_2Cu_3O_7$ sample irradiated with a pulsed ruby laser at an energy density of 0.2 $J\,cm^{-2}$. The profiles display the temperature in the sample at times of 50 ns, 100 ns, 150 ns and 200 ns after the initiation of the laser pulse. The maximum temperature at the surface at 50 ns was 1750 K. The development of temperature at greater depths and longer times into the sample is due to thermal conduction.

polymides and organics [221–223] then,

$$\frac{1}{\alpha} \gg (2D\tau^{\frac{1}{2}}), \tag{6.3}$$

and the energy deposited into the system and the temperature evolution of the interior of the sample depends primarily on the absorption distance of the laser pulse into the sample and not on heat conduction effects. In this study it is only necessary to consider the situation for $\frac{1}{\alpha} << (2D\tau)^{1/2}$ due to the relatively high absorption coefficient of the ruby laser in YBCO (α>10^5cm^{-1}). From the absorption coefficient the thickness of the layer directly heated by the laser pulse was found to be ≈65 nm. The larger absorption length as compared to that of excimer lasers (50 nm) [14] is

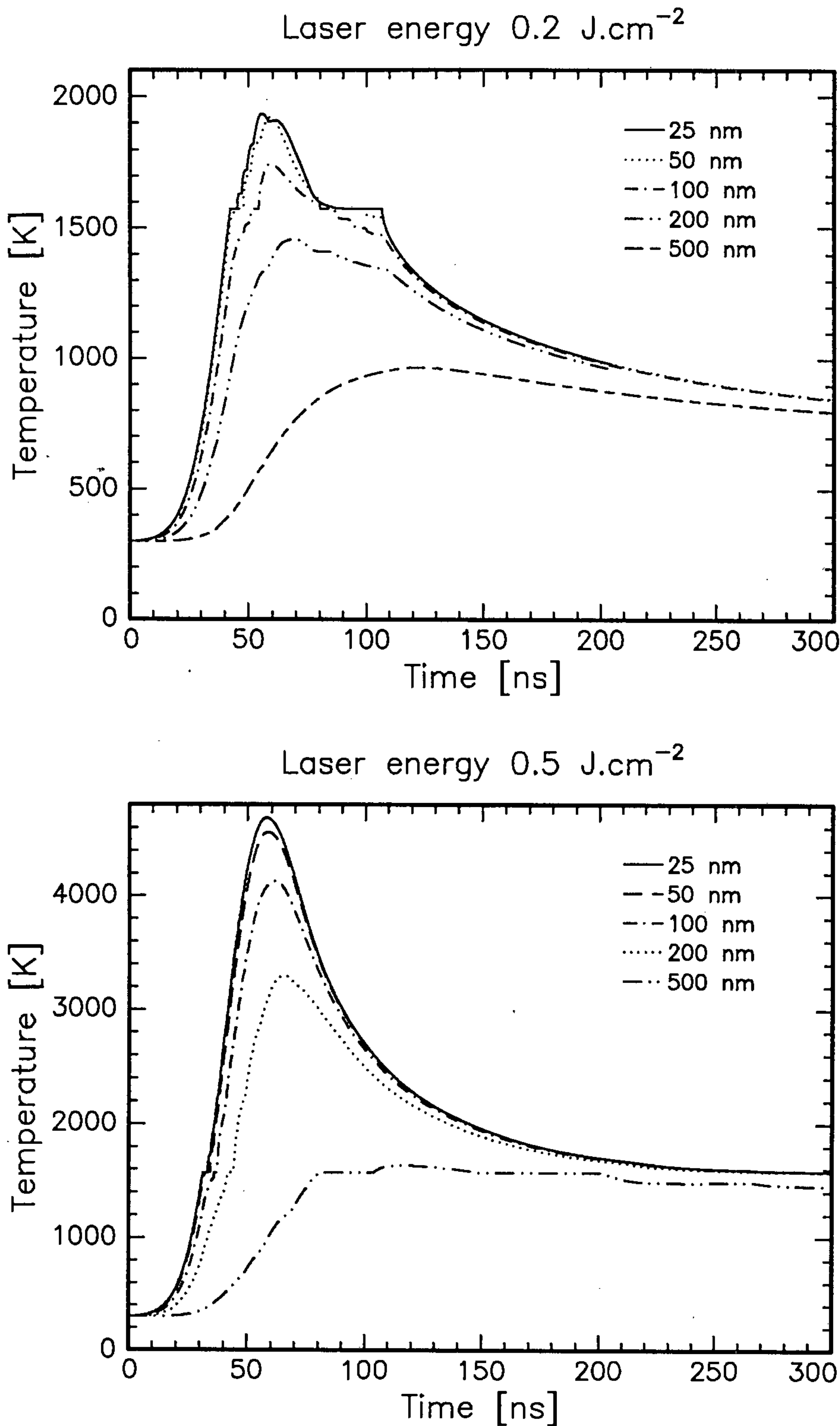

FIGURE 6.2: Simulated temperature development with time in a $Y_1Ba_2Cu_3O_7$ sample irradiated with a pulsed ruby laser at an energy density of $0.2\,J\,cm^{-2}$ and $0.5\,J\,cm^{-2}$. The profiles display the temperature at different depths into the sample. The maximum temperature at the surface layer (25 nm) was 1900 K for a laser flux of $0.2\,J\,cm^{-2}$ and 4900 K for a flux of $0.5\,J\,cm^{-2}$. The surface layer is above the melt temperature of $Y_1Ba_2Cu_3O_7$ for the lower flux and exceeds the vaporisation temperature at $0.5\,J\,cm^{-2}$. The plateau regions ($0.2\,J\,cm^{-2}$) correspond to the melting and solidification points.

due to the wavelength dependence of α. This small absorption length and the fact that relatively high temperatures are seen in the interior of the sample means that the thermal diffusivity plays the major role in the temperature development in the interior of the sample. Therefore the large melt depths that are simulated are pure thermal conduction effects and the melt front has no "memory" of the laser pulse. Layers deeper down in the sample receive heat primarily by thermal conduction and therefore show slow and small increases of temperature with time. Using the temperature-time profiles at different incident energy densities the threshold energy for surface melting was found to be ≈ 0.15 J cm^{-2}.

The surface melt time and how deep this molten layer extends into the sample has possible ramifications for laser patterning, etching and doping of superconductors **[224,225]**. The initiation of melting at prior times, and before the termination of the laser pulse, for higher incident laser energies will be discussed further when one considers the ablation of material. Ignoring the effect of material removal (and the heat of vaporization) on the attentuation of the incident laser energy and the energy absorbed by the ablated layer during vaporization, it is possible to theoretically calculate the melt depths for laser energies above the threshold of melting. **Fig. 6.3** shows the increase of melt depth with laser energy density. It is quite apparent that melting can occur deep into the sample even for a moderate energy density of 1 J cm^{-2} where the melt front propogates 1.2 μm into the target surface.

Using the temperature-time plots it was possible to determine the incident energy for onset of vaporisation by varying the incident laser energy until the surface temperature exceeds the vaporisation temperature ($\approx$2500 K). The minimum energy at which vaporization occurs is achieved when $T > T_{vaporization}$ and is referred to as the threshold energy for vaporization or ablation E_{ab} and is attained at an incident laser energy of ≈ 0.3J cm^{-2}. There is a range of laser fluences for which surface melting occurs without ablation and one is able to determine the depth to which this melting propagates. This effect can be used for laser patterning and producing depth controlled damage in high T_c thin films **[224,225]**. The use of the pulsed ruby laser to create depth controlled damage in high quality thin films is demonstrated

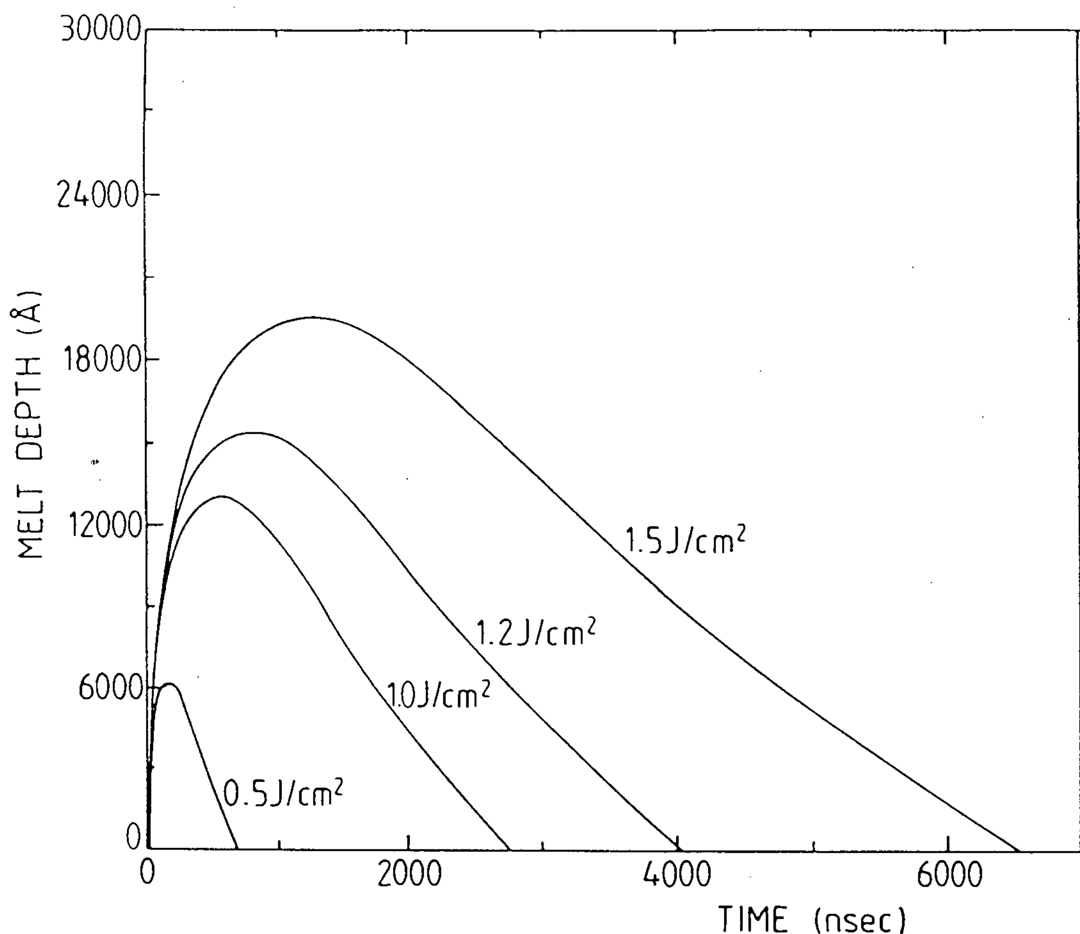

FIGURE 6.3: Evolution of the melt depth profile in a $Y_1Ba_2Cu_3O_7$ sample irradiated with a pulsed ruby laser at energy densities of 0.5, 1, 1.2, and 1.5 $J\,cm^{-2}$. The profiles display the increasing melt depth attained with higher laser energies. The peak of the profile represents the maximum depth of the melt front. The forward slope of the profile gives the average velocity of the melt front and the reverse slope represents the solidification velocity.

in section 6.3.

The variation of surface melt duration with increasing incident laser energy is shown in **Fig. 6.4**. The melt duration here is a measure of how long the "surface" is molten and increases rapidly with increasing energy. The relatively long lifetime of the molten state (compared to the laser pulse width) at high energies might be important in determining the amount of absorbed or desorbed gas in the irradiated area. This is particularly important for the YBCO superconductor and together with

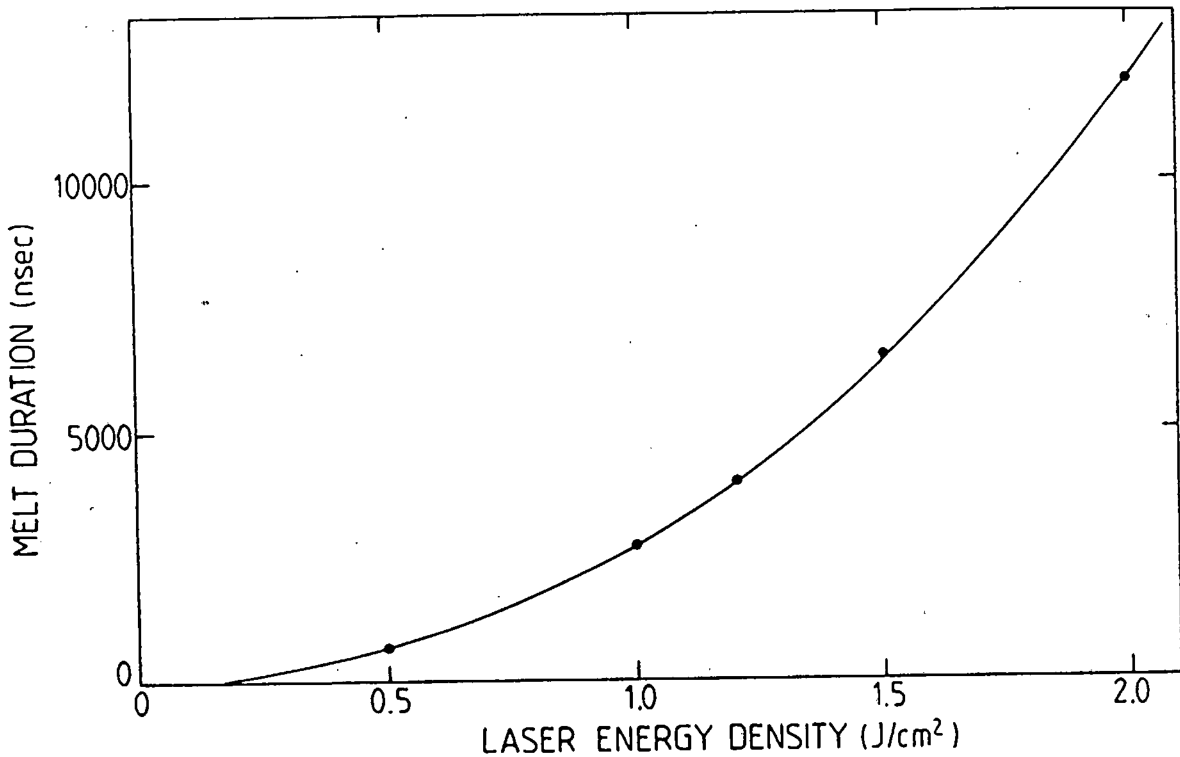

FIGURE 6.4: Determination of the effect of incident laser energy density on the melt duration of the surface of the $Y_1Ba_2Cu_3O_7$ sample.

the solidification velocity this aspect might determine why phase segregation often occurs at the target surface even though the laser interaction process is supposed to be non-equilibrium, resulting in stoichiometric deposition of YBCO [**37, 38, 40**]. The efficiency of energy loss can be assessed by considering the possible mechanisms for these losses. The duration of melting is dependent on conductive, convective and radiative heat losses. The radiative loss from a black body surface of temperature T is given by Stefans law,

$$E_{rad} = \sigma T^4, \tag{6.4}$$

where σ is the emissivity of the material. For a surface temperature of 4000 K, E_{rad} is less than 8 Wcm^{-2} and can therefore be ignored when considering the melt depth

and duration (laser power is of the order of 10^8Wcm^{-2}). The time constant for radiation is also much longer than for thermal diffusion [**217**] and thus heat loss due to radiation can be ignored. Convection is even slower, with a time constant of $\approx$ 1ms over a distance scale of 1 μm calculated for a liquid metal at temperatures near 1500 K [**217**]. The major heat loss mechanisms will then arise from conductive heat losses and material removal. The main uncertainty in the thermal conductivity is the temperature dependence of κ although data is available for thermal diffusivity of YBCO [**226**].

It is well established that a laser induced plasma is formed from the onset of ablation [**18, 38, 39, 219**]. The effect of the ablation threshold is to reduce the available energy in the system by the vaporization of material. Theoretically this would involve taking into account the latent heat of vaporization of the material. Since this was not done in this study, it was assumed that the experimentally determined threshold energy for ablation represents the energy used for plasma production (vaporization) and the energy lost due to conduction [**45, 220**],

$$E_{ab} = E_{plasma} + E_{conduction\,loss}. \tag{6.5}$$

As the effect of material removal was not considered, it is expected that the simulation will overestimate the values of melt depth, melt duration and temperature evolution into the sample. This is due to the energy lost as a result of material removal (evaporation or vaporization), possible beam attenuation due to laser plasma interaction and the effects of plasma-solid interaction [**45, 227–229**].

The effects of laser plasma interaction can be qualitatively assessed by considering the process of laser-solid interaction. For high power, short pulsewidth lasers a phenomenological description of evaporation by the laser [**45, 230, 231**] is as follows. If one considers a laser pulse of width τ (in nsec) then two regimes apply. If the time t at which a plasma is produced on the surface of the solid, with $t = 0$ describing the initiation of the pulse at the surface, is greater than τ,

$$t > \tau, \tag{6.6}$$

then the entire pulse is absorbed by the solid and laser plasma interaction does not

feature in considering the temperature evolution of the target. However, if

$$t < \tau, \tag{6.7}$$

then a plasma can be produced by the initial portion of the laser pulse. The continuing laser pulse can then heat the plasma by inverse bremsstrahlung which involves the absorption of a photon by a free electron, to a temperature of the order of several thousand Kelvin i.e. higher temperatures than the vaporization temperature are induced in the plasma by the laser [**223, 232**]. Fast imaging of the ablation process shows that ablation is a prompt process commencing in the early stages of the laser pulse [**233**]. The penetration and reflection of the laser pulse at the plasma depends primarily on the plasma density, which is generally the same for electrons and ions. The plasma frequency ω_p is given by [**220**] ,

$$\omega_p = 9 \times 10^3 n_e^{\frac{1}{2}}, \tag{6.8}$$

where n_e is the electron concentration in the plasma. For the ruby laser of wavelength $\lambda = 694\,\text{nm}$, the corresponding laser frequency f is $\sim 4 \times 10^{14}$ s^{-1}. Using equation (6), reflection of the laser beam occurs when $\omega_p > f$ i.e. the electron density n_e must be

$$n_e > 2 \times 10^{21} cm^{-3}. \tag{6.9}$$

This high density value is close to that of atoms in a liquid or solid and it is reasonable to assume that the high temperatures in the plasma lead to fast expansion of the plasma into vacuum and the presence of a diffuse plasma boundary results in a decrease of the plasma density away from the target surface [**219, 220, 234**]. Thus it is postulated that laser-plasma reflection only occurs in the immediate vicinity of the target surface, where the plasma density may be sufficiently high [**235**]. For a sufficiently high plasma density, near the target surface the plasma can absorb or reflect the laser radiation in the duration of the pulse while the edge of the plasma is transparent to the laser beam due to the lower plasma density [**220**].

An interesting situation arises at high energies where the density of ions and electrons near the surface is sufficiently high to cause a high degree of absorption of

the laser energy: a self regulating mechanism is initiated that limits the interaction of the laser and the solid target [40, 227, 220]. The situation may be considered as follows: when the density of ions in the plasma is high the laser light is absorbed or reflected by the plasma thereby limiting the evaporation of species from the target [no laser-solid interaction is occurring because the target is shielded from the laser pulse by the plasma]. The lowered evaporation implies a decrease in density of ionized species and hence the plasma becomes transparent to the laser pulse again, resulting in further laser-solid interaction. Absorption of the laser pulse by the plasma then reverses the process and the regulating cycle is initiated. The frequency of regulation depends on the incident laser energy (density of ions produced) and the rate of expansion of the plasma (ie. the rate of change of density) taking into account the absorbed laser energy. Work by Carusso et al. [236] shows that the density, temperature and length of the plasma adjusts itself in such a manner that it absorbs a constant amount of incoming laser radiation. This aspect, particularly at high energy densities has several implications for the relationship between energy density and amount of material deposited and will be discussed further in section 6.2.

For relatively low energy densities where the plasma density is low, plasma losses and energy attenuation of the incident beam by the plasma can be assumed to be insignificant. Also, at low energy densities the effect of plasma-solid interaction can be folded into the threshold energy for ablation and one can assume that this threshold is independent of the incident energy. At higher energy densities, however, the effects of laser-plasma interaction need to be taken into acount

Using these assumptions an equation for the rate of ablation, Δm, in terms of the specific heat C_p, the heat of vaporization ΔH_v the incident laser energy E, the reflectivity R of the surface to ruby laser light and the threshold energy for ablation, E_{ab} can be expressed as [220]:

$$\Delta m = (1 - R)\frac{(E - E_{ab})}{(C_p + \Delta H_v)}. \qquad (6.10)$$

For E_{ab} independent of the incident laser energy E, equation 6.10 shows a linear increase of amount of material evaporated with increasing incident energy. At higher

energy densities, however, one can expect plasma shielding effects to alter the linear relationship. Also, changes in reflectivity of the material at high temperatures [237, 238] are expected to cause deviation from equation 6.10. If one considers the removal of material within the framework of a surface evaporation model put forward by Kelly and Dreyfus [239], where it was assumed that a thin, dense vapor layer (Knudsen layer) exists above the surface wherein backscattering collisions lead to a fraction of the vaporizing species recondensing at the surface, then one can expect that the recondensing fraction will reduce the thickness of the deposit calculated from equation 6.10.

Using the heat flow concept of a melt front it was possible to define the unique concept of an ablation front and an ablation depth, which was defined in terms of the maximum depth in the sample in which the temperature at that depth is above the ablation temperature T_{ab}. The ablation front gives us a quantitative measure of the depth of material that could be evaporated. For low incident laser energies it was possible to simulate the development of the ablation depth (where $T>T_{ab}$) with increasing incident energy.

Fig. 6.5 shows a plot of ablation depth against incident energy with the linear relationship evident. This correlates well with equation 6.10. The simulation generates relatively large etch depths which is inconsistent with experimental data (see section 6.2). Notwithstanding the effect of omitting the heat of vaporization, the simulation cannot explain the lower deposition rate observed in this study and by others [240]. The recondensation of evaporated material [239] will reduce the amount of material deposited and Ready [241] has proposed a model whereby the recoil pressure of the laser suppresses evaporation. Recent evidence of extremely high pressures (>400 atmospheres) at the surface of laser ablated YBCO [242] shows that the expected vaporization temperature, which is calculated at standard pressure and constant volume, is no longer valid for the ablation process. The experimental results obtained for pulsed ruby laser ablation of YBCO were examined to see how these correlate with the predictions of the model.

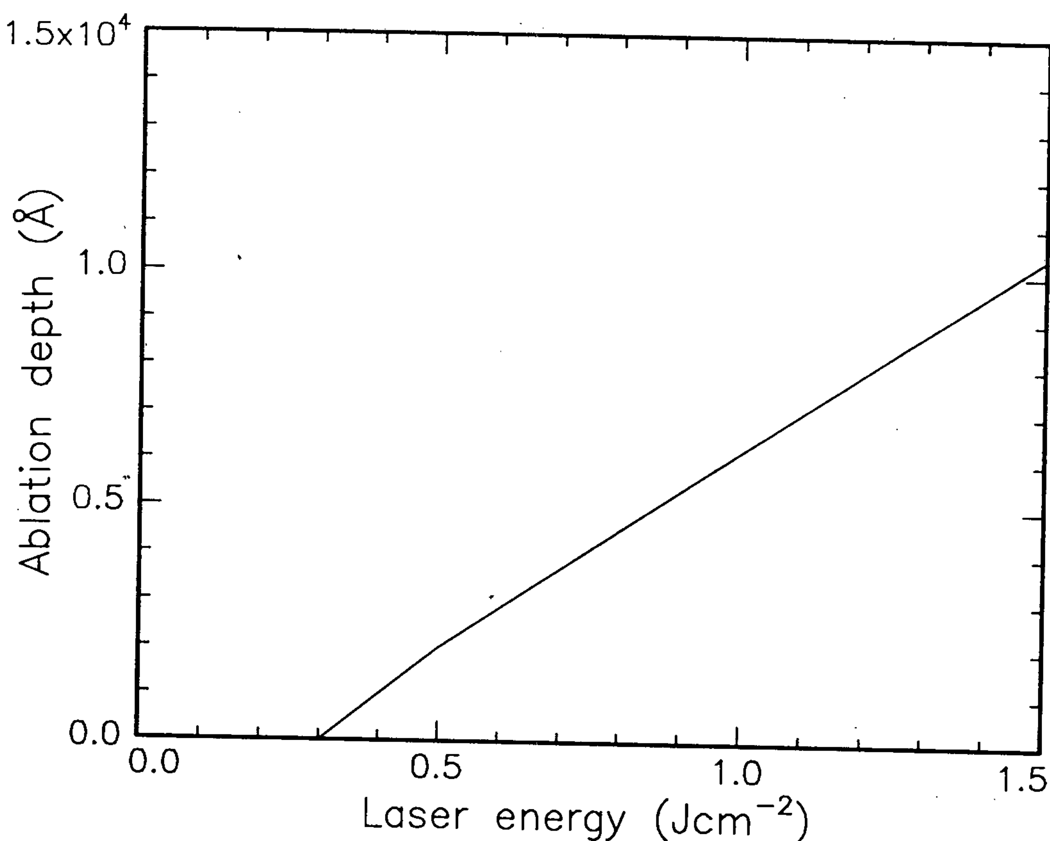

FIGURE 6.5: Simulation of the maximum ablation depth in the sample irradiated by a pulsed ruby laser. The simulation is for low energy densities and reveals unusually high vaporization depths (the depth of material above the vaporization temperature). The possibility of other mechanisms reducing the vaporized yield is dicussed in the text.

6.2 Experimental results

Experimental results for the interaction of the pulsed ruby laser with $Y_1Ba_2Cu_3O_7$ were obtained under various conditions. Measurement of the thickness and stoichiometry of the deposited films was done with RBS and with the aid of the simulation programme RUMP. Unless otherwise indicated the parameters during ablation were an incident energy density of $3\,J\,cm^{-2}$, oxygen pressure of 10^{-1} mbar, a target-substrate separation of 15 mm and a total irradiation of 20 shots per sample.

6.2.1 The effect of energy density

The effect of energy density on the amount of material and the stoichiometry of the material deposited was determined using RBS. The surface of the YBCO target was scraped clean with a blade and particles of dust were blown off with a high pressure jet of dry N_2. A fresh target spot was used for each incident energy and the deposit was collected on Si<100> substrates for 20 incident laser pulses. **Fig. 6.6** shows the thickness of deposit for increasing incident laser energies. Three aspects of the plot are of importance. Firstly, the experimentally determined value for the threshold energy density for ablation is closer to 0.40 J cm^{-2} than to the theoretical

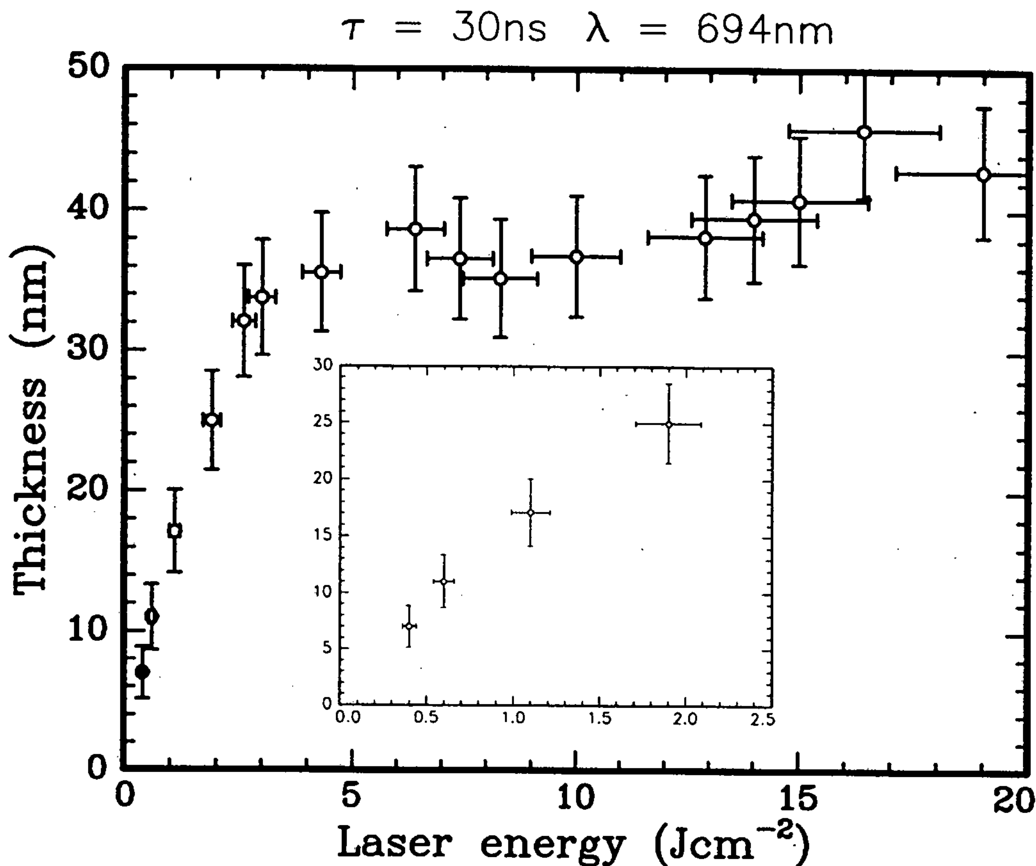

FIGURE 6.6: The variation of deposited thickness with laser energy for 20 pulses incident on the target. The threshold for the detection of a deposit was ≈ 0.4 J cm^{-2}. Thickness of the deposited material increases linearly for low energies and a plateau of thickness is reached at 5 J cm^{-2}. The insert shows the low energy region.

value of 0.30 J cm^{-2} predicted by the simulation (see section 6.1). The reported values for the energy threshold for ablation of YBCO vary from 0.11 to 0.60 J cm^{-2}, depending upon the surface preparation and porosity of the target and the incident laser wavelength [**37–41**]. Secondly, there is a regime of energy values for which the amount of material increases linearly. This occurs for low energy densities and extends up to $\approx$ 5 J cm^{-2}. Finally, there is seemingly a plateau for the amount of deposited material at approximately 5 J cm^{-2} and any further increase of incident laser energy has little effect on the thickness deposited. The non-linear increase of deposited thickness with increasing incident laser energy was also reported by Inam et al. [**240**] for pulsed excimer laser ablation of YBCO.

The first effect is not surprising in that one would expect that the assumptions made in the heat flow model would have meant smaller energy loss factors than experimentally realised. The absence of a term that takes in account the heat of vaporization in the simulation lowers the predicted ablation threshold and hence a higher experimental threshold energy for ablation was not unexpected. The higher threshold energy could also imply either inefficient coupling of the laser energy with the solid and/or a larger value of the reflectivity of the surface.

The linearly increasing region in **Fig. 6.6** tallies well with the prediction given by equation 6.10 for the linearity of amount of material ablated and lends credence to the argument that the amount of material deposited varies linearly with energy density. However, the presence of a deposition plateau does not fit in with the model and suggests that this linearity only exists for low energy densities and that other factors must be taken into account at higher densities. The deposition plateau itself is an important feature for it indicates that there is a window of useful energy densities. Any additional input energy will not result in increased yield. This can be qualitatively accounted for in terms of a plasma production mechanism at the surface of the target. The high energy densities result in a plasma that shields the surface from further ablation and absorbs the laser energy to increase the kinetic energy of the plasma. Further increases in energy density does not affect the yield because the frequency of the plasma shielding mechanisms varies with plasma density which is

in turn a function of incident energy. Thus the self-regulating mechanism ensures a nearly constant absorption of energy by the surface and hence the plateau develops. Higher energy densities are also more likely to result in etch pits and melt textured surfaces that could result in lowered deposition rates, especially since the target was not rotated during deposition [**37, 38, 40**].

Determination of the stoichiometry of the deposit as a function of energy density was accomplished by RBS analysis. **Fig. 6.7** shows the ratios of Ba and Cu content normalized to the Y content of films deposited with increasing energy density. The threshold energy for the deposition of near-stoichiometric films (Ba deficient) is ≈ 2 J cm^{-2}. Below this threshold the films are seriously deficient in Ba and have excess Cu content. This might be due to equilibruim melting and vaporization of the different elements which is dependent on the varying vapor pressure of the constituents. There is insufficient energy to cause stoichiometry retention. Above 10 J cm^{-2} the Cu content tends to vary erratically and the constancy of the Ba values confirms that this is not due to variation of Y content. An added complication at high incident energies is the deposition of clusters of material. The "spitting" of chunks or clusters of material during laser ablation has been noted previously [**40, 48, 243**] and are thought to arise from a supersaturation of the surface layer with increasing incidence of high energy pulses, with a resultant boil-off of portions from the surface [**42**]. This also causes smearing of the RBS spectra and hampers the exact determination of stoichiometry. The size of the deposited clusters vary considerably and SEM examination of the surface of a film with clusters point to the insulating nature of some of these clusters. Thus the model used to calculate the temperature and melt development must include a cut off for energy density beyond which it is no longer valid. For the purposes of this study an incident laser energy of ~ 5 J cm^{-2} can serve as the upper limit for the model.

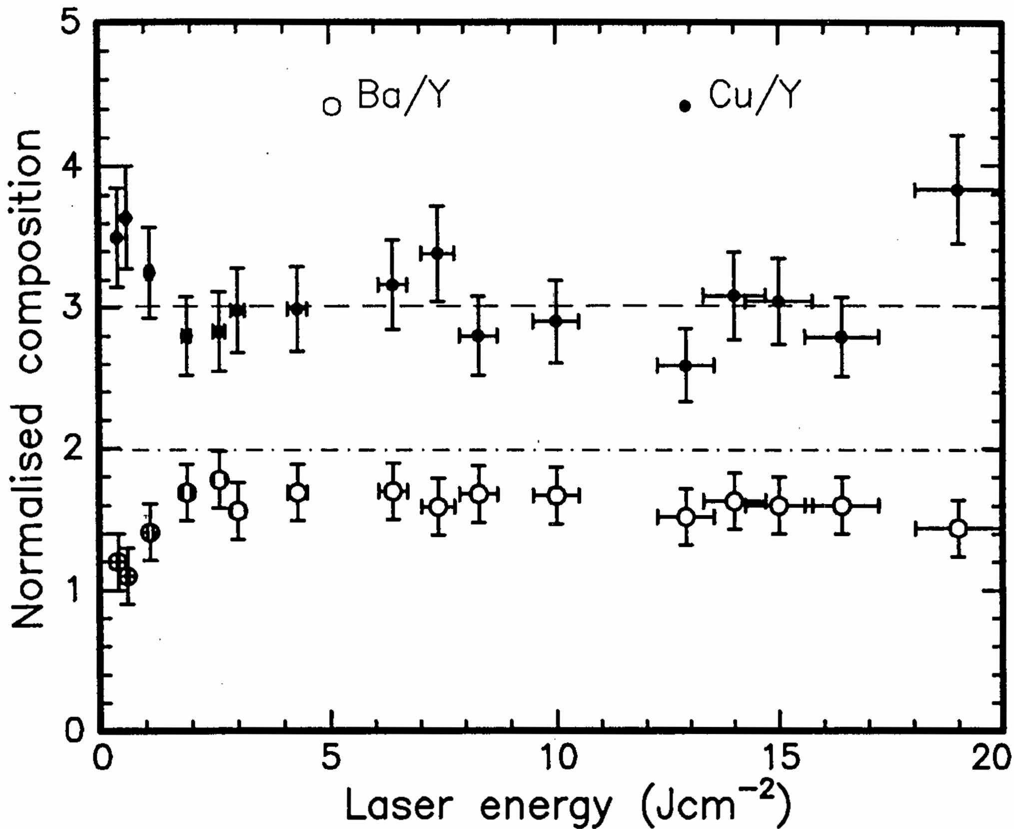

FIGURE 6.7: Determination of the stoichiometry of films deposited at various incident laser energy densities. The composition of the film was normalized to the Y-content. At low energies the films are non-stoichiometric due to the equilibruim phenomena of evaporation at the surface. The threshold for the deposition of near-stoichiometric films was 2 J cm^{-2}. A Ba-deficiency was observed at all energies. Large fluctuations in composition are noted at high energy densities ($\gg$7 J cm^{-2}).

6.2.2 Thickness variation of deposited material

It is known that the spatial variation of composition and thickness of layers deposited by laser ablation is quite different from those of other deposition methods. Thermal e-beam evaporation, for instance, has a cos θ spread of the evaporated beam from the target normal (assuming a point source). This denotes a slow change of thickness with increasing radial distance. Laser deposition by excimer laser ablation on the other hand, has been found to display a $\cos^n\theta$ distribution, where $8 \leq n \leq 12$ **[39, 244, 245]**. The form of this distribution is highly forward directed and implies

that a large portion of the evaporated material is deposited in a small area.

Fig. 6.8 shows the spatial variation in thickness of material deposited for an incident energy density of $3\,\mathrm{J\,cm^{-2}}$. The film was produced by focussing the beam to a spot on the target, the spot being elliptical due to the inclination of the target to the beam. The shape of the deposit followed that of the ablated spot

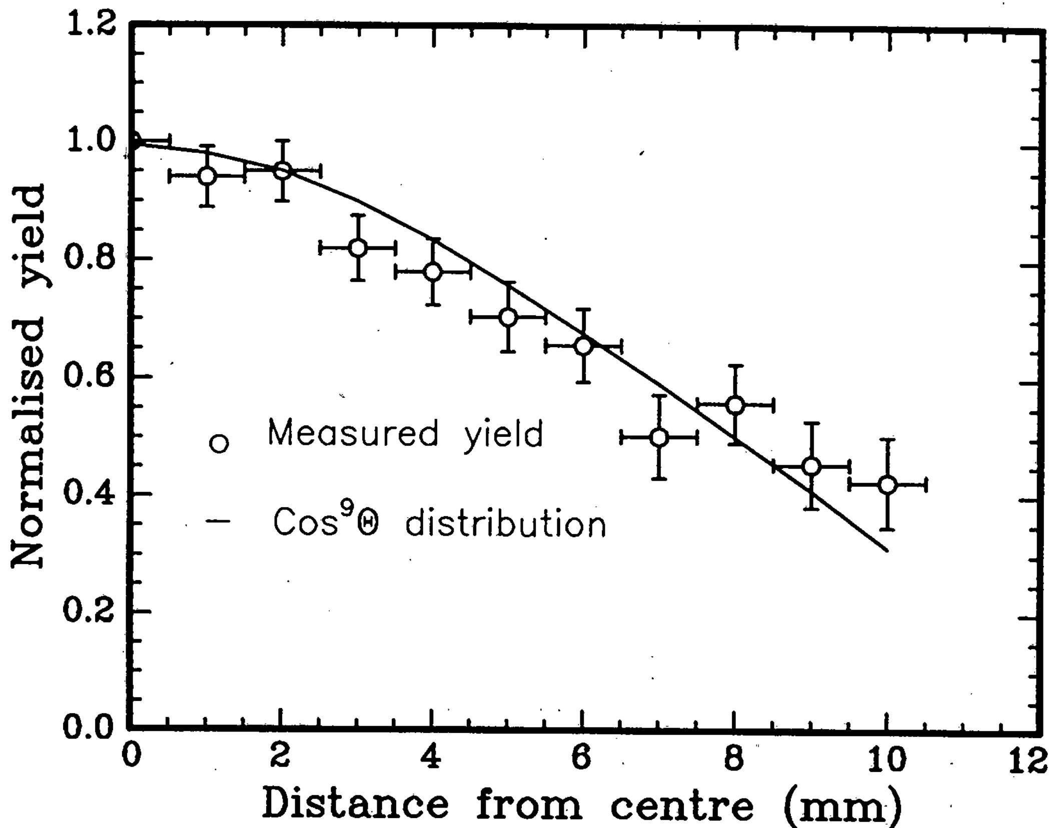

FIGURE 6.8: Distribution of thickness of a film across the area of a substrate mounted parallel to a target which was ablated at $3\,\mathrm{J\,cm^{-2}}$. The spatial variation of the spread is sharply forward peaked and fits well with a simulation (solid line) for a $\cos^9(\theta)$ distribution.

(i.e. elliptical) with the major axis of the deposited area parallel to that of the ablated spot. The spatial profile of film thickness as a function of distance along the major axis was measured with RBS using a 1mm diameter beam. Thickness and composition values were estimated from a comparison of the experimental data with the RBS simulation program RUMP [76]. The profile was normalized to the

maximum thickness which corresponded to the centre of the substrate i.e. the plane where the normal at the centre of the ablated spot intersects the substrate. The spread shows a rapid decrease of thickness with increasing distance away from the centre of the deposit. The observed thickness variation was fitted theoretically and found to agree well for a $\cos^n(\theta)$ distribution with $9 \leq n \leq 11$. The calculated distribution takes into account the target substrate separation, the finite size of the ablated spot and its elliptical area with the solid angle contribution being folded into the distribution. The model assumes non-averaging of the dispersion i.e. retention of the elliptical deposition shape which is achieved experimentally by not rotating the substrate. These forward peaked distribution profiles are known empirically to result in stoichiometric deposition of YBCO films using excimer lasers [**39**] and are therefore further evidence that the ruby laser can be used for pulsed laser deposition of superconductors. This high degree of forward peaking is visible in the conical ablation plume that is observed visually.

Measurement of normalized Ba and Cu yields across the deposit (**Fig. 6.9**) indicates a retention of relative ratios up to some distance from the centre beyond which the relative yields vary. This effect has also been seen by others [**39**]. The deviation at large distances from the centre corresponds to large angles of θ and have been attributed to a thermal component in the evaporated plume which follows a $\cos(\theta)$ distribution. This thermal component is overwhelmed by the $\cos^n(\theta)$ distribution at low angles but due to the rapid falloff in this distribution and the slower decline of the $\cos(\theta)$ thermal component, the thermal distribution dominates at large θ. The thermal region is non-stoichiometric due to the different vapor pressures and sticking coefficients of the elements. Singh et al. [**220**] have attempted to explain the forward directed nature of laser ablation in terms of the anisotropic expansion velocities of the plasma edges arising from density gradients in the gaseous plasma. Although they are successful in reproducing the $\cos^n(\theta)$ distribution with their model the deviation from $\cos^n(\theta)$ and the non-stoichiometric value at large θ are not considered. According to Venkatesan [**39**] the thermal component is due to surface melting that gives a small and constant thermal component to ablation i.e.

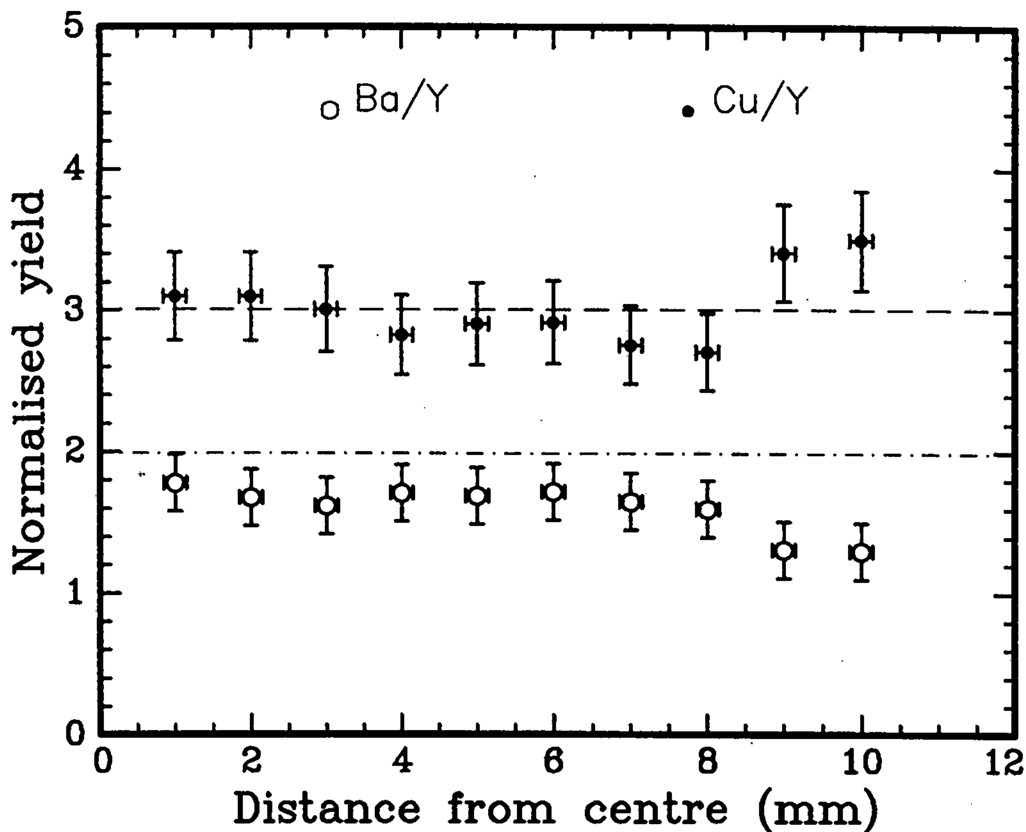

FIGURE 6.9: Measurement of the stoichiometry of a film, deposited at 3 J cm^{-2}, across the area of the substrate. The composition values are normalised to the Y-yield. At the edges of the substrate a deviation from ideal stoichiometry is observed.

the deposition consists of an overlapping forward-directed stochiometric component and a thermal non-stoichiometric aspect. The Knudsen layer model of Kelly and Dreyfus [239] can only account for a $\cos^4(\theta)$ spread and higher order corrections were considered necessary to simulate a $\cos^9(\theta)$ distribution.

Higher incident energy densities did not result in any increase in the forward peaking i.e. n did not increase. This is at odds with the Singh model [220] where an ever increasing energy will result in a corresponding increase of n. However, if one considers the plateau data presented then it may be that total reflection of the laser

energy occurs at these high energy densities thereby maintaining an upper limit to n by limiting the amount of energy absorbed by the surface and the plasma.

The highly forward directed nature of the laser deposition method has other consequences in terms of the economical use of the target where the dimensions of the target can be quite small and a large portion of the deposit can be collected within a small area. The carrying power of the plasma in the forward direction is further illustrated by studying the amount of material deposited as a function of the target-substrate separation distance. **Fig. 6.10** shows that an increase of target substrate separation does very little to reduce the deposited yield, unlike the case for sputter and e-beam deposition. Whilst it would be expected that doubling the

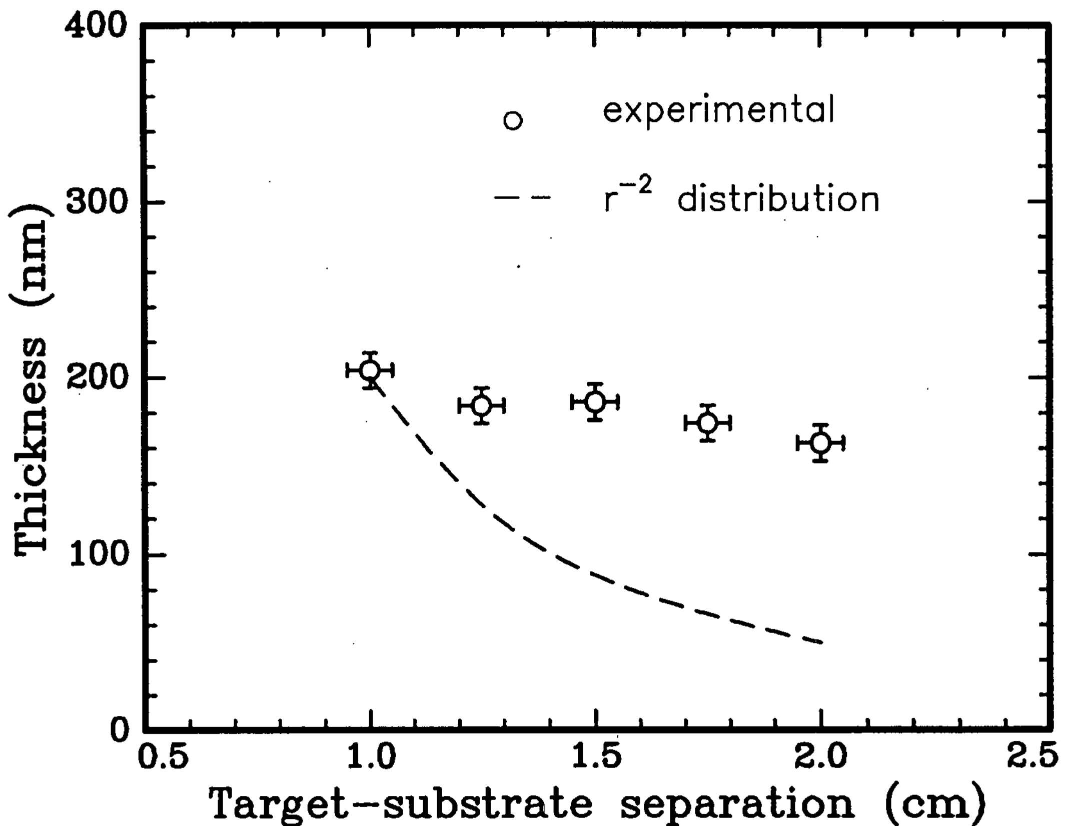

FIGURE 6.10: Determination of the effect of increased target-substrate separation on the thickness of the deposit. Increased separation distances do not lead to a drastic reduction in deposited thickness, due to the highly forward peaked distribution and the carrying power of the ablated plume. the dashed line denotes the expected drop in yield for a r^{-2} distribution.

separation should decrease the thickness 4-fold (because of the r^{-2} dependence) the drop in yield is much slower. The high energies of the ions, neutrals and clusters in the plasma promote the growth of high quality films at relatively low substrate temperature [**18, 32, 246**] due to the mobility they impart to the growing film. The retention of stoichiometry at these larger separation distances is further indication that the carrying power of the plasma extends over large distances. Even at relatively high oxygen pressures (10^{-1}mbar), thermalization of the plasma is minimal (even though the luminosity of the plasma decreases with increasing O_2 pressure), implying that although oxygen may be taken up by the plasma, the scattering effect of the gas up to 10^{-1} mbar is minimal.

6.2.3 Thickness dependence on oxygen pressure

The inclusion of high levels of oxygen into the deposited film during the deposition step is desirable for the formation of in-situ superconducting films and because of the critical dependence of the superconducting properties of the film on oxygen content. The crucial dependence on oxygen pressure for the ablation of oxides has been previously demonstrated [**19, 247**]. The amount of material deposited by the ruby laser as a function of oxygen pressure in the deposition chamber is shown in **Fig. 6.11**. While a high oxygen pressure during the deposition step is desirable, a cut-off (at approximately 0.5 mbar) is reached above which the addition of O_2 prevents the transfer of material onto the substrate. This pressure may be a function of the incident wavelength and/or energy density so it was necessary to measure the pressure dependence with the energy density set to the operational value for deposition i.e. $3\,\mathrm{J\,cm^{-2}}$. At low pressures there is a range (10^{-1} to 10^{-3} mbar) over which the amount of deposit is fairly constant. At high pressures (above 10^{-1} mbar) the thickness of deposit decreases rapidly. This corresponds to an observable decrease in the intensity of the plasma plume which is restricted close to the target at 10^{0} mbar and is not visible at 10^{1} mbar. The absence of a plasma and deposited material does not imply non-removal of material at high pressures as visual observation of the target surface indicates that some material might have been

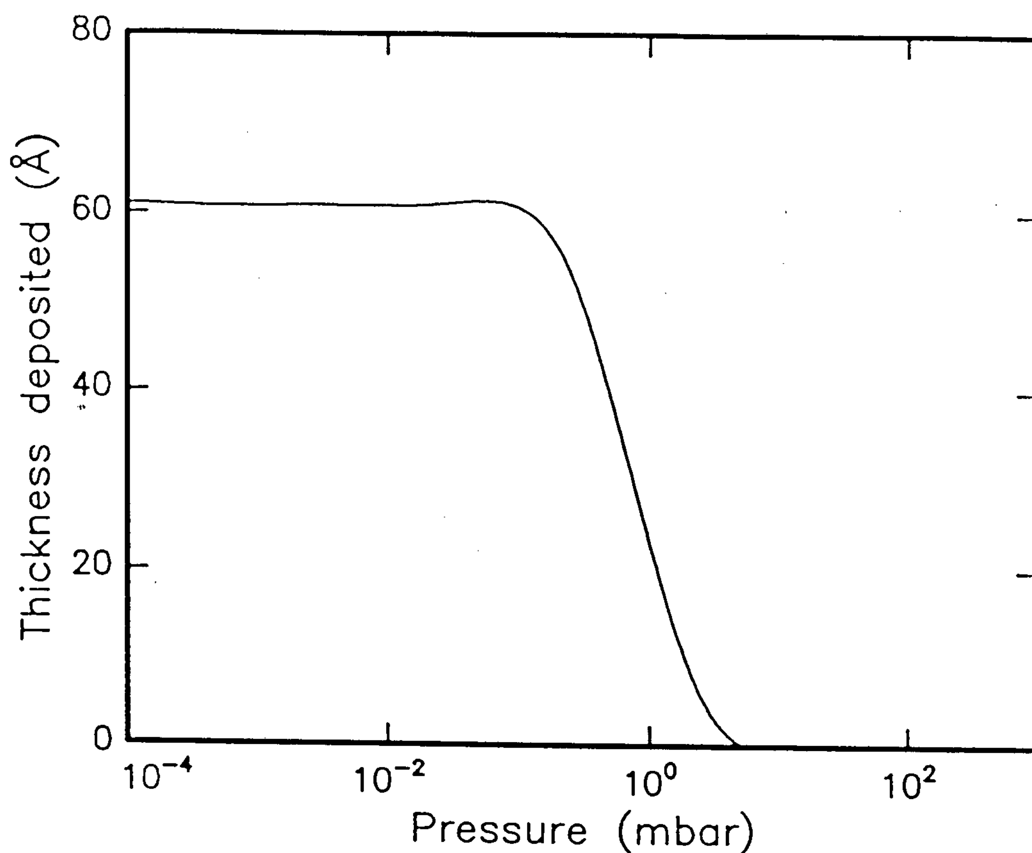

FIGURE 6.11: Variation of the thickness of the deposit with oxygen gas pressure for 5 incident laser pulses at an incident energy of $3\,\mathrm{J\,cm^{-2}}$ and a target–substrate separation of 25 mm. Increased pressures causes decreased luminosity of the plasma and at high pressures ($\gg 10^0$ mbar) the thickness drops off rapidly due to thermalisation of the plume.

removed. The high oxygen pressure results in multiple collisions and thermalization of the ablated species which are unable to traverse the separation distance between target and substrate. Thickness measurements (done with RBS) are integrated thickness for all the elements and do not reflect possible compositional variations with pressure. The pressure used during deposition (10^{-1} mbar) assured adequate O_2 incorporation without loss of deposit and corresponds to the values normally used in excimer laser deposition [16, 38, 39, 248].

6.2.4 Superconducting characteristics

Thin films of $Y_1Ba_2Cu_3O_7$ were grown on MgO substrates (**Fig. 6.12**) by pulsed ruby laser ablation at an incident energy of 3 J cm^{-2}, a target–substrate separation of 20 mm and an oxygen pressure of 10^{-1} mbar. The growth of *in-situ* superconducting films was not possible due to the fact that the heater in the ablation chamber is limited to a maximum temperature of 200°C . Post-deposition annealing of the film was necessary to make it superconducting. The deposited material closely

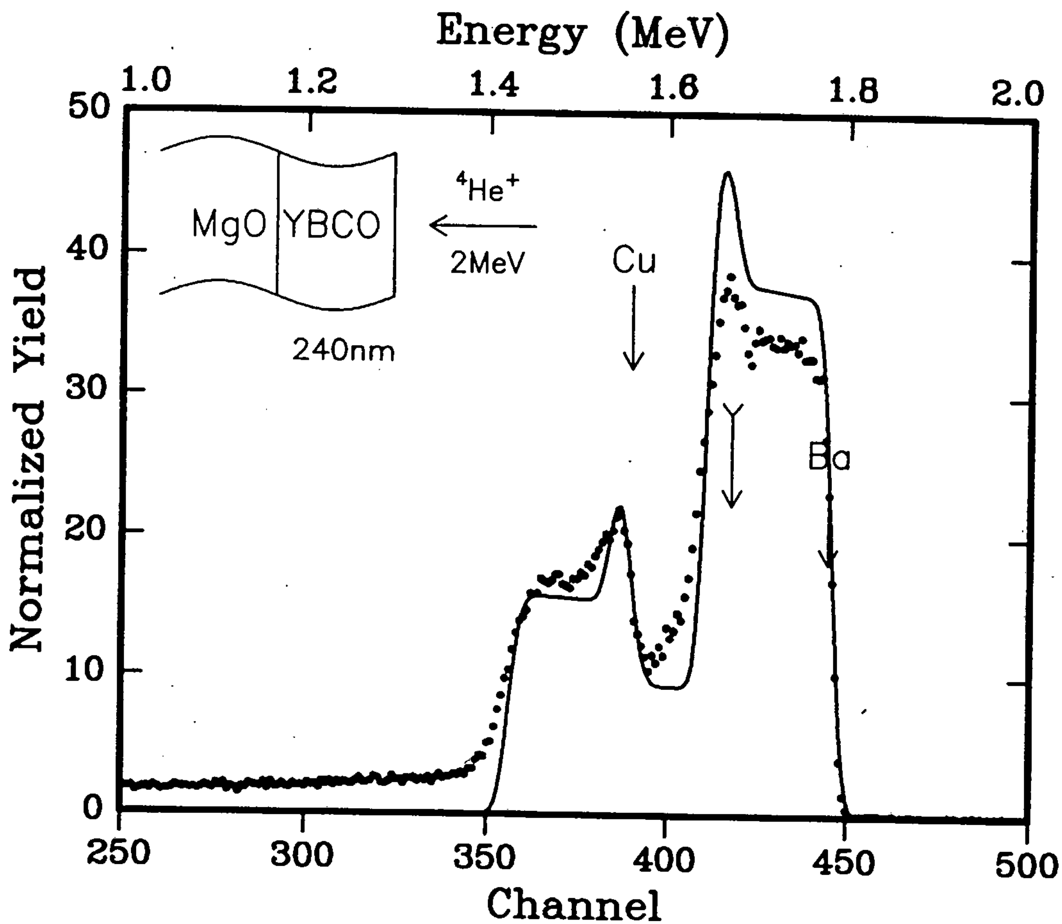

FIGURE 6.12: RBS spectrum of a YBCO film deposited onto MgO at 200°C by pulsed ruby laser ablation (λ=694 nm, τ=30ns) at an incident energy density of 3 J cm^{-2}. The film composition is close to ideal stoichiometry except for a Ba-deficiency. The smearing of the back edge of the signal is due to irregular granularity.

resembles the composition of the bulk $Y_1Ba_2Cu_3O_7$ for all the metallic elements, with the exception of the Ba content which is below the desired value as can be seen by comparison with the simulated spectrum. The deficiency of Ba is thought to be intricately linked to the substrate temperature [**140**]. Re-evaporation of Ba can occur at relatively low substrate temperatures due to its' low melting point. At high substrate temperatures Ba forms compounds with oxygen and the other metallic elements, due to the higher reactivity and mobility. These compounds are less prone to evaporation. This deficiency was observed for a large range of laser energies (see **Fig. 6.7**). The smearing of the tail of the film signal is an indication of irregular granularity in the film and may arise from the deposition of particulates during ablation. XRD analysis (**Fig. 6.13**) of the post-annealed film reveals a

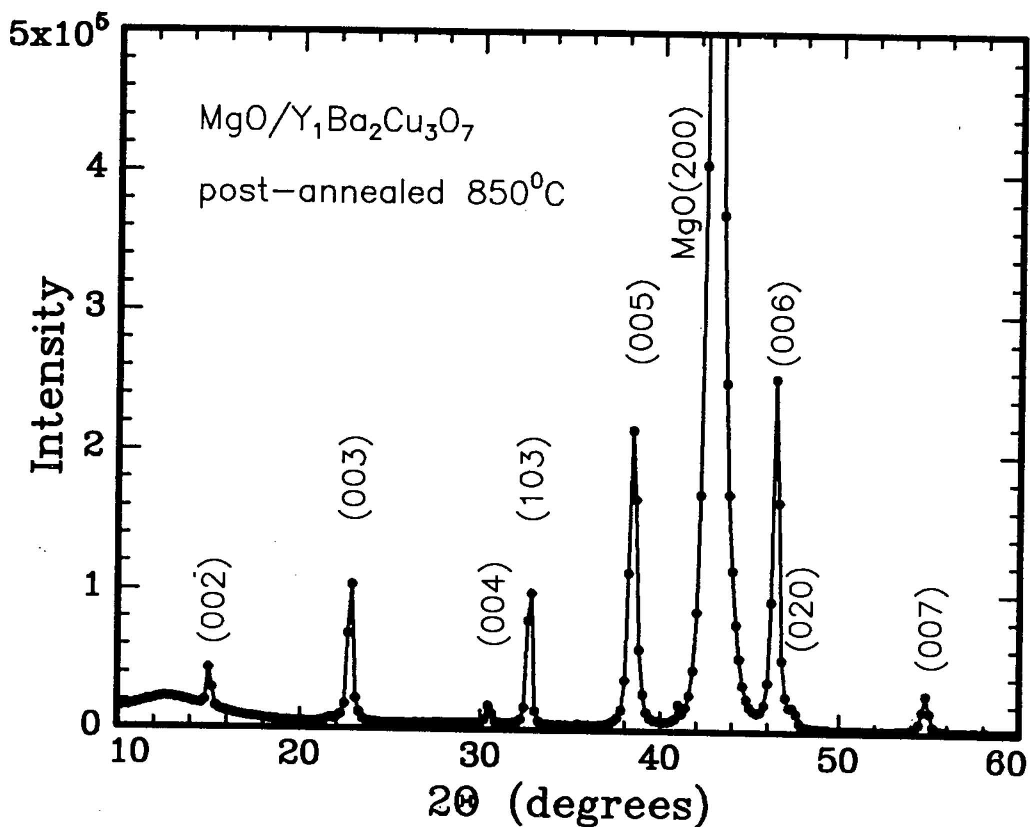

FIGURE 6.13: XRD spectrum of a YBCO film deposited onto MgO at 200°C by pulsed laser ablation at 3 J cm^{-2}cm and post-annealed at 850°C . The films is polycrystalline with evidence of some preferential c-axis orientation.

polycrystalline film with some preferential c-axis orientation. The polycrystalline nature of the films is expected in view of the post-annealing treatment of the films. Resistivity measurements gave (**Fig. 6.14**) a transition temperature of 84 K and a transition width of 2 K. The susceptibility measurement gave a transition temperature of 80 K and a transition width of 7 K. The lower transition temperature and larger transition width obtained with the susceptibility measurement is consistent with a polycrystalline film with weak links between grains.

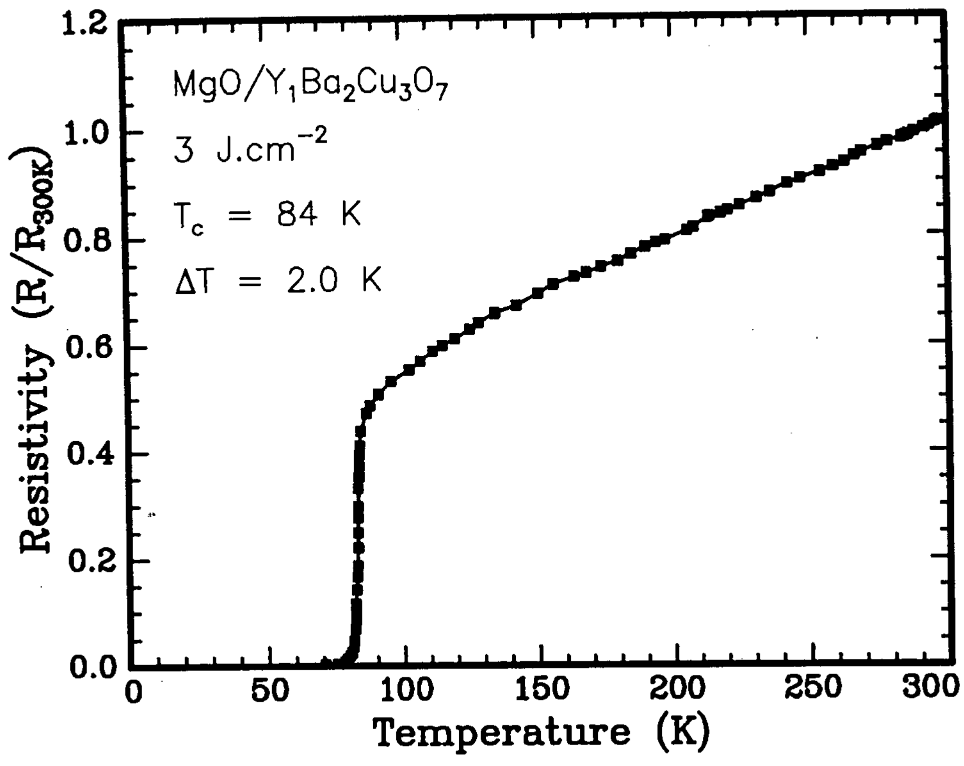

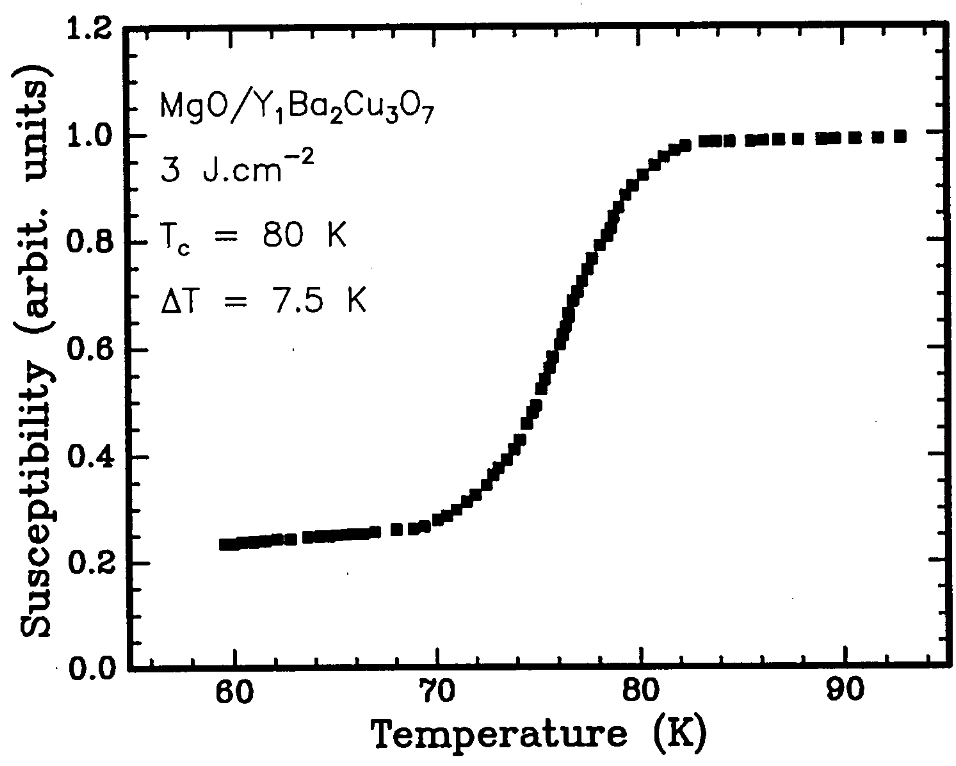

FIGURE 6.14: Electrical measurements on a thin film of YBCO deposited at 200°C by pulsed ruby laser ablation and post-annealed at 850°C . The resistivity and susceptibility measurements show high transition temperatures. The transition widths are consistent with a polycrystalline film with weak intergrain links.

6.3 Laser annealing of YBCO films

The possibility of a variety of potential optical applications for high T_c superconducting thin films, including infra-red detectors and optically triggered fast switches [**217**, **249**] is envisaged. The viability of these applications depends on the nature of the optical interaction of thin films of $Y_1Ba_2Cu_3O_7$. It is known that under illumination by a fast optical pulse a superconducting current shunt is rapidly converted to a normal conductor [**250**]. In addition, laser irradiation of semiconductors is known to cause laser annealing in the target [**251**]. Depth controlled damage for the creation of Josephson junctions and for patterning and etching of superconducting thin films also has usage in thin film superconductor technology.

Laser irradiation of high quality thin film superconductors prepared by ICM sputter deposition at 700°C onto single crystal MgO substrates was investigated. The films were superconducting as-deposited and had a minimum channeling yield of 11% at the Ba peak. Irradiation was carried out in air with a pulsed ruby laser (λ = 694 nm, τ = 30 ns). The irradiating pulse was homogenized with a right-angle quartz beam homogenizer to eliminate the possibility of "hot-spots" in the beam. The substrate size was such that the laser beam covered 85% of the film. Ion channeling results were taken at the central region of the irradiated area. **Fig. 6.15** shows the effect of a 50 mJ cm^{-2} pulse on the minimum yield of a film on MgO. From the heatflow calculations, it was noted that the incident energy was below the threshold for melting of the surface (150 mJ cm^{-2}). However, the damage induced at the surface is evident from the increased yield in both the Ba and Cu positions at the surface. The increased disorder induced at the surface by the laser pulse is of the order of 10-20 nm. Changes to the properties of the film by the outdiffusion of oxygen upon irradiation at these low energies might be expected, but the disorder created in the heavier elements of the lattice is surprising. Simulation of the heat generated at the surface reveals a maximum surface temperature of ≈500°C , which is far below that expected to cause re-crystallisation of the film (800-900°C). Post-deposition annealing in an oxgyen atmosphere at 500°C is frequently

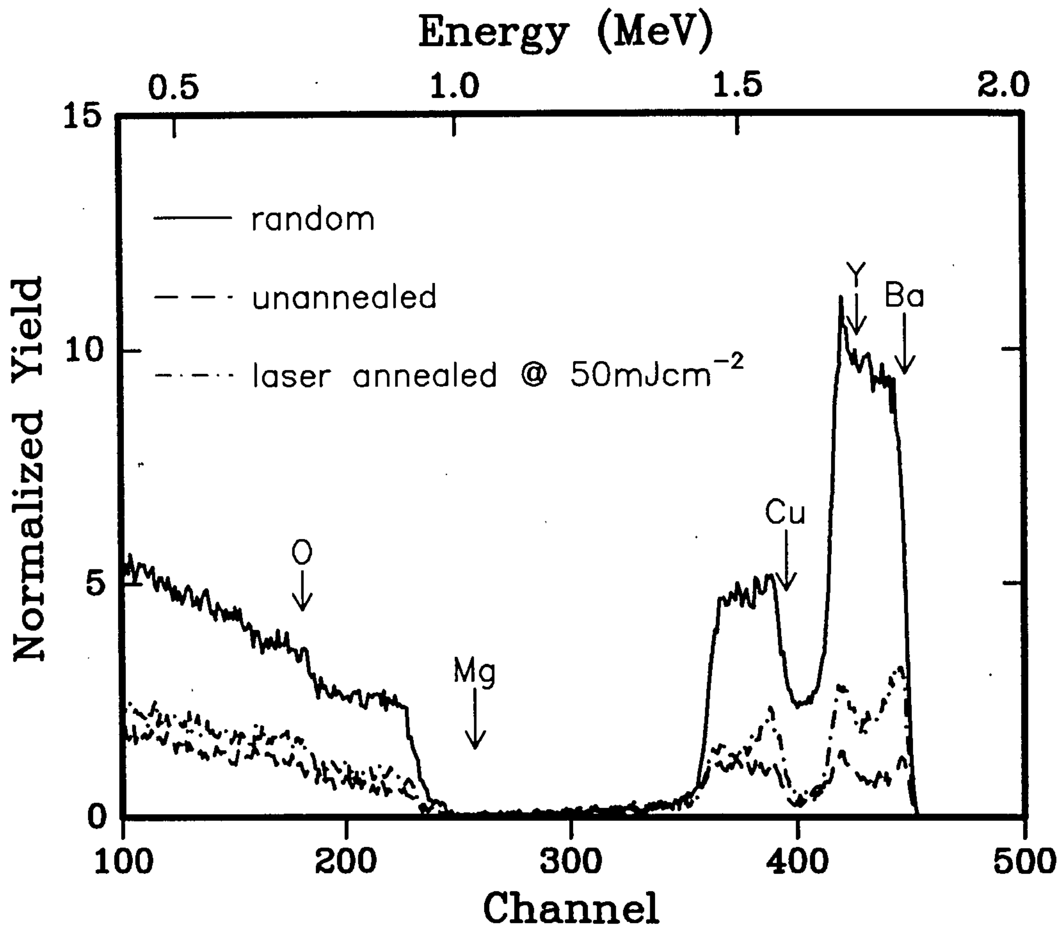

FIGURE 6.15: Ion channeling measurements on a $Y_1Ba_2Cu_3O_7$ film deposited at 700°C by ICM sputtering and irradiated by a pulsed ruby laser (λ=694 nm, τ=30ns) at an incident energy density of 50mJ cm^{-2}. The aligned spectra are for the film prior to and after irradiation. An increased dechanneling layer of $\approx$20 nm is induced on the surface. The interior of the film is not significantly affected.

used to oxygenate films and no disorder has been induced in such films. Also, the surface of the irradiated film shows little evidence of the effects of irradiation, with no melting or discoloration observed. The possibility of non-thermal mechanisms inducing a change in a $Y_1Ba_2Cu_3O_7$ film from a superconducting state to a highly resistive state upon irradiation with short optical pulses at low incident energy density has been postulated by Donaldson et al. [225]. The possibility of shock wave-induced surface damage in accordance with the high pressure results of Dyer et al. [242] must also be considered.

Higher energy irradiation of a thin film of $Y_1Ba_2Cu_3O_7$ at 250 mJ cm^{-2} reveals that the laser pulse has nearly almost completely destroyed the textured crystallinity in the film (**Fig. 6.16**). The surface of the film is specular and discoloured with clear indication of melting. The simulated heatflow generates a surface temperature above the melting point of $Y_1Ba_2Cu_3O_7$ with the melt depth extending to a depth of $\approx$ 200 nm, which is reasonably close to the thickness of the film (220 nm). The heat generated by the laser pulse has resulted in re-crystallization of the film in a random orientation, meaning that the classical sense of laser annealing as applied

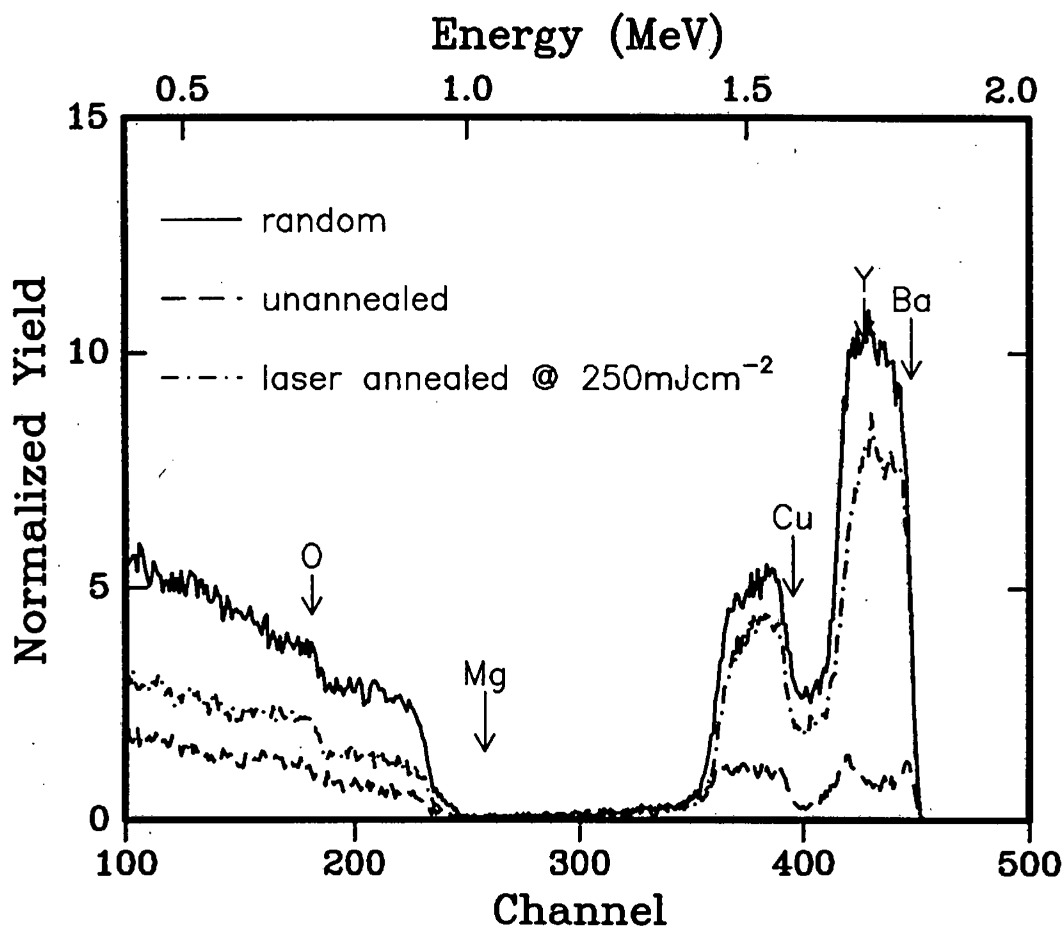

FIGURE 6.16: Ion channeling measurements on a $Y_1Ba_2Cu_3O_7$ film grown by ICM sputter deposition at 700°C and irradiated by a pulsed ruby laser (λ=694 nm, τ=30ns) at an incident energy density of 250mJ cm^{-2}. The aligned spectra are for the film prior to and after irradiation. The film is largely randomised through its' thickness after irradiation.

to semiconductors does not hold, as the substrate does not provide a seed for the epitaxial recrystallization of $Y_1Ba_2Cu_3O_7$. This may be due to the non-congruent melting of $Y_1Ba_2Cu_3O_7$ and the large number of sub-compounds that could form. It was noted in Chapters 3 and 4 that the c-axis orientation dominates when the deposition rate is slow enough to allow the kinetics of the c-orientation to determine the growth orientation. The explosive recrystallization expected at the receding melt front occurs on a time scale so small that the kinetics of c-orientation do not play a role. Post-irradiation annealing of these films at high temperatures (850°C) does not restore the original crystallinity in the films.

6.4 Summary and discussion

The large number of reports detailing the growth of YBCO films by pulsed laser deposition with excimer lasers [**14–19, 41, 240, 246**] prompted the investigation on the use of the pulsed ruby laser for ablation of bulk $Y_1Ba_2Cu_3O_7$ targets. Understanding the nature of the laser-solid interaction is also a field of considerable interest [**42–47, 220**]. At the commencement of this study no reports on the use of the pulsed ruby laser for the ablation of YBCO were available. Recently Roul et al. [**252**] investigated the effect of pulsed ruby laser irradiation on the superconducting properties of $SmBa_2Cu_3O_7$ and it was shown in that study that laser irradiation of a bulk pellet causes microstructural changes in grain growth due to laser induced sintering which improved the interconnectivity among superconducting grains. To the best of our knowledge, no reports on the growth of YBCO films by pulsed ruby laser ablation are available. The laser ablation process is wavelength dependent [**41, 48, 49**] and the use of a visible laser (λ=694 nm), as opposed to the commonly used ultraviolet lasers (λ=100-300 nm), is important for compiling a comprehensive understanding of the laser-YBCO interaction.

The interaction of the pulsed ruby laser (λ=694 nm, τ=30ns) and the solid $Y_1Ba_2Cu_3O_7$ target was modelled in terms of a one-dimensional heat which was solved numerically using a finite element method [**215**] and the evolution of temperature calculated as a function of time and depth into the target was simulated.

Using the development of temperature as a function of depth into the sample for various time intervals, it was shown that the simulation gave a threshold incident energy, for which the surface is melted, of 0.15 $J\,cm^{-2}$.

It was seen that the development of temperature further into the sample is primarily due to heat conduction effects and the layer thickness directly heated by the laser was computed to be $\approx$ 65 nm. Using the temperature time profiles it was deduced that the minimum incident energy density for which the surface temperature exceeds the vaporization temperature ($T_{vap} \approx 2500K$) was 0.3 $J\,cm^{-2}$.

The amount of material which is above the melting temperature is known as the melt depth and it was found that even moderate laser energies could cause melting deep into the sample, an incident energy of 1 $J\,cm^{-2}$ gaving a melt depth of more than 1 μm.

The heat loss mechanisms in the evolution of temperature were examined and it was concluded that radiative and conductive losses play a minor role in the development of the temperature profile into the target and the major loss mechanism after irradiation by the laser pulse is thermal conductivity. The effects of plasma production and laser-plasma interaction **[45, 227–229]** were expanded on and it was established that reflection of the laser pulse could occur if the plasma density was sufficiently high. With the assumption of folding the loss mechanisms into the threshold energy for ablation, it was seen that the mass transfer equation of Cheung **[45]** predicts a linear increase of material removed with increasing energy density. It was noted that plasma shielding effects and variation of the reflectivity at high temperatures would result in deviation from the linearity predicted by the mass transfer equation.

Using the concept of the melt depth a similar principle was applied in considering the thickness of material above the vaporization temperature and a new concept called an ablation depth was defined. The ablation depth is a quantitative measure, to first order, of the amount of material that could be vaporized during laser-solid interaction by considering how much of the material is above the vaporisation temperature. Comparison of the ablation depth with experimentally determined etch

depths and deposition rates shows that the calculated ablation depth gives larger material removal than expected or experimentally realised. The recondensation of evaporated material [239] and the possibility of the recoil pressure of the laser suppressing evaporation [241] were discussed as possible mechanisms to reduce the evaporated yield. Recent evidence [242] of extremely high pressures during ablation ($>$ 400 atmospheres) meant that the vaporization temperature, calculated at standard pressure and constant volume, is no longer valid and could also lead to reduced evaporation.

Experimental verification of the proposed model was obtained by irradiating a bulk $Y_1Ba_2Cu_3O_7$ target with a pulsed ruby laser. Measurement of the thickness and stoichiometry of the deposited films was done with RBS and with the aid of the simulation programme RUMP. The variation of the thickness of deposited material as a function of the incident laser energy gave a threshold for ablation of $0.4\,\mathrm{J\,cm^{-2}}$, higher than the $0.3\,\mathrm{J\,cm^{-2}}$ predicted by the heating model. The lower threshold predicted by the model was explained in terms of the lack of a vaporisation term in the heat flow simulation, which is expected to increase the loss factors during irradiation and therefore increase the ablation threshold. The amount of material deposited increases linearly with energy density up to an incident energy of $\approx$ $5\,\mathrm{J\,cm^{-2}}$, beyond which the rate of increase of deposited material increases very slowly with increasing energy. The loss of linearity at high energy densities suggests that the model can only be applied to low energy densities. This is a reasonable assumption if one considers that the models' frame of reference is an equilibrium thermal model, whereas at high energies non-thermal and non-equilibrium effects must be considered. The high energy behaviour was explained in terms of a plasma production mechanism at the target surface such that when the density of the plasma is high enough (at high laser energies) the plasma shields the target surface from the incident pulse and limits the amount of material removed from the target. From a consideration of the plasma density necessary to reflect or absorb the laser energy, it was shown that laser-plasma interaction can only occur in the near-surface region. Assessment of the stoichiometry as a function of laser energy density reveals that

there is a threshold for the deposition of near-stoichiometry films which is higher than the ablation threshold and was found at $2\,J\,cm^{-2}$. The discrepancy in ablation and stoichiometry thresholds was interpreted as an indication of different processes ocurring at the two energies. At low energy the removal of material is actually a thermal evaporation process, and the lack of stoichiometry observed is due the dependence of evaporation on the varying vapor pressures of $Y_1Ba_2Cu_3O_7$. The higher energy represents the onset of the non-equilibruim process which results in the stoichiometry retention. It was thus suggested that an upper limit of $\approx 5\,J\,cm^{-2}$ be used when considering the modelled heat flow results. The wavelength dependence of the onset for ablation is clearly demonstrated in **Table 6.1**, where the threshold energy for ablation by various wavelength lasers is considered. It is apparent that short wavelength excimer lasers require less incident energy to remove material from the $Y_1Ba_2Cu_3O_7$ target. This stems from the very small absorption

TABLE 6.2: A comparison of experimentally and theoretically determined incident ablation threshold energies for various wavelength lasers. The asterisk (*) denotes results from heat flow simulations. The results from this investigation are indicated as (++).

Laser	Wavelength λ(nm)	Ablation threshold $E_{ab}(J\,cm^2)$	Ref.
ArF	193	0.11	[38]
KrF	248	0.11	[240]
KrF	248	0.11	[40]
KrF*	248	0.23	[218]
XeCl	308	0.23	[220]
Ruby*	694	0.3	(++)
Ruby	694	0.4	(++)
Nd:YAG	1064	0.60	[49]
Nd:YAG*	1064	0.66	[218]

depth of excimer lasers in YBCO due to the shorter wavelengths **[41, 48, 49]**. This implies that a smaller volume of material is heated directly by the laser, resulting in the lower threshold required to vaporise material. The intermediate value (between the values obtained for ultra-violet and infra-red lasers) obtained experimentally for

the threshold energy for the pulsed ruby laser is in accordance with the observed wavelength dependence of ablation and the intermediate situation of the ruby laser wavelength. The heat flow simulations presented by Nakajima **[218]** for ablation by ultravoilet and infra-red lasers are consistently higher than the observed values. These results do not seem reasonable if one considers that both the solid-liquid and the liquid-gas phase transitions are ignored by Nakamiya. It is more reasonable to assume that ignoring these factors will result in a lower threshold prediction, which was precisely what was observed in the simulation presented in this study, where the liquid-gas transition was left out and the experimentally determined threshold was higher than the simulated value.

The material deposited by laser ablation with a pulsed ruby laser had a highly forward peaked distribution of deposited material i.e. the thickness of the deposit dropped off very sharply as one moved outwards from the centre of the deposited area. The experimentally observed spatial distribution was fitted theoretically and found to agree with a $\cos^9(\theta)$ distribution of the thickness, in accordance with results obtained by others **[39, 244, 245]**. Measurement of the composition of the sample across the deposit indicates a retention of stoichiometry up to some distance from the centre, beyond which the stoichiometry varies. This was explained in terms of an overlapping non-thermal ($\cos^9(\theta)$) and a thermal ($\cos(\theta)$) distribution. Such an overlap of distributions was also seen by Venkatesan **[39]**. The origin of the forward peaked distribution has been attributed to the adiabatic expansion of the plasma plume into vacuum **[220]**, but as a result of the equilibruim nature of the heat flow simulation and the fact that the simulation only considers the development of the target temperature after irradiation such factors could not be accounted for by the model. The highly forward directed nature of the ablation process implies efficient use of the target and the extensive carrying power of the ablated plume was demonstrated by showing that the thickness of material deposited does not decrease rapidly with increased target-substrate separation. This is in contrast with the r^{-2} fall-off expected with, for instance, electron-beam evaporation.

The inclusion of high levels of oxygen into the deposited film during the

deposition process is desirable for the formation of in-situ superconducting films because of the critical dependence of the superconducting properties on the oxygen content. The amount of material deposited as a function of oxygen pressure was investigated and it was found that the highest pressure sustainable without significant loss of thickness of the deposit was $\approx 10^{-1}$ mbar. The decrease of thickness observed at higher gas pressures is attributed to thermalisation of the ablated plume. The observed limit corresponds to the values commonly used during deposition [18, 38, 39, 248].

Thin films of YBCO deposited by pulsed ruby laser ablation at 3 J cm^{-2} were slightly Ba-deficient and required a post-deposition anneal at 850°C to make them superconducting. A transition temperature of 84 K was found for the resistive measurement, with a depressed transition of 80 K noted for the susceptibility reading. A broader transition width of 7 K was observed for the susceptibility reading as compared to 2 K for the resistive reading .

Laser annealing of high quality thin film superconductors, formed by ICM sputtering, with a pulsed ruby laser was investigated and it was shown that at low energy densities depth controlled damage could be created in $Y_1Ba_2Cu_3O_7$ thin films. With a 50 mJ cm^{-2} incident flux a disordered layer of 20 nm was created in a high quality $Y_1Ba_2Cu_3O_7$ film. Higher flux irradiation of $Y_1Ba_2Cu_3O_7$ thin films (250 mJ cm^{-2}) results in complete destruction of the preferred orientation of the film and a randomisation of the channeling spectrum

CHAPTER 7

Summary and Conclusions

The growth and characterisation of thin film $Y_1Ba_2Cu_3O_7$ superconductors on oxide, silicon and silicide substrates was studied. The growth of $Y_1Ba_2Cu_3O_7$ films was investigated for pulsed ruby laser ablation and Inverted Cylindrical Magnetron (ICM) sputtering. ICM sputter deposition was used because the off-axis sputter configuration limits the re-sputtering effects seen in conventional sputter deposition of YBCO films. Single crystal substrates of MgO, $SrTiO_3$ and Al_2O_3 were used for the deposition of YBCO thin films in order to test the viability of the deposition method of ICM sputter deposition, establish the optimal conditions for film growth and to ascertain the quality of films obtained by this deposition method. The quality of such films was assessed against that of films deposited by others onto oxide substrates using a variety of deposition techniques. The merging of superconductor and semiconductor technologies on a single integrated device is extremely attractive for device purposes. This may be achievable with the growth of YBCO films on Si and Si-based substrates. The growth of thin film superconductors such as YBCO on silicides forms part of an integrated approach to combining superconductor and semiconductor devices on the same monolithic chip.

In determining the ideal conditions for the deposition of high quality thin films of YBCO, Rutherford backscattering spectrometry (RBS) was used to ascertain the thickness and stoichiometry of the deposited films and to determine whether

interaction between the YBCO film and the substrates occurs. This analysis was supported by the use of a RBS simulation programme, RUMP. X-ray diffraction analysis was used to detect the crystallographic orientations present in the film(s) and the presence of specific phases such as impurity phases of the superconductor YBCO. The electrical properties of the YBCO thin films were checked with 4-pt probe resistivity measurements and A.C. susceptibility readings.

In the determination of the parameters needed for growth of YBCO films with adequate thickness and ideal stoichiometry, MgO substrates were used and it was found that the total gas pressure and the oxygen partial pressure were of primary importance in influencing the effect of re-sputtering of deposited films. Stoichiometric films were deposited for a total pressure ($Ar+O_2$) of 4.5×10^{-1}mbar and oxygen partial pressure of 1.5×10^{-1}mbar, as the re-sputtering effect was found to be minimised at these values. From a measurement of the thickness homogeneity across the depositing area, it was established that thickness variation of less than 10% is observed for a radius of 10 mm from the centre of the deposit. Compositional homogeneity also exists within this radius.

It is known that MgO substrates react minimally with $Y_1Ba_2Cu_3O_7$. It was shown that the lowest substrate temperature for which good quality c-axis preferentially oriented films could be obtained on MgO was 700°C . The stoichiometry of these films was nearly exactly correct and no film-substrate interaction was observed. The good crystalline quality of these films was verified with ion channeling analysis which gave a minimum yield of $\chi_{min} = 7\%$ for the Ba peak in the YBCO film. The effect of substrate surface quality on the growth of high quality YBCO films on MgO was also investigated and it was shown that films on annealed substrates (1000°C for 1 hr in O_2) had superior electrical properties as compared to films on unannealed substrates. This was explained in terms of the ease of nucleation of the YBCO film on the annealed substrate. The oxygen resonance in the $^{16}O(\alpha,\alpha)^{16}O^*$ reaction at 3.045 MeV is an effective method to ascertain the oxygen stoichiometry in YBCO films. Using this technique it was confirmed that the YBCO films deposited by ICM sputter deposition at 700°C were highly oxygenated, having an oxygen composition

>6.7, which could be correlated with the superconducting nature of these films as shown in the electrical measurements. Ion channeling was used for structure analysis of the growth of high quality films (χ_{min} = 7%, T_c = 85 K, ΔT = 1 K) of $Y_1Ba_2Cu_3O_7$ on single crystal MgO<100> substrates. Using angular scans of the backscattering yields for the film and from the substrate, taken for both normal incident and for inclined incidence (45°), it was verified that the assumption of c-axis orientation is correct. Strain relieving defects were observed at the MgO-YBCO interface but the nature of these defects could not be positively ascertained. The mosaicity of the YBCO film on MgO was examined and a mosaic spread of 0.22° was calculated, which denotes a narrow directional spread of the YBCO film crystallites and points to good (hetero) epitaxial film growth.

The growth of YBCO on $SrTiO_3$ was similar to that on MgO. Films deposited at 700°C were preferentially c-axis oriented and showed formation of the superconducting phase in-situ. Examination of these films with ion channeling analysis gave a minimum yield of 6% for the Ba signal. The dechanneling at the interface was lower than for films on MgO and this was explained in terms of the smaller lattice mismatch of YBCO with $SrTiO_3$. The mosaicity of the film was calculated to be 0.15°, lower than that found for MgO substrates and proving that the film quality is improved because of the better lattice matching conditions. The transition temperature for the onset of superconductivity, T_c, for films on $SrTiO_3$ was found at 87 K and a sharp transition width ΔT of 1 K was detected. The normal state resistivity extrapolates to zero resistance at zero Kelvin. A.C. susceptibility measurement of the magnetic flux expulsion, i.e. the Meissner effect, gave a transition temperature of 87 K and a transition width of <2 K as proof that the film is homogenous and of good quality.

The growth of YBCO films in-situ by ICM Sputter deposition at 700°C onto Al_2O_3 did not yield good superconducting films because of severe interaction between YBCO and Al_2O_3. Weakly superconducting behaviour at relatively low temperatures was observed. A MgO buffer layer was therefore used to prevent the film-substrate interaction. The electrical properties of the YBCO film on the MgO buffered Al_2O_3 substrate was substantially improved in that a high transition tem-

perature for the resistive measurement (T_c=83 K) and a relatively sharp transition width (3 K) was observed.

A comparison of the quality of films produced on oxide substrates in this work by ICM sputter deposition, with other deposition methods and with the work of others shows that the results obtained in this study are as good as (or sometimes even better than) the results from other studies.

In studying the growth of $Y_1Ba_2Cu_3O_7$ films on Si it was found that a severe reaction between single crystal Si and YBCO occurs upon deposition by ICM sputtering at 700°C . Poor superconducting properties were observed for the YBCO film. The Si-YBCO interaction was studied in greater detail by considering the reaction of the systems Si-Cu, Si-Ba, Si-Cu-Ba and Si-Ba-Cu at different annealing temperatures in an O_2 flow and it was shown that Cu and Ba in combination react vigorously with the Si substrate. The use of oxide buffer layers on Si was thus considered. The thermal stability of MgO, Y_2O_3 and ZrO_2 layers on Si was first assessed and it was established that the oxide layers are stable at the sputter deposition temperature of 700°C . Thin film superconductors grown on the Si-metal oxide structures by ICM sputter deposition at 700°C were found to be superconducting in-situ, with high T_c values (83 K) and relatively sharp transition widths (5 K), thus demonstrating that the buffer layers were effective in preventing the film-substrate reaction and in retaining the superconducting properties of the YBCO film. A comparison of results obtained in this study and by others for depositions onto Si, either direcly or with buffer layers, showed that the use of buffer layers considerably improves the quality of YBCO films on Si.

The growth of Si-silicide-superconductor and Si-silicide-metal oxide- superconductor (SSMOS) structures was also investigated. The growth of YBCO films by ICM deposition onto the silicides PtSi, PdSi, $CrSi_2$, $NiSi_2$ and $CoSi_2$ was attempted but it was found that the YBCO layer reacts severely with all of the silicides and superconductivity in the YBCO layer was destroyed. Unlike the case for the deposition of YBCO onto single crystal Si, where some superconducting behaviour was observed (albeit poor) no evidence for superconductivity was found, demonstrating

that the YBCO-silicide interaction is more severe than that of YBCO with single crystal Si. A possible mechanism for the enhanced reaction between YBCO and silicides was suggested in terms of the increased mobility of the silicon in the silicide as compared to silicon in the single crystal form.

The severe interaction between silicides and YBCO prevented the deposition of YBCO films directly onto silicides and necessitated the use of MgO, ZrO_2 and Y_2O_3 buffer layers to preserve the film quality of the superconductor and silicide layers. From an examination of the thermal stability of the semiconductor-silicide-metal oxide subsystem it was found that the Si/silicide/metal oxide structures were stable at 700°C for all the metal oxide and silicide layers. The growth of YBCO films on the silicon/silicide/metal oxide structures by ICM sputter deposition at 700°C gave polycrystalline YBCO films, with varying degrees of c-axis orientation noted. The growth of highly textured YBCO films on polycrystalline buffer layers was attributed to the anisotropic growth of YBCO, where the a-b plane grows an order of magnitude faster than the c-axis direction. In terms of the electrical measurements, Y_2O_3 performed worst as a buffer layer, the best results being obtained on MgO buffer layers with intermediate results for ZrO_2 buffer layers.

Work on the use of an amorphous Co-Zr alloy to simultaneously form an epitaxial $CoSi_2$ layer on Si<111> buried beneath a capping ZrO_2 layer is, as far as could be ascertained, unique to this study. It is found to be an extremely promising method of forming epitaxial silicides at temperatures which are more compatible with device fabrication. The formation of the alloy was brought about by a solid state amorphization reaction in which the elements Co and Zr were reacted with each other at a temperature below the crystallization temperature of amorphous Co-Zr. Annealing the Si<111>/α-CoZr sample in O_2 at 650°C gave a Si/$CoSi_2$/ZrO_2 structure, the $CoSi_2$ layer growing epitaxially on the Si<111> substrate. The growth of the $CoSi_2$ layer directly and without intermediate phase formation was considered in terms of the Effective Heat of Formation model, which was successfully applied to predict the phase formation in terms of a reduced Co availability. Thin films of YBCO deposited onto the Si/$CoSi_2$/ZrO_2 structures by ICM sputter deposition

at 700°C were superconducting as-deposited. Electrical measurements gave high T_c values (81 K) for the resistivity readings. A slightly depressed susceptibility measurement of 78 K was found.

Laser ablation has become a popular deposition technique because of the ease of deposition, the ability to work at high pressures and the ability to retain the stoichiometry of complex targets. As far as can be ascertained, this is the first study detailing the growth of YBCO films by pulsed ruby laser ablation. The modelling of the ruby laser-YBCO interaction has also not been reported previously. The interaction of the pulsed ruby laser (λ=694 nm, τ=30ns) and the solid $Y_1Ba_2Cu_3O_7$ target was modelled in terms of a one-dimensional heat flow equation, which was solved numerically using a finite element method and the evolution of temperature calculated as a function of time and depth into the target. Using the heat-flow simulations it was deduced that the minimum incident energy density for which the surface temperature exceeds the vaporization temperature ($T_{vap} \approx$ 2500K) was 0.3 J cm^{-2}. This incident laser energy was referred to as the threshold energy for vaporization or the ablation threshold E_{ab}. Similarly the threshold for melting was found to occur at an incident laser energy of 0.15 J cm^{-2}. The heat loss mechanisms in the evolution of temperature were examined and it was concluded that radiative and convective losses play a minor role in the development of the temperature profile into the target and the major loss mechanism after irradiation by the laser pulse is thermal conductivity. The effects of plasma production and laser-plasma interaction were expanded on and it was established that reflection of the laser pulse could occur if the plasma density was sufficiently high. Using the concept of melt depth a similar principle was applied in considering the thickness of material above the vaporization temperature and a new concept called an ablation depth was defined. The recondensation of evaporated material, the possibility of the recoil pressure of the laser suppressing evaporation and evidence of extremely high pressures during ablation were discussed as possible mechanisms to reduce the evaporated yield. Experimentally, an ablation threshold of 0.4 J cm^{-2} was found. Examination of the amount of material deposited as a function of

incident energy led to the conclusion that the heat flow simulation (and hence the thermal model) is only valid for low energy densities. The high energy data could be phenomenologically explained in terms of a plasma production mechanism.

Assessment of the stoichiometry as a function of laser energy density, reveals that there is a threshold for the deposition of near-stoichiometry films which is higher than the ablation threshold and which was found to be $2\,\mathrm{J\,cm^{-2}}$. The discrepancy in ablation and stoichiometry thresholds was interpreted as an indication of different processes ocurring at the two energy regimes. At low energy the removal of material is dominated by a thermal process, and the high energy regime represents a non-equilibruim process which results in the stoichiometry retention. The wavelength dependence of the onset for ablation was clearly demonstrated when the threshold energy for ablation by various wavelength lasers was examined. The material deposited by laser ablation with a pulsed ruby laser had a highly forward peaked distribution which was fitted theoretically and found to agree with a $\cos^9(\theta)$ distribution. The highly forward directed nature of the ablation process implies efficient use of the target and the extensive carrying power of the ablated plume was demonstrated by showing that the thickness of material deposited does not decrease rapidly with increased target-substrate separation. The amount of material deposited as a function of oxygen pressure was investigated and it was found that the highest pressure sustainable, without significant loss of thickness of the deposit, was $\approx 10^{-1}$ Torr. Thin films of YBCO deposited by pulsed ruby laser ablation at $3\,\mathrm{J\,cm^{-2}}$ were post-annealed at 850°C to the superconducting phase and had a transition temperature of 84 K with resistive measurements and 80 K with susceptibility measurements. The as-deposited YBCO films were slightly Ba-deficient. It is noteworthy that relatively good quality post-annealed films could be obtained with laser ablation but not with ICM sputtering. This is attributed to the high O_2 content during sputtering and the high energies of the ablated particles.

Laser annealing of high quality thin film superconductors, formed by ICM sputtering, with a pulsed ruby laser was also investigated and it was shown that at low energy densities depth controlled damage could be created in $Y_1Ba_2Cu_3O_7$ thin

films. With a 50 mJ.cm^{-2} incident flux a disordered layer of 20 nm was created in a high quality $Y_1Ba_2Cu_3O_7$ film. Higher flux irradiation of $Y_1Ba_2Cu_3O_7$ thin films (250 mJ.cm^{-2}) results in complete destruction of the preferred orientation of the film.

References

[1] R.M. Silver, J. Talvacchio, and A.L. de Lozanne, Appl. Phys. Lett. **51**, 2149 (1987).

[2] W.Y. Lee, J. Salem, Y. Lee, C.T. Retter, and G. Lim, AIP Conf. Proc. **165**, 95 (1987).

[3] H.C. Li, G. Linker, F. Ratzel, R. Smithey, and J. Geerk, Appl. Phys. Lett. **52**, 1098 (1988).

[4] G.K. Wehner, Y.H. Kim, D.H. Kim, and A.M. Goldman, Appl. Phys. Lett. **52**, 1187 (1988).

[5] J. Gao, Y.Z. Zhang, B.R. Zhao, P. Oat, C.W. Yuan, and L. Li, Appl. Phys. Lett. **53**, 2675 (1988).

[6] H. Adachi, K. Hiroshi, K. Setsune, M. Kitabatake, and K. Nasa, Appl. Phys. Lett. **51**, 2263 (1987).

[7] P. Berberich, J. Tate, W. Dietsche, and H. Kinder, Appl. Phys. Lett. **53**, 925 (1988).

[8] Q.X. Jia, K.L. Jiao, and W.A. Anderson, J. Appl. Phys. **70**, 3364 (1991).

[9] A. Lubig, Ch. Buchal, J. Frohlingsdorf, W. Zander, and B. Stritzker, Nucl. Instrum. Meth. **B50**, 114 (1990).

[10] T. Venkatesan, E.W. Chase, X.D. Wu, A. Inam, C.C. Chang, and F. Shokoohi, Appl. Phys. Lett. **53**, 243 (1988).

[11] M. Migliuolo, A.K. Stamper, D.W. Greve, and T.E. Schlesinger, Appl. Phys. Lett. **54**, 859 (1989).

[12] D.K. Fork, F.A. Ponce, J.C. Tramontana, and T.H. Geballe, Appl. Phys. Lett. **58**, 2294 (1991).

[13] B.J. Kellet, J.H. James, A. Gauzzi, B. Dwir, and D. Pavuna et al., Appl. Phys. Lett. **57**, 1146 (1990).

[14] X.D. Wu, R. Muenchausen, S. Foltyn, R.C. Estler, and R.C. Dye et al., Appl. Phys. Lett. **57**, 523 (1990).

[15] R.K. Singh, J. Narayan, A.K. Singh, and J. Krishnaswamy, Appl. Phys. Lett. **54**, 2271 (1989).

[16] S. Witanachi, S. Patel, D.T. Shaw, and H.S. Kwok, Mater. Lett. **8**, 53 (1989).

[17] B. Roas, L. Schultz, and G. Endres, Appl. Phys. Lett. **53**, 1557 (1988).

[18] S. Witanachi, H.S. Kwok, X.W. Wang, and D.T. Shaw, Appl. Phys. Lett. **52**, 1825 (1988).

[19] J. Narayan, N. Niunno, R. Singh, O.W. Holland, and O. Auciello, Appl. Phys. Lett. **51**, 1845 (1987).

[20] S.H. Liou, M. Hong, B.A. Davidson, R.C. Farrow, and J. Kwo et al., AIP Conf. Proc. **165**, 79 (1987).

[21] S.J. Lee, E.D. Rippert, B.Y. Jin, and S.N. Song, Appl. Phys. Lett. **51**, 1194 (1987).

[22] S.I. Shah and P.F. Garcia, AIP Conf. Proc. **165**, 50 (1987).

[23] J.L. Makous, L. Maritato, C.M Falco, and J.P. Cronin, Appl. Phys. Lett. **51**, 2164 (1987).

[24] S.Y. Lee, B. Murdock, D. Chin, and T van Duzer, AIP Conf. Proc. **165**, 427 (1987).

[25] T.I. Selinder, G. Larson, U. Helmersson, P. Olsen, and S. Rudner et al., Appl. Phys. Lett. **52**, 1907 (1988).

[26] R.L. Sandstrom, W.J. Gallagher, T.R. Dinger andR.H. Koch, and R.B. Laibowitz et al., Appl. Phys. Lett. **53**, 444 (1988).

[27] N.D. Westwood, MRS Bulletin **13**, 47 (1988).

[28] M. Muroi, T. Matsui, Y. Kornuwa, Y. Okamura, K. Tsuda, M. Nagano, and K. Mukae, J. Mater. Res **4**, 781 (1989).

[29] R.B. Laibowitz, R.H. Kah, P. Chaudhari, and R.J. Gambino, Phys. Rev. **B35**, 8821 (1987).

[30] B. Oh, M. Naito, S. Arnason, P. Rosenthal, and R. Barton et al., Appl. Phys. Lett. **51**, 852 (1987).

[31] X.D. Wu, A. Inam, T. Venkatesan, C.C. Chang, and E.W. Chase et al, Appl. Phys. Lett **52**, 754 (1988).

[32] H.S. Kwok, P. Mattocks, L. Shi, X.W. Wang, and S. Witanachi et al., Appl. Phys. Lett. **52**, 1825 (1988).

[33] H. Koinuma, M. Kawasaki, S. Nagata, K. Takeuchi, and K. Fueki, J. J. Appl. Phys. **27**, L376 (1988).

[34] X.X. Xi, G. Linker, O. Meyer, E. Nold, B. Obst, R. Smithey F. Reitzel, B. Strehlau, F. Weschenfelder, and J. Geerk, Z. Phys. **B74**, 13 (1989).

[35] K.Char, M.S. ColClough, S.M. Garrison, N. Newman, and G. Zaharchuk, Appl. Phys. Lett. **59**, 733 (1992).

[36] S.J. Rosner, K.Char, and G. Zaharchuk, Appl. Phys. Lett. **60**, 1010 (1992).

[37] S. Foltyn, R. Muenchausen, R. Estler, E. Petersson, and W.B. Hutchinson et al., Mat. Res. Soc. Symp Proc. **191**, 205 (1990).

[38] U. Sudarson, N.W. Cody, M. Bozack, and R. Solanki, J. Mater. Res. **3**, 825 (1988).

[39] T. Venkatesan, X.D. Wu, A. Inam, and J.B. Wachtman, Appl. Phys. Lett. **52**, 1193 (1988).

[40] D.B. Geohayan, N.D. Mashburn, R.J. Culbertson, S.J. Pennycook, and J.D. Budai et al., J. Mater. Res. **3**, 1169 (1988).

[41] O. Eryu, K. Murakami, K. Takita, and K. Masuda, Nucl. Instrum. Meth. **B39**, 640 (1989).

[42] R. Kelly, J.J. Cuomo, P.A. Leary, J.E. Rothenberg, B.E. Braren, and C.F. Aliotta, Nucl. Instrum. Meth. **B9**, 329 (1985).

[43] J.E. Rothenberg and R. Kelly, Nucl. Instrum. Meth. **B1**, 291 (1984).

[44] R.F. Kelly and J.E. Rothenberg, Nucl. Instrum. Meth. **B7**, 755 (1985).

[45] J.T. Cheung and H. Sankur, CRC Crit. Rev. Sol. Stat. Mater. Sci. **15**, 63 (1988).

[46] N. Itoh, Nucl. Instrum. Meth. **B27**, 155 (1987).

[47] P. Avouris, F. Bozso, and R.E. Walkup, Nucl. Instrum. Meth. **B27**, 136 (1987).

[48] G. Koren, A. Gupta, R.J. Baseman, M.I. Lutwyche, and R.B. Laibowitz, Appl. Phys. Lett. **55**, 2450 (1989).

[49] O. Eryu, K. Murakami, K. Takita, K. Masuda, and H. Uwe et al., Jap. J. Appl. Phys. **27**, L628 (1988).

[50] O. Kubaschewski and C.B. Alcock, *Metallurgical Thermochemistry* (Pergamon Press, Oxford, 1979), p. 268.

[51] E.S. Machlin, *An Introduction to Aspects of Thermodynamics and Kinetics Relevant to Materials Science* (Giro Press, New York, 1991).

[52] R.E. Watson and L.H. Bennett, Phys. Rev. Lett. **43**, 1130 (1979).

[53] A. Pasturel, C. Colinet, and P. Hicter, CALPHAD **9**, 349 (1985).

[54] J. van der Rest, F. Gautier, and F. Brouers, J. Phys. F **5**, 2283 (1975).

[55] Jr. C.D. Gelatt, A.R. Williams, and V.L. Moruzzi, Phys. Rev. B **27**, 2005 (1983).

[56] A.R. Miedema, P.F. de Châtel, and F.R. de Boer, Physica **100B**, 1 (1980).

[57] F.R. de Boer, R. Boom, W.C.M. Mattens, A.R. Miedema, and A.K. Niessen, in *Cohesion in Metals*, edited by F.R. de Boer and D.G. Pettifor (North Holland, Amsterdam 1988) Vol 1 of Series on Cohesion and Structure.

[58] D.B. Fenner, D.K. Biegelsen, and R.D. Bringans, J. Appl. Phys. **66**, 419 (1989).

[59] B.H. Moeckly, S.E. Russeck, D.K. Lathrop, R.A. Buhiman, J. Li, and J.W. Mayer, Appl. Phys. Lett. **57**, 1687 (1990).

[60] M.G. Norton, S.R. Summerfelt, and C.B. Carter, Appl. Phys. Lett **56**, 2246 (1990).

[61] C.B. Eom, J.Z. Sun, K. Yamamoto, A.F. Marshall, K.E. Luther, and T.H. Geballe, Appl. Phys. Lett. **55**, 595 (1989).

[62] A.C. Westerheim, B.I. Choi, M.I. Flik, M.J. Cima, R. Slattery, and A.C. Anderson, J. Vac. Sci. Technol. **10**, 3407 (1992).

[63] A. Inam, M.S. Hegde, X.D. Wu, T. Venkatesan, and P. England et al., Appl. Phys. Lett. **53**, 908 (1988).

[64] G. Koren, E. Polturak, B. Fisher, D. Cohen, and G. Kimel, Appl. Phys. Lett **53**, 2230 (1988).

[65] C.T. Blue, C.A. Blue, and P. Boolchand, J. Appl. Phys. **72**, 1021 (1992).

[66] J.L. Vossen and W. Kern, *Thin Film Processes* (Academic, New York, 1978).

[67] E. Akoh, F. Shinoki, M. Takahashi, and S. Takada, Appl. Phys. Lett. **52**, 1732 (1988).

[68] R. Roth, M.R. deGuire, L.E. Dolhert, and A.F. Hopp, J. Mater. Res. **6**, 2041 (1991).

[69] D.G. Xenikos and T.R. Lemberger, Rev. Sci. Instrum. **60**, 831 (1989).

[70] R.L. Sandstrom, E.A. Giess, W.J. Gallagher, A. Siegmuller, and E.I. Cooper, Appl. Phys. Lett. **53**, 1874 (1988).

[71] K. Shinohara, V. Matijasevic, P.A. Rosenthal, R.H. Hammond A.F. Marshall, and M.R. Beasley, Appl. Phys. Lett. **58**, 756 (1991).

[72] B.T. Ahn, V.Y. Lee, and R. Beyers, Physica C **167**, 529 (1990).

[73] S. Maniv and W.D. Westwood, J. Vac. Sci. Technol. **17**, 743 (1980).

[74] W.D. Westwood, *Physics of Thin Films* (Academic, New York, 1989), p. 14.

[75] D.K. Lathrop, S.E. Russek, and R.A. Buhrman, Appl. Phys. Lett. **51**, 1554 (1987).

[76] L.R. Doolittle, Nucl. Inst. Meth. **B9**, 344 (1985).

[77] J.B. Nilson and D.P. Riley, Proc. Phys. Soc. **57**, 160 (1945).

[78] L.C. Feldman, J.W. Mayer, and S.T. Picraux, *Materials Analysis by Ion Channeling* (Academic, New York, 1982).

[79] M.G. Norton, L.A. Tietz, S.R. Summerfelt, and C.B. Carter, Appl. Phys. Lett. **55**, 2348 (1989).

[80] F.J. Muller, J.C. Gallop, and A.D. Caplin, Supercond. Sci. Technol. **5**, 501 (1992).

[81] Y. Chen, J. Zang, and Z. Wu, Supercond. Sci. Technol. **5**, 463 (1992).

[82] G. Cannelli, R. Cantelli, and F. Trequanttrini, Supercond. Sci. Technol. **5**, 247 (1992).

[83] W.K. Chu, J.W. Mayer, and M.A. Nicolet, *Backscattering Spectometry* (Academic Press, New York, 1978).

[84] B.K. Patniak, C.V. Barros-Leite, G.B. Baptista, E.A. Schweikert, D.L. Coche, L. Quinones, and N. Magnussen, Nucl. Instrum. Meth. **B35**, 159 (1988).

[85] B. Blanpain, P. Revez, L.R. Doolittle, K.H. Rurserand, and J.W. Mayer, Nucl. Instrum. Meth. **B34**, 459 (1988).

[86] J.R. Tesmer and M. Nastasi, Nucl. Instrum. Meth. **B45**, 476 (1990).

[87] S.T. Picraux, L.R. Dawson, J.Y. Tsao, B.L. Doyle, and S.R. Lee, Nucl. Instrum. Meth. **B33**, 891 (1988).

[88] O. Meyer, J. Geerk, Q. Li, G. Linker, and X.X. Li, Nucl. Instrum. Meth. **B45**, 483 (1990).

[89] E. Ramesh, D. Hwang, T.S. Ravi, A. Inam, J.B. Bamer, S.W. Chan R. Ramesh, C.Y. Chen, B. Dutta, T. Venkatesan, and X.D. Wu, Appl. Phys. Lett. **56**, 2243 (1990).

[90] S. Tong-Lee, S. Chen, L.S. Hung, and G. Braunstein, Appl. Phys. Lett **55**, 286 (1989).

[91] H. Ishiwara and S. Furukawa, J. Appl. Phys. **47**, 1686 (1976).

[92] N.G. Stoffel, P.A. Morris, W.A. Bonner, and B.J. Wilkens, Phys. Rev. **B37**, 2297 (1988).

[93] M. Gurvitch and A.T. Fiory, Appl. Phys. Lett. **51**, 1027 (1987).

[94] P.K. Gallagher, H.M. O'Bryan, S.A. Sunshine, and D. Murphy, Mater. Res. Bull. **22**, 885 (1987).

[95] J.J. Cuomo, M.F. Chisholm, D.S. Yee, D.J. Mikalsen, P.B. Madakson, and J. Karasinski, AIP Conf. Proc. **165**, 141 (1987).

[96] P. Houdy, J.A. Sirat, J.B. Theetan, J.P. Landesman, and H. Baudry et al., AIP Conf. Proc. **164**, 114 (1987).

[97] S. Hatta, H. Higashino, K. Hirochi, H. Adachi, and K. Wasa, Appl. Phys. Lett. **53**, 148 (1988).

[98] M. Futamoto and Y. Honda, Japn. J. Appl. Phys. **27**, 273 (1988).

[99] H. Nakajima, S. Yamaguchi, K. Iwasaki, H. Morita, and H. Fujimori, Appl. Phys. Lett. **53**, 1437 (1988).

[100] C.X. Qui and I. Shih, Appl. Phys. Lett. **52**, 587 (1988).

[101] D. Dijkkamp, T. Venkatesan, X.D. Wu, S.A. Shaheen, and N. Jisrani et al., Appl. Phys. Lett. **51**, 619 (1987).

[102] A.M. de Santolo, M.L. Mandich, M.F. Jarrold, J.E. Bower, and S. Sunshine, AIP Conf. Proc. **165**, 174 (1987).

[103] T. Venkatesan, C.C. Chang, D. Dijkkamp, S.B. Ogale, and E.W. Chase et al., J. Appl. Phys. **63**, 4591 (1988).

[104] R.J. Lin, Y.C. Chen, J.H. Kung, and P.T. Wu, in *MRS Symposium Proceedings 99*, edited by M. Brodsky, R. Dynes, K. Kitazama, and H.L. Tuller Materials Research Society, Pittsburgh, 1988, p. 319.

[105] C.T.Cheung and E.Ruckenstein, J. Mater. Res. **4**, 1 (1989).

[106] R.M. Silver, A.B. Berezin, W. Wendman, and A.L. de Lozanne, Appl. Phys. Lett. **52**, 2174 (1988).

[107] B. Dam, T.S. Baller, G.N.A. van Veen, H.A.M. van Hal, J.W.C. de Vries, and G.M. Stollman, in *MRS Symposium Proceedings 99*, edited by M. Brodsky, R. Dynes, K. Kitazama, and H.L. Tuller Materials Research Society, Pittsburgh, 1988, p. 303.

[108] R. Hu, C. Jiang, and H.L. Luo, Mater. Res. Bull. **23**, 1159 (1988).

[109] L.S. Hung, L.R. Zheng, and T.N. Blanton, Appl. Phys. Lett. **60**, 3129 (1992).

[110] W.Y. Hsu and R. Raj, Appl. Phys. Lett. **60**, 3105 (1992).

[111] C. Nguyen M.Z. Tseng, E. Tarsa, L.D. Change, E.L. Hu, and H. Kroemer, Appl. Phys. Lett **61**, 601 (1992).

[112] K. Nashimoto, D.K. Fork, and T.H. Geballe, Appl. Phys. Lett **60**, 1199 (1992).

[113] L.D. Chang, M.Z. Tseng, E.L. Hu, and D.K. Fork, Appl. Phys. Lett. **60**, 1753 (1992).

[114] A.B. Berezin, C.W. Yuan, and A.L. de Lozanne, Appl. Phys. Lett. **57**, 90 (1990).

[115] P. Vouristo, T. Mantyla, and P. Ketrunen, Vacuum **42**, 1001 (1991).

[116] D.K. Fork, K. Nashimoto, and T.H. Geballe, Appl. Phys. Lett. **60**, 1621 (1992).

[117] W.Y. Lee, J. Salem, V. Lee, T. Huang, and R. Savoy et al., Appl. Phys. Lett. **52**, 2263 (1988).

[118] T. Asano, K. Tran, A.S. Byrne, M.M. Rahman, and C.Y. Yang, Appl. Phys. Lett. **54**, 1275 (1989).

[119] S. Chromik, J. Sith, V. Strbik, J. Schilder, and V. Smatko et al., J. Appl. Phys. **66**, 1477 (1989).

[120] D.K. Fork, D.B. Fenner, R.W. Barton, J. Phillips, G. Connell, J. Boyce, and T.H. Geballe, Appl. Phys. Lett. **57**, 1161 (1990).

[121] A. Tsukamoto, K. Imagawa, M. Hiratani, T. Aida, and K. Miyauchi, J. Appl. Phys. **68**, 5278 (1990).

[122] J.J. Yeh, M.Hong, and R. Felder, Appl. Phys. Lett. **54**, 1163 (1989).

[123] N. Missert, R. Hammond, J.E. Mooij, V. Mailasevic, and P. Rosenthal et al., IEEE Trans. Magn. **25**, 2418 (1989).

[124] J. Kwo, M.Hong, D.J. Trevor, R.M. Fleming, and A.E. White et al., Physica C **162**, 623 (1989).

[125] Q.X. Jia and W.A. Anderson, Appl. Phys. Lett. **57**, 304 (1990).

[126] D. Hwang, E. Ramesh, C.Y. Chen, X.D. Wu, and A. Inam et al., J. Appl. Phys. **68**, 1172 (1990).

[127] S.Muira, T. Yoshita, S. Matsubra, and Y.Miyasaka et al., Appl. Phys. Lett. **53**, 1967 (1988).

[128] A. Bardal, M. Zwerger, O. Eibl, J. Wecker, and Th. Matthee, Appl. Phys. Lett. **61**, 1243 (1992).

[129] Th. Matthee, J. Wecker, H. Behner, and G. Friedel, Appl. Phys. Lett. **60**, 1240 (1992).

[130] S. Hontsu, N. Mukai, J. Ishii, T. Kawai, and S. Kawai, Appl. Phys. Lett. **61**, 2709 (1992).

[131] A. Mogro-Campero, B.D. Hunt, L.G. Turner, M.C. Burrell, and W.E. Balz, Appl. Phys. Lett. **52**, 584 (1988).

[132] H. Koinuma, K. Fukuda, T. Hashimoto, and K. Fueki, Japn. J. Appl. Phys. **27**, L1216 (1988).

[133] A. Chourasia, D. Chopra, A.H. Bensaoula, A. Bensaoula, and P. Ruzakowski, J. Vac. Sci. Technol. **10**, 115 (1992).

[134] D.B. Fenner, A. Viano, D.K. Fork, G. Connell, and J.B. Boyce et al., J. Appl. Phys. **69**, 2176 (1991).

[135] S.Q. Hong, C.M. Comrie, S.W. Russell, and J.W. Mayer, J. Appl. Phys. **70**, 3655 (1991).

[136] D. Pavuna, W. Baer, H. Berger, V. Gasporov, and M. Schmidt et al., in *MRS Symposium Proceedings 99*, edited by M. Brodsky, R. Dynes, K. Kitazama, and H.L. Tuller Materials Research Society, Pittsburgh, 1988, p. 681.

[137] B.J. Lee and D.N. Lee, J. Am. Ceram. Soc. **74**, 78 (1991).

[138] C.W. Nieh, L. Anthony, J. Josefowicz, and F.G Krajenbrink, Appl. Phys. Lett. **56**, 2138 (1990).

[139] D.P. Norton, D.H. Lowndes, J.D. Budai, D.K. Christen, and E.C. Jones et al., J. Appl. Phys. **68**, 223 (1990).

[140] R.F. Kwasnick, F.E. Luborsky, E.L. Hall, M.F. Garbauskas, K Borst, and M.J. Curran, J. Mater. Res. **4**, 257 (1989).

[141] A. Lubig, C. Buchal, J. Schubert, C. Copetta, and D. Guggi et al., J. Appl. Phys. **71**, 5560 (1992).

[142] K. Hirata, K. Yamamoto, K. Iijima, J. Takada, and T. Terashima et al., Appl. Phys. Lett. **56**, 683 (1990).

[143] M. Gurvitch, L. Manchandra, and J.M. Gibson, Appl. Phys. Lett. **51**, 919 (87).

[144] A.B. Berezin, C.W. Yuan, and A.L. de Lozanne, IEEE Trans. Magn. **27**, 970 (1991).

[145] I. Shih, S.L. Wu, L. Li, C.X. Qiu, P. Grant, and M.W. Denhoff, Mater. Lett. **11**, 161 (1991).

[146] M. Sayer and M.S. Martin, Thin Solid Films **6**, 261 (1970).

[147] Q.Y. Ying, C. Hilbert, N. Kumar, D. Eichmann, M. Thompson, and H. Kroger, Appl. Phys. Lett. **59**, 3036 (1991).

[148] A. Oishi, T. Teshima, K. Ohata, H.Izumi, and S. Kawamoto et al., Appl. Phys. Lett. **59**, 1902 (1991).

[149] K. Takayi, T. Fukazawa, and K. Susa, J. Appl. Phys. **61**, 1030 (1987).

[150] K. Onisawa, M. Fuyama, K. Tamura, K. Taguchi, T. Nakayama, and Y.A. Ono, J. Appl. Phys. **68**, 719 (1990).

[151] H. Fukumoto, T. Imura, and Y. Osaka, Appl. Phys. Lett. **55**, 360 (1989).

[152] M. A Nicolet and S.S. Lau, *Formation and Characterization of Transition Metal Silicides VLSI Electronics - Microstructural Science* Volume 6 (Academic Press, New York, 1983).

[153] S.P. Murarka, *Silicides for VLSI Applications* (Academic Press, New York, 1983).

[154] R.T. Tung, J.M. Poate, J.C. Bean, J.M. Gibson, and D.C. Jacobson, Thin Solid Films **93**, 77 (1982).

[155] R.T. Tung, J.M. Gibson, and J.M. Poate, Phys. Rev. Lett. **50**, 429 (1983).

[156] J. Vrijmoeth, A.G. Schins, and J.F. Van der Veen, Phys. Rev. **B40**, 3121 (1989).

[157] S.A. Chambers, S.B. Anderson, H.W. Chen, and J.H. Weaver, Phys. Rev. **B34**, 913 (1986).

[158] L. Luo, R.E. Muenchausen, C.J. Maggiore, J.R. Jimenez, and L.J. Schonwalter, Appl. Phys. Lett. **58**, 419 (1991).

[159] A. Kumar and J. Narayan, Appl. Phys. Lett. **59**, 1785 (1991).

[160] S. Saitoh, H. Ishiwara, and S. Furukawa, Appl. Phys. Lett. **37**, 203 (1980).

[161] H.M. Meyer, D.M. Hill, J.H. Weaver, K.C. Goretta, and U. Balachandran, J. Mater. Res. **6**, 270 (1991).

[162] H.M. Meyer, D.M. Hill, J.H. Weaver, and K.C. Goretta, J. Appl. Phys. **67**, 1995 (1990).

[163] H.M. Meyer, D.M. Hill, J.H. Weaver, K.C. Goretta, and D.L.Nelson, Appl. Phys. Lett. **53**, 1004 (1988).

[164] R.D. Frampton, E.A. Irene, and F.M. d'Heurle, J. Appl. Phys. **62**, 2972 (1987).

[165] H. Jiang, C.S. Peterson, and M.A. Nicolet, Thin Solid Films **140**, 115 (1986).

[166] A. Hiraki, E. Lugujjo, and J.W. Mayer, J. Appl. Phys. **43**, 3643 (1972).

[167] R. de-Reus, *Stability of thin film amorphous metal alloys*, PhD thesis Rijks University, Utrecht 1990.

[168] R. de Reus, H.C. Tissink, and F.W. Saris, J. Mater. Res. **5**, 341 (1990).

[169] W.A.M. Aarnink, D.H.A. Blank, D.J. Adelerhof, J. Flokstra, and H. Rogalla et al., Appl. Surf. Sci. **47**, 195 (1991).

[170] W.A.M. Aarnink, *Interfaces in high T_c superconducting multilayers*, PhD thesis Twente University, Enschede 1992.

[171] J.M. Phillips, J.C. Hensel, D.C. Joy, and W.M. Augustyniak, MRS Symp. Proc. **74**, 609 (1987).

[172] J.M. Phillips, Mater. Res. Soc. Symp. Proc. **37**, 143 (1985).

[173] B.D. Hunt, N. Lewis, E.L. Hall, L.G. Turner, and L.J. Schowatter et. al., Mater. Res. Soc. Symp. Proc. **56**, 151 (1986).

[174] M.F. Wu, A. Vantomme, H. Pattyn, and G. Langouche et al., Nucl. Instrum. Meth. **B45**, 658 (1990).

[175] J.M. Phillips and W.M. Augustyniak, Mat. Res. Soc. Symp. Proc. **54**, 307 (1986).

[176] R.W. Fathauer, D.B. Hunt, and L.J. Schowalter, Appl. Phys. Lett. **49**, 64 (1986).

[177] C.C. Cho, H.Y. Liu, and H.L. Tsai, Appl. Phys. Lett. **61**, 270 (1992).

[178] S. Chan, E.W. Chase, B.J. Wilkens, and D.L. Hart, Appl. Phys. Lett. **54**, 2032 (1989).

[179] R.B. Schwarz and W.L. Johnson, Phys. Rev. Lett. **51**, 415 (1983).

[180] S. Herd, K.N. Tu, and K.Y. Ahn, Appl. Phys. Lett. **42**, 597 (1983).

[181] K. Samwer, Physics Reports **161**, 41 (1988).

[182] F. Hong, B. Patniak, and G.A. Rozgoyni, MRS Symp. Proc. **298**, 587 (1992).

[183] G.A. Rozgoyni, J.H. Lee, D. Knoesen, and D. Adams, Appl. Phys. Lett. **58**, 729 (1991).

[184] M.L.A. Dass, D.B. Fraser, and C.S. Wei, Appl. Phys. Lett. **58**, 1308 (1991).

[185] T. Jagielinski, J. Appl. Phys. **61**, 3237 (1987).

[186] K. Hayashi, M. Hayakawa, and Y. Ochiai et al., J. Appl. Phys. **61**, 2983 (1987).

[187] G.A. Bertero, T.C. Hufnagel, and R. Sinclair, J. Mater. Res. **8**, 771 (1993).

[188] G. Suran, M. Naili, and J. Sztern, J. Appl. Phys. **63**, 4318 (1988).

[189] J.I. Guzman and M.H. Kryder, J. Appl. Phys. **61**, 3240 (1987).

[190] L. Smardz, U. Kobler, and W. Zinn, J. Appl. Phys. **71**, 5199 (1992).

[191] J.J. Hauser, Phys. Rev. **B32**, 1985 (2887).

[192] Y.T. Cheng, W.L. Johnson, and M.A. Nicolet, Appl. Phys. Lett. **47**, 800 (1985).

[193] H. Schroder and K. Samwer, J. Mater. Res. **3**, 461 (1988).

[194] J.C. Barbour, Phys. Rev. Lett. **55**, 2872 (1985).

[195] R.T. Tung, A.F.J. Levi, and J.M. Gibson, Appl. Phys. Lett. **48**, 635 (1986).

[196] R.T. Tung, J. Vac. Sci. Technol. **A7**, 598 (1989).

[197] J.C. Hensel, R.T. Tung, J.M. Poate, and F.C. Unterwald, Phys. Rev. Lett. **54**, 1840 (1985).

[198] F.A. D'vitaya, S. Delage, E. Rosencher, and J. Derrien, J. Vac. Sci. Technol. **B3**, 770 (1985).

[199] K. Maex, J. Vanhellemont, S. Peterson, and A. Lauwers, Appl. Surf. Sci. **53**, 273 (1991).

[200] R. Jebasinski, S. Mantl, L. Vescan, and C. Dieker, Appl. Surf. Sci. **53**, 264 (1991).

[201] R. Pretorius, MRS Proc. **25**, 15 (1984).

[202] R. Pretorius, Vacuum **41**, 1038 (1990).

[203] R. Pretorius, R. de Reus, A.M. Vredenberg, and F.W. Saris, Materials Letters **9**, 494 (1990).

[204] R. Pretorius, R. de Reus, A.M. Vredenberg, and F.W. Saris, J. Appl. Phys. **70**, 3636 (1991).

[205] R.Pretorius, C.C. Theron, and T.K. Marais, Mat. Sci. Eng. **10**, 1 (1993).

[206] E.C. Cahoon, C.M. Comrie, and R. Pretorius, Appl. Phys. Lett. **44**, 511 (1984).

[207] E.C. Cahoon, C.M. Comrie, and R. Pretorius, MRS Proc. **25**, 57 (1984).

[208] S.S. Lau, J.W. Mayer, and K.N. Tu, J. Appl. Phys. **49**, 4005 (1978).

[209] F. d'Heurle, Thin Solid Films **128**, 283 (1985).

[210] L. Van den Hove, R. Wolters, K. Maex, R. de Keersmaecker, and G. Declerck, J. Vac. Sci. Technol. **B4**, 1358 (1986).

[211] C.D. Lien, M.A. Nicolet, and S.S. Lau, Appl. Phys. Lett. **34**, 249 (1984).

[212] R.Pretorius, M.C. Chen, and H.A. Ras, Mater. Lett. **3**, 282 (1985).

[213] A.H. Reader, J.P.W.B. Duchateau, J.E. Crombeen, and E.P. Naburgh, Appl. Surf. Sci. **53**, 92 (1991).

[214] H.S. Carslaw and J.C. Jaeger, *Conduction of Heat in Solids, 2nd Ed.* (Clarendon Press, Oxford,1959).

[215] T.K. Marais, R. Pretorius, M.S. Allie, and M. Shackleton, S. Afr. J. Phys. **13**, 103 (1990).

[216] R.F. Wood and G.E. Giles, Phys. Rev. **B23**, 2923 (1981).

[217] R.K. Singh and J. Narayan, Mater. Sci. Eng. **B3**, 217 (1989).

[218] T. Nakamiya, K. Ebihara, P.K. John, and B.Y. Tong, Mat. Res. Symp. Proc. **191**, 109 (1990).

[219] X.D. Wu, T. Venkatesan, A. Inam, X.X. Xi, and Q. Li et al., Mat. Res. Soc. Symp. Proc. **191**, 129 (1990).

[220] R.K. Singh, O.W. Holland, and J. Narayan, J. Appl. Phys. **68**, 233 (1990).

[221] G.D. Mahan, H.S. Cole, Y.S. Liu, and H.R. Philipp, Appl. Phys. Lett. **53**, 2377 (1988).

[222] R.E. Walkup, J.M. Jasinski, and R.W. Dreyfus, Appl. Phys. Lett. **48**, 1690 (1986).

[223] R. Srinivasan, J. Vac. Sci. Technol. **B1**, 923 (1983).

[224] T. Nakayama, M. Okigawa, and N. Itoh, Nucl. Instrum. Meth. **B1**, 301 (1984).

[225] W.R. Donaldson, A.M. Kadin, P.H. Ballentine, and R. Sobolewski, Appl. Phys. Lett. **54**, 2470 (1989).

[226] C. Uher and A.B. Kaiser, Phys. Rev. **B36**, 5680 (1987).

[227] H. Katsuragawa and T. Minowa, Nucl. Instrum. Meth. **B43**, 259 (1989).

[228] M.M. Murnane, H. Kapteyn, and R.W. Falcone, Nucl. Instrum. Meth. **B43**, 463 (1989).

[229] R.F. Haglund, M.H. Mendenhall, and N.H. Tolk, Nucl. Instrum. Meth. **B32**, 321 (1988).

[230] H. van Brug, K. Murakami, F. Bijkerk, and M.J. van der Wiel, J. Appl. Phys. **60**, 3438 (1986).

[231] R.W. Dreyfus, R. Kelly, and R.E. Walkup, Appl. Phys. Lett. **49**, 1478 (1986).

[232] Q.Y. Ying, D.T. Shaw, and H.S. Kwok, Appl. Phys. Lett. **53**, 1762 (1988).

[233] A. Gupta, B. Braren, K.G. Casey, B.W. Hussey, and R. Kelly, Appl. Phys. Lett. **59**, 1302 (1991).

[234] J. Krishnaswamy, A. Rengan, J. Narayan, K. Vedam, and C.J. McHargue, Appl. Phys. Lett. **54**, 2455 (1989).

[235] P.A. Eschbach, J. Dickinson, and S.C. Langford, J. Vac. Sci. Technol. **A7**, 2943 (1989).

[236] A. Caruso and R. Gratton, Plasma Phys. **10**, 867 (1968).

[237] G.E. Jellison and F.A. Modine, Phys. Rev. **B27**, 7466 (1983).

[238] S.J. Thomas, R.F. Harrison, and J.F. Figuera, Appl. Phys. Lett. **40**, 200 (1982).

[239] R. Kelly and R.W. Dreyfus, Nucl. Instrum. Meth. **B32**, 341 (1988).

[240] A. Inam, X.D. Wu, T. Venkatesan, S. Ogale, and C.C. Chang et al., Appl. Phys. Lett. **51**, 1112 (1987).

[241] J.F. Ready, J. Appl. Phys. **36**, 462 (1965).

[242] P.E. Dyer, S. Farrar, and P.H. Key, Appl. Phys. Lett. **60**, 1890 (1992).

[243] C.H. Becker and J.B. Pallix, J. Appl. Phys. **64**, 5152 (1988).

[244] M.A. Kadar-Kallen and K.D. Bonin, Appl. Phys. Lett. **54**, 2296 (1989).

[245] R.J. von Gutfeld and R.W. Dreyfus, Appl. Phys. Lett. **54**, 1212 (1989).

[246] X.D. Wu, D. Dijkkamp, S. Ogale, A. Inam, and E.W. Chase et al., Appl. Phys. Lett. **51**, 861 (1987).

[247] S.B. Ogale and R. Nawathey, J. Appl. Phys. **65**, 1367 (1989).

[248] X.D. Wu, B. Dutta, M.S. Hegde, A. Inam, and T. Venkatesan et al., Appl. Phys. Lett. **54**, 179 (1989).

[249] J.F. Ready, *Effects of high power laser radiation* (Academic, New York, 1971).

[250] I.D. Raistrick, F. Gargan, J.G. Beery, and D.K. Wilde et al., *Science and technology of thin film superconductors* (Plenum Press, New York, 1989), p. 121.

[251] *Laser ablation for materials synthesis*, edited by D.C. Paine and J.C. Bravman Volume 191 of MRS Symp. Proc. (Materials Research Society, Pittsburgh, 1991).

[252] B.K. Roul, A.K. Pradhan, V.V. Rao, and P. Bhattacharya et al., Bull. Mater. Sci. **14**, 713 (1991).